Doctoral Dissertation
Doctoral Program in Material Science and Technology (36th Cycle)

Materiomics analysis of metallic and ceramic materials for musculoskeletal regeneration

Mari Lallukka

******

Supervisor(s):
Prof. E. Verné., Supervisor
Prof. S. Spriano, Co-Supervisor

Doctoral Examination Committee:
Prof. A.B. , Referee, University Of Erlangen-Nuremberg
Prof. D.T. , Referee, Turin Polytechnic University in Tashkent

Politecnico di Torino
2024

Declaration

I hereby declare that, the contents and organization of this dissertation constitute my own original work and does not compromise in any way the rights of third parties, including those relating to the security of personal data.

Mari Lallukka

2024

* This dissertation is presented in partial fulfillment of the requirements for **Ph.D. degree** in the Graduate School of Politecnico di Torino (ScuDo).

Acknowledgment

Embarking on this doctoral journey has been a transformative experience, filled with challenges, growth, and invaluable lessons. I am deeply grateful to Prof. Enrica Verné, Prof. Silvia Spriano, and Dr. Cristiano Carlomagno for their invaluable support and supervision throughout the duration of my thesis and the PREMUROSA project. Their mentorship and encouragement have been instrumental in shaping my academic journey, and I am truly fortunate to have had the opportunity to work under their guidance on such an engaging project. I would also like to extend my heartfelt appreciation to Prof. Marta Miola, Dr. Sara Ferraris, and Prof. Francesco Baino for their indispensable assistance and dedication to my thesis activities. Their willingness to share their expertise, answer my queries, and welcome me into the GLANCE group has been immensely beneficial to my research endeavors.

This PhD project was conducted within the framework of the PREMUROSA project, supported by the European Union's Horizon 2020 research and innovation programme under the Marie Skłodowska-Curie grant agreement No 860462. I am deeply appreciative of all the PREMUROSA project partners, early-stage researchers and collaborators whom I had the privilege of working with during the project. Their contributions and collaborative spirit have enriched my research journey immeasurably.

Throughout my thesis I was lucky to collaborate with various PREMUROSA project partners and spend secondment periods in their laboratories. First, I want to thank Prof. Jonathan Massera, Prof. Susanna Miettinen, and Dr. Amel Houaoui from Tampere University, as well as the Tampere University Microscopy Center,

for their collaboration and support during my secondment period in Tampere, Finland. Their assistance with cell experiments was invaluable to the progression of my research. I am also grateful to Prof. Lia Rimondini, Prof. Andrea Cochis, Dr. Ziba Najmi, Dr. Alessandro C. Scalia, and other colleagues at Università degli Studi del Piemonte Orientale "Amedeo Avogadro" for their guidance and assistance with biological experiments during my secondment at UPO CAAD institute. Furthermore, my sincere thanks go to Kuntay Aktas, Ece Tutsak, Beril Demirbakan and all the other colleagues from BTech Innovation for their hospitality during my secondment in Ankara, Turkey. Their support made my secondment experience in Ankara both productive and enjoyable.

I extend my gratitude to all my colleagues at DISAT, especially the wonderful members of the GLANCE group, who I had the honor to meet while working at the laboratories during these years. This thesis work would have not be possible without your contribution and support.

Finally, I would like to express my gratitude to my family and friends for their love, encouragement, and support throughout this journey. Their belief in me has been a constant source of strength and inspiration, for which I am truly grateful.

Abstract

This PhD thesis combines the results from an individual PhD project part of PREMUROSA project aimed at optimizing materials to elicit targeted cellular responses and laying the groundwork for the production of PREMUROSA reference materials pivotal for the advancement of *in vitro* and *in silico* testing technologies for musculoskeletal applications. By studying a diverse array of tunable material surface properties, this work focuses on the intricate role of biomaterial surface characteristics to modulation of biological response, particularly focusing on titanium alloys and bioactive glasses.

In particular, this project will delve into understanding the role of surface of biomaterials through the characterization and production of reference materials featuring diverse tunable properties. The focus is on titanium alloys and bioactive glasses, either as bulk, micro-, and nano-powders, hierarchical scaffolds with multiscale porosity; tailored compositions obtained by doping with antimicrobial ions or by modulating the surface reactivity and surface functionalization with antimicrobial agents able to modulate the biological response.

A paramount challenge addressed in this research refers to combatting bacterial biofilm formation while concurrently facilitating bone regeneration—a critical aspect in orthopedic infection treatment. Traditional systemic antibiotic therapies often fall short due to biofilm resilience and concerns over bacterial resistance. Thus, the pursuit of antibiotic-free alternatives capable of fostering bone regeneration while preventing bacterial infection remains imperative.

Multifunctional biomaterials, such as those investigated here, hold promise in addressing these challenges.

The first part of this work centers on optimizing the surface functionalization process to immobilize the antimicrobial peptide nisin onto titanium alloy surfaces without resorting to toxic linkers and preventing the surface micro- and nanoroughness. Through systematic adjustments of process parameters such as pH value, enhanced efficacy of nisin immobilization was achieved, culminating in promising anti-microfouling activity against *Staphylococcus aureus (S.aureus)*. Notably, the chemically treated titanium condition exhibited antibacterial effect, due to a synergistic interplay and between nanotextured surfaces and nisin, underscoring its potential in bone-related applications.

In the next part, bioactive glass disc surfaces, were successfully doped with either ionic Cu^{2+} (Cu-SBA3) or Ag^{+} (Ag-SBA2) through an ion exchange process in aqueous solution. The concentration of the Cu(II)acetate ion exchange solution was optimized, with 0.001 M being chosen for further analyses. The Cu-doping of SBA3 surfaces was found to maintain their amorphous nature and enhance *in vitro* bioactivity, while also demonstrating significant antibacterial activity against *S.aureus.* While challenges regarding cytocompatibility of doped glasses with respect to human adipose stem cells (hASCs) were encountered, particularly with Cu-SBA3, strategies such as pre-incubation and indirect culture hold promise in mitigating cytotoxic effects. In addition, in the case of Ag-SBA2, cytocompatibility was significantly improved with an adsorbed layer of fibronectin protein on the glass surface before cell seeding.

The study also explores the fabrication of porous bioactive glass-ceramic scaffolds by foam replica method. Two different sintering temperatures were compared: one resulting in an amorphous scaffold (620 °C), and another one yielding a glass-ceramic one (850 °C). Both scaffolds closely resembled the 3D architecture of natural trabecular bone and exhibited high porosity of

approximately 75 vol.%. However, due to its superior mechanical properties, only the glass-ceramic scaffold was the focus of further analysis. The scaffolds demonstrated high *in vitro* bioactivity and mechanical strength, and additional antibacterial properties provided by silver doping by ion exchange. The scaffold developed in this study could find a possible application as a bone substitution material with antibacterial properties without using traditional antibiotics.

Despite the remaining challenges, the findings presented in this thesis provide valuable insights into the varied biological responses induced by various biomaterial surfaces, serving as a promising basis for future research endeavors to advance multifunctional biomaterial surfaces for musculoskeletal applications.

Contents

List of Figures

List of Tables

Introduction

The PREMUROSA project, standing for “Precision medicine for musculoskeletal regeneration, prosthetics, and active aging” embodies a foundational concept of “to take care with care”. The ultimate goal of the project is to combine the personalized clinical approach with individual “omic” characterization and the discerning selection of medical devices. The suffix -omic deals with the collective characterization and quantification of pools of biological molecules that translate into the structure, function, and dynamics of an organism or organisms. Generally speaking, it refers to approaches considering a totality of features. This approach holds the potential to yield reliable tools for treatment selection, leveraging the development of *in vitro* tests and decision support systems (DSS). Specifically, these tools are tailored towards precise, patient-centered applications of regenerative technologies within the musculoskeletal field, encompassing tailored diagnostic measures and customized targeted therapies, thereby presenting a new perspective in musculoskeletal healthcare.

The scientific objectives of the PREMUROSA project include:

1) To gain a deep understanding of the role and interactions among materials, extracellular matrix, cells and tissues in musculoskeletal regeneration, taking into account patient morbidity, immunological status, and age;

2) To develop new *in vitro* assays to test medical devices under conditions closer to clinical reality than the ones currently available, and to forecast personalized clinical healing and regeneration response;

3) To develop new *in silico* models and DSS to test medical devices under conditions closer to clinical reality;

4)To generate a biologically integrated multi-OMIC signature to predict healing and regeneration.

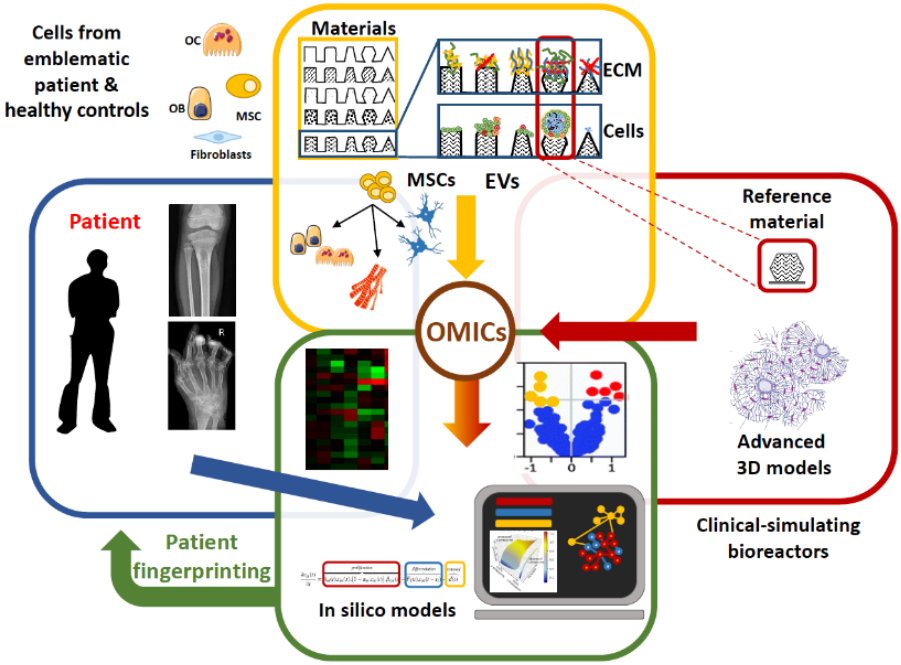

Figure 1. The scientific objectives of the PREMUROSA project

The PREMUROSA project, funded by the European Commission under the Horizon 2020 programme (Marie Skłodowska-Curie Actions Innovative Training Network) involves 13 Early-Stage Researchers working with individual Ph.D. projects, hosted by the PREMUROSA European Consortium of universities, research institutes and companies in Italy, Switzerland, Portugal, Finland, Latvia, Ireland, and Serbia. My Ph.D. project is one of these 13 projects, hosted by Politecnico di Torino, in Turin, Italy.

The specific goal of my Ph.D. project, entitled “Materiomics analysis of metallic and ceramic materials for musculoskeletal regeneration” is to explore the correlation between the physicochemical attributes of metallic and ceramic materials—such as chemistry, surface morphology, and hierarchical porosity—

and the functionality of cells and tissues. By definition, the term materiomics refers to this study of the relationships between molecular, physicochemical, and/or processing properties for materials (1). The project seeks to optimize the materials to elicit specific cellular responses, collecting basic data on biomaterials' main properties, and based on this information to produce project reference materials. These reference materials can be then utilized in the new *in vitro* and *in silico* testing technologies developed by the PREMUROSA project, ultimately enhancing the performance of biomaterials in tissue regeneration and healing. For instance, the ion-doped bioactive glasses described in Chapter 4 of this thesis are a part of PREMUROSA project reference materials, and have been prepared by me and then utilized by other ESRs of the project for immunological analyses (Appendix B).

In particular, this project will delve into understanding the role of surface and porosity of biomaterials through the characterization and production of reference materials featuring diverse tunable properties. The focus is on titanium alloys and bioactive glass, either as bulk, micro-, and nano-powders, hierarchical scaffolds with multiscale porosity; tailored compositions obtained by doping with therapeutic ions or by modulating the surface reactivity; and surface functionalization with various moieties able to modulate the biological response.

The thesis has been organized with the following structure.

Chapter 1: a brief description of the most relevant surface properties of biomaterials and their characterization.

Chapter 2: a summary of the biological phenomenon occurring after the implantation into the body.

Chapter 3: this chapter covers the work regarding surface functionalization with an antimicrobial peptide nisin, performed both on titanium alloy and

bioactive glass surfaces. The results of this chapter are included in two published manuscripts:

1) M. Lallukka et al., “Surface Functionalization of Ti6Al4V-ELI Alloy with Antimicrobial Peptide Nisin”, 2022, Nanomaterials;
2) V.A. Gobbo, **M.Lallukka** et al., ”Functionalization of a chemically treated Ti6Al4V-ELI alloy with nisin for antibacterial purposes”, 2023, Applied Surface Science.

In addition, another work regarding titanium alloys os covered in the Appendix A, where a titanium alloy 3D lattice structure was chemically treated and characterized in terms of the effect of the chemical treatment to lattice structure and morphology.

Chapter 4: the focus of this chapter is the surface doping of bioactive glasses with therapeutic metal ions, with emphasis on antimicrobial activity. The experimental part of this chapter covers both physicochemical and biological characterization of doped glass surfaces. The results of this chapter are included in two published manuscripts:

1) M.Lallukka et al., “In vitro cytocompatibility of antibacterial silver and copper-doped bioactive glasses”, 2023, Ceramics International;
2) M.Lallukka et al., “Cu-doped bioactive glass with enhanced in vitro bioactivity and antibacterial properties”, 2024, Ceramics International.

Chapter 5: the realization of 3D porous bioactive glass-ceramic scaffolds doped with antibacterial silver ions.

Chapter 6: the final conclusion and future outlooks for this research work.

Appendix A: Characterization of nanotextured titanium alloy lattice structure surfaces for bone integration

Appendix B: Article: Human T-cell responses to metallic ion-doped bioactive glasses

Chapter 1: Surface properties of biomaterials and their characterization

1.1 Introduction

Distinguishing between material bulk properties and surface properties is essential. The surface of the material consists of the zone where the structure and composition differ from the average (bulk) (2). Bulk properties of a material include elastic modulus, hardness, fracture toughness, wear resistance, and elemental composition. Instead, regarding the surface properties, factors such as topography, surface chemical composition, surface energy, and wettability are of interest.

In the context of implantable orthopedic devices, the surface assumes great importance as it is the initial interface with the biological environment. Surface properties play a direct role in post-implantation protein adsorption and subsequent biological responses from immune cells, as will be discussed in the next chapter (3). Factors such as chemical composition, surface energy, roughness, and topography significantly influence osseointegration, eventual bacterial contamination, and foreign body reaction, ultimately determining the fate of the implant.

A surface can be described by a multitude of different parameters. The more of these parameters are measured the more complete idea of the surface properties is achieved. Regarding the different surface characterization methods, each technique has its advantages and limitations, but when used in conjunction, they offer comprehensive analyses of surface properties. Table 1 summarizes some of

the most common surface characterization methods of biomaterials, which will be further elaborated in the upcoming sections of this chapter.

Table 1: Summary of common methods for biomaterial surface characterization (2)

Method	Principle	Analyzing depth	Spatial resolution	Analytical sensitivity
Contact angle	Measure of surface energy by wetting the surface	3-20 Å	1 mm	Depending on the chemistry and topography
XPS	X-rays induce the emission of electrons of characteristic energy	10-250 Å	5-150 µm	0.1 at%
SIMS	Ion bombardment sputters secondary ions from the surface	10Å-1µm	100Å	Very high
FTIR-ATR	IR radiation is adsorbed and excites molecular vibrations	1-5µm	10 µm	1 mol%
AFM	Mechanical probe interacts with sample surfaces through interatomic forces	20 Å	20-30 Å in the lateral direction, 1Å in the vertical direction	High
SEM-EDS	Secondary electron emission induced by a focused electron beam is spatially imaged; EDS: analysis of emitted X-rays from sample bombarded with electron beam	0.3-5.0 µm	10-40Å	High
Solid surface Zeta potential	The measurement of electrokinetic effect to assess charging behavior at solid-	-	-	Depending on specimen and measurement

	liquid interface			conditions
Profilometry	The measurement on height variations across surface	Up to 2.5 mm	Vertical resolution 5 Å, lateral resolution limited by the tip shape	High but less than AFM

This chapter comprises a literature review of the properties of material surface that can influence biological response, and the most common methods to characterize them. In addition, surface functionalization and modification in order to enhance material osseointegration and antibacterial activity, for example, are discussed.

1.2 Surface morphology and topography

Surface roughness refers to the small-scale fluctuations in the height of a physical surface, distinct from larger-scale variations inherent in the surface geometry. Numerous roughness parameters exist, with the most commonly utilized one being the roughness arithmetic average height parameter (Ra) (4). Ra represents the mean of the average height differences, providing an overview of the roughness level across the analyzed surface (Figure 2). However, Ra solely addresses the 2D profile. For a more comprehensive assessment encompassing the 3D surface area, the Sa value, an extension of Ra, is employed. Sa describes the arithmetic mean height of the scale-limited surface and it is the areal (3D) equivalent of two-dimensional Ra, calculated across the entire area of the dataset (5).

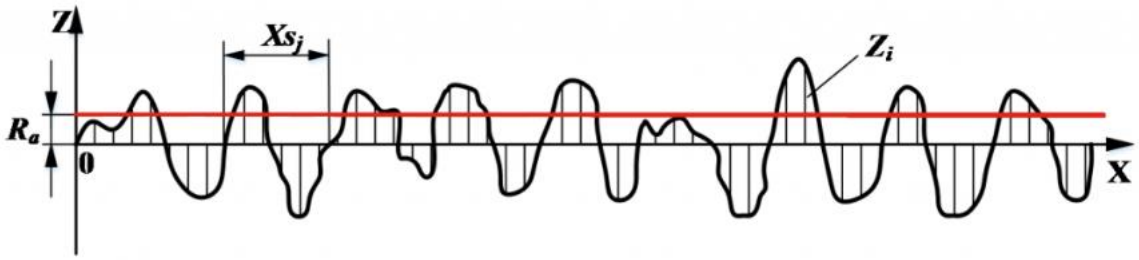

Figure 2: Roughness parameters. Ra: arithmetic average height; Xsj: spacing length of profile element; Zi: height of a single discrete point on the surface (6)

For a deeper understanding of roughness, additional profile roughness parameters such as R_z, R_q, and R_{sk} offer valuable insights. R_z quantifies the measurement between the highest peak and lowest valley within the sampling length, essentially providing the maximum height of the profile. R_q, on the other hand, calculates the root-mean-square deviation of the profile, offering a measure of the overall roughness. Meanwhile, R_{sk} indicates the skewness, or asymmetry, of the profile about the mean line (4).

Various types of surface topographies have been identified, each with distinct characteristics and implications (7):

●Irregular topography: Characterized by irregular shapes, exhibiting random distribution and profiles in both 2D and 3D observations.

● Ultrafine grains: Surface preparation techniques can reveal grain boundaries in ultrafine materials, serving as nanostructuring defects. The homogeneity of this structuring is determined by the form of the grains.

● Hierarchical architecture: Features in this topography display periodic and homogeneous distributions. Beam-based techniques are instrumental in replicating microbumps, pillars, or polygonal figures.

● Grooves: Specific surface patterning consisting of channel-like forms with varying widths and depths.

●Multiscale surface topography.

Surface roughness measurements can be conducted using tools like a profilometer or laser scanner, as well as confocal microscopy. A profilometer serves to analyze the surface topography of solid samples, enabling the determination of surface roughness and morphological features by tracking surface changes. Contact profilometry involves a stylus, making vertical contact with the sample while traversing laterally. Instead, non-contact optical profilometry presents an alternative without physical contact. In general, contact profilometry offers superior lateral resolution compared to optical profilometry, and it exhibits resilience against sample surface contaminants. However, optical profilometry can be useful in some situations. A significant benefit lies in high vertical resolution and its non-destrcutive nature, safeguarding both instrument and samples from wear or mishandling (8).

Atomic Force Microscopy (AFM) offers subnanometer resolution surface imaging and detailed surface mechanics and molecular interactions. AFM measures the deflection of a tip mounted on a flexible cantilever arm due to van der Waals forces and electrostatic interactions between the tip and the surface atoms. Various modes such as contact, tapping, and noncontact are based on specimen properties. Contact mode AFM is relatively similar to contact profilometry, except having a higher spatial resolution and a smaller measurement range (8). Kelvin Probe Microscopy (KPFM), on the other hand, maps the spatial distribution of surface potential, providing additional insights into surface properties. (9)

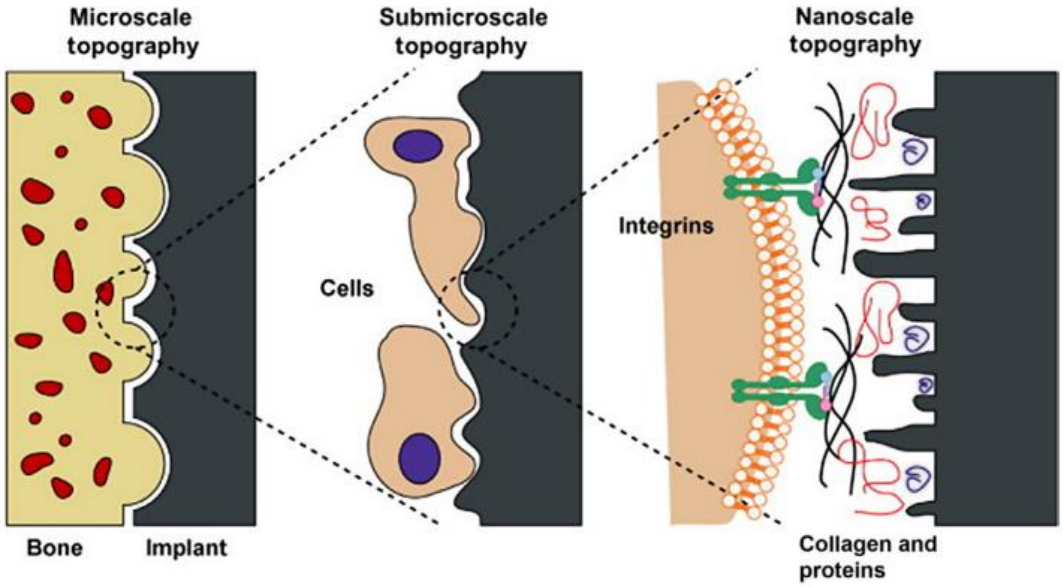

Figure 3: Cell response to material in different topographical scales (10)

Surface topography plays an important role in modulating various cellular responses and interactions. Designing specific structures on material surfaces at micro or nanoscales can mimic natural environments for cells, as illustrated in Figure 3. Micrometer-scale topography influences cell activities by providing attachment points for stabilization and facilitating bone growth (11). At the nanoscale, surface topography enhances interaction with the extracellular matrix (ECM) (12,13) by increasing the surface area available for interaction with proteins, cytoskeleton components, and more.

Parameters like size, width, sharpness, spacing, and height-to-width ratios, along with nature-mimicking strategies, impact both morphology and physicochemical properties such as surface energy or wettability. By manipulating the height and depth of surface features, the density of adsorbed proteins can be controlled, influencing inflammatory cytokine secretion, macrophage fusion, biofouling, focal cell adhesion, proliferation, and fibrotic encapsulation (3). Typically, osteoblastic cells, which are twice the size of fibroblasts, and bacteria tend to adhere more readily to rough surfaces, whereas fibroblasts exhibit a

preference for smoother surfaces, likely due to the contact guidance effect. (7). Additionally, topography and roughness affect cellular orientation and contact guidance (14). Cells exhibit specific morphological responses to substrates with features as small as 100 nm and depths as small as 75 nm, favoring reduced cell spreading, adhesion complex formation, and filopodia formation on nanoposts and nanopits. However, exceptions exist, with certain cell types like human-derived leukocytes, keratinocytes, and monocytes responding differently to nanogratings (15).

Regarding cell proliferation, the mechanism behind cell–nanotopography interactions involves a complex interplay of geometry, length scale, substrate material, and cell types (16). Nonetheless, reduced proliferation rates are observed on nanogratings compared to planar surfaces (17). Interestingly, enhanced proliferation occurs under specific combinations of nanoposts and pits, further demonstrating the complexity of the effect of topography on cell responses. Moreover, cellular migration is influenced by nanotopography, with migration biased towards the grating axis and increased migration velocities observed in various cell types including endothelial cells, epithelial cells, osteoblasts, and C6 glioma cells (18).

The integration of multiscale roughness has the potential to enhance the adhesion, proliferation, and/or differentiation of various cell types. However, it also raises the likelihood of biofilm formation (bacterial adhesion) if the roughness threshold of 0.2μm is exceeded (19). The impact of micro-nanoscale topography on bacterial adhesion is primarily determined by bacterial characteristics. Bacterial cells, being smaller and more rigid than other cell types (such as osteoblasts, fibroblasts, and epithelial cells), do not necessarily require the presence of an extracellular matrix (ECM) to adhere and proliferate on surfaces (20). Generally, bacterial adhesion is enhanced on rough surfaces due to surface irregularities such as valleys, irregular shapes, and edges, as well as

sensitivity to nanoscale features on the material surface, which are smaller than the size of bacteria (21).

Surface nano-texturing seems to be less important in the case of bioactive glasses that are inherently reactive upon contact with biological fluids and tend to be coated by a surface HCA layer. It was demonstrated that the higher the surface nano-porosity, the higher the specific surface area and, hence, higher the apatite-forming kinetics of bioactive glasses (highly-porous sol-gel vs. melt-derived material, however, fast bioactive reactions were observed both in vitro and in vivo (actual bonding to hard and soft tissues) also when non-porous biomedical glasses are used (22).

1.3 Surface chemistry and composition

The surface of a material exhibits distinct chemical bond characteristics compared to its bulk, necessitating separate consideration. While assemblies of atoms and/or molecules within the bulk experience uniform exposure to various types of attractive forces as detailed in Table 2, surface structural units undergo asymmetric pulling solely from the units beneath them. This lopsided attraction distorts the electron distributions of surface atoms or molecules, leading to the emergence of surface energy as excess energy linked to this disparity. Consequently, surfaces always possess unique reactivities and properties (23).

Table 2:Summary of interatomic forces (23)

Interatomic force	Explanation	Relative Strength	Examples
Van der Waals	Transient fluctuations in the spatial localization of electron clouds surrounding atoms lead to transient positive and negative charges, and consequent interactive forces in molecules can have permanent or transient polarity	Weak	Protein structure
Ions	Ions with a positive charge attract ions with a negative charge	Very strong	Na-Cl
Metallic	The attractive force between positively charged nuclei and delocalized electrons	Medium-strong	Titanium
Covalent	A sharing of electrons between two atoms	Strong	C-C

Characterization of the surface chemistry is necessary if the properties and performance of the native or modified surface of any material are to be understood. Surface chemistry and composition analysis include various techniques offering information about the elemental composition and molecular environment of materials.

Among these techniques X-ray photoelectron spectroscopy (XPS) relies on the photoelectric effect, where X-rays are directed onto the sample, causing the emission of core level (inner shell) electrons (2). By measuring the energy of these emitted electrons, information about the atoms' nature and chemical environment is obtained. Because atoms contain varying numbers of electrons with differing binding energies, every element generates distinct peaks in the photoelectron spectrum. The intensity of these peaks directly correlates with the concentration of the element (8).

XPS commonly starts with a survey scan spanning 1000 eV, followed by scanning smaller energy ranges in higher resolution to identify specific features. XPS provides semiquantitative determination of the surface elemental composition within the outermost 10 nm, with the ability to identify elements present at concentrations > 0.1 atomic % (excluding H and He). It also offers insights into molecular environment factors such as oxidation state and bonding atoms. XPS allows non-destructive elemental depth profiling up to 10 nm into the sample, with destructive profiling reaching several hundred nanometers. Despite its high information content and rapid analysis, due to the extreme surface sensitivity, any contamination on the surface can lead to false results (8). In addition, XPS can be high in cost, and it requires vacuum compatibility, which can impact the specimen.

Another technique, aside from XPS, for gathering supplementary insights into the molecular structure of a material's surface is secondary ion mass spectrometry (SIMS)(24). This method involves bombarding the surface with a beam of accelerated primary ions or atoms within ultra-high vacuum conditions. Upon impact, these particles traverse the surface, dissipating their kinetic energy through a collision cascade. Consequently, neutral particles, electrons, and positively or negatively charged "secondary" ions are emitted. SIMS exclusively measures these secondary ions, contrasting with XPS, which analyzes the energy

of emitted particles (electrons). SIMS determines the mass of emitted ions using a time-of-flight (TOF) mass analyzer, magnetic sector analyzer, or quadrupole mass analyzer, generating a mass spectrum representing the outermost 1-2 nm of a surface (2).

Scanning electron microscopy (SEM) is an electron microscopic technique that scans a focused energetic electron beam from an electron gun to the sample and this way imaging the sample surface. It provides high-resolution surface imaging, primarily used for material topography visualization. For non-conductive materials, a metallic coating is necessary, with the resulting image reflecting the coating surface rather than the underlying material. SEM is generally equipped with an Energy-Dispersive X-ray Analysis (EDS) detector for elemental analysis or chemical characterization. EDS relies on the detection and investigation of the characteristic X-rays produced by the primary electrons of the sample to identify elements deeper within the specimen (>1 micron) (2). Therefore, EDS is not a very surface sensitive method, and in addition, the overlapping peaks of several elements in the EDS spectrum affect the result.

When infrared (IR) light irradiates a sample, absorption transpires if the IR frequency aligns with a bond's vibrational frequency. Consequently, analyzing the transmitted or absorbed IR light provides insights into the molecular structure, constituting the method known as IR spectroscopy (8). Particularly, Fourier Transform Infrared (FTIR) spectrometry in Attenuated Total Reflectance (ATR) mode in the context of biomaterials, offers insights into molecular bond vibrations. It is widely used due to its versatility and low cost compared to other techniques. While its penetration depth ranges from 1-5 μm, making FTIR less surface-sensitive, it observes a broad region near the surface, providing valuable information on specific chemistries and structural orientation (25).

The interaction between the surface and the biological environment is determined by the surface chemical composition, directly impacting protein

adsorption and cell behavior on the material. (26). Research has demonstrated that a range of physical and chemical characteristics of materials play a significant role in shaping cell behavior. Among these factors, functional groups serve as crucial chemical cues, influencing the fate of various cell types including stem cells, osteoblasts, and myoblasts. For instance, Cao et al. (2017) observed that neutral surfaces containing $-CH_3$ and un-charged $-OH$ groups resulted in reduced protein adsorption, cell spreading, and adhesion, but facilitated a greater extent of chondrogenic induction compared to charged surfaces containing $-COOH$ and $-NH_2$ group (27).

1.4 Surface energy and wettability

Wettability, a crucial characteristic, is often quantified through the contact angle—a numerical indicator of a solid's interaction with a liquid. Geometrically, this angle (denoted as θ) is formed at the three-phase boundary where liquid, gas, and solid intersect. The contact angle serves as a classifier for materials, categorizing them as either hydrophobic (water contact angle exceeding 90°) or hydrophilic (water contact angle below 90°). The common method for measuring involves assessing the sessile drop contact angle, where the droplet remains static, and the three-phase boundary remains stationary. This approach not only determines the contact angle but also allows for the measurement of the surface free energy of the substrate.

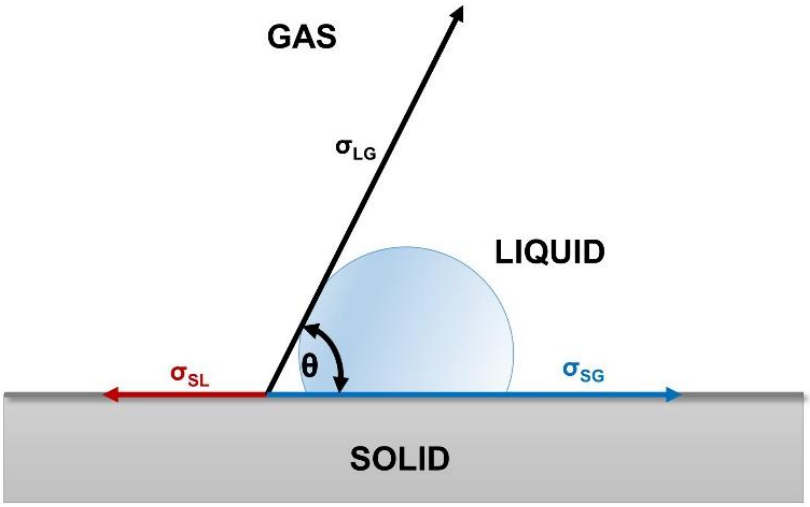

Figure 4: Contact angle. σ_{SG}: surface tension at the solid and gas interface; σ_{SL} : interfacial surface tension between solid and liquid; σ_{LG} : surface tension of the liquid.

The surface free energy, a relative measure of surface energy, is closely linked to the strength of bulk interactions and the extent of surface exposure. In essence, a higher surface energy indicates either stronger bulk interactions or a greater degree of surface exposure.

In general, a surface characterized by low surface energy tends to exhibit a high contact angle, indicative of low wettability. This is attributed to the surface's inability to form strong bonds, resulting in minimal energetic reward for the liquid to disrupt bulk bonding in favor of interacting with the surface. Conversely, surfaces with higher surface energy typically show lower contact angles, translating to better wetting. Materials like glasses, ceramics, metals, and others, held together by stronger bonds, generally possess elevated surface energy.

The relationship between contact angle and surface energy is articulated through Young's equation:

$$\sigma_{SG} = \sigma_{SL} + \sigma_{LG} \cdot \cos\theta$$

From the biological standpoint, a threshold at the contact angle of 65-70° (about 40 mN/m in terms of surface energy) is often reported considering that surfaces with a contact angle below this threshold are usually tissue integrated, surfaces at the threshold level are usually cytocompatible, but non-adhesive for several cells, and surface above this threshold are often cytotoxic (the Berg limit) (28). According to existing literature, increased surface hydrophilicity corresponds to enhanced cell adhesion, observed in both osteoblasts and fibroblasts (29,30). Surfaces with almost 0° of contact angle are a different case because of the very limited adsorption of proteins included those with the RGD sequence which are needed for osteoblasts and/or mesenchymal cells adhesion. Regarding bacteria, a hydrophilic surface and, conversely, a super-hydrophobic surface (water contact angle above 150°) tend to inhibit bacterial attachment (31). However, environmental factors such as pH, shear stresses, forces, and certain bacterial strains with hydrophobic characteristics can influence adhesion. Consequently, studying the isolated impact of surface wettability on cell and bacteria adhesion is complex. Ideally, achieving a balance between preventing bacterial attachment and facilitating the adhesion of desired cells involves considering factors like the equilibrium between hydrophobic and hydrophilic groups.

1.5 Surface charge and zeta potential

Zeta potential characterizes the charging dynamics at interfaces, prevalent in colloidal systems and macroscopic solid surface analysis. In solid-liquid interface, zeta potential provides insights into the surface charge when in contact with water, particularly vital for materials employed in applications within aqueous systems, such as biomaterials interfacing with fluids in the human body. The electrostatic forces of attraction and repulsion are intricately linked to the solid surface zeta potential, offering valuable information about the functional groups on the surface that interact with the surrounding solution. This charging behavior

can be further demonstrated through the model of the electrical or electrochemical double layer (EDL).

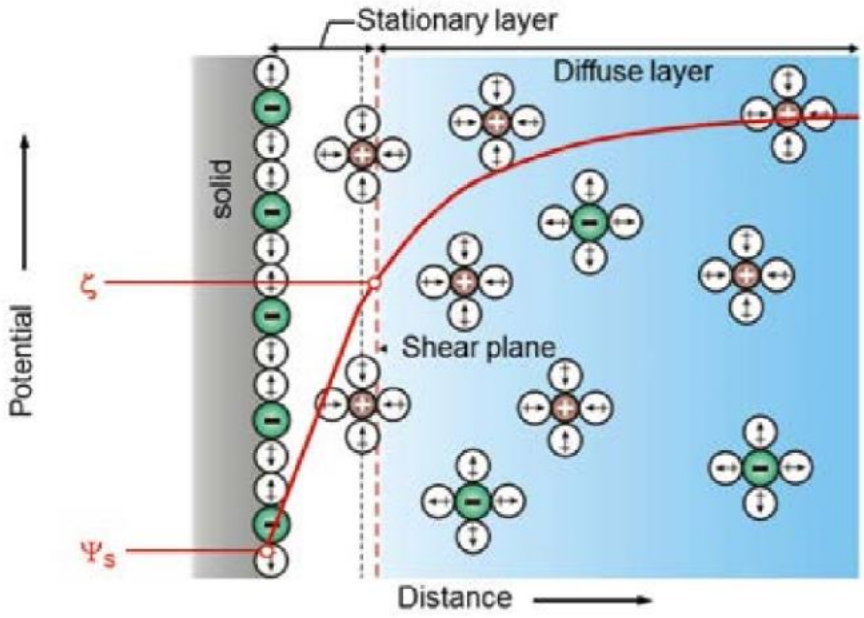

Figure 5: EDL model at the solid-liquid interface (32)

The model discerns between a stationary, immobile layer and a diffuse, mobile layer of counterions, compensating for the surface charge, and establishing inner and outer Helmholtz planes. Zeta potential ζ can be defined as the potential at the boundary (or "shear plane") between the stationary layer and diffuse layer.

Surface charge generation at the interface occurs through two primary mechanisms:

1) Acid-base reactions between surface functional groups and aqueous solution. The acidic groups dissociate, maintaining a negative charge, while basic groups get protonated, assuming a positive charge. The pH of the aqueous solution acts as the driving force, with a higher pH resulting in an increased

concentration of OH^- ions, rendering the surface negatively charged, and vice versa.

2) Adsorption of water ions. Even surfaces lacking functional groups exhibit a zeta potential due to the hydrophobic nature of the surface. Water molecules are replaced by water ions, and the preferential adsorption of OH^- ions typically leads to a negative zeta potential on hydrophobic surfaces.

In the case of planar solids, the Helmholtz-Smoluchowski equation can be used:

$$\zeta = \frac{dl_{str}}{d\Delta p} \times \frac{\eta}{\varepsilon \times \varepsilon_0} \times \frac{L}{A}$$

Where $\frac{dl_{str}}{d\Delta p}$ is the streaming current coefficient,

L is the length of the rectangular slit channel between two planar surfaces,

A is the cross-section, channel width multiplied by gap height,

η is the viscosity of the electrolyte solution,

ε x ε_0 is the dielectric coefficient of the electrolyte solution.

Zeta potential is subject to various influential factors. Among them, the pH value stands out as the most critical parameter, offering valuable insights through pH titration. The isoelectric point (IEP), characterized by a zeta potential of 0 mV, (where the electrokinetic net charge density becomes 0 C/m^2) signifies an equilibrium between negatively and positively charged surface groups. IEP is a strong indicator of the surface's functional group chemistry. In cases where only one type of surface group is present, the IEP becomes linked to the acidic or basic

strength of that group and its corresponding pK value. Or in other words, the complete dissociation for acidic surface groups or the complete protonation for basic surface groups. Regarding other properties, zeta potential decreases with increasing ionic strength, attributed to the compression of the electrochemical double layer at higher ionic strengths. Therefore, the recommended ionic strength for solid surface analysis is 0.001 mol/L. However, zeta potential remains independent of temperature, sample size, roughness, and surface porosity. While bulk material porosity can influence streaming current measurements, the method remains unaffected by electronic conductance, enabling the analysis of metal surfaces.

The impact of surface charge extends its influence over crucial aspects such as protein adsorption and interactions with immune cells (3). Contrary to atomic-scale electrostatic interactions, protein adsorption is intricately guided by the overall charge of the surface (33). Understanding the isolated effects of surface charge alone poses challenges, yet the general consensus underscores the efficacy of negative surface charges in preventing nonspecific protein adsorption (34).

The prevention of protein adsorption to material surfaces is often associated with maintaining a neutral net charge (35). Zwitterionic materials, composed of moieties featuring both positive and negative charges, adopt a specific structure that achieves a balanced neutral charge. This distinctive arrangement fosters the creation of a hydration layer through electrostatic interactions with water molecules. Consequently, zwitterionic materials exhibit remarkable antifouling properties, efficiently impeding protein adsorption on their surfaces (36).

Surface charge plays a pivotal role as the second factor controlling protein adsorption, with higher adsorption rates observed at pH levels closer to the isoelectric point (IEP) of the protein (37). At the IEP, proteins have a neutral net charge, minimizing electrostatic repulsion between proteins and the surface and allowing for higher packing densities. Additionally, protein spreading is reduced

at the IEP due to increased structural stability and intramolecular electrostatic interactions (38,39). Changes in pH can lead to protonation or deprotonation of functional groups on proteins and surfaces, altering their electrostatic interactions (40). Although adsorption rates are higher when protein and substrate bear opposite charges, the total mass load is typically maximized at the IEP (41).

The physicochemical characteristics of material surfaces, such as surface charge, wettability, and topography, significantly influence bacterial adhesion and biofilm formation. In aqueous mediums with nearly neutral pH, bacteria typically exhibit a negative surface charge, though this can vary based on species, surface structure, population, culture time, and ion strength (42). Bacterial wettability in aqueous mediums tends to be hydrophobic, facilitating adhesion to hydrophobic surfaces by interacting with deposited proteins (43). Surface charge type moderates protein adsorption, cell, and bacterial adhesion. Surfaces with positive charges, often aided by metal oxides, promote protein adsorption and stimulate osteoblast cell attachment (44). Despite bacterial adhesion being primarily influenced by topography, a negative surface charge can help reduce bacterial deposition on material surfaces (43).

1.6 Surface functionalization

Surface functionalization represents a pivotal step in biomedical material engineering, involving the alteration of surface properties through the attachment of molecules or substances using physical or chemical methods, or a combination thereof. This process aims to enhance various aspects including physical, chemical, and biological characteristics (45). The surface engineering focus revolves around controlling physicochemical properties such as wear and corrosion resistance, mechanical attributes like strength and toughness, as well as biochemical features such as cell assembly and growth, biofilm inhibition, and protein adsorption.

Diverse methodologies are employed for surface functionalization, broadly categorized as physical or chemical approaches. Certain technologies can have the involvement of multiple physical and chemical processes. Thus, it is impossible to strictly separate physical and chemical methods. The classification mainly depends on the main idea behind each technology. Physical methods entail processes like surface coating, roughening, grafting, and patterning, while chemical techniques involve surface activation and covalent or wet chemical modifications.

Physical approaches typically involve non-destructive methods such as physical adsorption or "immobilization," where target molecules are absorbed onto the substrate through forces like electrostatic interactions or hydrogen bonding. Examples include techniques like the Langmuir-Blodgett method and electrophoretic deposition. Conversely, chemical approaches encompass surface activation methods like alkali hydrolysis or covalent adsorption, facilitating covalent bonding between molecules and the substrate surface.

The development of multifunctional surfaces represents a popular approach in response to the rise of antibiotic-resistant bacteria. Especially strategies for antibacterial action while simultaneously enhancing osseointegration are gaining traction. Antibacterial methods can be either passive, aimed at preventing bacterial adhesion and biofilm formation through structural or chemical modifications without releasing bactericidal agents, or active, involving the release of antibacterial agents killing the bacteria (46,47). Inherent antimicrobial properties of materials, including their chemical composition, wettability, surface energy, and topography, play a role in their effectiveness. Furthermore, delivering antimicrobial agents directly onto material surfaces enables targeted delivery of substances such as metal oxides, polymers, antimicrobial peptides, enzymes, quorum sensing drugs, or bacteriophages, offering versatile options for combating bacterial contamination (48). These agents offer the advantage of localized

delivery with reduced dosages compared to systemic administration. The metallic therapeutic ions will be explored further in Chapter 4, while organic choices involve biomolecules such as antimicrobial peptides with further discussion available in Chapter 3. Additionally, the incorporation of nanostructured coatings and biomimetic interfaces can augment antibacterial efficacy.

Balancing the need for fast versus long-lasting effects is essential. Simple adsorption followed by diffusion may lead to a burst release, while surface degradation can yield more controlled and reproducible kinetics. Bulk erosion, however, can result in unpredictable release patterns, highlighting the importance of tailored release mechanisms for specific applications.

1.6.1 Functionalization of bioactive glass

The functionalization of bioactive glass surfaces draws inspiration from established techniques used on various substrates such as pure silica, common glasses, metals, and polymers. These modifications aim to enhance several aspects of bioactive glasses, including biological activity, biomolecule bonding, cellular behavior modulation, drug delivery optimization, toxicity mitigation, antimicrobial properties, anti-cancer capabilities, and disease identification and management (49,50).

The primary objective of introducing reactive sites on bioactive glass surfaces is to facilitate the grafting of biomolecules or drugs, thereby enhancing the biological response of artificial substrates. Upon exposure to water-based media, glasses naturally expose -OH functionalities, which can be exploited for functionalization purposes. Researchers have extensively investigated optimizing hydroxyl group exposure and activation through methods such as washings and soaking in aqueous solutions with varying pH levels (acetone, water, H_2SO_4, NaOH, and SBF) (51–53).

Some efforts to introduce functional groups on bioactive glass surfaces serve as preliminary steps for subsequent biomolecular grafting. Silanization stands out as a well-established and widely utilized technique for effectively and stably introducing reactive functionalities on inert glass surfaces. Silanes, particularly 3-aminopropyltriethoxysilane (APTES), are commonly employed for introducing amino groups (-NH_2) on bioactive glass surfaces. APTES grafting can be achieved using aqueous (54,55), toluene (56), or ethanol (51) solutions. Glutaraldehyde (GA) is another agent often associated with APTES use, serving to facilitate protein attachment on glass surfaces and enhance protein binding ability (22).

Various functionalization strategies are employed to improve the bone integration of bioactive glass implants. These strategies include grafting proteins from the extracellular matrix (ECM proteins), peptides, bone morphogenetic proteins (BMPs), angiogenic growth factors (VEGF), collagen, fibronectin, and alkaline phosphatase onto different substrates. Biomolecules are anchored using techniques such as silanization, tresyl chloride activation, plasma surface activation, and the electrospray technique.

Additionally, tetraethoxysilane (TEOS) can be employed as a surface-modifying agent for bioactive glass, forming a silica layer with a negative charge (i.e., Si-O−). In another example, collagen was successfully used to cover the surface of bioactive glass-based porous scaffolds, leading to improved biological activity and mechanical properties without compromising scaffold macroporosity (57). The modification of bioactive glass surfaces using ion exchange techniques, such as the BG core-shell system, has shown promise in conserving non-crystalline structure and increasing surface reactivity (58).

Functionalized bioactive glasses also hold potential in anticancer applications, such as surface grafting of chemotherapeutic drugs combined with specific targeting molecules like folic acid. Natural polyphenols grafted onto bioactive glass surfaces have demonstrated the ability to promote the growth of healthy

osteoblast cells while selectively targeting cancerous cells. This approach offers controlled drug uptake and release, harnessing the benefits of natural biomolecules for enhanced biocompatibility and reduced toxicity (59). The utilization of functionalized bioactive glasses in combination with natural herbal medicines is an emerging area of interest, driven by their potential health benefits and low toxicity (60).

1.6.2 Functionalization of titanium and its alloys

Titanium and its alloys play a significant role in the biomedical field due to their exceptional properties (61–63). However, they are often considered inert metals, lacking the ability to adequately stimulate osteoblast proliferation and bone growth. (64,65). Moreover, implant-related infections remain a leading cause of failure in titanium implants. As a result, extensive research has focused on enhancing the antibacterial properties and biological functions of titanium implants while improving their wear and corrosion resistance (66,67).

Various surface modification techniques have been employed to address these challenges, including physical and chemical methods such as plasma spray, plasma immersion ion implantation (PIII), plasma immersion ion implantation and deposition (PIII&D), physical vapor deposition (PVD), chemical vapor deposition (CVD), sol-gel, and micro-arc oxidation (MAO) (67).

Plasma spray technology offers a cost-effective and reliable means of coating titanium alloys, with recent advancements like vapor-induced pore-forming atmospheric plasma spraying (VIPF-APS) showing promise in producing bioactive porous hydroxyapatite (HA) coatings that enhance osteoblast attachment and differentiation (68). Similarly, bioactive glass-ceramic coatings, such as the M2 coating (including $CaO–MgO–SiO_2$), have demonstrated improved biological performance in vivo and potential as replacements for HA coatings in load-bearing bone implants (69). In another example, tricalcium magnesium silicate is

recommended as a new coating, which has almost the same thermal expansion properties as Ti-6Al-4V, and also it has the potential to enhance the corrosion and biological behavior of permanent metallic implants (70). In another interesting example titanium and stainless steel surfaces were coated with bioactive glass powder doped with antibacterial silver ions. This approach resulted in the realization of a coated device for bone-related applications with added antibacterial effect (71).

The Plasma Immersion Ion Implantation (PIII) technique offers the capability to incorporate a diverse range of elements into the near-surface region of various substrates. Studies have shown that PIII can enhance the hardness, corrosion resistance, wear resistance, bioactivity, and antibacterial properties of biomaterials (72). Titanium dioxide (TiO_2) has garnered significant attention as a common surface coating in Ti-based alloys using PIII. By employing PIII alongside optical emission spectrometry (OES), Lin et al. have successfully produced TiO_2 coatings, leveraging its super-hydrophilicity to potentially improve implant osseointegration (73).

Utilizing Plasma Immersion Ion Implantation and Deposition (PIII&D) technology allows for the creation of a three-dimensional film characterized by strong adhesion, thickness, and minimal stress. Widely employed in forming metal coatings on titanium and its alloys (74) PIII&D facilitates the injection of metal ions into the surface of the titanium substrate. As the metal phase acts as an anode, releasing metal ions, this process enhances the material's antibacterial properties (67). Additionally, PIII&D has been instrumental in improving cell response to titanium. Treatment with Mg–Ag PIII&D has been shown to not only inhibit the adhesion and proliferation of *Escherichia coli* bacteria but also to promote the initial adhesion and alkaline phosphatase (ALP) expression of MG63 cells (75). Research by Hempel et al. (2014) demonstrated that copper-doped and coated titanium can effectively prevent and treat implant-associated infections

(76). However, it is important to note that an excessive concentration of copper on the titanium surface can lead to negative biocompatibility (77).

Physical vapor deposition (PVD) involves a coating process where solid metal is evaporated within a vacuum environment and then deposited onto a conductive substrate (78). The main methods of PVD include vacuum evaporation, ion plating, and sputter coating. PVD is a well-established technique known for forming highly adherent layers of materials that maintain surface topography and exhibit favorable tribological properties. However, the bonding force between the coating and substrate is weakened due to a mismatch in their coefficients of thermal expansion, limiting the scope of this coating method (67). Sarraf et al. (2017) demonstrated the preparation of tantalum pentoxide nanotubes (Ta_2O_5 NTs) on biomedical grade Ti-6Al-4V alloy, revealing the formation of a bone-like apatite layer on the nanotubular coating after just one day of immersion in simulated body fluid (SBF), highlighting the significance of nanotubular configuration for in vitro biological activity (79).

Chemical vapor deposition (CVD) is another coating method used to form thin film layers on substrate surfaces through chemical reactions involving vapor compounds or elements containing the desired film elements. While CVD has been successfully utilized in industrial applications for synthesizing inorganic materials such as carbon nanotubes, graphene, and TiO_2, its application for biomedical surface modification on titanium alloy substrates remains limited (67).

Based on the principle of plasma-electrolytic oxidation, MAO facilitates the creation of a macro-porous and firmly adherent TiO_2 film on the titanium substrate. Organic substances applied to this layer can achieve a balance between antibacterial properties and cell compatibility (80). Moreover, bioactive elements such as boron, silver, calcium, and strontium can be incorporated into the TiO_2 coating to enhance its bioactivity and biological properties. MAO, as a prominent technology for surface modification, has been widely employed in various

research endeavors, including the preparation of titanium dioxide and hydroxyapatite (HA) layers. The increased surface hydrophilicity of the porous coating produced by the MAO method can promote interaction between the implant and the surrounding biological environment, while also imparting excellent antibacterial properties due to the presence of metal ions. Despite its convenience and cost-effectiveness, the bonding strength of anodic oxidation technology with the titanium matrix requires further enhancement (67).

For titanium and titanium alloys, the inherent titanium oxide (TiO_2) layer typically exhibits bioinert properties. Various chemical treatments have been suggested to impart bioactivity to titanium and its alloys (81). For instance, acid treatments involving HCl, H_2SO_4, HNO_3, HF, and their combinations have been utilized on titanium dental implants to enhance bone contact (82). These treatments induce micro-scale roughness on the surface, thereby increasing total surface area, wettability, and surface energy to facilitate osseointegration (83,84). In another instance, a crack-free nanostructure was achieved on titanium alloy through a multistep solution treatment using HF and H_2O_2, resulting in enhanced wettability, corrosion resistance, cell attachment, and proliferation (85). Additionally, alkaline treatments (86,87) have been shown to produce a bioactive surface conducive to apatite formation.

To mitigate bacterial adhesion on implants, there has been extensive exploration into the use of antimicrobial and anti-biofouling coatings such as metallic nanoparticles or bioactive molecules like chitosan and hyaluronic acid (88,89). However, these coatings may lead to challenges such as low osteoblast adhesion and differentiation, or even cytotoxic effects (90). The adsorption of silver nanoparticles (AgNPs) on titanium has been extensively researched as an antimicrobial coating for medical devices (88,91). Another approach involves modifying the titanium surface to simultaneously induce bone tissue integration and prevent infection through chemical etching–oxidation treatment and in situ

reduction of silver nanoparticles (92,93). A balance between cytocompatibility and anti-bacterial action must be found when using AgNPs and it is not a trivial issue because of the strong cytotoxic effect of AgNPs through a contact mechanism, even if in the absence of a relevant ion release, and its relationship with NP dimensions (the smaller the NPs the larger the cytotoxicity).

Combining different therapeutic agents with specific properties presents a promising strategy to address these issues. Nonetheless, these strategies may also pose drawbacks such as complex fabrication processes, polymer degradation in physiological environments, and the potential for non-controlled release of antimicrobials leading to cytotoxicity, reduced drug efficacy, and persistent bacterial resistance (94,95).

Chapter 2: Biomaterial- host tissue interface interactions

2.1 Introduction

In instances of severe injuries, where the body's innate healing processes may be compromised, particularly by increasing aging, biomaterials emerge as essential tools in restoring various bodily systems. Departing from traditional autologous or allogeneous methods, nowadays biomaterials play a vital role in the regeneration of essential systems like musculoskeletal, cardiovascular, neural, and dermal systems (96). Biomaterials, broadly defined as either synthetic or natural substances, or their combinations, are employed for varying durations to either partially or completely augment and replace any tissue, organ, or function of the body. This definition also highlights the purpose of the biomaterial to maintain and/or improve the quality of life of the individual (97).

Central to the effectiveness of biomaterials is the concept of biocompatibility, emphasizing the need to align the physicochemical characteristics of biomaterials with the biological responses observed *in vivo*. From the material science point of view, each physicochemical property of a biomaterial surface exerts a profound influence on the intricate interplay between the biomaterial and the biological environment. Important to this dynamic relationship is the need for biomaterials to not only offer mechanical support but also foster enhanced cell survival and function, ultimately promoting autologous tissue growth (96).

This chapter summarizes the complex interactions occurring at the interface of a biomaterial and the host tissue. We start with the description of the initial host

response occurring immediately after implantation, also covering the following foreign body reaction. The option of prolonged inflammation leading to fibrous tissue encapsulation and the possibility of infection and bacterial biofilm formation is also discussed. Finally, we touch a bit of the topic of material toxicity and the osseointegration through bioactivity mechanism.

2.2 Host response after implantation

The fate of the implanted material depends on the host's response, categorized by various outcomes. Bioinert materials exhibit no alteration in physical structure or chemical composition upon interaction with surrounding tissues, preserving their functionality (98). Bioresorbable materials gradually dissolve within the body through controlled metabolization, eventually being replaced by surrounding tissues. Finally, bioactive materials are materials that are able to elicit strong bonding of the material to bone and soft tissue.

However, unsuccessful implantation may result in chronic inflammation due to material toxicity or bacterial biofilm formation from infection. Before delving deeper into these potential issues, let's begin at the initial stage.

In general, the implantation of any biomaterial within the host induces an injury. This injury brings the material into direct contact with blood, triggering a dynamic interplay between biomaterials and living tissue. This sets off a rapid and intricate cascade of events that ultimately shapes the fate of the biomaterial. Figure 6 illustrates the simplified steps of these events.

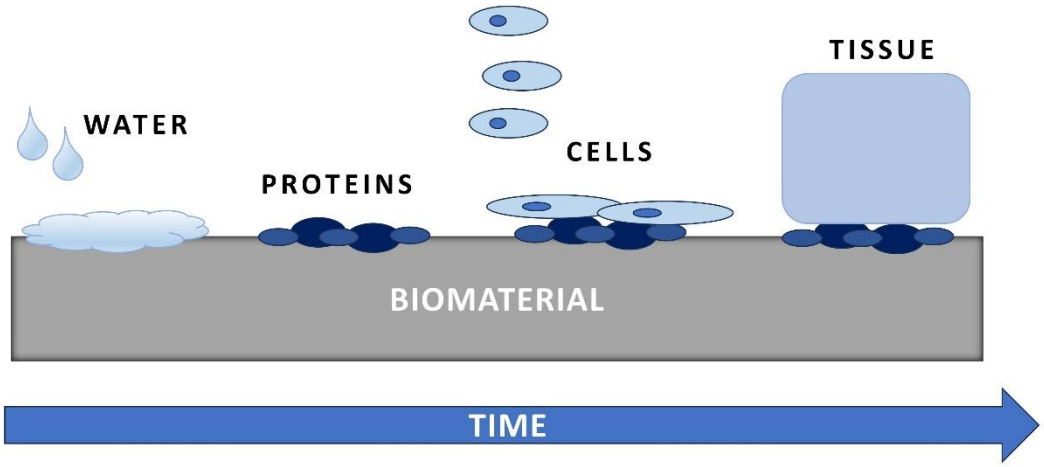

Figure 6: Simplified illustration of events occurring after implantation of a biomaterial

In the initial phase, water molecules, low molecular weight solutes, and ions intricately engage with the material's surface, swiftly forming a foundational layer. The water shell enveloping the biomaterial interacts with the hydration shell surrounding the biomolecules, a phenomenon governed by the kinetic and thermodynamic processes at the interface (99). This hydration layer serves as a platform for the subsequent rapid adsorption of proteins, a process unfolding within nanoseconds.

As the biomaterial comes into contact with physiological fluids such as blood, the adsorbed proteins at this stage are mainly derived from the blood plasma. This protein coating serves as a catalyst for subsequent cell-biomaterial interactions (100). Depending on the surface properties of the material, proteins undergo conformational changes. This adherence triggers the infiltration and binding of various cells, including platelets, monocytes, and macrophages. Therefore, the modification of protein adsorption is also a tool to modulate the immune host response.

2.2.1 Foreign body reaction (FBR)

Even if the implated biomaterial is not outright “rejected” by the host tissues, inevitably triggers an immune response known as the foreign body response (FBR). The FBR can be defined as interactions between the immune microenvironment and biomaterials (101), setting off complex signaling cascades that ultimately result in the biological encapsulation of the implant (99). This process critically influences the success of integration and the overall biological performance of the biomaterial.

Every biomaterial inevitably disrupts the local host tissue environment, triggering FBR when at the injury site. This response involves the sequential steps of blood clot formation, recruitment of immune cells, and initiation of the inflammatory response. While the typical healing process rapidly transits from inflammation to cell proliferation, granulation tissue formation, and remodeling, in the context of FBR, the inflammation phase may persist and become chronic. This inflammation can result in two distinct outcomes: the formation of a fibrotic capsule around the foreign body (chronic-inflammation) or, alternatively, osseointegration.

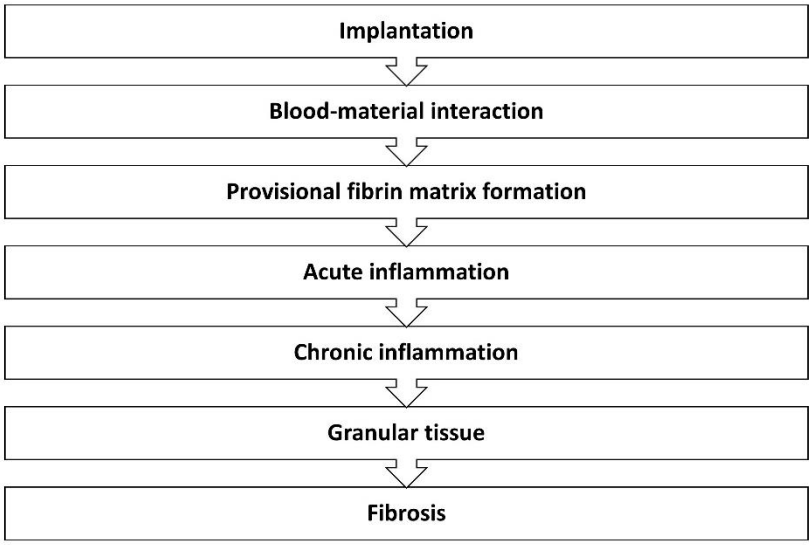

Figure 7: Foreign body reaction following implantation of a material (99)

The host response and FBR involve a complex interplay of inflammatory cells, mitogens, chemo-attractants, cytokines, and other bioactive agents. More detailed descriptions of the events of each stage (101) are listed below:

In the first step, occurring within seconds, the host immune system is activated, leading to the recruitment of neutrophil infiltration. Vascular endothelial damage during implantation triggers a blood coagulation cascade, resulting in the deposition of a provisional fibrin matrix and platelet aggregation around the implant. The subsequent processes include the activation of extrinsic and intrinsic coagulation systems, the complement system, the fibrinolytic system, the kinin generating system (102), and platelets (99). Platelets release chemoattractants such as PDGF and TGF-β for leukocytes, promoting healing (103).

Cellular recognition occurs through the interaction of adhesion receptors with adhesion proteins, forming focal contacts that later mature into focal adhesions. These cells release cytokines and chemokines, initiating the recruitment of tissue repair cells like fibroblasts and mesenchymal stem cells to the inflammation site.

Recruited cells will play a crucial role in depositing a collagen matrix and the following encapsulation of the material within a protective fibrous tissue layer (104).

The following step is the acute inflammation, which lasts for a few hours to a few days, depending on the extent of injury at the implant site. This stage is characterized by the presence of neutrophils (polymorphonuclear leukocytes), the primary defense of the host system. Many growth factors and chemokines are released, recruiting mast cells and lymphocytes. According to this description, it is evident that an early pro-inflammatory reaction is needed for healing close to the physiological one.

The following inflammation or the remodeling phase occurs after a few days after the previous stage (99). The duration of this phase depends on the immunomodulatory outcomes of the previous stages. Options include inflammation, marked by the presence of mononuclear cells such as monocytes and lymphocytes. Monocytes migrate to the wound site and differentiate into macrophages, serving as the second line of defense (105). Macrophages clear the site of cellular debris, bacteria, or foreign material through receptor-mediated phagocytosis. Macrophages release inflammation mediators, such as oxygen free radicals, and reactive oxygen intermediates. A switch toward the anti-inflammatory action (M2 polarization of macrophages) is needed at this stage to avoid chronic inflammation, otherwise, macrophages may undergo fusion into foreign body giant cells (FBGCs) and chronic inflammation occurs. FBGCs attempt to engulf surfaces too large for phagocytosis, resulting in "frustrated phagocytosis" (103). The adaptive immune system is activated when chronic inflammation occurs.

The development of granulation tissue is also a part of inflammation, signifying healing. Fibroblasts and vascular endothelial cells arrive at the implant site, leading to excessive granulation, collagen fiber deposition, and fibrous tissue

formation (106). Successful cases involve the recruitment of fibroblasts and mesenchymal stem cells (MSCs) for further repair, neovascularization, collagen synthesis, and isolation of the implant through fibrosis (102). The crucial role of fibroblasts in the healing of every biological tissue is here evident.

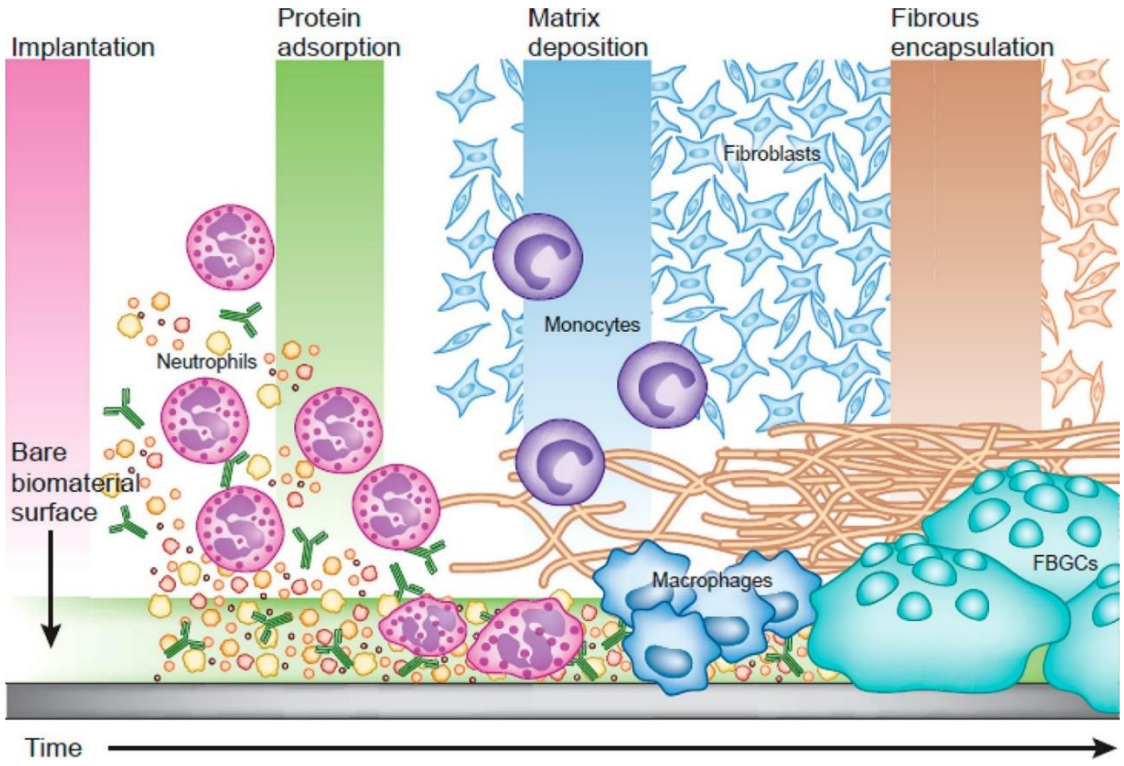

Figure 8:Schematic illustration of the foreign body reaction (107)

The influence of FBR on materials is multifaceted (3). Body fluid ions and pH levels, for instance, can induce corrosion in metallic materials and potentially lead to leaching. FBR poses a challenge for long-term implantation by disrupting the tissue-implant interface through cellular responses. This inflammatory reaction may result in biomaterial degradation, including stress cracking of surfaces.

Conversely, the relationship between materials and FBR is bidirectional, shaped by both implant properties and host-related factors such as the implantation site and surrounding tissue type. Implant properties, including chemical composition, specific orientation, dimensions, shape, size, surface

topography, and elastic modulus, play pivotal roles, with special consideration for potential mismatches in mechanical properties, particularly in metallic implants (108).

To prevent excessive FBR, diverse strategies have emerged in material development. One approach focuses on preventing nonspecific protein adsorption, which is thought to distort protein conformation and orientations. This can be achieved by masking the material surface through coatings (109), such as hydrophilic poly(ethylene glycol) (PEG) surface grafting and the use of zwitterions (110). Another strategy involves incorporating various biomolecules into the implant, with subsequent release (111). Examples include the integration of angiogenic or anti-inflammatory drugs (99). In the case of osseointegration, it is challenging to find a balance between surface features fastening osseointegration and modulating the inflammatory reaction. For instance, large (>150 microns) pores are needed to get bone in-growth and vascularisation but such pores easily induce chronic inflammation or super-hydrophilic surfaces (PEG coatings) result to be non-adhesive for osteoblasts.

2.3 Toxicity of implanted materials

Understanding the potential toxicity of implanted materials is crucial, with various biocompatibility endpoints providing a comprehensive assessment. These include cytotoxicity, sensitization, irritation or intracutaneous reactivity, acute, subchronic, and chronic systemic toxicity, material-mediated pyrogenicity, genotoxicity, hemocompatibility, carcinogenicity, reproductive or developmental toxicity, and, in the case of absorbable materials, biodegradation. The evaluation depends on the expected duration of device contact and its anticipated permanence (112).

A fundamental principle in toxicology is encapsulated in the phrase "the dose makes the poison." Biomaterial constituents, upon exposure, absorb into local

tissues and distribute systemically through blood and lymph vessels. The journey involves traversing cell membranes and tissue layers for whole-body distribution, metabolism, and eventual excretion through urine, feces, sweat, hair, and nails. A biomaterial is considered non-toxic if it is neither absorbed nor distributed to a target organ in concentrations that would elicit an adverse biological response (113).

Concerning metals and metal alloys, frequently used in implants such as stainless steel, cobalt-based alloys, chromium alloys, titanium, and nickel-titanium-based alloys, as well as refractory metals like molybdenum, tungsten, vanadium, and tantalum used as alloying elements, there is a need for cautious consideration (114). Even essential metals like iron and zinc can become toxic in excess concentrations or altered valence states (112). Metal-on-metal (MoM) implants, particularly prone to nanosized wear particles, can pose challenges despite modern designs being highly resistant to wear (115). Poor placement or replacement of failed implants can lead to increased debris, potentially impacting the immune system and causing adverse reactions (116)

While not necessarily toxic, foreign compounds may induce hypersensitivity or allergic reactions in susceptible individuals. Implantation inherently involves innate immune or inflammatory responses, which can escalate into pathological foreign body reactions. Debris and wear particles taken up by phagocytic cells can trigger inflammatory responses, releasing systemic effects. In the worst cases, these responses may exacerbate local tissue destruction and lead to device failure. Immune or delayed hypersensitivity reactions can be disproportionate, involving the amplification of lymphocytes bearing antibodies targeting foreign substances. Metal allergies, particularly to nickel, cobalt, and chromium, are among the most common contact hypersensitivities (116).

In the scope of orthopedic devices, specific bone-related immune responses are paramount. Aseptic loosening and instability can result from local

inflammatory responses caused by sensitization to metal or bone cement components, cement failure, or inadequate bone formation (117). The balance of osteoclastogenesis and osteogenesis, crucial for maintaining skeletal integrity, involves dynamic processes integrating inflammatory, metabolic, and immune inputs (118). Osteoclasts, implicated in inflammatory responses, can be influenced by implant material selection to either suppress inflammatory responses or promote osteogenesis. Careful consideration of these factors is essential to ensure the safety and efficacy of orthopedic implants.

2.4 Biofilms, and related infections

The risk associated with infections, particularly those related to biofilms, tends to escalate with permanent implants. Conventional approaches such as oral or intravenous antibiotics often fall short in resolving these infections, necessitating surgical interventions like debridement or partial/total revision, adding complexity to the situation. A significant challenge in such cases is the formation of microbial biofilms (119).

A bacterial biofilm represents a community of bacteria that adheres and proliferates on a surface. Upon attachment, these bacteria colonize the surface, forming a biofilm where they embed themselves within a self-produced extracellular polymeric substance (EPS) (120). This EPS consists of exopolysaccharides, extracellular and cell surface-associated proteins/adhesions, lipids, and extracellular DNA, and may even incorporate host material (120,121). The biofilm's thick structure shields bacteria from antibiotics, while also providing channels for nutrient and waste transport, contributing to their survival. Simultaneously, the transport through the biofilm is constrained, making bacteria within biofilms more resistant to various environmental stresses such as dehydration, metal toxicity, and UV light exposure compared to free-floating planktonic bacteria (119).

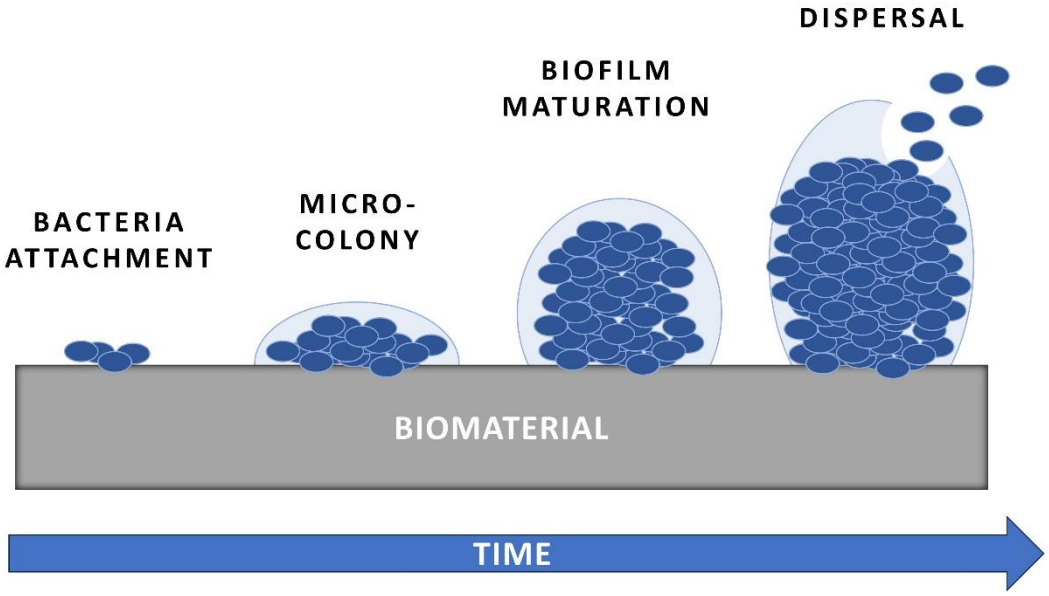

Figure 9: Steps of biofilm formation

The tolerance of the bacteria against environmental factors is not fully yet understood but the most common mechanisms involve bacterial dormancy due to nutrient depletion (122), interactions of antimicrobial agents with the EPS through binding/degradation (123), and the emergence of recalcitrant populations like slow-growing small colony variants or "persister" cells (124). However, it is essential to note that these tolerance mechanisms differ from genetically inherited bacterial resistance.

Biofilm defense mechanisms involve EPS matrix production, protecting bacteria from phagocytes and reducing antibody penetration (125). While biofilm formation aids evasion of host immune responses, many biofilm-associated infections are linked with chronic inflammation. Interestingly, even when the inflammatory response fails to eradicate the biofilm, it contributes to pathology by damaging host tissue (126).

In the context of osteomyelitis, a bone infection resulting from trauma, surgery, or vascular insufficiency (particularly in diabetes cases), antibiotics are

administered orally or intravenously for 4-6 weeks (127). Full surgical removal of infected tissue can leave large defects, inhibiting normal function. The gold standard for "dead space management" involves bone grafting using autologous or allogeneic tissue (128). However, this approach has limitations such as donor site morbidity, postoperative pain, lack of available tissue, immune rejection, and the risk of further infection. Another approach involves bone cement mixed with antimicrobials, but the non-biodegradable nature of bone cement necessitates a second surgery, increasing the risk of reinfection.

Antibiotics, whether administered systemically or locally, face challenges like suboptimal release profiles and reduced osseointegration of antibiotic-loaded implants. Furthermore, the increasing development of antibiotic resistance has prompted research into multifunctional non-antibiotic antimicrobial biomaterials that combat resistant bacteria locally and serve as templates for bone tissue ingrowth. The emphasis is on developing synergistic materials that address both infection control and tissue integration simultaneously.

2.5 Osseointegration and Bioactivity

In the realm of bioactive glasses, a specific reaction at the material-tissue interface facilitates a bonding process with bone, termed bioactivity. This innovation emerged as a response to the historical design of materials as bioinert, leading to fibrous encapsulation post-implantation (129).

A bioactive material is defined as one that elicits a positive response from the body, notably by bonding to host tissue, particularly bone, and stimulating bone growth beyond the bone-implant interface. The key mechanism behind this bone bonding is the formation of a hydroxycarbonate apatite (HCA) layer on the glass surface. Resembling the mineral composition of bone, HCA interacts with collagen fibrils to bond with the host bone (130). The osteogenic properties of the

glass are attributed to the dissolution products that stimulate osteogenic cells to produce bone matrix (131).

The formation of the HCA layer involves a mechanism similar to conventional glass corrosion (132), with the following steps:

1) Rapid cation exchange, where Na^+ and/or Ca^{2+} from the glass surface exchange with H_3O^+ (H^+ for simplicity) from the solution. This creates silanol (Si-OH) bonds on the glass surface:

$$Si - O^-Na^+ + H^+ + OH^- \rightarrow Si - OH^+ + Na^+(aq) + OH^-$$

2) The dissolution products elevate the solution's pH, leading to the formation of a silica-rich, cation-depleted region near the surface. Phosphate may also be lost from the glass composition during this step.
3) The high local pH prompts OH^- to attack the silica glass network, breaking Si-O-Si bonds, resulting in the loss of soluble silica $Si(OH)_4$ to the solution. This leaves more silanols at the interface:

$$Si - O - Si + H_2O \rightarrow Si - OH + OH - Si$$

4) Silanol groups near the surface condense, leading to the re-polymerization of the silica-rich layer.
5) Migration of Ca^{2+} and PO_4^{3-} groups to the surface through the silica gel layer and from the solution. This culminates in the formation of a film rich in amorphous $CaO\text{-}P_2O_5$.
6) Incorporation of hydroxyls and carbonate from the solution and crystallization of the $CaO\text{-}P_2O_5$ film into HCA.
7) Adsorption of proteins
8) Attachment of macrophages
9) Attachment of stem cells

10) Osteoblast differentiation and proliferation
11) Matrix production
12) Matrix crystallization
13) Bone formation.

The composition of the glass, particularly the silica content and other modifying cations, significantly influences the rate of bioactivity. Lower silica content results in a less connected silica network, making it more prone to dissolution. This process is well illustrated in Figure 10.

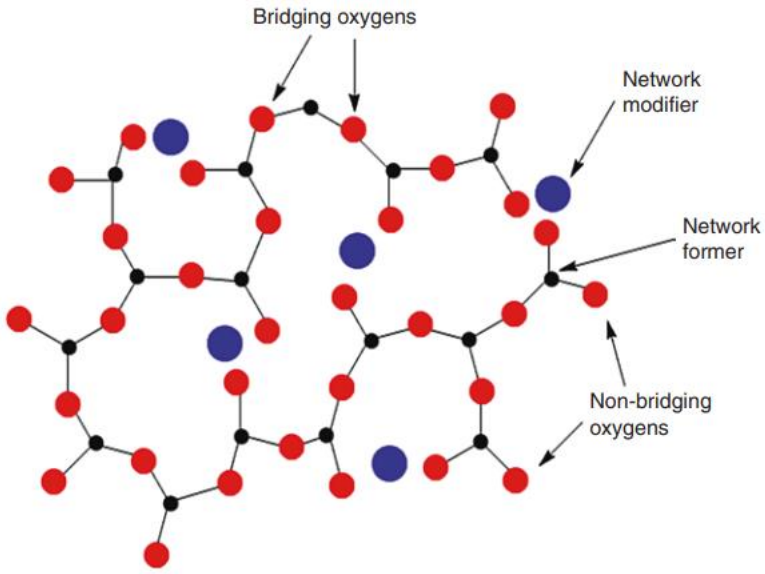

Figure 10: Bioactive glass network (133)

While the steps mentioned are well-characterized, subsequent stages, including protein adsorption to the HCA layer, cell attachment, differentiation, and the production of bone matrix, are less clear but have been shown to play crucial roles in the bioactivity process.

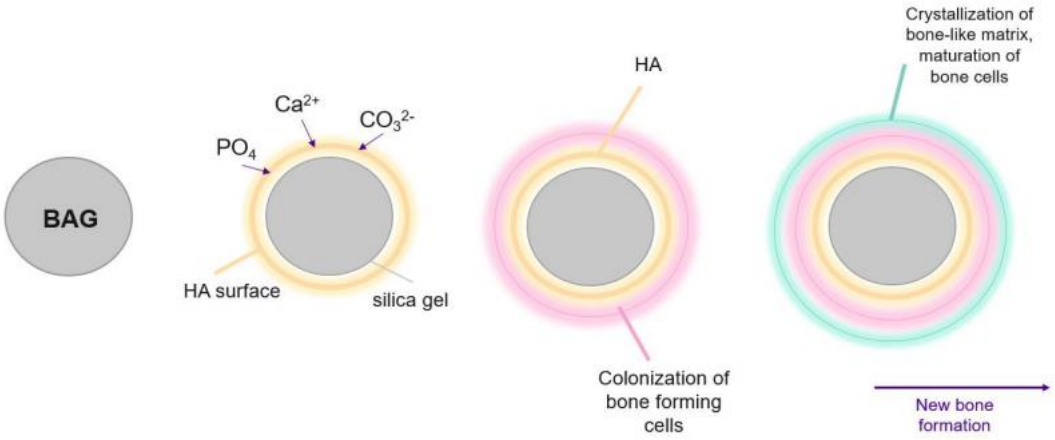

Figure 11: The bioactivity steps (134)

In addition to glass, bioactivity can also be induced in titanium and its alloys, eliminating the formation of interfacial fibrous tissue. Techniques such as plasma-sprayed coatings (apatite, bioactive glass), electrochemical processes (anodic oxidation), or chemical surface treatments enable the bioactivation of titanium and its alloys (81).

Chapter 3: Biological surface functionalization by antimicrobial peptides

3.1 Introduction

Implant-associated infections represent a major clinical challenge, often resulting in implant failure, and substantial social and economic burden (135). In response, the introduction of antimicrobial properties into implant materials has emerged as a compelling avenue to combat bacterial adhesion, subsequent biofilm formation, and infections. Notably, alternative methods to traditional antibiotics are of interest due to the wide-spread threat of antibiotic-resistant bacteria (136). Biomaterial surface coating and functionalization utilizing non-antibiotic antimicrobial agents, such as polymers, metal ions, and antimicrobial peptides, present viable strategies for addressing these challenges.

This chapter comprises a bibliographic part regarding antimicrobial peptides, specifically nisin, and their use in biomedical applications. The experimental part describes the surface functionalization process of titanium alloy, both polished and chemically treated, with nisin, including physicochemical characterization and evaluation of the antimicrobial properties.

3.2 Antimicrobial peptides

Antimicrobial peptides (AMPs), represent a class of small proteins naturally produced by all living organisms, both prokaryotes and eukaryotes, serving as a

fundamental component of their innate immune system (137). Renowned for their broad-spectrum antimicrobial activity, AMPs exhibit efficacy against a diverse array of microorganisms, including bacteria, yeasts, fungi, viruses, and parasites (138). To this day, more than 3000 AMPs have been discovered and characterized (139). Commonly, AMPs share defining features, characterized by small size (less than 100 amino acids), typically with positive net charge and amphipathic structure with both hydrophobic and hydrophilic regions, giving them structural flexibility (140).

AMPs tend to target primarily the negatively charged lipidic bi-layer membranes of microbial cells, thanks to their positive net charge. This mode of action makes it difficult for bacteria to develop resistance against AMPs (137). AMPs can either destabilize and disrupt bacterial membranes, or translocate across the membranes, thereby destabilizing normal cell functions (141).

The scope of AMP applications extends across diverse domains, ranging from food preservation to agriculture (142). From the biomedical point of view, the predominant use of AMPs has been in topical applications, owing to their susceptibility to proteolysis and susceptibility to changes in salt concentrations or pH levels (143). However, thanks to the immunomodulatory, antioxidant, anticancer, and anti-inflammatory activities of AMPs, in the future they could be utilized for several other applications, such as treatment for cancer, inflammatory disorders, or wound healing, alone or in combination with other drugs (144).

3.2.1 Nisin

Nisin($C_{143}H_{230}N_{42}O_{37}S_7$) is one of the oldest known antimicrobial peptides, with origins tracing back to its discovery in 1928 within fermented milk cultures. Derived from *Lactococcus lactis* bacteria, nisin is a pentacyclic post-translationally modified peptide comprising 34 amino acids with a weight of

3354.12 Daltons (145). Its distinctive attributes derive from enzyme-mediated post-translational modifications, leading to the presence of unusual thioether amino acids such as lanthionine (Lan) and/or methyllanthionine (MeLan) (146). Characterized as an amphiphilic molecule, nisin includes both hydrophilic and hydrophobic residues in its structure (Fig.12) (147). The hydrophobic residues of nisin are identified to be responsible for its antimicrobial activity (148,149).

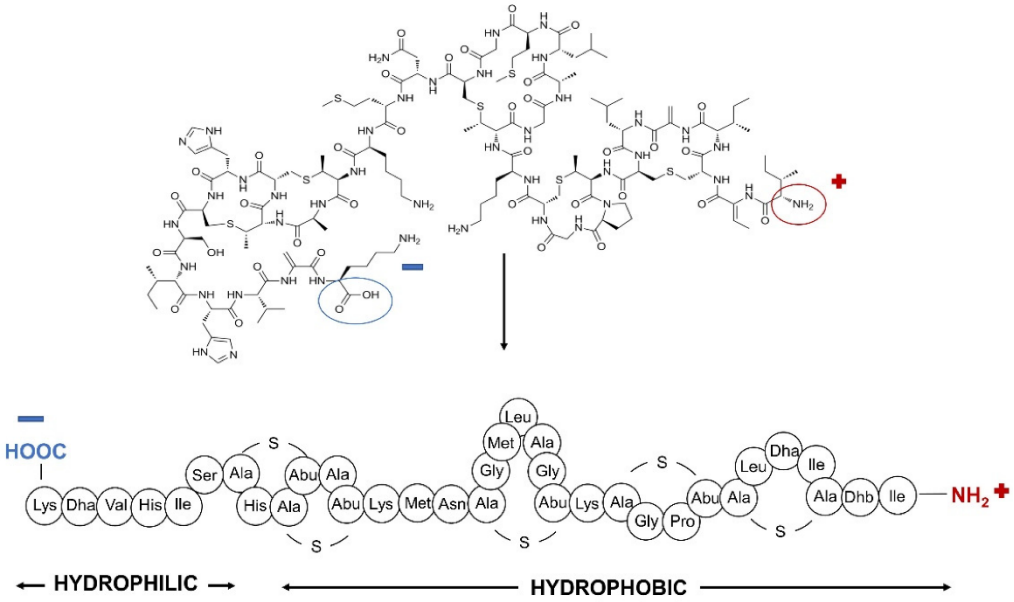

Figure 12. Chemical and primary structures of the nisin polypeptide (150).

Nisin's mechanism of action is multifaceted and involves several steps. Initially, nisin binds to the anionic phospholipids (lipid II) situated within the cytoplasmic membrane of the bacteria. This binding event disrupts the bacterial cell wall formation. Subsequently, nisin proceeds to form an ion channel or a pore in the membrane. This structural modification leads to a fatal efflux of intracellular products, notably including adenosine triphosphate (ATP) and potassium, preventing essential cellular processes of bacteria (149).

Remarkably, nisin's impact primarily extends to Gram-positive bacteria. Instead, Gram-negative bacteria pose a challenge due to their outer membrane barrier, which impedes nisin access to the lipid II in the inner membrane.

However, nisin is effective against Gram-negative bacteria when employed in conjunction with chelating agents such as ethylenediaminetetraacetic acid (EDTA), citrate monohydrate, trisodium orthophosphate, or with thermal treatments (148).

Nisin, traditionally employed in food preservation as a safe food additive approved by the Joint Food and Agriculture Organization/World Health Organization, has increasingly gained attention for its potential therapeutic applications in combating infections. Within the realm of infections, nisin has demonstrated antimicrobial efficacy against various conditions, including mastitis (151), respiratory infections (152), gastrointestinal infections (153,154), and skin infections (155). Moreover, nisin has shown selective cytotoxicity towards cancer cells and impacted tumor growth, as evidenced in multiple studies (156–158).

In addition to its antimicrobial attributes, emerging research indicates that nisin may exhibit immunomodulatory properties, particularly influencing cytokine production(159). Further evidence has suggested an influence on both innate and adaptive immune cells (160). However, given the variances in results and considerable variability in experimental models, the need for additional studies is emphasized to substantiate and elucidate nisin's effects (147).

AMPs, including nisin, can be grafted onto material surfaces with covalent bonds through their inherent structural components such as amines, carboxylic acids, thiols, and hydroxyl groups (161). An ideal outcome involves the peptide maintaining stability and retaining its active form within the coating, unaffected by environmental conditions impacting the exposed contact surface. Simultaneously, it should possess the capability to be released from the surface to exert antimicrobial activity (162).

The immobilization and release of nisin nanoparticles have been the subject of previous research, exploring diverse metallic substrates across stainless steel (162–164), titanium (162,163), and gold surfaces (165). In addition to metallic materials, nisin has also been grafted onto glass substrates by using dopamine as a coupling agent (166) to polymers such as polycaprolactone electrospun fibers (167), and monocalcium phosphate monohydrate (168).

Incorporating AMPs as a coating on biomaterial surfaces presents challenges, particularly concerning potential hydrolysis and denaturation of the coating due to variations in pH and temperature, which might compromise antimicrobial efficacy. Moreover, there is a risk of decreased AMP activity due to the covalent linkage of its essential functional groups for antimicrobial action to the surface, potentially rendering the peptide inactive (161).

3.3 Materials and Methods

3.3.1 Sample preparation

Ti6Al4V-ELI discs (Grade 23, Titanium Consulting and Trading S.r.l., Firenze, Italy) with a diameter of 10 mm and a thickness of 2 mm were employed for the experimental study. The discs were polished with SiC abrasive papers up to 4000 grit. Subsequently, the polished discs were then subjected to a cleaning regimen, which included a single sonication in acetone for 5 minutes followed by two separate sonication processes in ultrapure (Milli-Q) water, each lasting 10 minutes. This sequential cleaning procedure was executed to ensure the removal of any potential contaminations present on the sample surfaces. From now on, these samples will be named MP (mechanically polished).

Moreover, a subset of the samples underwent a chemical treatment, as previously described (85,169). This patented protocol involves an acid etching stage utilizing hydrofluoric acid (HF), designed to eliminate the native oxide

layer, followed by a controlled oxidation process in hydrogen peroxide (H_2O_2). The goal of this treatment is to induce the creation of a micro- and nanotextured titanium oxide layer, enriched in -OH functional groups, which creates bioactive surface suitable for osseointegration with anti-microfouling properties (85,170). Consequently, the samples derived from this process are denoted as Chemically Treated (CT).

3.3.2 Surface functionalization with Nisin

Before nisin functionalization, both MP and CT samples underwent UV-C irradiation (UV-C 40 W, 253.7 nm, Philips TUV T8) for one hour. This step aimed to eliminate potential atmospheric contaminations and adsorbed water molecules, while concurrently enhancing the reactivity of the surface by promoting the exposure of –OH groups.

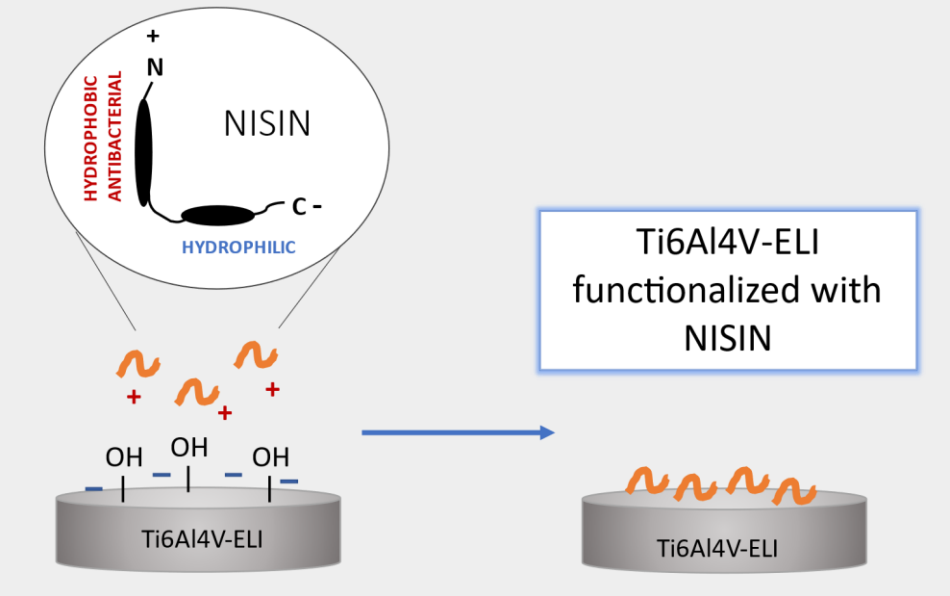

Figure 13: Surface functionalization with nisin

The antimicrobial peptide nisin (Nisin Ready Made Solution, 20,000–40,000 IU/mL in 0.02 N HCl, Sigma-Aldrich, Milan, Italy) was utilized for the biological functionalization. A nisin concentration of 1 mg/mL in ultrapure water was employed for the study, with solutions at three different pH values: pH 5, pH 6, and pH 7. The original nisin solution (pH = 3.39 ± 0.05) was buffered to the desired pH by incremental addition of 0.05 M NaOH buffer solution. These pH conditions were chosen to prevent substrate corrosion and to optimize the electrostatic attraction between the molecule and the substrate, as detailed in the Results section. In the case of CT samples, the chosen pH range also aimed to avoid potential deleterious effects on the titanium surface morphology and the previously obtained textured oxide layer. The adjustment was monitored using a pH meter (Edge pH, HANNA Instruments Italia S.r.l., Padova, Italy).

Each sample was treated with 5 mL of the functionalization solution and left to functionalize for 24 hours at room temperature within sealed containers. Subsequently, the samples underwent two washes with ultrapure water and were air-dried. Following this process, the nisin-functionalized samples were denoted as MP/CT NISIN pH = 3/5/6/7. Additionally, control samples (MP/CT CTRL pH = 5/6/7) were prepared by immersing the MP/CT samples in 5 mL of ultrapure water, pre-adjusted to the corresponding pH values.

3.3.3 Physical-Chemical Characterization

Contact profiler and confocal microscopy

The surface roughness of the MP and CT samples was quantified using a contact profiler (Talysurf Intra Touch, Taylor Hobson) and a confocal laser scanning microscope (LSM 900, Zeiss). Both sets of samples were analyzed for comparison. The contact profiler collected data from (5x5) mm^2 areas, while the

confocal microscope examined areas of (250x250) μm². Each experiment was performed in triplicate.

Subsequently, acquired data from both instruments underwent identical processing. Using the AnalysisTool software, images were untilted and underwent filtering through a series of processes. This involved the application of a high-pass filter with a cut-off wavelength of 8 μm for waviness, and a low-pass filter with a cut-off wavelength of 250 μm for roughness. Parameters of interest, such as superficial roughness (Sa), root mean square height (Sq), skewness (Ssk), and kurtosis (Sku), were then extracted in nanometers, in concordance with standards DIN EN ISO 4287 and DIN EN ISO 4288.

Field Emission Scanning Electron Microscopy / Energy-Dispersive X-ray Spectroscopy (FESEM/EDS)

FESEM/EDS (FESEM - SUPRATM 40, Zeiss) was used to observe the surface of both MP and CT samples. The images were acquired at two different magnifications, respectively 60kx and 150kx. The electron high tension (EHT) voltage was set at 10 kV. The observations were made in triplicate. The EDS analysis was carried on to quantify the amount (expressed as an atomic percentage, atomic %) of titanium (Ti), aluminum (Al), vanadium (V) and oxygen (O). The electron high tension (EHT) voltage was set at 15 kV for the EDS analysis. Three areas per each image were randomly selected and the atomic content of the elements of interest was measured.

UV–Vis Spectroscopy and Reflectance

Reflectance measurement was performed for both bare and nisin-functionalized samples by means of a UV–Vis spectrophotometer (UV-2600

Shimadzu, Kyoto, Japan, equipped with ISR-2600Plus integration sphere). The spectrum of 190–750 nm was evaluated in the measurements.

Surface Wettability and Surface free energy calculation

The evaluation of sample surface wettability was conducted using the sessile drop method for static contact angle measurement via the Krüss DSA 100 instrument (KRÜSS GmbH, Hamburg, Germany). Ultrapure water served as the wetting fluid, where a 5 µL water droplet was deposited on the surface using a pipette. Contact angles were subsequently measured with the instrument's accompanying software (DSA-100, Dropshape Analysis, KRÜSS GmbH, Hamburg, Germany).

Furthermore, static contact angle measurements were performed employing the FTA 1000C instrument, which integrated a video camera and image analyzer, maintaining a room temperature setting. This involved the use of three probe liquids: ultrapure water, hexadecane, and ethylene glycol (all sourced from Sigma Aldrich, St. Louis, USA), possessing surface tensions of 72.1 mN/m, 28.1 mN/m, and 48.8 mN/m, respectively. For each sample, three measurements were conducted, with liquid drops placed in different areas of the sample surface to derive a mean value and calculate the corresponding error. The overall surface energy, as well as its polar and dispersive components, were determined using the Owens-Wendt geometric mean method (171), in which contact angle values obtained with water and hexadecane were employed for computation.

Zeta Potential

The zeta potential measurements were conducted using an electrokinetic analyzer (SurPASS 2, Anton Paar, Graz, Austria), equipped with an adjustable gap cell. The surface zeta potential was assessed in a 0.001 M KCl electrolyte solution, measuring it as a function of pH. To avoid any potential surface

reactions during the measurements, separate couples of TI64ELI discs were utilized for both acidic and basic titrations. Specifically, the acidic titration was executed by introducing 0.05 M HCl, followed by the basic titration involving 0.05 M NaOH. Each pH point was measured in four parallel measurements.

In addition to solid sample zeta potential measurements, the zeta potential of a 1 mg/mL nisin solution was assessed utilizing a dynamic light scattering (DLS) particle size and zeta potential analyzer (Nanosizer Nano Z, Malvern Instruments Ltd., Malvern, Worcestershire, UK). The zeta potential curve of the functionalizing solution was obtained by measuring the electrophoretic mobility, progressively altering the pH from 2.5 to 9 using increments of 0.05 M HCl or NaOH.

Kelvin Probe Force Microscopy (KPFM)

A solution of 1 mg/mL nisin at pH 6 was dispensed onto the polished sample surface as a droplet, where it was allowed to functionalize overnight. The intention was to establish an interface between untreated areas and those treated with nisin on the same sample surface. Surface potential measurements for both the untreated and nisin-functionalized Ti64ELI samples were conducted using Kelvin Probe Force Microscopy (KPFM) in tapping mode, employing a Bruker Innova AFM located in Billerica, MA, United States. Subsequently, the acquired data was processed using the Gwyddion software (Gwyddion Version 2.62, Brno, Czech Republic) for analysis.

X-ray Photoelectron Spectroscopy (XPS)

XPS (Kratos Axis UltraDLD, Kratos Analytical Co., Ltd., Manchester, UK) measurements were performed (survey spectra and high-resolution analyses of elemental regions) on the bare and nisin-functionalized samples to investigate the chemical composition of the outermost layer and, in addition, the presence of

characteristic chemical groups for nisin. The hydrocarbon C 1s peak (284.80 eV) was used for the calibration of the binding energy scale.

Release Test

The release tests were conducted in accordance with the procedure outlined in (170). Specifically, the examinations were carried out using PBS (pH 7.4, Sigma Aldrich, Milan, Italy) and in a hydrogen peroxide solution (50 mM H2O2, 30% w/v, PanReac Applichem, Monza, Italy; in PBS) with a pH adjustment to 4.50—simulating physiological and inflammatory conditions, respectively. Each nisin-functionalized sample was immersed in a 5 mL solution for 7 days at 37 °C, with evaluations performed on both days 1 and 7. Following the immersion period, the samples underwent a single wash with ultrapure water and were allowed to air dry. Additionally, the contact angles of the samples were measured after soaking.

3.3.4 Biological characterization

Antibacterial activity evaluation

Strain Growth Condition

Bacteria were purchased from the American Type Culture Collection (ATCC, Manassas, VA, USA). Specimens' antibacterial properties were assayed towards the methicillin/oxacillin (MRSA) resistant *Staphylococcus aureus* strain (Gram-positive, ATCC 43300). Bacteria were cultivated in trypticase soy agar plates (TSA, Sigma-Aldrich, Milan, Italy) and incubated at 37 °C until round single colonies were formed; then, 2–3 colonies were collected and spotted into 15 mL of Luria Bertani broth (LB, Sigma-Aldrich, Milan, Italy) and incubated overnight at 37 °C under agitation (120 rpm). The day after, a fresh broth culture was prepared before the experiments by diluting bacteria into a fresh medium to a final

concentration of 1×10^3 bacteria/mL, corresponding to an optical density of 0.00001 at 600 nm wavelength using a spectrophotometer (Spark, from Tecan Trading AG, Mannedorf, Switzerland) (172).

Bacterial Metabolism, Number of Viable Colonies, and Morphology Evaluation

The International Standard ISO 22196 was applied to evaluate specimens' antibacterial properties (173). Accordingly, the specimens) were located into a 24-multiwell plate; then, 50 μL of the bacterial suspension was adjusted at a final concentration of 1×10^3 bacteria and it was directly dropped onto the specimens' surfaces. To confirm the nisin bioactivity at pH = 6, the samples prepared with the pH = 3 nisin stock solution from the manufacturer were also evaluated for their ability to prevent bacterial colonization.

The inoculated specimens were placed in an incubator at 37 °C for 24 h. Afterwards, the colorimetric Alamar blue assay (AlamarBlue™, Life Technologies, Milan, Italy) was applied to test viable bacteria metabolic activity by spectrophotometry following the manufacturer's instructions. Briefly, the ready-to-use Alamar solution at concentration 0.0015% in PBS was added to each well containing the test specimen (1 mL per specimen), and the plate was incubated in the dark for 4 h at 37 °C allowing resazurin dye reduction into fluorescent resorufin upon entering living cells. Then, 100 μL were spotted into a black-bottom 96-well plate to minimize the background signal. The metabolic activity of bacteria was measured via spectrophotometer (λex = 570 nm and λem = 590 nm), and the results were presented as relative fluorescent units (RFU).

Then, to investigate the number of viable bacteria adhered to the samples' surface the colony forming unit (CFU) count was performed. Briefly, after washing 2 times with PBS to remove non-attached bacterial cells, the samples

were submerged into 1 mL of PBS, sonicated, and vortexed for 5 min and 30 s, respectively (three times each). Next, an aliquot of 200 µL of the bacteria suspension was collected and transferred to a new 96 wells plate; here, 6 serials 1:10 dilutions were performed by mixing progressively 20 µL of the bacterial suspension with 180 µL of PBS. Then, 20 µL of each serial dilution were spotted into an LB agar plate and incubated for 24 h until round colonies were visually checked; the final number of CFU was calculated by using the following formula (174):

$$\text{CFU} = [(\text{number of colonies} \times \text{dilution factor})\ (\text{serial dilution})].$$

Finally, scanning electron microscopy (SEM, JSM-IT500, JEOL, Tokyo, Japan) imaging was used to investigate the bacterial microcolonies formed on the samples' surfaces; briefly, specimens were dehydrated by the alcohol scale (70–90–100% ethanol, 1 h each), swelled with hexamethyldisilazane, mounted onto stubs with conductive carbon tape and covered with a gold layer. Images were collected at different magnifications (2000× and 5000×) using secondary electrons. Additionally, the presence of single microcolonies or 3D biofilm-like aggregates on the samples' surfaces as well as their distribution were analyzed through 3D reconstructed images extracted from SEM images using the SMILE VIEWTM map software (JEOL, Tokyo, Japan).

Statistical Analysis of Data

Experiments were performed in triplicate. Results were statistically analyzed using the SPSS software (v.20.0, IBM, New York, NY, USA). Groups were compared by the one-way ANOVA using Tukey's test as a post hoc analysis. Significant differences were established at $p < 0.05$.

3.4 Results and discussion

3.4.1. Physicochemical characterization of MP and CT samples

Roughness and topography assessments of CT and MP were conducted using both a contact profiler and a confocal laser scanning microscope. The results are combined in Figure 14 and Table 3.

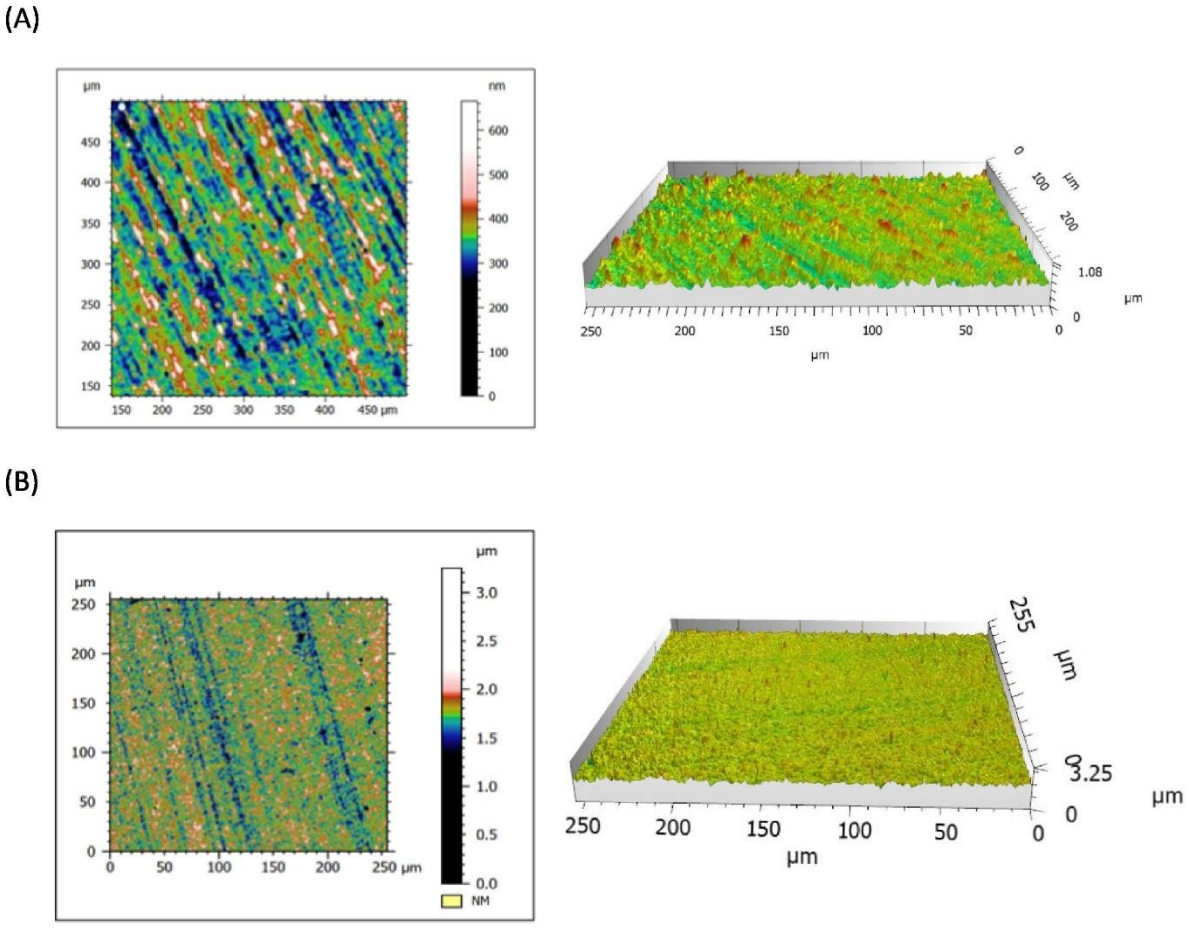

Figure 14:Roughness and topography analysis by confocal microscope of the surface of (A) MP and (B) CT.

Table 3: Roughness of MP and CT evaluated through contact profiler and confocal microscope

SAMPLE	Ti64-ELI	
	Contact profiler	Confocal microscopy
	Sa (nm)	
MP	39.6	38.4
CT	56.2	74.7

Both methodologies confirmed a substantial increase in the CT substrate's roughness following the chemical treatment.

While the optical measurements (confocal microscope) offer superior accuracy at the nanoscale, the contact profiler excels at the microscale, leading to the complementary nature of these techniques as they unveil distinct features. The observed increase in surface roughness found in the CT samples, as indicated by both the profilometer and confocal microscope (Sa values, Table 3), can be ascribed to the micro- and nanostructuring induced by etching, thus validating the efficacy of the surface treatment (85). The presence of this specific topography on the CT surface is promising for enhancing the physical entrapment of the nisin polypeptide during the adsorption process and has already been shown to enhance osteoblast differentiation.

FESEM was conducted on the CT samples to observe the micro- and nanoscale morphology of the substrate, using MP samples as a control. In Figure 15, the FESEM images of MP and CT surfaces are depicted, at two different magnifications (60kx, 150kx).

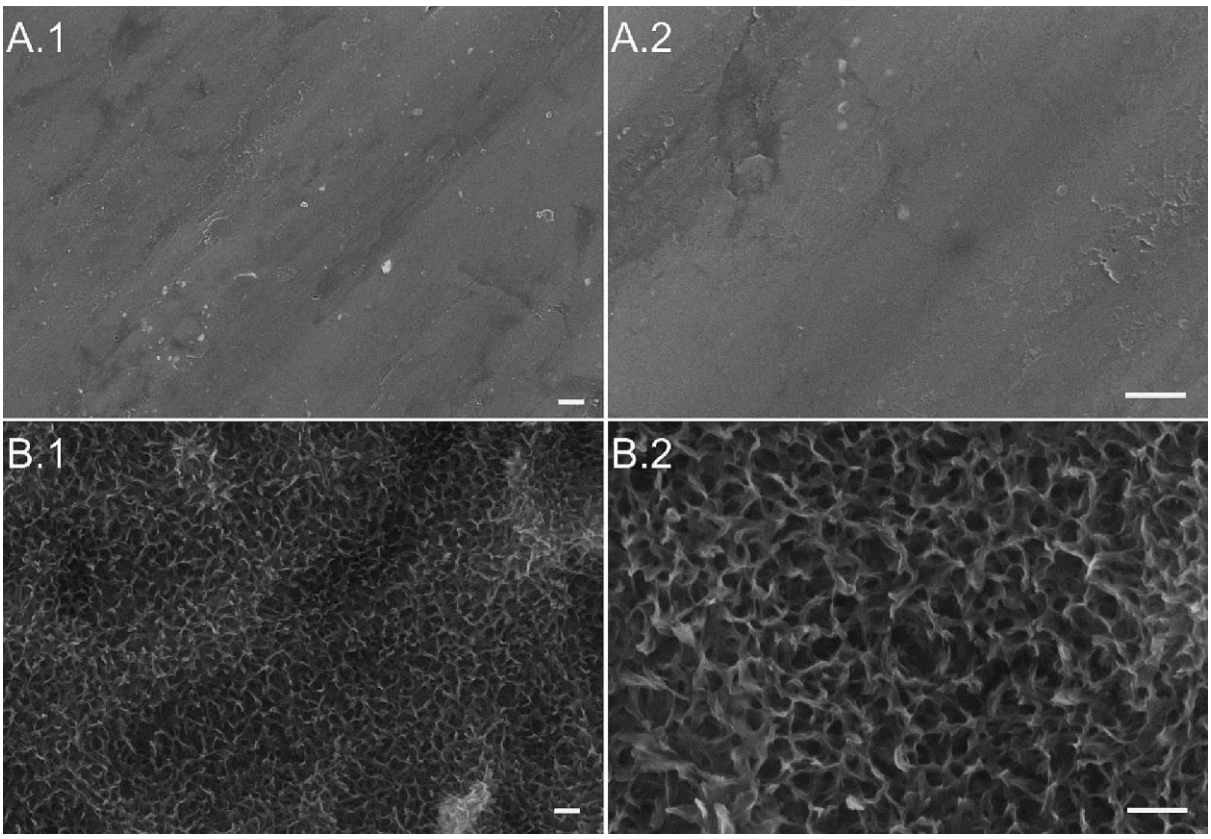

Figure 15: FESEM images of the surface of the MP samples with (A.1) magnification 60kx, (A.2) magnification 150kx, and of the surface of the CT samples with (B.1) magnification 60kx, (B.2) magnification 150kx. The scalebar corresponds to 200 nm on all the panels.

The MP samples exhibited a generally smooth surface, displaying some irregularities attributable to the mechanical polishing process. In contrast, the CT samples featured a consistently textured surface apparent at both micro- and nanoscales. Notably, the microscale roughness (evident in Figure B.1, as smooth ridges and valleys spaced approximately 1 μm apart) arises from the chemical etching in HF. Additionally, the surface revealed nanoscale porosity stemming from oxidation in hydrogen peroxide, covering the entire sample surface. These findings aligned with the roughness analysis and affirmed the beneficial influence of micro- and nano-roughness on osseointegration (85). In addition, this

multiscale roughness could be conducive to successful nisin polypeptide adsorption.

EDS analysis revealed a substantial alteration in the chemical composition of Ti64ELI following etching. The atomic percentage of titanium (Ti) underwent a notable reduction from 63% to 40%, while the oxygen (O) content approximately doubled, ascending from 27% to 54%. This outcome underscored the augmented thickness of the titanium oxide layer on CT in contrast to the native oxide on MP, reflecting the efficacy of the chemical treatment in producing a thicker layer. Notably, the features of the resulting surface oxide layer on CT were congruent with those previously published by the authors on a Ti6Al4V alloy grade 5 (85) in terms of chemistry, roughness, and topography. The presence of a thicker and continuous oxide layer on the CT surface is crucial as it augments corrosion resistance during the adsorption process and the lifespan of the implant, while further enhancing the polypeptide grafting potential.

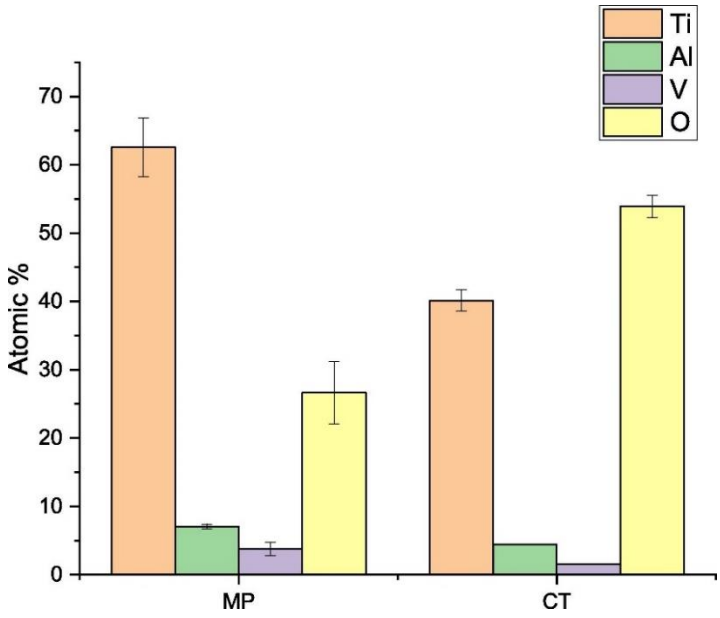

Figure 16: EDS analysis of Ti64ELI samples before (MP) and after (CT) the chemical treatment. The chemical composition is expressed as atomic percentage (Atomic %).

3.4.2 Characterization of the nisin functionalization solution

Through DLS, the zeta potential and hydrodynamic diameter of nisin in aqueous suspensions (1 mg/mL) at different pH were measured (Figure 17).

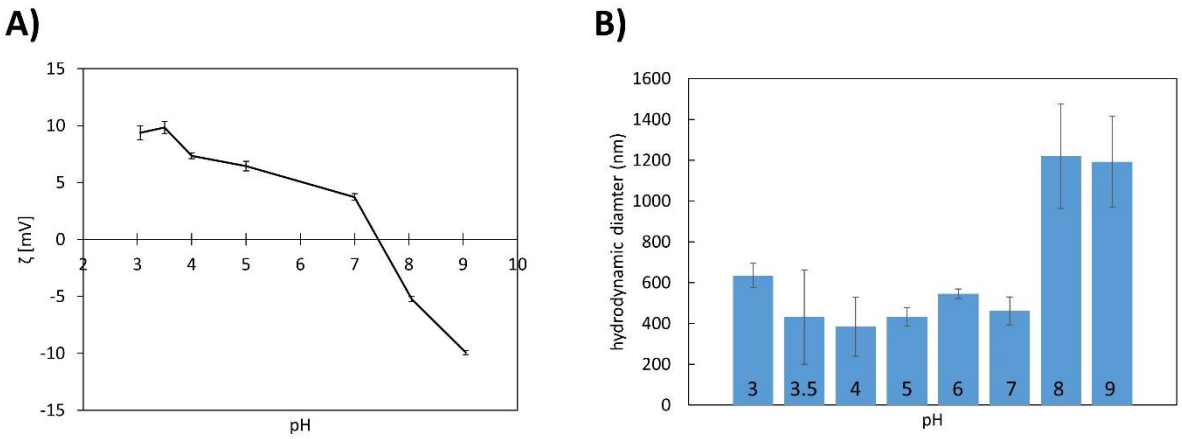

Figure 17: Characterization of 1 mg/ml nisin solutions by A) zeta potential analysis, and B) The hydrodynamic diameter of nisin, measured by DLS analysis, in aqueous suspension (1mM KCl) as a function of pH.

The isoelectric point (IEP) was detected at pH 7.5, dividing the curve into two distinct sections. At alkaline pH (above 7.5) the prevalent negative charge of amino acids primarily results from the deprotonation of carboxylic groups. Conversely, in the acidic pH range, amino acids reveal a net positive charge. The absolute value of the zeta potential does not surpass 12 mV for both the basic and acidic ranges, indicating that the net charge of nisin under these conditions is relatively weak. This aligns with similar findings reported in (175). The theoretical calculation for the IEP of nisin stands at 8.8 (176); the disparity can be rationalized by considering the low absolute value of the registered zeta potential and the high sensitivity of the zeta potential to the ionic strength of the solution.

As seen in Figure 17, the hydrodynamic diameter measured approximately 400–600 nm within a pH range of 3 to 7. The diameter notably expands to 1.2

microns beyond pH 8, signifying decreased solubility and stability of the colloidal suspension at alkaline pH levels. These findings indicated that the functionalization process should not be conducted at a pH of 8 or higher, particularly if the formation of agglomerates needs to be averted. This aligns with existing literature underscoring the decline in nisin solubility with escalating pH values (177).

Based on the zeta potential titration curve results, the decision was made to conduct the nisin adsorption processes at pH 5, 6, and 7. Within this range, nisin exhibits an overall positive charge, progressively increasing due to the augmentation of deprotonated carboxylic groups and the zwitterionic form as the pH approaches 7. Avoiding any alkaline pH levels was crucial due to the observed instability of the colloidal suspension, revealed by the measured hydrodynamic diameter of nisin in aqueous media. Additionally, pH values below 5 were avoided to prevent any potential corrosion of the metal substrate.

3.4.3 Physicochemical characterization of nisin-functionalized samples

The EDS analysis of the bare and nisin-functionalized samples (Figure 18) evidenced the presence of all the elements characteristic of the surface of the titanium alloy: Ti, Al, V, and O. A slight increase in nitrogen (N) was noticed comparing the bare and functionalized surfaces, suggesting the presence of the nisin polypeptide on the sample surface; this enhancement was much more significant for the sample functionalized at pH 6, where an increase in carbon (C) was also detectable. Considering the high penetration depth of EDS (higher than 1 micron) and the expected low thickness of the functionalized surface layer, the high standard deviation obtained by this analysis was not surprising. The surface chemical analysis was confirmed through XPS quantitative analysis, which is

much more suitable for the chemical characterization of the outermost surface layer thanks to its nanoscale sampling depth, which makes it a more sensitive surface analysis technique.

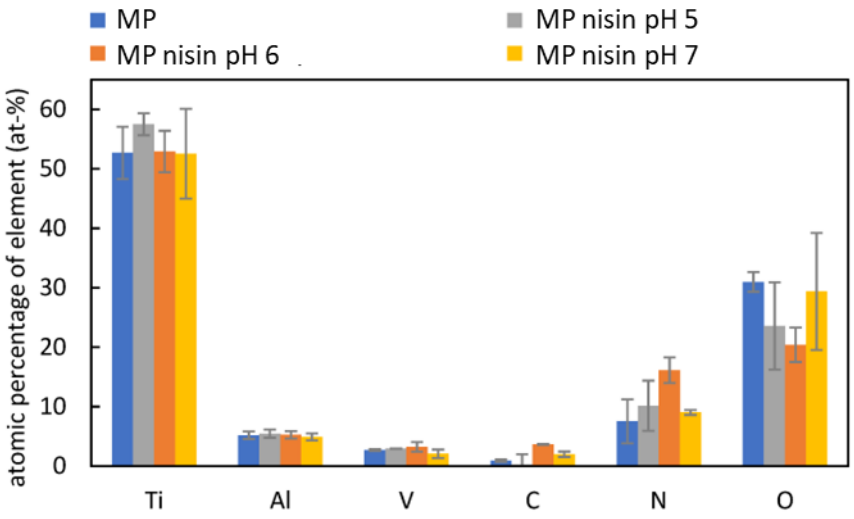

Figure 18:EDS analysis of MP samples, both bare and functionalized surfaces with processes at different pH values (pH = 5/6/7).

The UV–Vis spectra of the bare and functionalized samples (Figure 19) have been measured in reflectance. These data evidence an attenuation, after functionalization, of the surface reflectance along all the measured ranges of wavelength. This agrees with the presence of a surface adsorbed layer able to reduce the high reflectance of the metal surface. No significant difference among the surfaces functionalized at different pH values can be detected by this technique.

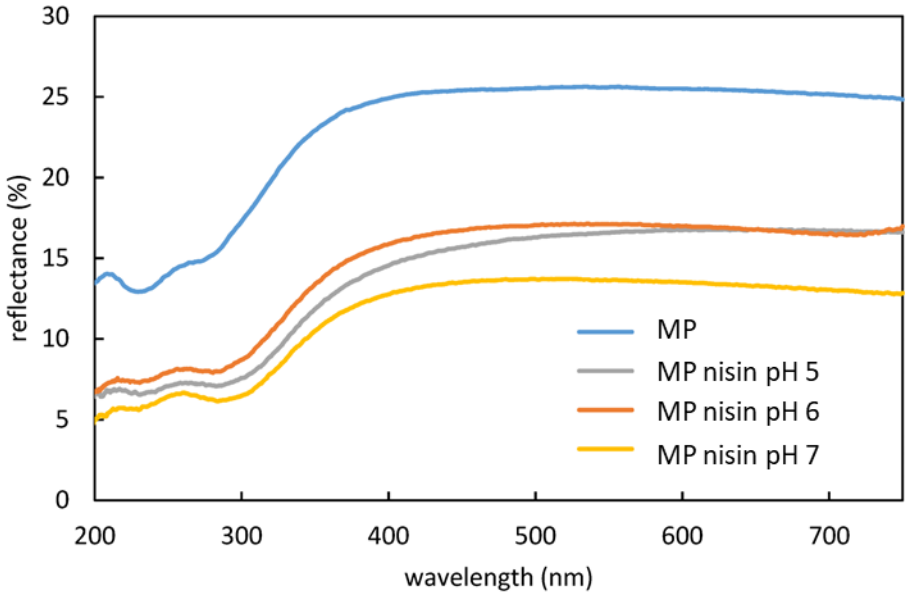

Figure 19: UV–Vis reflectance spectra of the MP samples both bare and surfaces functionalized with processes at different pH values.

In addition, KPFM has been used for imaging the functionalized surface (Figure 20). A sample functionalized at pH 6 has been chosen for this experiment due to its highest amount of the adsorbed nisin evidenced by EDS and XPS (see below) measurements. An internal control surface was needed for this analysis. For this purpose, a sample functionalized only on the half surface and with a sharp border between the functionalized and un-functionalized area was prepared.

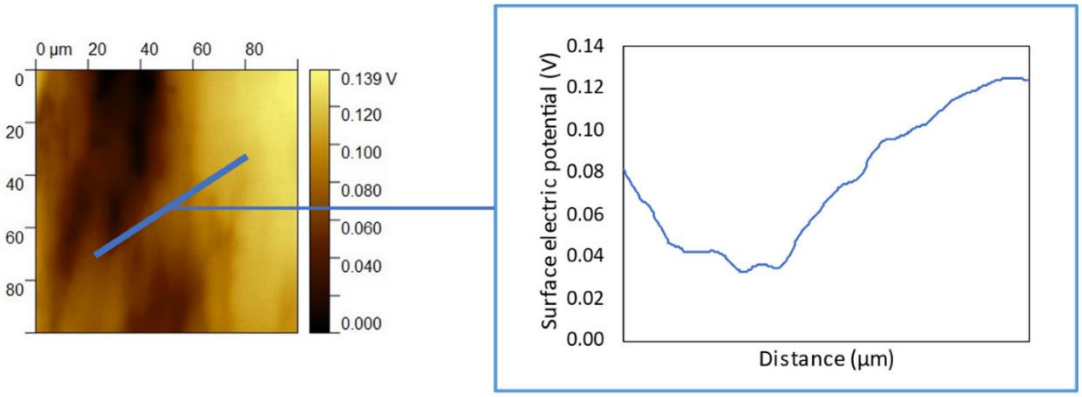

Figure 20: KPFM surface potential as a function of the distance across the interface between a bare (light area) and nisin-functionalized (darker area) region (functionalization at pH 6).

When comparing the bare (lighter area) and functionalized (darker) areas of this sample, a clear difference in the surface electrical potential was detected across the interface (Figure 20). This was a further confirmation of the presence of the functionalized surface layer. No evident formation of nisin micrometric aggregates on the surface could be evidenced while the covering seemed not homogeneous.

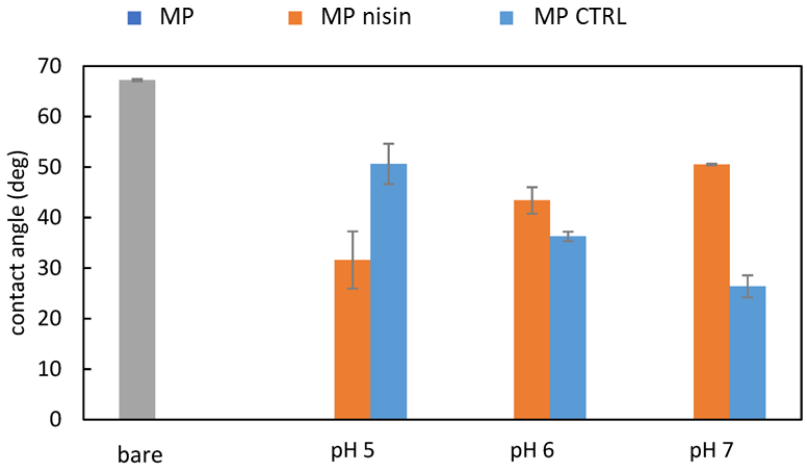

Figure 21: The contact angles measured on the bare MP sample (grey), samples functionalized with processes at different pH values (orange), and control samples soaked in solutions at different pH without nisin (blue).

Surface free energy was calculated on the surface of Ti64ELI before (MP), after the chemical treatment (CT), and after nisin adsorption at pH 6 (CT Nisin6). For this characterization, the CT surface coated with nisin at pH 6 was selected according to the previous results and considering the expected relevant role of polar functional groups on this substrate. The values of the total surface energy (γ), together with its dispersive γd and polar γp components, are reported in Table 4.

Table 4: Surface energy γ, and its dispersive γd and polar γp components, of the surface of chemically treated Ti64ELI before (CT) and after nisin adsorption (CT Nisin6). MP is reported as a control.

	Surface energy (mN/m)		
	γ	**γ^d**	**γ^p**
MP	55.7 ± 1.3	27.4 ± 0.1	28.3 ± 1.3
CT	73.0 ± 0.1	27.4 ± 0.0	45.6 ± 0.1
CT Nisin pH6	72.7 ± 0.3	27.4 ± 0.0	45.3 ± 0.3

Comparing MP and CT, it was clear that the chemical treatment was inducing an increase in the total surface free energy of the substrate, which was mainly due to the higher polar component characterizing CT, while the dispersive component remained constant. This was in accordance with the zeta potential and XPS analysis, which highlighted the presence of hydroxyl groups on the CT surface, the main cause of a more hydrophilic surface and, consequently, a higher polar component. After nisin adsorption, no significant difference was detected, since comparable values of γ, γp, and γd were observed on the substrate both before (CT) and after (CT Nisin6) nisin adsorption. This was of relevance because a

threshold of 40 mN/m is reported as a general rule for cell adhesion on surfaces and tissue integration: hydrophobic surfaces with lower surface energy are usually cytotoxic, while hydrophilic surfaces with higher surface energy are usually suitable for tissue integration, and surfaces with surface energy just at the threshold value are nor cytotoxic neither adhesive for the cells (e.g. osteoblasts).

CT substrate both before (CT) and after (CT Nisin6) nisin adsorption has proven to show a super-hydrophilic behavior (contact angle with water of (4.5 ± 0.9)° and (7.1 ± 1.6)° for CT and CT Nisin6, respectively). Interestingly, the same behavior was observed also towards organic solvents (e.g., hexadecane and ethylene glycol), characterized by different polarities and surface tensions. The contact angles of CT and CT Nisin6 were in fact (3.7 ± 0.4)° and (4.6 ± 0.3)° for hexadecane, (4.2 ± 0.7)° and (5.4 ± 0.5)° for ethylene glycol, respectively. This was of relevance considering that the simulated and real physiological fluids have lower surface tension than water (as low as 55 mN/m) and that good wettability by physiological liquids is required for tissue integration. In conclusion, the nisin-coated surface here developed can be supposed to be suitable for integration with the biological tissues.

In Figures 22 and 23 the zeta potential titration curves of MP and CT before and after nisin adsorption are reported. In Table 5, the IEP values of each surface of interest and nisin solution are shown.

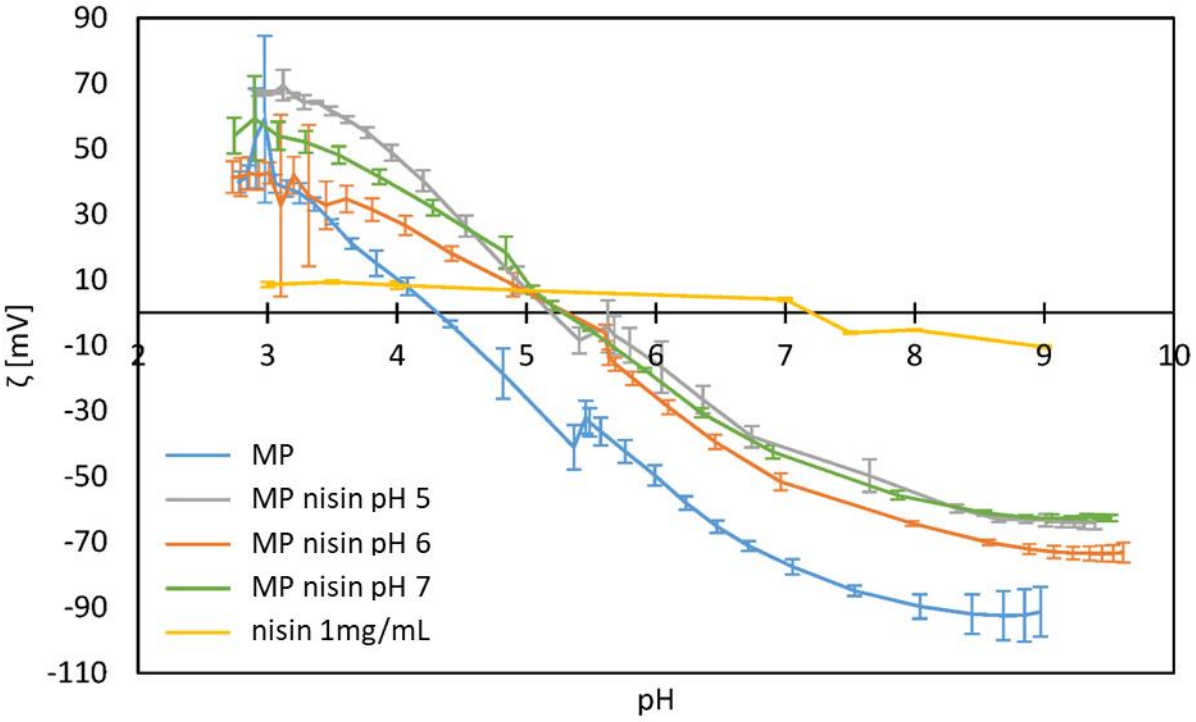

Figure 22: Zeta potential titration curves of the bare MP sample, surfaces functionalized with processes at different pH values, and a solution of nisin.

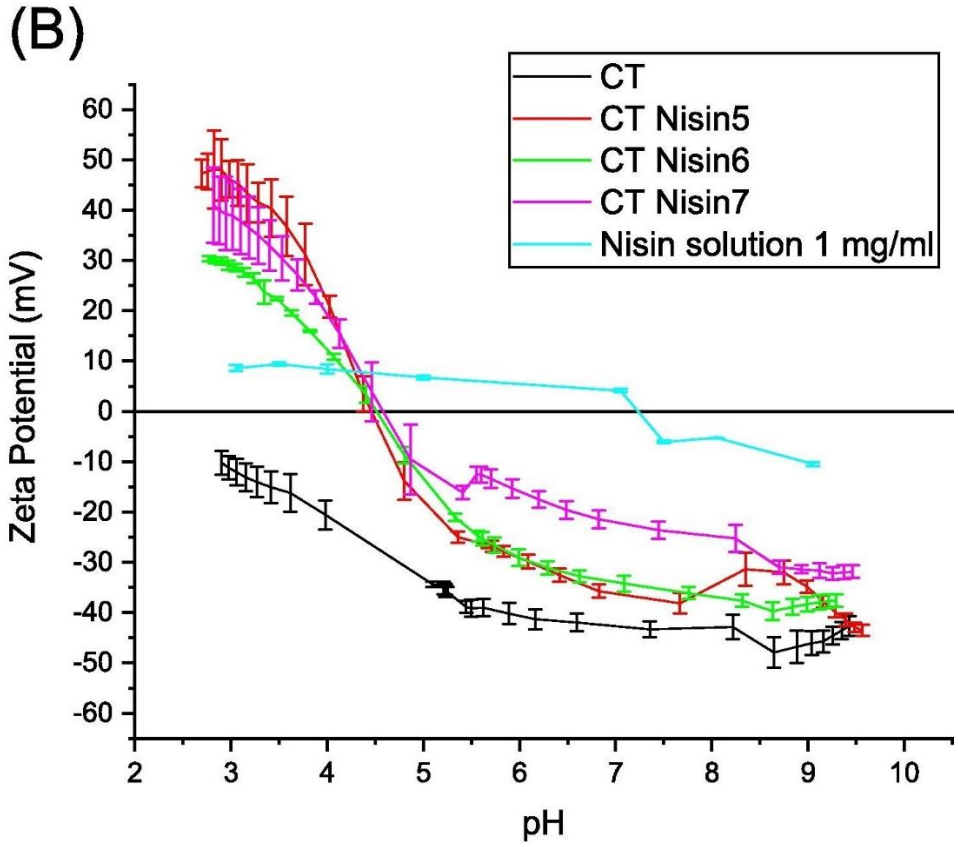

Figure 23: Zeta potential titration curves of Ti64ELI before (CT) and after (CT Nisin5, CT Nisin6, CT Nisin7) nisin adsorption; the zeta potential titration curve characterizing the nisin solution (1 mg/ml) is also reported.

Table 5: IEP of MP and CT before and after nisin functionalization in pH 5,6, and 7. IEP of nisin solution (1mg/mL) is also reported.

	MP	MP NISIN 5	MP NISIN 6	MP NISIN 7	CT	CT NISIN 5	CT NISIN 6	CT NISIN 7	NISIN 1MG/ ML
IEP	4.4	5.3	5.4	5.4	2.2	4.5	4.5	4.6	7.5

The impact of chemical treatment on the surface characteristics was evident through the examination of titration curves, specifically in relation to the shape and isoelectric points (IEPs). The IEP identified in the untreated MP samples (pH = 4.4) aligned with established literature values for the standard titanium alloy Ti6Al4V, signifying a surface with minimal functional groups with a strong acid-base reactivity (93,178). Upon chemical treatment, a notable shift of the isoelectric point was observed, lowering it to 2.2 in the treated CT samples. This alteration was attributed to the introduction of functional groups exhibiting strong acidic characteristics. Both CT and MP samples displayed chemical stability across a broad pH spectrum, as evidenced by consistently low standard deviations in zeta potential at each data point. This stability was particularly significant given the dynamic pH variations *in vivo* during inflammatory conditions, where the pH can range from 7.4 to 4.5 (179). Furthermore, in the case of CT, the chemical treatment resulted in the formation of a thicker oxide layer, a critical factor in impeding corrosion phenomena. This corrosion resistance is pivotal, especially in the context of functionalization processes, where maintaining structural integrity is paramount.

The titration curve for the CT exhibited a distinct characteristic—a lower slope around the isoelectric point (IEP) when compared to the MP curve. This phenomenon was linked to higher hydrophilicity, indicative of strong water molecule adsorption on the CT surface. The strong adhesion of water molecules prevents their displacement by ions in the solution, whether they be hydroniums or hydroxyls, upon alterations in pH. The CT curve showed a plateau at approximately −45 mV within the pH range of 5–6 and maintained near-constant values throughout the entire basic region. These observed characteristics (IEP shift, high hydrophilicity, and the plateau in the alkaline range) can be rationalized by the presence of a substantial quantity of hydroxyl groups on the surface, displaying strong acidic tendencies. These hydroxyl groups underwent progressive deprotonation within the pH range of 2–6 and achieved complete

deprotonation at higher pH levels (93,170). The abundance of such functional groups enhanced the potential for nisin grafting, a topic that will be further explored in the subsequent discussion.

Following the adsorption of nisin, an altered shape emerged in the titration curves for both MP and CT samples. Notably, the IEP of the nisin-functionalized samples in both cases shifted towards more basic pH values compared to the unmodified samples, aligning with the IEP of nisin itself. This shift was indicative of a successful and consistent functionalization with nisin across all tested surfaces. Crucially, the IEP of the nisin-functionalized samples differed from that of the nisin solution, implying that a uniform coating was not formed on the surface. Instead, it suggested the presence of a layer comprising adsorbed nisin molecules, allowing the substrate to remain exposed to the surrounding solution.

Moreover, distinctions were apparent among the functionalized samples prepared at different pH values within the CT series.

Both MP Nisin6 and CT Nisin6 exhibited a unique curve, particularly in the acidic range with lower zeta potential values, potentially owing to a different orientation (or lower quantity) of the grafted polypeptide compared to other samples. CT Nisin5 and CT Nisin7, instead, shower a stronger and comparable zeta potential with no statistical difference in the basic range, while MP Nisin 7 showed some slight difference in the acidic range. The curves of CT Nisin5 and CT Nisin7 both exhibited an unstable behavior in the acidic range, as indicated by the high standard deviations of zeta potential. Meanwhile, MP Nisin 5-7, and CT Nisin 6 demonstrated low standard deviations, suggesting greater stability. This difference may be attributed to variations in the stability of the bond between the surface and the grafted polypeptide. A tentative explanation states that –OH groups on the CT surface were not entirely deprotonated at pH 5, and the zwitterionic form of the polypeptide was dominant at pH 7, resulting in a lower

net charge on the molecule. In both cases, weaker electrostatic attraction between the substrate and biomolecule was anticipated. In contrast, the maximized electrostatic interaction at pH 6 suggested a more stable grafting through electrostatic attraction, leading to the selection of CT Nisin6 for further release and antibacterial analyses.

In the case of MP, physisorption involving electrostatic attraction between the negatively charged metal surface and the overall positively charged polypeptide was anticipated during functionalization processes. Given that MP nisin at pH 7 is close to its IEP (with almost no net charge on the biomolecule), and the absolute value of the zeta potential of bare MP was the lowest at pH 5 (indicating the minimum surface charge of the substrate within the explored pH range for functionalization), the highest electrostatic interaction between the MP substrate and the physisorbed biomolecule was expected to occur at pH 6.

To compare the presence of nisin on the different surfaces and quantify the elements of interest on each surface, XPS analysis was performed on MP, MP Nisin5-7, CT, and CT Nisin5-7. In Table 6, the composition of the considered surfaces is reported.

Table 6: Composition of the surface of each sample by XPS. The results are expressed as atomic percentages (at%).

Elements (at-%)	MP	MP Nisin pH5	MP Nisin pH6	MP Nisin pH7	CT	CT Nisin pH5	CT Nisin pH6	CT Nisin pH7
C	35.9	64.3	60.2	56.2	20.7	49.9	46.5	51.0
O	43.3	24.4	25.3	28.4	53.1	32.4	33.5	30.5
N	0.5	4.7	4.5	4.2	2.0	7.8	8.4	7.3
Ti	11.1	4.3	5.4	6.0	21.6	8.4	9.7	8.2
Al	3.4	0.6	2.0	1.6	2.6	0.9	1.0	1.3
S	0.3	0.2	0.2	0.3	0.0	0.4	0.8	0.9
Others	5.5	1.4	2.6	3.2	0.0	0.3	0.2	0.7

When comparing MP and CT samples, distinctive differences emerged in the elemental composition. The CT samples exhibited a notably higher presence of Ti and O, the constituents of the oxide layer. In the context of all nisin-functionalized samples, regarding both MP and CT, a substantial increase in C and N is observed in comparison to the control samples (MP or CT). This aligned coherently with the anticipated formation of a polypeptide surface layer. In the case of CT, there was a more pronounced increase in C and N, indicating potentially more effective nisin adsorption. Conversely, there was a noticeable decrease in Ti, O, and Al on the surfaces functionalized with nisin. This reduction was rationalized by the coverage of the titanium oxide layer and metal alloy by the adsorbed nisin layer. The persistence of a detectable Ti signal after nisin adsorption suggested either partial surface coverage or the presence of a uniformly thin nisin layer, with a

thickness below 5–10 nm (180). The detected amount of S was too low in comparison to the control samples to be considered significant.

The successful adsorption of nisin was also appreciable by the significant modifications of the high-resolution spectra acquired on the surfaces before (MP and CT) and after nisin adsorption at the three considered pH conditions.

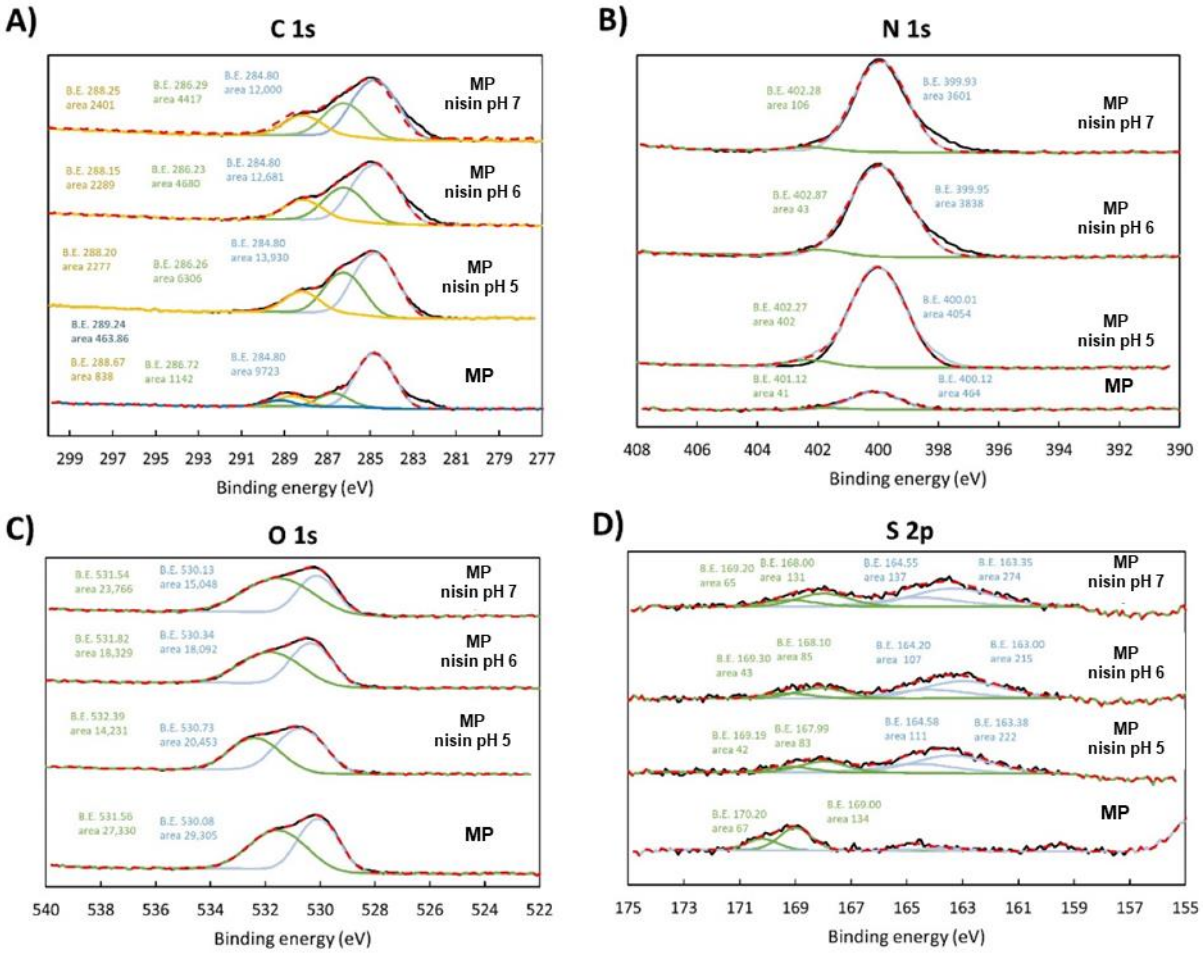

Figure 24: High-resolution spectra of (A) C 1s, (B) N 1s, (C) O 1s, and (D) S 2p regions of the bare MP sample and surfaces functionalized with processes at different pH values. Black line (-): spectrum line, red dashed line (- - -): composite line.

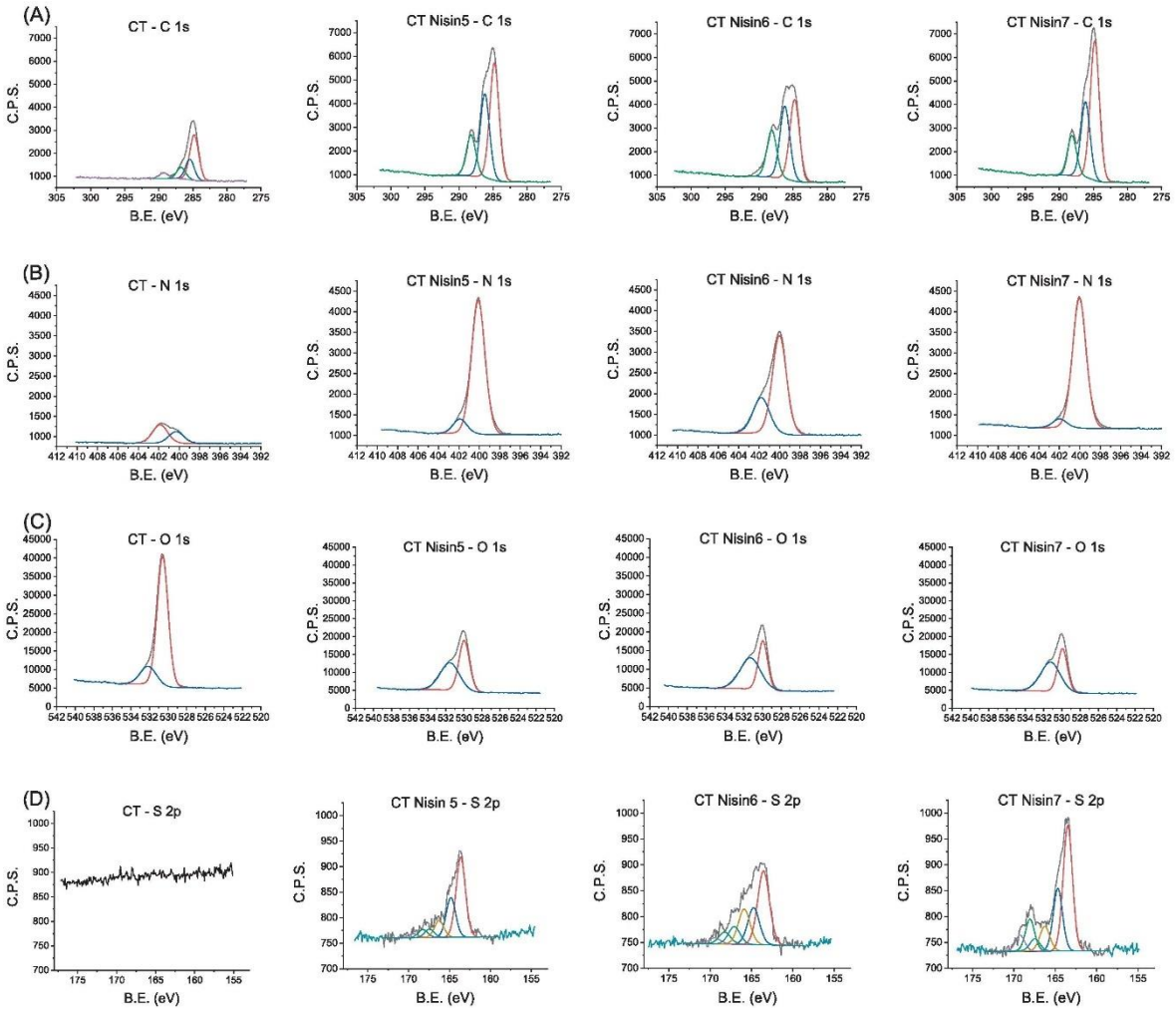

Figure 25: High-resolution spectra of (A) C 1 s, (B) N 1 s, (C) O 1 s, and (D) S 2p acquired on CT, CT Nisin5, CT Nisin6, CT Nisin7 by XPS analysis. The binding energy (B.E.) is expressed in eV and the relative area in arbitrary units.

After nisin adsorption, an intense C 1 s peak at (286.2 ± 0.2) eV appeared for both MP and CT samples, which was attributed to the presence of C-O/C-N and C = O bonds (166). Furthermore, the presence of the component at (288.2 ± 0.2) eV, characteristic of carbon in peptide bonds (O=C-N), ulteriorly confirmed the presence of nisin on the surfaces and the effective adsorption (181).

In the case of the MP functionalized samples, the N 1s peak exhibited a significant elevation in the functionalized samples, corroborating the presence of an adsorbed layer of the polypeptide, as previously observed. Notably, the peak attributed to charged/protonated amino groups (NH_3^+) at 401.9 ± 0.2 eV consistently remained at a lower intensity compared to the peak of neutral aminic groups (NH_2) at 400.1 ± 0.2 eV, as discerned through profile fitting. This disparity aligned with the assumed physisorption mechanism for the functionalization, which was consistent with the absence of any functional group possessing a net charge or high chemical reactivity on the substrate. An exception to this pattern was evident in the CT Nisin 6 sample, where the relative proportion of NH_3^+ groups was higher. This suggested a distinctive bonding mechanism of the polypeptide at this particular pH, potentially involving charged amino groups. The presence of these positively charged functional groups was particularly noteworthy, given that nisin exerted its antimicrobial activity by electrostatically interacting through these groups with the cell wall precursor lipid II, which is tethered to the cytoplasmic membrane of the target bacteria. This interaction can disrupt the membrane equilibrium, inducing the formation of pores and ultimately leading to the death of the microorganism (182).

The confirmation of the adsorbed layer's non-covering nature on the functionalized samples was evident through profile fitting of the oxygen region. The Ti-O bond peak (~530 eV), characteristic of the titanium oxide layer, consistently exhibited reduced intensity on all coated samples, aligning with expectations, but was visible in any case. A distinct peak at approximately 531.5 eV was detected, attributed to OH-functional groups exposed by both the substrates (CT and MP). This analysis underscored that the MP substrate did possess functional groups, specifically hydroxyl groups. However, these groups lacked strong acidic or basic behavior and resisted facile protonation or deprotonation when in contact with liquid media, as indicated by information derived from the zeta potential titration curve. Consequently, they remained

unavailable for a chemisorption mechanism. Notably, a shift in this peak, attributed to the presence of the peptide bond, was observed in the functionalized samples. This shift was particularly pronounced in the sample functionalized at pH 5, aligning with the higher detected levels of C and N in the survey chemical analysis (Table 6).

Concerning S 2p, this element was not detectable on unfunctionalized MP or CT, while the spectra acquired after nisin adsorption can be interpreted assuming the presence of three different sulphur states. Each S chemical state was fitted with a doublet of peaks, separated by 1.2 eV and with a ratio of 2:1 between the so-called 3/2 (component at lower binding energy) and 1/2 (component at higher binding energy) components. The main one, with S 2p3/2 centered at (163.6 ± 0.2) eV, was attributed to the thiol -SH groups which are present in the molecular structure of amino acids constituting nisin (181). The others were characterized by S 2p3/2 centered at (166.1 ± 0.2) eV and (168.2 ± 0.2) eV; both are symptomatic of oxidation of the thiol groups to sulphonyl and sulphonate groups, respectively (183). However, as shown in the XPS survey scan (Table 6), no sound conclusion about the S contribution, especially in the case of MP samples, could be made due to the low detected amount similar to control samples without nisin.

3.4.4 Characterization after the release tests

The eventual release of nisin from the coated surfaces during soaking in two solutions, respectively mimicking the physiological and pro-inflammatory conditions, was tested. A surface nisin-coated at pH6 has been selected according to the previous results. The eventual presence of nisin on the surface after the release tests was tested through the contact angle analysis. Control samples (with no nisin adsorption) soaked in the same conditions have been also tested as a reference.

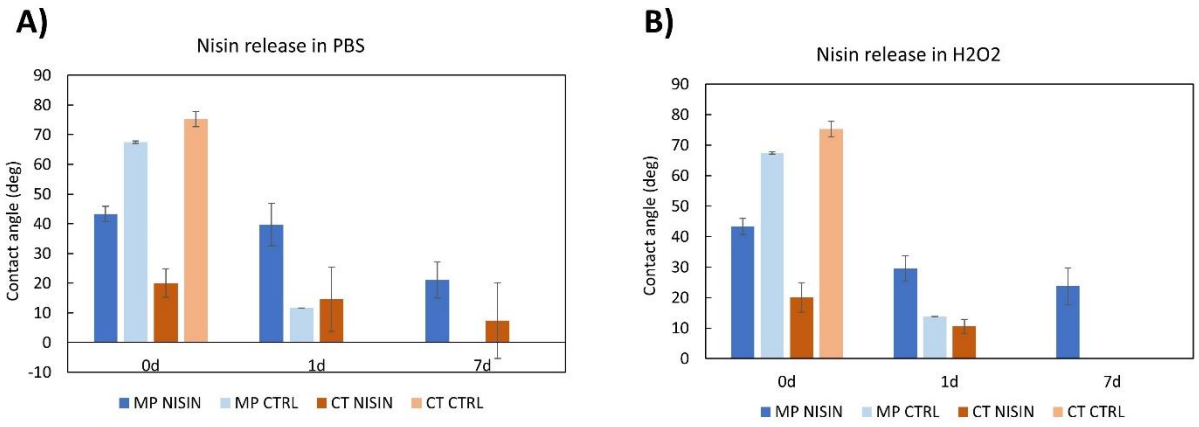

Figure 26: (A) The contact angles measured from non-soaked (0 d) and PBS- soaked (1 d, 7 d) samples. (B) The contact angles measured from non-soaked (0 d) and H2O2- soaked (1 d, 7 d) samples. Functionalization has been performed at pH 6.

In a general trend observed for both MP and CT, soaking in the solutions resulted in increased wettability on all surfaces, evidenced by a reduction of the contact angles after soaking. Notably, in the case of CT, the nisin-coated samples exhibited a less pronounced decrease of the contact angle compared to the control, after one day of soaking in both solutions, indicating the continued presence of nisin on the surface at this time point. This behavior contrasted significantly with that of MP, where the change in contact angle after the release test was consistently lower in all cases. This suggests that the CT surface was capable of releasing a greater amount of grafted nisin compared to the polished surface, hinting at a potential role of physisorption rather than chemisorption in the differential release mechanism.

The release of nisin holds significance in combatting the heightened risk of infection in the initial days after surgery (184). Based on these findings, a dual mechanism of action is anticipated from the functionalized surface in a biological environment: firstly, a release into the surrounding fluids that can counteract

floating planktonic bacteria, and secondly, direct inhibitory contact with biofilm bacteria attempting to adhere and colonize the device's surface. This dual functionality is particularly noteworthy considering that antimicrobial peptides (AMPs), like nisin, possess both direct and indirect activities against bacteria. AMPs grafted on the surface can bind directly to negatively charged membrane phospholipids, inducing bacteria death through irreversible pore formation and inhibition of ATPase activity (185). Simultaneously, released AMPs in physiological fluids can recruit neutrophils to the infection site, activating the immunological cascade and indirectly countering infection (186). In the specific case of nisin, even at concentrations lower than the minimum inhibitory concentration (MIC), this molecule exhibits regulatory effects on bacterial toxicity by downregulating the expression of toxin-encoding genes (186,187).

3.4.5 Biological characterization

According to the previous physicochemical characterization, the CT and MP Nisin6 specimens were selected for the antibacterial evaluation due to their superior ability in terms of nisin adsorption in comparison to the Nisin 5 and 7, besides the non-functionalized control (MP and CT ctrl). Moreover, considering that the bioactivity of nisin is known to be pH-dependent, specimens obtained by using the pH3 nisin stock solution from the manufacturer (here named as CT/MP Nisin3) were exploited, even if pH 3 was not promising in terms of the chemisorption mechanism (see above), and compared to the Nisin6 specimens' results to confirm that the grafted nisin at pH 6 did not reduce its biological activity due to the pH variation.

The pathogen *Staphylococcus aureus* was used to directly infect the surface of the materials. *S. aureus* was selected because it is frequently involved in bone

infections after clinical revisions, as well as the inoculum concentration ($1x10^3$ bacteria) was applied as it is reported by literature being the minimum number of bacteria potentially leading to septic condition after surgery (188).

The results of the colorimetric metabolic assay Alamar blue and SEM images are reported in Figure 27, respectively, whereas Table 7 shows the viable bacterial colonies number (at serial dilution 10^5) from the CFU assay.

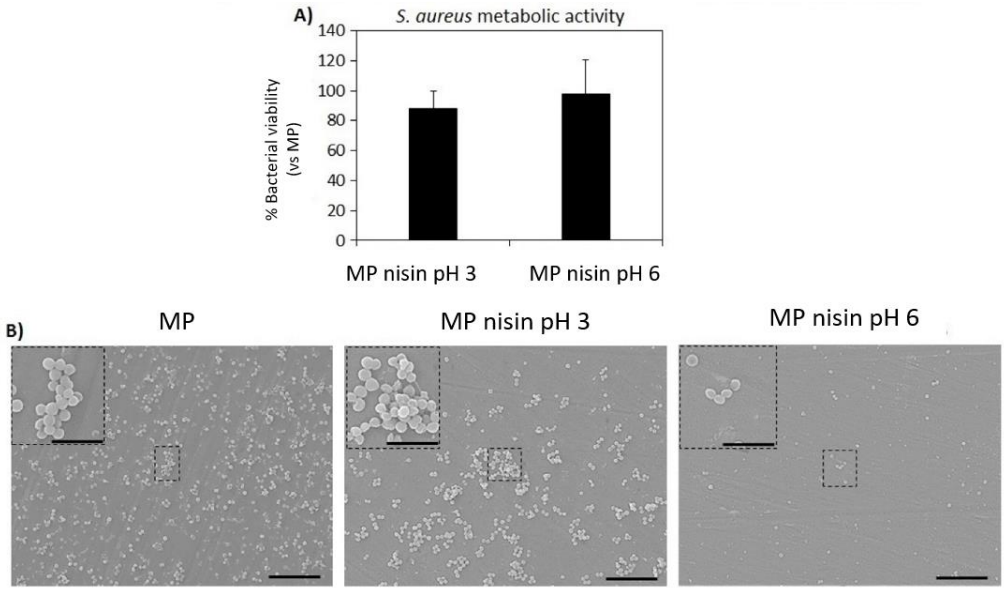

Figure 27: Antibacterial activity evaluation of MP functionalized with nisin at pH 3 and pH 6 after 24 h; (A) metabolic activity of bacterial cells normalized towards bare substrate MP; (B) SEM images at two magnifications: 2000× (scale bar 10 µm) and 5000x (scale bar 5µm).

Table 7: Viable bacterial colonies number (CFU count, means ±dev.st) after 24 h specimens' direct infection.

Specimen	Viable Colonies Count (CFU, $\times 10^5$)
MP	11 (±1)
MP nisin pH 3	9 (±0.5)
MP nisin pH 6	6.5 (±0.5)

In the case of MP, according to the metabolic activity assay, the samples functionalized with nisin at both pH 3 and pH 6 did not seem to show any statistically significant differences concerning bare MP substrates (Figure 27A, $p > 0.05$). However, viable bacterial colonies counting at serial dilution 10^5 (Table 7) showed a reduction of about 40% and 28% in colonies number for MP nisin pH 6 in comparison to bare MP and MP nisin pH 3 samples' surfaces, respectively; this reduction was clearly noticed in SEM images collected from sample surfaces after 24 h of direct infection with bacteria (Figure 27B). In fact, mostly single-round colonies were detected on the nisin-functionalized surfaces at pH 6 (MP nisin pH 6) whereas on the control (MP) and nisin-functionalized surfaces at pH 3 (MP nisin pH 3) the formation of many 3D microcolonies (biofilm-like aggregates) was observed. Therefore, a promising anti-microfouling activity preventing the formation and maturation of microcolonies (biofilm-like aggregates) seemed to be obtained by the functionalization with nisin, and the efficacy of the protocol at pH 6 was confirmed.

In the case of CT, according to bacterial metabolic activity (Fig. 28(B)) detected after 24 h of direct contact with the specimens' surfaces, the viability of

bacteria adhered to the CT Nisin6 significantly decreased up to 80% (±11%, ≈6-folds reduction) in comparison with non-functionalized CT controls (Fig. 28(B), $p < 0.05$ indicated by the §); moreover, the CT Nisin6 resulted as significant towards the CT Nisin3 specimens too (Fig. 28(B), $p < 0.05$ indicated by the #), thus confirming the surface absorption of bioactive nisin at pH6 as previously suggested by the physical–chemical characterization.

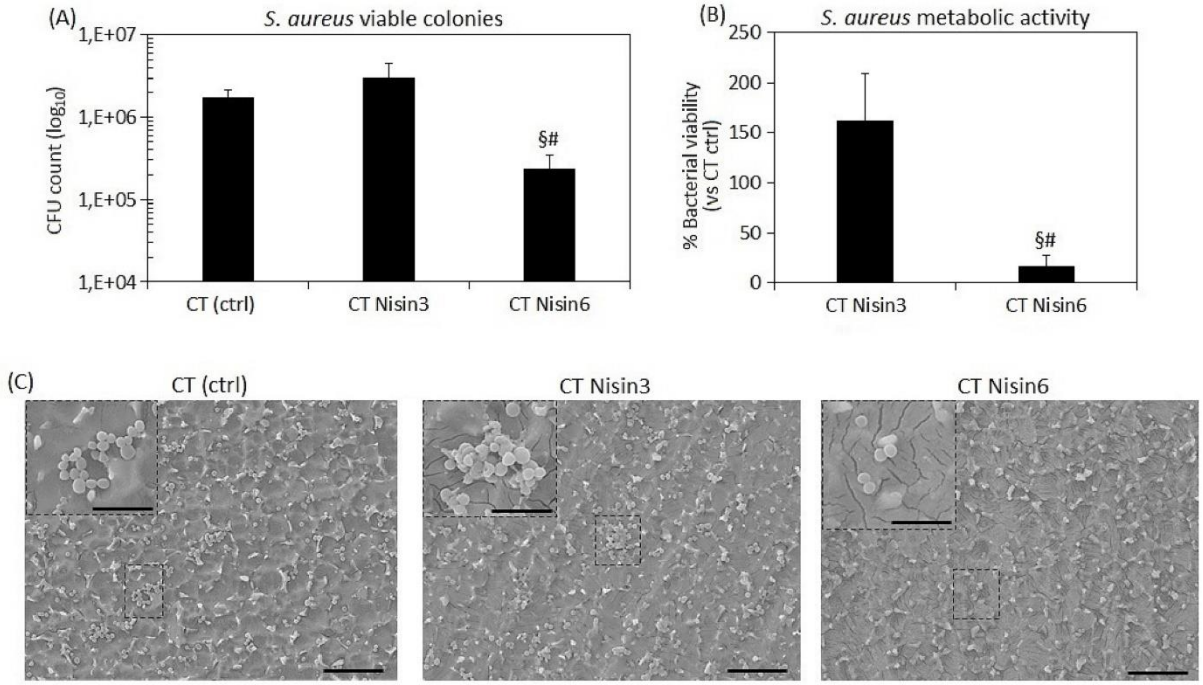

Figure 28: Antibacterial activity of Ti-functionalized with nisin at pH3 and pH6. A) Metabolic activity of bacterial cells normalized towards non-functionalized CT (ctrl); B) Viable bacterial colonies count (CFU). C) SEM images at two magnifications: 2000X (scalebar = 10 mm) and 5000X (scalebar = 5 mm). § and # indicates $p < 0.05$. Replicates n = 3.

The metabolic evaluation was then confirmed by the CFU count (Fig. 28(A); in fact, a significant reduction of the number of viable colonies (between 1 and 1.5 logs) colonizing specimens' surface was detected by comparing CT Nisin6 with the CT controls (Fig. 28(A), $p < 0.05$ indicated by the §) and the CT Nisin3 as well (Fig. 28(A), $p < 0.05$ indicated by the #); therefore, it can be hypothesized that the reduction of the metabolic activity detected onto the specimens' surface

was due to the significant reduction of the viable colonies adhered onto the CT Nisin6 specimens. Therefore, the antibacterial effect of the nisin grafted onto the CT surface resulted as much more evident in comparison to the MP specimens where only an inhibition of 3D colonies and biofilm formation was observed whereas the CFU number resulted as not significantly decreased with respect to the untreated controls. Such improvement can be probably ascribed to the higher affinity of the nisin towards the negatively charged CT surface as well as to a synergistic effect of the nanotexture preventing adhesion and nisin counteracting proliferation and biofilm formation.

Finally, as further confirmation of the nisin bioactivity, SEM images were collected to check the colonization degree of the specimens as well as the morphology of the bacteria (Fig. 28(C)). In line with previous results, the surface of the CT Nisin6 specimens showed a lower degree of contamination in comparison to the CT control and CT Nisin6. Moreover, higher magnification images revealed that bacteria adhering to the CT Nisin6 surfaces were mostly growing as single colonies whereas, in the CT control and CT Nisin3, some 3D biofilm-like aggregates were found, thus suggesting anti-microfouling activity due to the nisin higher bioactivity onto the CT Nisin6 specimens as previously observed for the MP specimens, too.

To investigate the microfouling activity of MP samples in detail, 3D reconstructed images were prepared from SEM images at magnification 2000× and shown in Figure 29. As reported in the cross-section of 3D reconstructed images of MP (Figure 29C,D extracted from SEM image of MP shown in Figure 29A) and MP nisin pH 3 (Figure 29G,H; extracted from SEM image of MP nisin pH 3 shown in Figure 29E), almost all *S. aureus* formed 3D microcolonies aggregates on the samples' surfaces; in fact, Figure 29B,F show that the size of such microcolonies range between 4–5 μm for both MP and MP nisin pH 3

samples in comparison to the size of *S. aureus* of about 1–1.5 µm indicating that these 3D microcolonies are made up of about 3–4 layers of bacterial cells. The calculation of occupied surfaces with biofilm-like aggregates revealed 19.1% and 16.39% on the MP and MP nisin pH 3 were colonized by *S. aureus*, respectively (these data were extracted from the field of view of Figure 27B,F as representatives of whole samples' surfaces). Surface analysis of 3D reconstructed images of MP nisin pH 6 (Figure 29K,L; extracted from SEM image of MP nisin pH 6 shown in Figure 29I) indicated that few bacterial colonies were able to form aggregates of more than 4 µm and most *S. aureus* remained as single cells (Figure 29J,K,L); additionally, only 6.8% of the sample surface was occupied by bacterial microcolonies (these data were extracted from the field of view of Figure 29J as a representative of whole samples' surfaces) in comparison to 19.1% for MP and 16.39% for MP nisin pH 3.

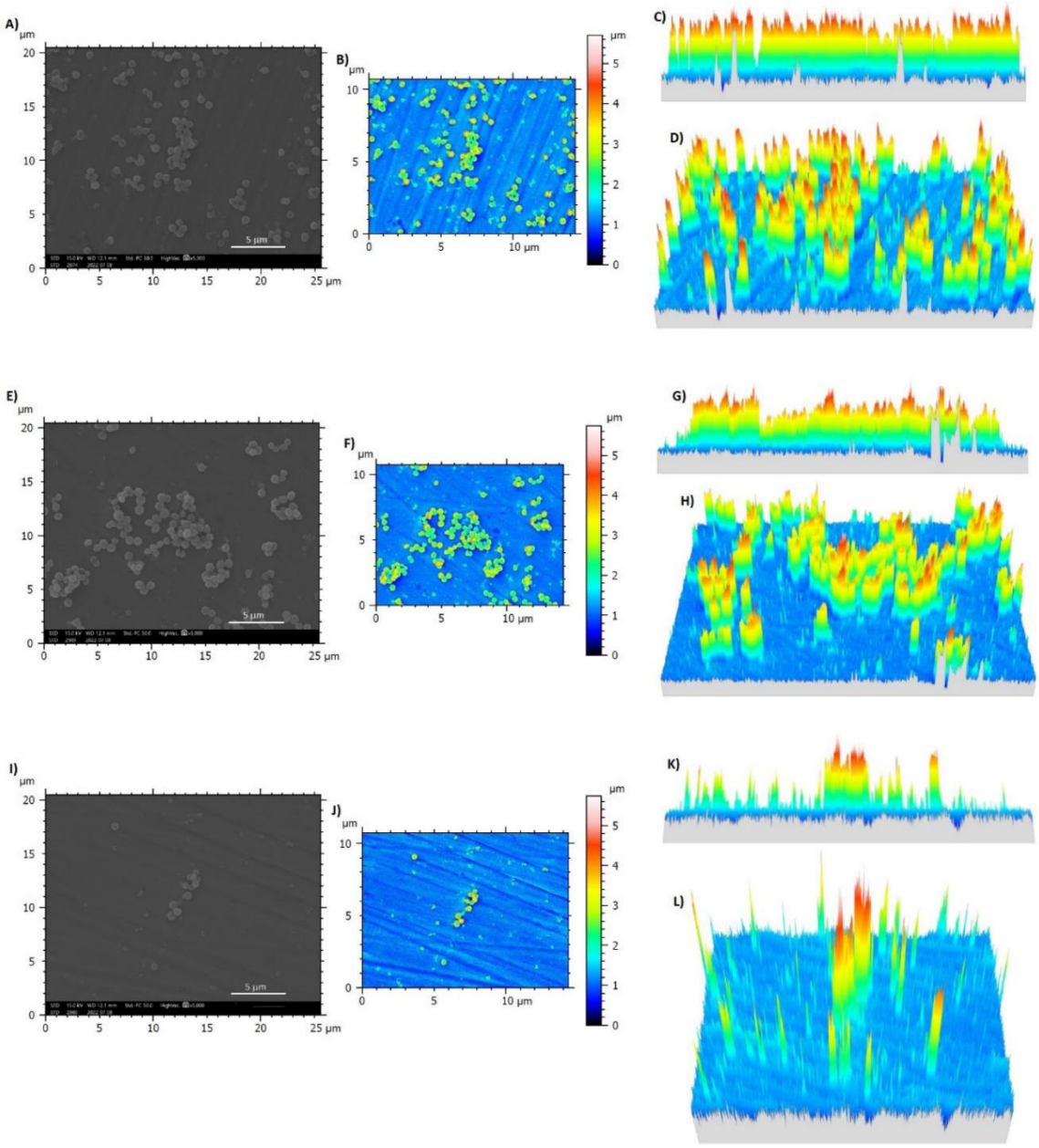

Figure 29: Three-dimensional reconstructed images of bacterial microcolonies on samples' surfaces extracted from SEM images with SMILE VIEWTM software. MP: (A) SEM image at magnification 2000× (scale bar= 5 µm); (B) reconstructed 3D image extracted from (A); (C) cross-section image of the bacterial microcolonies on the sample surface; (D) whole view of bacterial microcolonies from the selected section; MP nisin pH 3: (E) SEM image at magnification 2000× (scale bar= 5 µm); (F) reconstructed 3D image extracted from (E); (G) cross-section of the bacterial microcolonies on the sample surface; (H) whole view of bacterial microcolonies from the selected section; MP nisin pH 6: (I) SEM image at magnification 2000× (scale bar= 5 µm); (J) reconstructed 3D image extracted from (I); (K) cross-section of the bacterial microcolonies on the sample surface; (L)

whole view of bacterial microcolonies from the selected section. Bars indicate the height of microcolonies (µm).

From the results obtained from the metabolic activity, viable bacterial colonies count (at serial dilution 10^5), SEM, and 3D reconstructed images analysis it can be concluded that MP functionalized with nisin at pH 6 have no bactericidal activity; however, it successfully prevented the bacterial aggregation into 3D biofilm-like aggregates thus reporting a promising antifouling activity. Similar results were found in another study where the synergistic antifouling properties of nisin and dopamine adsorbed to microstructured glasses with different sizes of grooves were reported against *Bacillus sp.* with respect to the control sample after 16 h (166). Additionally, this similar effect was previously obtained by the authors introducing a controlled nano-topography onto Ti alloys by electron beam technology that prevented aggregates formation through a physical hindrance (189); here, the nisin seemed to play a similar role but via biochemical induction acting as an anti-aggregation signal for adhered bacteria. Few comparable works can be found in the literature, but the presence of nisin was previously shown by Blackman et al. (190) to reduce the surface contamination from bacterial aggregates in combination with a specific patterning as well as Kim et al. (191) demonstrated that the presence of nisin conferred outstanding fouling resistance to ultrafiltration PDMA membranes when infected.

One possible explanation for the observed ability of the nisin layer to prevent bacterial aggregates is the impact on biofilm maturation. In general, the formation of biofilm is known to consist of several steps including bacteria adhesion, irreversible attachment, biofilm maturation, bacteria dispersal, and bacterial migration. In addition, materials can behave as either anti-microfouling with bacteriostatic action, or as bactericides, acting with different mechanisms and on different stages of biofilm formation (192). It can be speculated that the nisin-functionalized surface influences the maturation of the biofilm, therefore preventing the aggregation of bacteria. In the literature, nisin is also found to

affect the composition and structure of the biofilm. Andre et al. evidenced the presence of nisin to result in a reduction of *S. aureus* biofilm polysaccharides and extracellular DNA, which can be associated with disrupted or decreased biofilm formation (193).

Summarizing these results, it can be hypothesized that the chemical treatment applied to the Ti surface was successful in increasing or stabilizing the nisin adsorption probably due to the negatively charged nanotextured layer and a chemisorption mechanism. However, it seemed evident that in the case of MP, even though adsorbed nisin at pH 6 could prevent the formation of bacterial aggregates on the surface to some extent, the well-known antibacterial potential of nisin was not here fully maintained after surface functionalization. Similar results were found in another study where the antibacterial properties of nisin adsorbed to stainless steel against *Listeria monocytogenes* were similar with respect to control after 24 h (164). The results obtained from the functionalization by using the nisin solutions at pH 3 and pH 6 excluded the hypothesis that the low antibacterial activity was due to the molecule's sensitivity to pH variation: the functionalization at pH6 was revealed to be more effective in surface grafting and against microfouling and biofilm maturation. The contact-killing activity of nisin was mainly due to its binding with the bacterial membrane causing irreversible deadly pores (186). So, further studies are still needed to improve the antibacterial efficacy of nisin, as well as other functionalization mechanisms, which could also be investigated to improve either the exposure of nisin's antibacterial groups or the release of the peptide to the solution.

3.5 Conclusion

The primary objective of this work was to optimize the surface functionalization process, achieving the immobilization of the antimicrobial peptide nisin onto titanium alloy surfaces without resorting to toxic linkers.

Through adjustments of process parameters, such as the pH level of the nisin solution during functionalization, efforts were made to enhance the degree of nisin immobilization systematically. The efficacy of surface functionalization was validated through multiple methodologies, followed by release assessments conducted under conditions mimicking physiological and inflammatory environments to elucidate the anticipated antibacterial mechanism.

Subsequently, the antimicrobial performance of the adsorbed nisin coating was scrutinized against the *Staphylococcus aureus* (*S. aureus*) strain, contrasting samples with and without nisin. Nisin functionalization was executed under two distinct conditions: on polished titanium (MP) and on chemically treated titanium (CT). Notably, effective surface adsorption of nisin was achieved at pH 6 for both conditions, alongside the initial evidence of gradual nisin release observed under physiological and inflammatory conditions.

MP condition exhibited anti-microfouling activity against bacteria and showed promising signs regarding its potential impact on biofilm maturation. In contrast, the CT condition, in addition to these attributes, demonstrated a moderate antibacterial effect against *S. aureus*. The confluence of CT nanotextured surfaces preventing bacteria adhesion and the active antibacterial properties of nisin suggests a synergistic mechanism in avoiding biofilm formation, underscoring the possible applications of these coatings in bone-related applications. However, further optimization and biological characterization, such as the effect of nisin coating to cytocompatibility and immunological systems remain imperative to fully harness their potential.

Chapter 4: Antimicrobial ion doping of bioactive glasses

4.1 Introduction

The prevalence of bone defects is expected to become more pronounced in the future due to the aging population (194). While a considerable number of surgeries are successful, the attachment of various microorganisms, including bacteria, viruses, or fungi, to the implantation site remains a significant factor leading to implant failure (195). The increase in orthopedic surgeries, coupled with the challenging bacterial resistance phenomenon and the diminishing availability of novel antibiotics, has created an urgent need for non-antibiotic alternatives beyond traditional methods for addressing orthopedic infections (196).

The treatment options for bacterial infections are becoming increasingly limited, posing a substantial global healthcare threat (136). Typically, systemic administration of antibiotics is employed to combat bone infections (197). However, the effectiveness of conventional antibiotic treatments is compromised by the formation of biofilms, defined as clusters of bacteria enclosed within their self-produced biopolymeric structures. Biofilms not only impede antibiotic penetration but also enhance bacterial survival through the provision of nutrient and waste transport channels (48). Gram-positive staphylococci, particularly

Staphylococcus aureus and its methicillin-resistant variant (MRSA), are the primary culprits behind orthopedic infections (198).

Given the challenges associated with bacterial resistance and biofilm formation, there is a pressing need to explore alternative approaches to treat orthopedic infections outside the realm of conventional antibiotics.

The focus of this chapter is to cover the work regarding the surface doping of bulk bioactive glass discs with inherently antimicrobial metals silver and copper. First, role of silver and copper as antimicrobial agents is discussed, followed by the literature review regarding silver and copper doped bioactive glasses. The physicochemical characterization of the glasses is the focus of the experimental part of this chapter, in addition to the biological characterization regarding the glasses´ cytocompatibility and antibacterial activity.

4.2 Inherently antimicrobial metals

Metal ions play an essential role in the biological processes of all living organisms. In bacteria, many essential enzymes that catalyze crucial biochemical reactions contain metal ions, such as nickel, copper, iron, zinc, cobalt, and manganese (199).

Interestingly, certain metals, when administered in sufficient quantities, can lead to bacterial death, making them potential candidates for antimicrobial applications.

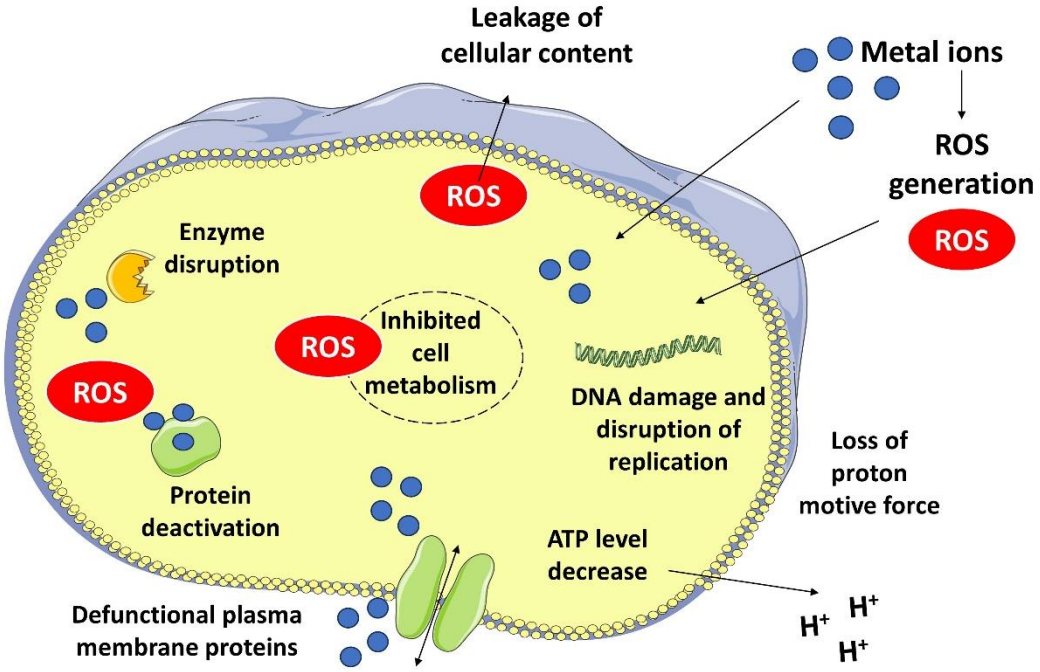

Figure 30: Summary of the bactericidal effect of metal ions

Silver ions are well-established for their broad-spectrum antibacterial efficacy and low bacterial resistance. Silver, historically and in modern times, serves as a prominent antimicrobial agent (200,201). Its antibacterial activity can be harnessed through various forms such as nanocrystalline silver, nanoparticles, colloidal silver, or silver nitrate, with silver ions being the presumed antibacterial component (199). The precise mechanism by which silver induces bacterial death is yet to be fully elucidated, likely involving effects on the cell wall or membrane, DNA interactions, enzyme and membrane protein inhibition, and the generation of reactive oxygen species (ROS) (202). ROS, resulting from incomplete oxygen reduction, lead to oxidative stress and subsequent protein and DNA damage (203).

Copper, another commonly studied antibacterial metal, generally exhibits low toxicity to humans and plays a crucial role in bone formation and healing. It has dual functionality as an antibacterial particle, such as nanoparticles, and a surface

agent effective against various bacterial strains (204). Copper's ability to eliminate bacteria involves well-defined mechanisms, including damage to the outer plasma membrane, leading to subsequent disruption of membrane integrity, transport protein activity, and ion permeability (205). Additionally, copper induces oxidative stress, generating reactive oxygen species (ROS), and contributes to DNA degradation, causing damage to lipids, proteins, and nucleic acids (206). Various factors, including size, shape, concentration, and the type of microorganisms, can influence the antibacterial properties of copper (207).

In addition to silver and copper, also other metals have been exploited as antibacterial agents, such as zinc, cerium, and gallium (208). Zinc, also important in the development, formation and metabolism of bone cells (209,210), provides antibacterial activity by inhibiting glycolysis, transmembrane proton translocation and acid tolerance in bacterial cells (210,211). There are also research about its role in would healing and angiogenesis (212,213). In the case of cerium, its antibacterial properties are hypothesized to arise from its ability to dissociate the outer membrane of bacterial cells (214,215). Gallium instead, has found use also in treatments for bone resorption (216), autoimmune diseases and cancer treatments (217), while also preventing bacterial infections (218). Poorly explored elements such as tellurium, can have antioxidant and antibacterial properties (219).

4.3 Metal-ion doped bioactive glasses

Silver and copper are both extensively studied in combination with bioactive glass (220,221). It is done usually by adding the metal as an oxide during glass synthesis, either melt-quenching or sol-gel synthesis. Less common strategies include incorporation of metal ions by ion-exchange or coatings. Table 9 below summarizes some examples.

Table 8: Examples of Cu and/or Ag-doped bioactive glasses for antibacterial activity

Material	Composition	Synthesis method	Ref
Cu or Ag-silicate BGs	SiO_2-P_2O_5-CaO-CuO/Ag2O	Sol-gel route	(222)
Cu or Ag-silicate BGs	SiO_2-P_2O_5-CaO-CuO/Ag2O	Sol-gel route	(223)
Cu-Borate and borosilicate BGs	Na_2O-K_2O-MgO-CaO-B_2O_3-P_2O_5-SiO_2-ZnO-CuO	Melt-quenching route	(224)
Ag phosphate BG	P_2O_5–CaO–Na_2O-Ag_2O	Melt-quenching route	(225)
Cu MBGs NPs	SiO_2-CaO-CuO	Sol-gel route	(226)
Ag silicate BG	SiO_2-P_2O_5-CaO-Ag_2O	Sol-gel route	(227)
Ag MBGS microspheres	SiO_2-P_2O_5-CaO-Ag_2O	Sol-gel route	(228)

However, the challenge lies in releasing metal ions at concentrations effective for bactericidal action without causing harm to other cells. Some concerns are raised due to silver toxicity, especially in the case of silver nanoparticles (AgNPs) (220). For instance, Xie and co-workers found AgNPs to compromise the viability of osteoblast-like MG-63 cells when exposed to AgNPs, with the effect continuing even after the removal of AgNPs from the culture medium (229).

Copper, however, is known to be less cytotoxic to human cells, and it also plays an important role in the metabolism of bone regeneration and angiogenesis (221). In general, for both ions, the antibacterial performance is known to be dose-dependent, with bacteria commonly being more sensitive toward silver ions (230).

In addition, one interesting option to introduce metallic ions to bioactive glass is surface doping via the ion exchange method in an aqueous solution or in molten salts (231). In this process, the monovalent ions from the surface of the glass are released and replaced by the ions of interest present in the ion exchange aqueous solution, such as silver or copper ions. This method is beneficial due to its simplicity and possibility to introduce ions of interest on the surface without unwanted crystallization phenomena. The ion-exchange process for SBA2 to obtain Ag-doped glass Ag-SBA2 (232), and for SBA3 to obtain Cu-doped glass Cu-SBA3 has been previously optimized by Miola et al. (233,234).

The glass Ag-SBA2, also in focus for this work, has been previously studied in a co-culture with human osteoblast progenitor cells (hFOBs) and a pathogenic drug-resistant (Methicillin-Oxacillin) certified strain of *Staphylococcus aureus*, evidenced its antibacterial performance and cytocompatibility (173). In addition, initial evaluation of the antibacterial performance of Cu-SBA3 powder has performed with satisfactory results against *S. aureus* (234).

4.4 Materials and Methods

4.4.1 Synthesis of the glasses and ion-exchange process

Two different silica-based bioactive glasses, SBA2 (232), and SBA3 (234) (that belong to SiO_2–Na_2O–CaO–P_2O_5–B_2O_3–Al_2O_3 system) were prepared in the bar form using the melt-quenching technique. The oxide compositions are summarized in Table 10.

Table 9: Nominal compositions of SBA2 and SBA3 glasses

mol-%	SiO_2	Na_2O	CaO	P_2O_5	B_2O_3	Al_2O_3
SBA2	48.00	18.00	30.00	3.00	0.43	0.57
SBA3	48.00	26.00	22.00	3.00	0.43	0.57

Shortly, the glass precursors were mixed and then melted in a platinum crucible at 1450 °C for 1 h, poured into a pre-heated cylindrical brass mold (Ø = 10 mm) to obtain bars, and then annealed at 500 °C for 13 h. All the cylindrical glass bars were cut into 2 mm thick discs (Buehler IsoMet High Speed Pro), which were then polished (Struers LaboPol-2) with SiC abrasive papers ranging from 320 to 1200 grid to level the disc surfaces.

Then, the sample discs went through a previously optimized and published ion-exchange process in an aqueous solution in order to incorporate therapeutic ions on the samples' surface (232,234). As shown in these previous works, the ion-exchange solution concentrations were chosen based on their ability to cause an antibacterial effect without modifying the phase composition of the glass with nucleation of unwanted crystalline peaks of silver/copper salts. Ag-SBA2 and Cu-SBA3 were produced by soaking the discs in a 0.03 M $AgNO_3$ and 0.001 M copper acetate ($Cu(CH_3COO)_2 \cdot H_2O$) solution, respectively, for 1 h at 37 °C. After the process, the samples were rinsed with bi-distilled water and dried at room temperature overnight.

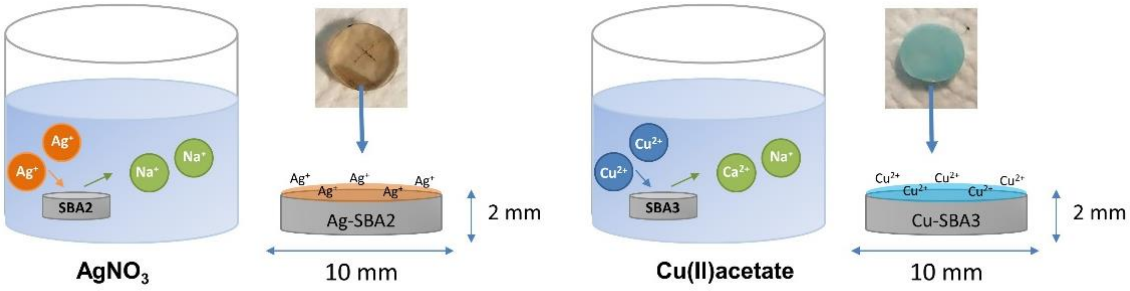

Figure 31: Ion exchange protocol

4.4.2 Sample physicochemical characterization

Field emission scanning electron microscopy (FESEM)

Field emission scanning electron microscopy (FESEM) equipped with Energy-dispersive X-ray spectroscopy (EDS) (SupraTM 40, Zeiss) was performed on all the samples in triplicates to assess their morphology and composition. Samples were mounted on double-sided carbon tape and coated with platinum.

X-ray diffraction (XRD)

The SBA3 and Cu-SBA3 sample discs were characterized in terms of their phase composition by X-ray diffraction (XRD, Malvern PANalytical X'Pert PRO diffractometer), using the Bragg-Brentano camera geometry and the Cu Kα incident radiation. The 2θ range used for sample measurements was from 10° to 70°. The data from the obtained spectra were further analyzed by using the X-Pert HighScore Software and PCPDF database.

In-vitro bioactivity testing and Cu^{2+}-ion release in Simulated Body Fluid (SBF) and pH5 sodium acetate buffer

The glass samples of SBA3 and Cu-SBA3 were subjected to in vitro bioactivity tests by soaking them in simulated body fluid (SBF). The SBF

was prepared using the protocol developed by Kokubo et al. (235). In addition to soaking samples in SBF, a sodium acetate/acetic acid (HAc/NaAc) buffer was implemented as a second soaking solution to mimic Cu^{2+}-release in inflammatory-mimicking low pH conditions, occurring in infections (236,237). The HAc/NaAc buffer was prepared at the concentration of 0.1 M and pH was adjusted to 5 by adding 1 M NaOH.

Polished glass discs were immersed in 50 mL of SBF for fixed periods (1, 3, 7, 14, and 28 days), with five replicate samples of each glass per time point. Samples were maintained at 37 °C in an incubating shaker with an orbital speed of 120 rpm to simulate the physiological fluid flow.

The change in the solution pH was recorded for each immersion time by pH meter (Hanna Edge HI2020, accuracy ± 0.01) and compared to a blank sample containing only SBF. Then samples were rinsed carefully with bi-distilled water and let dry at room temperature.

Both solutions at each time point were collected and the cumulative ion release for each sample was calculated by adding the ion release value at the selected time point to the previous ones. The cumulative curves were obtained by using the average of each sample. The Cu^{2+}ion release was determined by an inductively coupled plasma mass spectrometer (ICP-MS, iCAPTM Q, Thermo Fisher Scientific).

Zeta potential titration

The measurements were performed both on as-prepared glasses and SBF-soaked ones to measure the surface zeta potential as a function of pH and the isoelectric point utilizing the streaming potential technique. The used instrument was an electrokinetic analyzer for solid surfaces (SurPASS, Anton Paar, Austria). An aqueous solution of KCl (0.001 M) was used as an electrolyte.

Both acidic and basic titrations were performed starting from a pH of 5.5 for all the samples, with instrument washing with ultrapure water in between each step. Two different couples of samples per glass were used respectively for the acidic and basic titration. An adjustable gap cell was used for the measurements. The gap between a couple of samples was adjusted to approximately 100 μm and the electrolyte flow to 100 mL/min, as suggested by the instrument provider (32).

Glasses immersion and ion release analysis

The Ag-SBA2 and Cu-SBA3 samples along with their undoped controls SBA2 and SBA3 were immersed in 1 mL of α-Minimum Essential Medium pure culture medium (α-MEM, Gibco, Thermo Fisher Scientific, without serum and antibiotics) for 7 days. To analyze the Ag- and Cu-ion release, the glass dissolution products were collected and analyzed using inductively coupled plasma-optical emission spectrometry (ICP-OES; Agilent 5100 ICP-OES). The analyzed elements included Ag (λ = 328.068 nm), and Cu (λ = 223.009 nm). The measurements were conducted in three separate samples at each time point for each composition and the results are presented as mean ± standard deviation.

Contact angle

The wettability of the doped glasses compared to the undoped ones was assessed by static contact angle measurement by the sessile drop method (Krüss DSA 100, KRÜSS GmbH). Ultrapure water was used as a wetting fluid. A drop of water (5 μL) was deposited on the surface with a pipette and the contact angles were measured through the instrument software (DSA-100, Dropshape Analysis, KRÜSS GmbH).

EDS analysis

In addition, before and after three days of soaking in the α-MEM pure culture medium, the sample surfaces were analyzed by energy-dispersive X-ray spectroscopy (0 day results: JCM-6000 Plus Benchtop SEM, Jeol, equipped with EDS; 3 day results: EDS, Oxford Instruments X-MaxN 80) to study the effect of soaking to the ion-exchanged surface layer of Ag- or Cu-ions.

4.4.3 Biological characterization

4.4.3.1 Sample cytocompatibility

Before cell culture experiments, the sample discs were heat sterilized for 3 h at 100 °C and stored at room temperature until use.

Ethics statement

Human adipose stem cells (hASCs) were isolated from a subcutaneous abdominal tissue sample obtained from a female donor (age 49 years, BMI 21.4) at the Tampere University Hospital Department of Plastic Surgery with the donor's written informed consent and processed under ethical approval of the Ethics Committee of the Expert Responsibility area of Tampere University Hospital (R15161).

Adipose stem cell isolation and expansion

The cells were isolated as described previously (238). The mesenchymal origin of hASCs was confirmed by surface marker expression analysis with flow cytometry (239) and the ability of adipogenic and osteogenic differentiation (240) by Oil Red O and Alizarin Red staining, respectively. The cells were characterized as MSCs due to positive expression of CD73 (97%), CD90 (99%), and CD105 (99%), and low or negative expression of CD14 (1%), CD19 (0.6%), CD45 (2.6%), CD34 (8%) and HLA-DR (0.9%) (241,242) as well as

accumulation of lipid droplets by Oil Red O and mineralized matrix deposition by Alizarin Red staining.

The isolated hASCs were maintained in T-75 polystyrene flasks (BioLite, Thermo Fisher Scientific) in α-Minimum Essential Medium (α-MEM, Gibco, Thermo Fisher Scientific) supplemented with 5% Human Serum (HS, Serana Europe GmbH), and 1% antibiotics (100 U/ml penicillin and 0.1 mg/ml streptomycin; Gibco, Thermo Fisher Scientific). The cells were cultured in an atmosphere of 5% CO2 at 37 °C. When 80–100% confluence was reached, hASCs were cryo-preserved in gas-phase nitrogen in a freezing solution (HS supplemented with 10% dimethyl sulfoxide; DMSO Hybri-Max®, Sigma–Aldrich) and thawed when needed for the experiments.

For all experiments, confluent cells between passages 3–5 were used. All the experiments were conducted in 48 well plates (Nunc, Roskilde, Denmark), with α-MEM culture medium supplemented with 5% HS and 1% antibiotics (basic culture medium). A cell amount of 10 000 cells/well was used. Cells controls were seeded in tissue culture polystyrene (TCPS) 48 well plate (Nunc).

Direct and indirect cell culture

Experiments done in direct culture: Glass discs of 1 cm in diameter were placed in 48 well plate and hASCs were seeded on the discs (10 000 cells/well). The culture medium was changed every 72 h and the experiment was carried out for up to 7 days.

Experiments done in indirect culture: Glass discs were immersed in 1 mL of basic culture medium for 24 h at 37 °C. In parallel, the hASCs were seeded in 48 well plates (10 000 cells/well), in a basic culture medium. After one day of culture, the basic culture medium was replaced by the conditioned medium coming from the glass discs' incubation (Fig. 32). A fresh basic culture medium was added to the glass discs and every 48 h, the dissolution products were used as a culture medium for the cells (conditioned medium), to investigate the effect of

the ion release during the time on cells without having any contact between the cells and the glass discs. Finally, this test was done for up to 7 days of culture. Both Ag-SBA2 and Cu-SBA3 were tested, and cells cultured in TCPS 48 well plate only with basic culture medium were used as a control. One day after each time the dissolution products were put in contact with cells, the cells were observed by imaging with the microscope Nikon Eclipse Ts2-FL combined with a camera DFK 33UX174 from The Imaging Source.

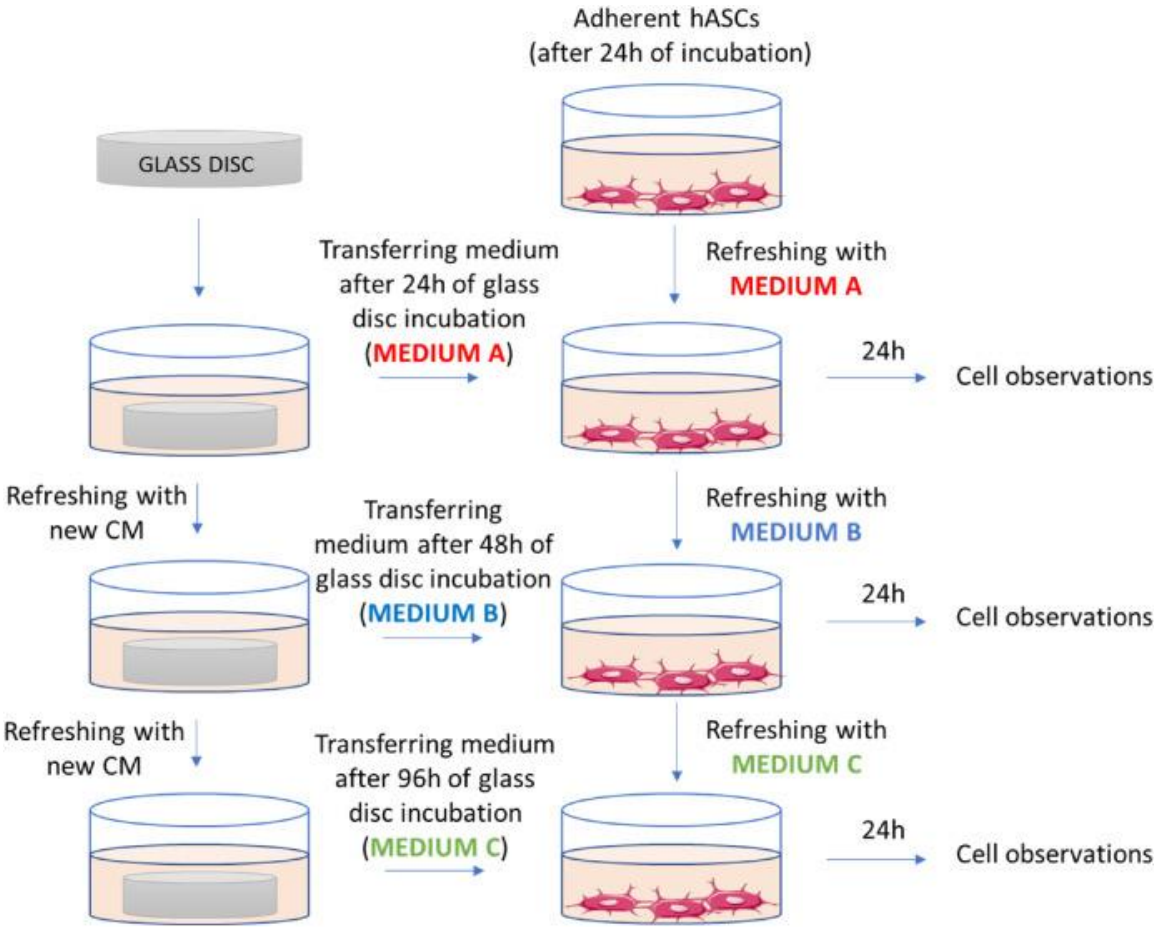

Figure 32: Protocol of indirect culture. CM = basic culture medium (alpha-MEM, 5% HS, 1% P/S), glass disc incubation medium (Medium A, B, C) includes glass disc dissolution products (conditioned medium).

Fibronectin coating

Fibronectin coating on the glass discs was tested to see if it can improve cell attachment and viability. The surfaces of the discs were Fibronectin-coated before cell culture. A solution of Fibronectin was prepared in PBS (69 mM NaCl, 1.3 mM KCl, 19.6 mM $Na_2HPO_4 \cdot 2H_2O$, 3.3 mM KH_2PO_4, pH 7.4) at a concentration of 15 µg/mL. The whole surface of each sample (a drop of 200 µL) was covered with Fibronectin solution for 1 h at 37 °C.

Before cell culture, the grafting of Fibronectin on the glasses was ensured by using fluorescently labeled fibronectin (Alexa Fluor 488 NHS Ester, AAT Bioquest, Inc., CA). The labeling was done by fluorescent tag, and it was performed according to instructions of the manufacturer and confirmed by laser scanning confocal microscope observations (Zeiss LSM 800).

Pre-incubation step

A pre-incubation step was tested for cell culture. The samples were pre-incubated for 24 h in 1 mL of basic culture medium before cell culture to investigate if cell viability could be improved.

The different methods used to investigate the behavior of hASCs with the glass discs are summarized in Figure 33:

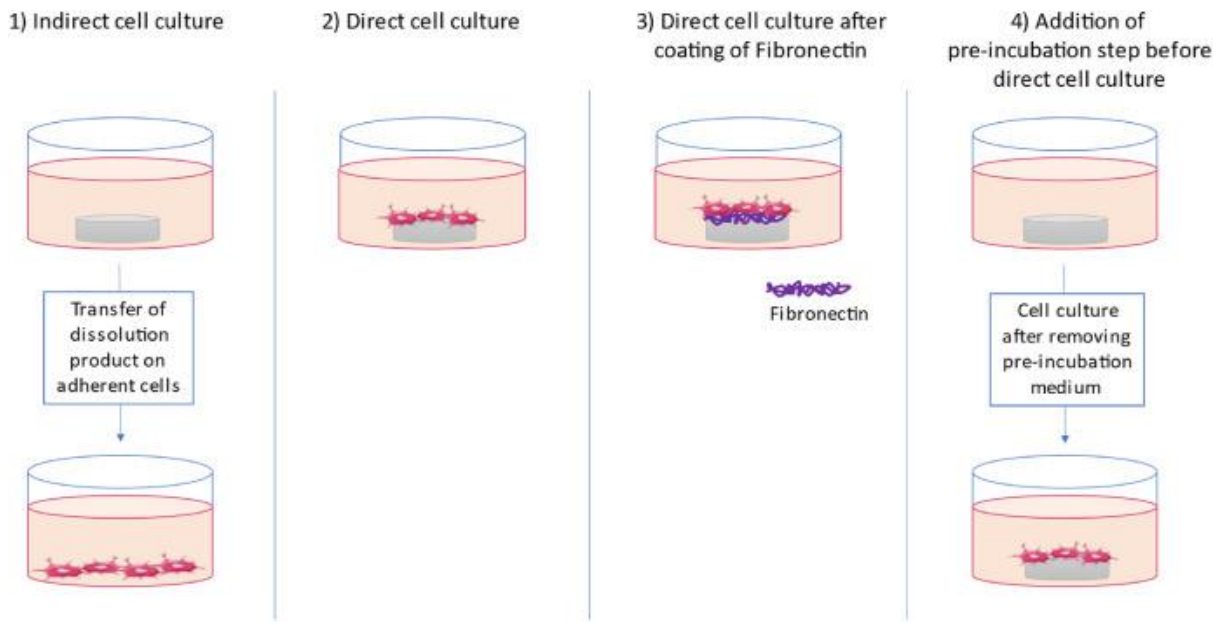

Figure 33: Methods used to study the cytocompatibility of the ion-doped specimens. 1) Indirect cell culture with adherent cells in contact with specimen dissolution products as presented in Fig. 1, Fig. 2) Direct cell culture on top of the specimen discs, 3) Direct cell culture on top of fibronectin-coated specimen discs, and 4) Direct cell culture on top of pre-incubated specimen discs.

Cell viability and proliferation

Cell viability on BAG discs after 1, 3, and 7 days were analyzed with Live/Dead staining (Invitrogen, Thermo Fisher Scientific). Briefly, cells were incubated in a working solution containing 0.25 µM EthD-1 and 0.5 µM Calcein-AM for 40 min at room temperature. This was followed by immediate imaging (IX51, Olympus, Tokyo, Japan, equipped with a fluorescence unit and Hamamatsu Orca Flash 4.0LT + sCMOS camera).

Cell proliferation on BAG discs was assessed after 1, 3, and 7 days of culture using CyQUANT Cell Proliferation Assay (Invitrogen, Thermo Fisher Scientific), according to the manufacturer's protocol. Shortly, samples were lysed in 0.1% TritonX-100 lysis buffer (Sigma-Aldrich) and stored at −80°. Three parallel 20 µl replicates of each lysate were pipetted to a 96-well plate (Nunc) and mixed with

180 µl working solution containing CyQUANT GR dye and cell lysis buffer. The fluorescence at 480/520 nm was measured using a plate reader (Victor 1420 Multilabel counter, Wallac, Turku, Finland).

Cytochemical staining

The morphology of the cells seeded on pre-incubated samples was observed after 1, 7, and 14 days of culture. At each time point, the cells were fixed with 4% (w/v) para-formaldehyde solution for 15 min, then permeabilized with 0.1% (v/v) Triton X-100 for 10 min. Non-specific binding sites were blocked by incubating the samples in PBS with 1% Bovine Serum Albumin (BSA) for 1 h. The actin cytoskeleton was stained with 1:500 FITC-labeled phalloidin and the nuclei with 1:1000 4',6-Diamidino-2-phenylindole dihydrochloride (DAPI) in PBS-BSA 0.5% for 1 h. The incubation of antibodies was performed in a moist chamber covering them from light. After incubation, the samples were washed with PBS-BSA 0.5% and pure water and observed using a fluorescence microscope (IX51, Olympus, Tokyo, Japan, equipped with a fluorescence unit and a camera DP30BW, Olympus).

Culture medium analysis

The ion release of the samples in the culture medium during the pre-incubation step and/or the cell culture were analyzed as presented above (2.2) by ICP-OES. To analyze the ion release, the glass dissolution products during pre-incubation and cell culture were collected and the elements Ag (λ = 328.068 nm), B (λ = 208.956 nm), Ca (λ = 396.847 nm), Cu (λ = 223.009 nm), Na (λ = 589.592 nm), P (λ = 213.618 nm), Si (λ = 251.611 nm) were analyzed. The measurements were conducted in three separate samples at each time point for each composition and the results are presented as mean ± standard deviation.

Statistical analysis

Data were analyzed using GraphPad Prism Software. Statistical significance between groups is assessed by one-way analysis of variance (ANOVA). Experimental results are expressed as means ± standard deviation. Statistical significance is taken for values of $p < 0.05$.

4.4.3.2 Sample antibacterial activity evaluation

Bacterial strains growth conditions

Bacteria were purchased from the American Type Culture Collection (ATCC, Manassas, Virginia, USA). To test SBA3 specimens' antibacterial and antibiofilm activity, the Gram-positive *Staphylococcus aureus* Multi-Drug resistance (*S. aureus* MDR, ATCC 43300) was used as representative of the pathogens affecting bone implants after surgery and in the case of severe infection, extra surgeries are required to remove the infected implants (188). Bacteria were cultivated on Trypticase Soy Agar (TSA, Merck, Milan, Italy) and incubated at 37 °C until round single colonies were formed; afterward, some colonies were collected and diluted into 20 mL of Luria Bertani broth (LB, Merck, Milan, Italy). Broth cultures were incubated overnight at 37 °C under agitation (120 rpm in an orbital shaker). A fresh broth culture was prepared before each experiment to test bacteria in their exponential growth phase; accordingly, bacteria concentration was further diluted into fresh LB broth to a final concentration of 1×10^3 cells mL^{-1}, corresponding to an optical density (OD) of 0.00001 at wavelength 600 nm determined by spectrophotometer (Spark, Tecan, Switzerland). Fresh LB medium was used as a blank to normalize the OD values.

Antibacterial activity evaluation

Prior to biological assays, the samples were sterilized at high temperature (at 100 °C for 1 hour). Two different protocols, the ISO 22196 standard and the one that has been published by the authors (243) considered here as UPO protocol were used to investigate antibacterial, antiadhesive, and antibiofilm properties of specimens towards *S. aureus* MDR. The international standard ISO 22196 protocol is designed to analyze the antibacterial behaviour of samples' surfaces by exposing them directly to a bacterial suspension (173). Instead, the UPO protocol aims to investigate bacterial adhesion to the specimens' surfaces and then evaluate the antibiofilm properties of samples by forcing bacterial strains to create microcolonies or biofilm onto their surfaces.

To perform ISO22196 standard protocol, the sterile specimens were located into a 24-multiwell plate, and then, 50 µL of the bacterial suspension was directly dropped onto the specimens' surface and covered with a sterile polyethylene film. The inoculated specimens were placed in an incubator at 37 °C for 24 hours. Afterward, the colorimetric metabolic assay (AlamarBlue™, Life Technologies, Milan, Italy) was applied to test viable bacteria metabolic activity by spectrophotometry following the manufacturer's instructions. Briefly, the ready-to-use Alamar blue solution at concentration 0.0015% was added to each well containing the test specimen (1 mL per specimen), and the plate was incubated in the dark for 4 h at 37 °C allowing resazurin dye reduction into fluorescent resorufin upon entering living cells. Then, 100 µL were spotted into a black-bottom 96-multiwell plate to minimize the background signal. The metabolic activity of bacteria was measured via fluorimetric analysis (λex = 570 nm and λem = 590 nm), and results were presented as Relative Fluorescent Units (RFU); Alamar blue solution (intended as cells-free) fluorescence was considered blank. Then, each specimen was washed with phosphate buffer solution (PBS, 1 mL) sonicated (5 min, 3 times), and vortexed (30 s, 3 times) to recover the bacteria. The colony- forming units (CFU) were counted by mixing 20 µL of bacteria with 180 µL of PBS and performing six-serial 10-fold dilutions as previously described

by the Authors (243,244); the total CFU count was done applying the following formula:

$$CFU = [(\text{number of colonies} \times \text{dilution factor})^{(\text{serial dilution})}]$$

Then, scanning electron microscopy (SEM, JSM-IT500, JEOL, Tokyo, Japan) imaging was used to investigate the bacterial microcolonies or biofilm formed on the samples' surfaces; briefly, specimens were dehydrated by the alcohol scale (70–90–100% ethanol, 1 hour each), swelled with hexamethyldisilazane, mounted onto stubs with conductive carbon tape and covered with a gold layer. Images were collected at different magnifications using secondary electrons detector.

In the UPO protocol, the sterile samples were transferred in a 24-multiwell plate and submerged fully into 500 µL of LB broth including 1×10^3 cells mL^{-1} of *S. aureus* MDR (as explained in detail in section 2.3.1). The multiwell plate was incubated at 37 °C and agitated on a small bench shaker (BenchRocker™ 3D, Sayreville, USA) at 100 rpm; afterward, the metabolic activity of adherent bacterial strains, viable CFU count, and SEM analysis were performed after two different time points: early time point (6 hours) and late time point (24 hours) to evaluate antiadhesive and antibiofilm properties of Cu doped SBA3 in comparison to undoped SBA3, respectively. To create a bacterial biofilm on specimens' surfaces, after 6 hours of agitation at 100 rpm, the surplus of LB broth containing planktonic bacteria were removed from the wells and replaced with 1 mL of fresh LB broth to allow surface-adherent bacterial microcolonies to grow and form a layer of biofilm; after 24 hours of incubation, antibiofilm properties of the Cu doped SBA3 were compared to undoped SBA3 as a control sample. After each time point (6 and 24 hours), the specimens were washed with sterile PBS to remove non-adherent bacterial cells and bacterial metabolic activity and bacterial viable colonies were analyzed as mentioned above by colorimetric metabolic assay and CFU; the obtained results were visually confirmed by SEM .

Finally, the results of CFU count were expressed by means of antibacterial activity (R) indicating the effectiveness of an antibacterial agent, which was calculated according to the ISO 22196 protocols as follows (245):

$$R = (U_t – U_0) – (A_t – U_0) = U_t - A_t$$

Where

R is the antibacterial activity;

U_0 is the average logarithm of the number of viable bacterial colonies recovered from the untreated test specimens immediately after inoculation;

U_t is the average logarithm of the number of viable bacterial colonies recovered from the untreated test specimens after 24 hours;

A_t is the average logarithm of the number of viable bacterial colonies recovered from the treated test specimens after 24 hours.

Statistical analysis

Experiments were performed in triplicate. Results were statistically analyzed using the SPSS software (v.20.0, IBM, USA). First, data normal distribution and homogeneity of variance were confirmed by Shapiro-Wilk's and Levene's test, respectively; then, groups were compared by the one-way ANOVA using Tukey's test as post-hoc analysis. Significant differences were established at $p < 0.05$.

4.5 Results and discussion

4.5.1 Physicochemical characterization

Some data from physicochemical surface characterization of Ag-SBA2 and Cu-SBA3 were previously reported by the authors (173,232,234). To summarize, the surface composition of Ag-SBA2 has been analyzed with XPS and EDS, showing the uniform distribution of Ag-ions on the glass surface replacing the Na-ions. In addition, the transmission electron microscopy (TEM-EDS) on the glass cross-sections showed the presence of silver as a very thin layer on the glass surface For Cu-SBA3 the physicochemical characterization has been performed to the glass in a powder form, as reported by the authors (234). In the study, a layer of copper was found on a glass surface as ionic Cu(II) replacing Ca- and Na-ions, as evidenced by EDS and XPS. In this work the Cu-SBA3 is thoroughly characterized as a bulk form. Similar work regarding Ag-SBA2 has been previously performed and published, and therefore not shown here.

The ion exchange in Cu(II)acetate solution was performed in three different concentrations 0.05 M, 0.01 M, and 0.001 M. Fig. 34 shows the surface morphology of SBA3 discs before and after ion exchange.

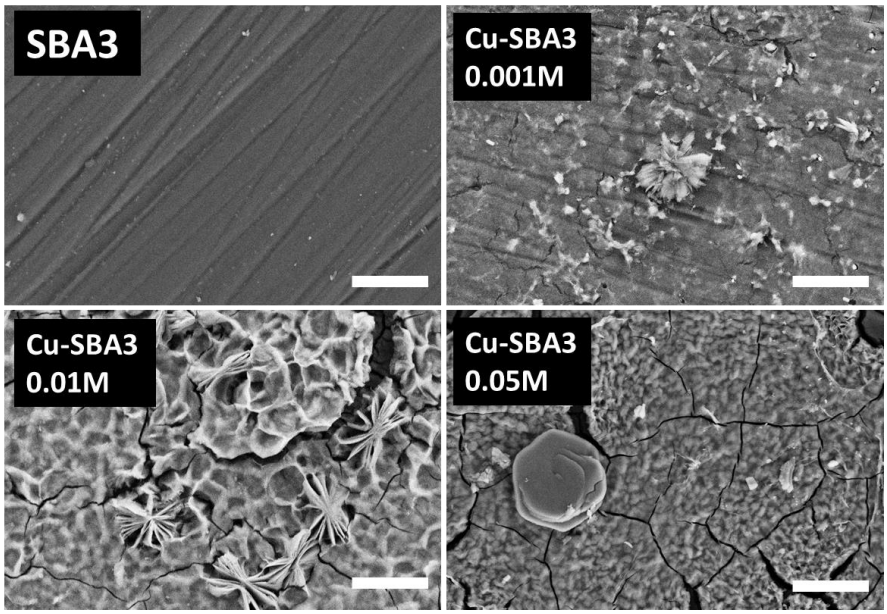

Figure 34: FESEM images on the surface of SBA3 before and after ion exchange in Cu(II) acetate solution with different concentrations. Scale bars 10 µm.

For all ion-exchanged samples (Fig. 34), some precipitation layers were observed on the surfaces compared to the undoped SBA3 surface. With a higher concentration of the ion exchange solution, a more evident surface layer was detected compared to the pristine SBA3 surface. The 0.001 M ion-exchanged surface was found to have only a few precipitates compared to higher concentrations. When further analyzing the elemental composition of the detected crystals by EDS analysis (Fig. 35, Fig. 36), it was evident that they contained a large amount of Cu, also a higher amount of Cu was detected on the surface precipitation by using a greater concentration of Cu in the ion-exchange solution.

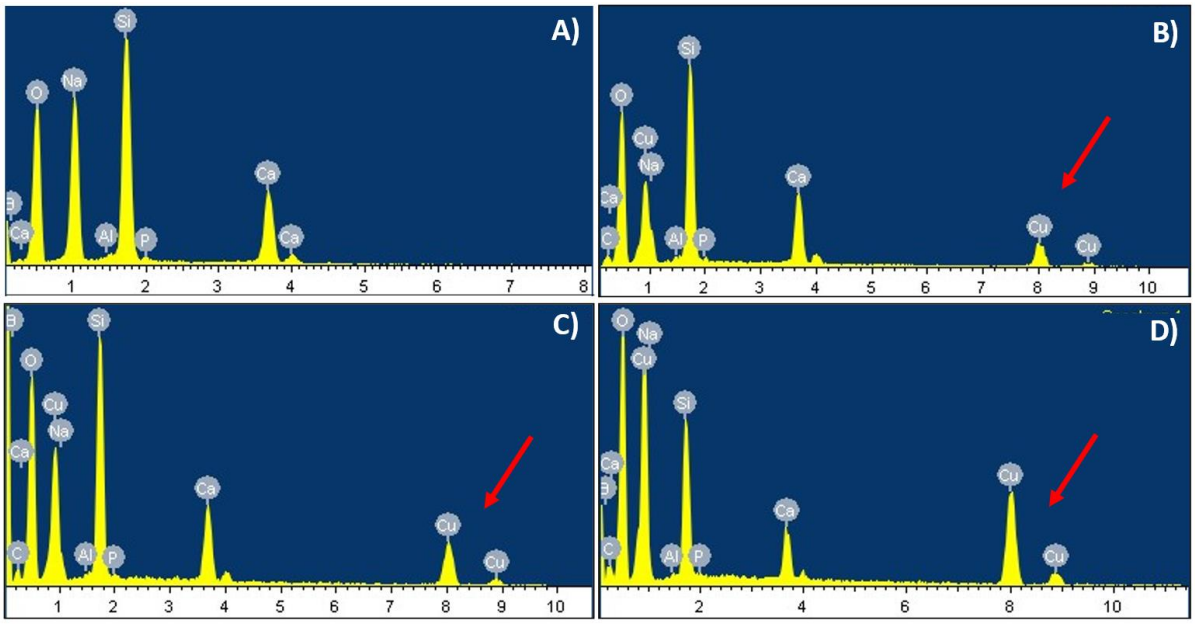

Figure 35: EDS analysis of the surface of ion-exchanged samples, using A) Undoped SBA3, B)0.05 M solution (Cu-SBA3 0.05 M), C) 0.01 M solution (Cu-SBA3 0.01 M), and D) 0.001 M solution (Cu-SBA3 0.001 M) of Cu(II) acetate.

As can be observed in Fig. 35, the compositional EDS analysis from the surface of sample discs before and after ion exchange confirmed the presence of all the elements characteristic of the SBA3 and Cu-doped SBA3 glasses. However, boron is excluded from EDS analysis due to its low atomic weight and hence low detectability. When comparing glasses before and after ion exchange, Cu^{2+} seems to replace the sodium (Na^{+}) and calcium (Ca^{2+}) on the surface, which is seen as a reduction of those elements within ion-exchanged surfaces. It is also evident that the more concentrated ion exchange solution leads to greater replacement of Na^{+} and Ca^{2+} by Cu_{2+} on sample surfaces. For both the highest concentrations, the atomic percentage of Cu was found to be very high: for 0.05 M around 50 at-%, and 0.01 M 20 at-%. This information, combined with the high number of precipitates on the surfaces of 0.05 M and 0.01 M Cu-SBA3, the lowest concentration (0.001 M) seems the most suitable for biomedical applications and it is chosen to be further analyzed.

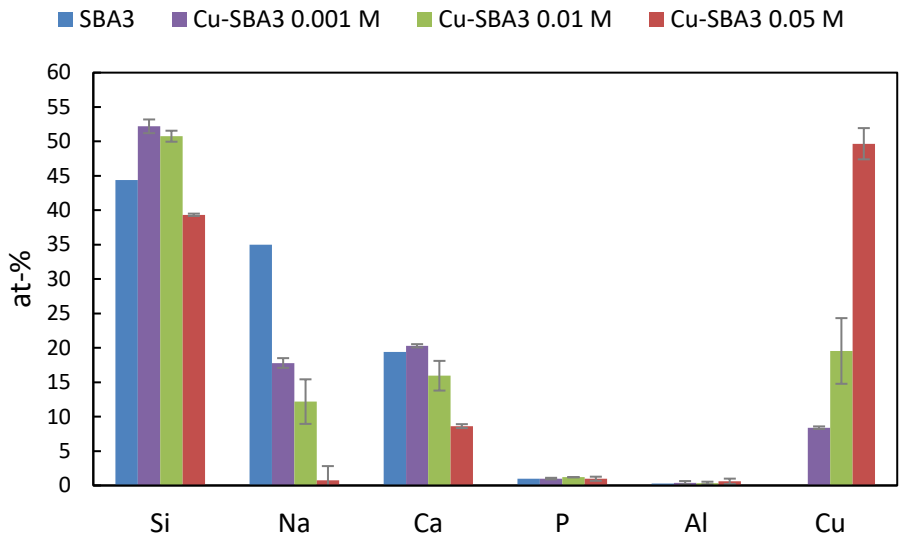

Figure 36: EDS analysis of SBA3 and Cu-SBA3.

However, even though in the FESEM images (Fig. 34) some precipitates were present on the ion-exchanged surfaces, the XRD analyses of the surfaces (Fig. 37) did not detect any additional crystalline phases, except for the highest concentration tested. However, this result was expected as XRD analysis has a high penetration depth, and the phase detection has its limitations with phases present in very small amounts (246). For Cu-SBA3 0.05 M, two peaks were detected approximately at 19°, and 28°, corresponding to copper acetate hydroxide hydrate $C_2H_6Cu_2O_5 \cdot H_2O$ (ref 00-050-0407), which was expected considering the Cu(II)acetate solution used for the ion-exchange process. These results are in agreement with the previous analysis where no crystalline phases were detected when using similar ion-exchange process parameters (234).

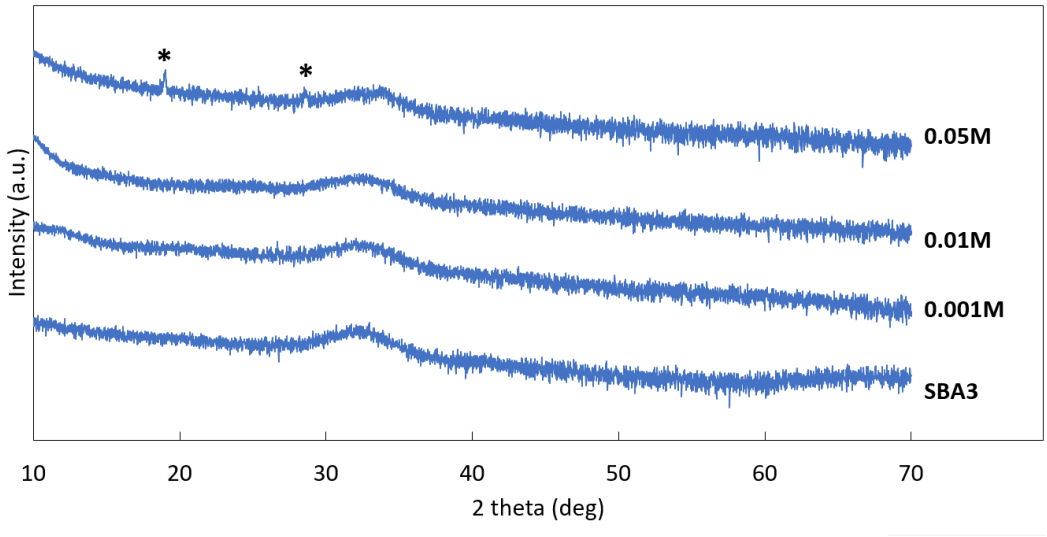

Figure 37: Optimization of the ion-exchange process: XRD patterns of undoped SBA3 and Cu-SBA3 ion-exchanged in different concentrations. *) $C_2H_6Cu_2O_5 \cdot H_2O$.

Based on the morphological and phase analysis, the lowest ion-exchange concentration (0.001 M) was chosen to be further studied. The pristine SBA3 and the chosen ion-exchange concentration Cu-SBA3 0.001 M were also subjected to in vitro bioactivity test in SBF. The goal was to evaluate whether the introduction of Cu^{2+} through ion exchange would impact the hydroxyapatite formation, and hence, bioactivity.

The SEM/EDS analysis of SBF-soaked samples is shown in Fig. 38.

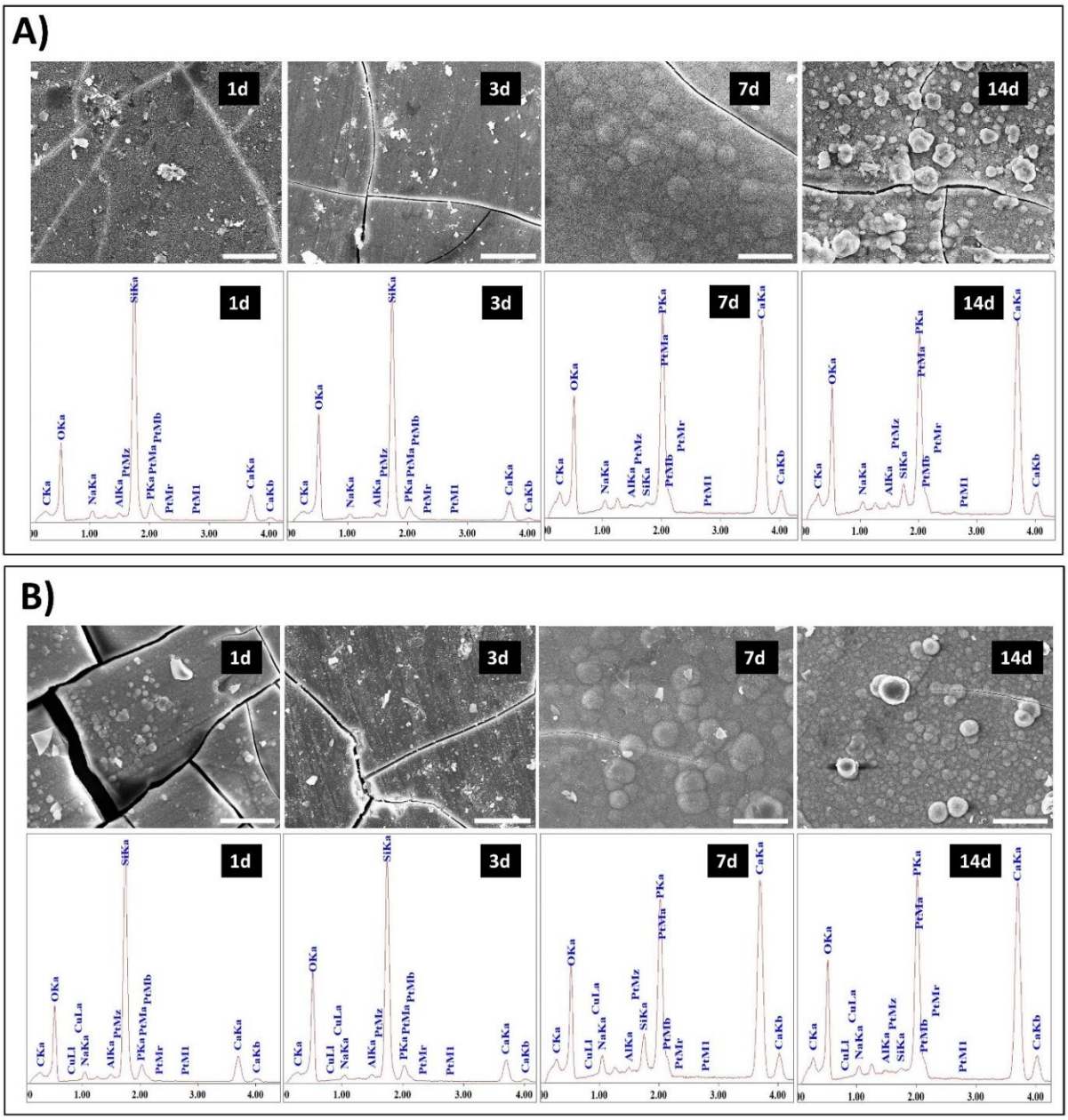

Figure 38: SEM/EDS analysis of SBF-soaked A) control specimens (SBA3), and B) Cu-doped specimens (Cu-SBA3 0.001 M). Scale bars 20 µm.

The samples soaked for 28 days are not shown because the results were very similar to the 14 days ones. The typical morphology of in vitro grown hydroxyapatite was detected for both undoped and doped discs after 7 days of soaking in SBF. Before that (1–3 days), silica gel formation occurred (cracks are

due to the drying step before SEM observation). Regarding the EDS analysis, only a qualitative analysis of the Ca and phosphorus (P) peaks was possible instead of a quantitative one. This is due to the use of platinum (Pt) coating on the specimens, and the Pt peak is known to overlap with the P peak. However, the Ca and P content increases after 7 days for both undoped and doped specimens, also evidencing the presence of a Ca and P rich layer.

XRD analysis was carried out to confirm the presence of hydroxyapatite on glasses surface. Fig. 39 shows the XRD spectra from the two specimens before and after SBF immersion for up to 28 days.

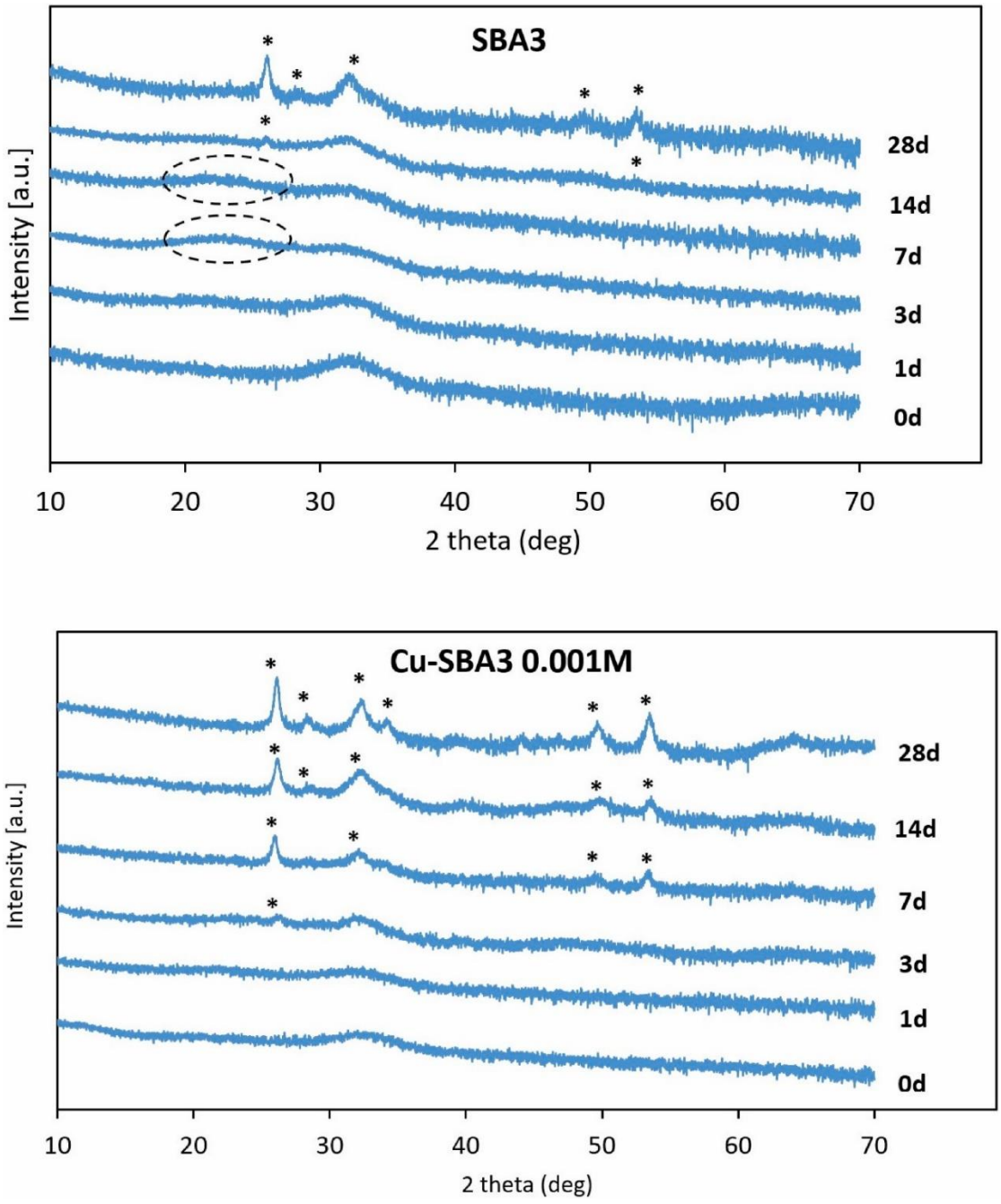

Figure 39: XRD patterns of pristine and SBF-soaked SBA3 and Cu-SBA3 0.001 M. (-- -) silica gel, *) hydroxyapatite.

For the undoped SBA3 specimen, a broad halo between 2 theta 20° and 25°, which is attributed to silica gel formation, was noticed approximately after 3 days of soaking in SBF. Regarding the Cu-SBA3 0.001 M, a peak corresponding to hydroxyapatite was already detected after the 3-day soaking. Moreover, hydroxyapatite precipitation seems more evident also on the later time points for Cu-SBA3, suggesting that the Cu^{2+} addition by ion exchange could enhance the hydroxyapatite formation. However, as demonstrated in the EDS compositional analysis (Fig. 36), Cu was found to partially substitute Na and Ca on the glass, which could be hypothesized to lead to decelerated dissolution rate of the glass. Still, it should be noted that the Cu is introduced only into a very thin layer of the surface of the glass , where it unlikely has a great impact on the glass bulk properties. In the literature, there is no consensus on the effect of Cu inclusion on the BAG hydroxyapatite-forming ability, and hence, bioactivity (221). In some studies, the bioactivity mechanism was found to be improved by adding a Cu precursor to bioactive glass nanoparticles (247), while, according to other studies, Cu addition as an oxide to melt-derived borosilicate glass foam scaffolds lead to a more stable glass network and lower degradation ability (248). However, in both mentioned experiments Cu was introduced using different approaches and the used BAG was not used as a bulk, which makes comparison difficult.

Considering the Cu^{2+}-ion release from the BAG surface, a leaching test was performed both in physiological (SBF, pH 7.4) and inflammatory pH (HAc/NaAc buffer, pH 5.0). The experiment was performed only for the lowest ion exchange concentration of 0.001 M (Cu-SBA3 0.001 M). The pH evolution and the release of Cu^{2+} in both soaking solutions are demonstrated in Fig. 40.

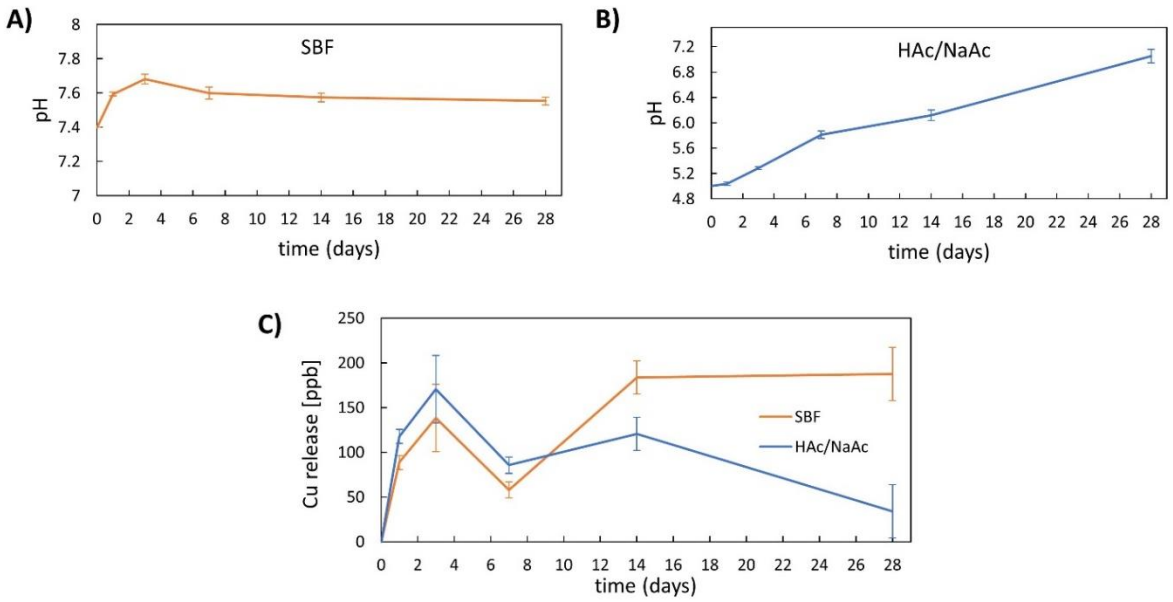

Figure 40: A) pH evolution of SBF solution as a function of time of Cu-SBA3 soaking, B) pH evolution of pH5 acetate buffer as a function of time of Cu-SBA3 soaking, and C) Release of Cu^{2+}-ions from glass surface as a function of soaking time in SBF (orange)or pH5

Regarding the pH value of SBF during the soaking of Cu-SBA3 (Fig. 40A), there were no significant differences observed. It is noteworthy that pH 5 acetate buffer exhibited a lower buffering capacity and displayed a consistent increase in pH over the 28-day soaking period without reaching any plateau (Fig. 40B). The pH increased from a slightly acidic level to a neutral pH of around 7. These phenomena can likely be attributed to the different acid-base characteristics of the two buffer solutions. The sodium acetate buffer is based on a weak acid (acetic acid) with a buffering range of approximately 3.6–5.6 and a pKa value of 4.76 (249)). On the other hand, the SBF is buffered with TRIS-buffer, based on a stronger acid (HCl) with a buffering range of pH 7.0 to 9.0. During the soaking process, bioactive glasses tend to rapidly exchange cations with H_3O^+ ions into the aqueous environment, leading to an increase in pH towards more alkaline values. Consequently, the buffering capacity of the acetate buffer in our particular case was comparatively more limited due to its weaker acid-base characteristics.

As seen in Fig. 40, the major amount of Cu^{2+} seems to be released from the glass during the first three days of soaking, independent of the soaking solution. A similar trend was found in the previous work where Miola et al. found the majority of Cu^{2+} release from Cu-doped glass/PMMA composites during the first days of the soaking, but on the contrary, they did not detect a plateau similar to what was found in present work after around 3 days of soaking in both conditions (233). It must be underlined that in the mentioned study the Cu-doped glass was uniformly dispersed into a PMMA matrix, while in the present paper, low amounts of Cu^{2+} ions are concentrated on the glass surface and can be fast released.

The decrease of the Cu concentration in solution at 7 days can be related to the precipitation of hydroxyapatite, which occurs mainly from day 7, as detected by SEM observations (Fig. 38, Fig. 39), and could involve the re-precipitation of Cu^{2+} ions that can partially replace Ca^{2+} ions in the hydroxyapatite lattice, as reported in the literature (250,251). This hypothesis could be strengthened by further phase analysis, for example by estimating the average crystallite size and lattice parameters, but this is out of the aim of this thesis. A further release can be observed from day 7 on, which can be explained by the Cu^{2+} confinement on the very outer glass surface, that reasonably does not negatively affect the ion release involved in the bioactivity mechanism, as already observed by authors in a previous paper (234).

When comparing the Cu^{2+}-release in SBF and inflammatory condition-mimicking buffer solution, no notable differences were detected. The HAc/NaAc buffer-soaked specimens initially showed a slightly higher release of Cu^{2+} ions than the SBF solution. This phenomenon is also reported in other studies, for example, Bingel et al. reported that in general lower pH of the used immersion, the solution increases ion release due to more protons being available for ion exchange reactions between glass modifier ions and protons from the dissolution

medium (236,252). However, the effect of solution pH on Cu^{2+} ion release specifically has not been previously reported. In addition, the more aggressive initial ion release during the first 3 days of soaking could also explain the more prevalent Cu^{2+} re-precipitation after 14 soaking in HAc/NaAc compared to SBF.

Zeta potential titration measurements were performed both on pristine SBA3 and ion-exchanged Cu-SBA3 (Fig. 41, Fig. 42) before (0 day) and after different times of soaking in SBF (1-7-28 days).

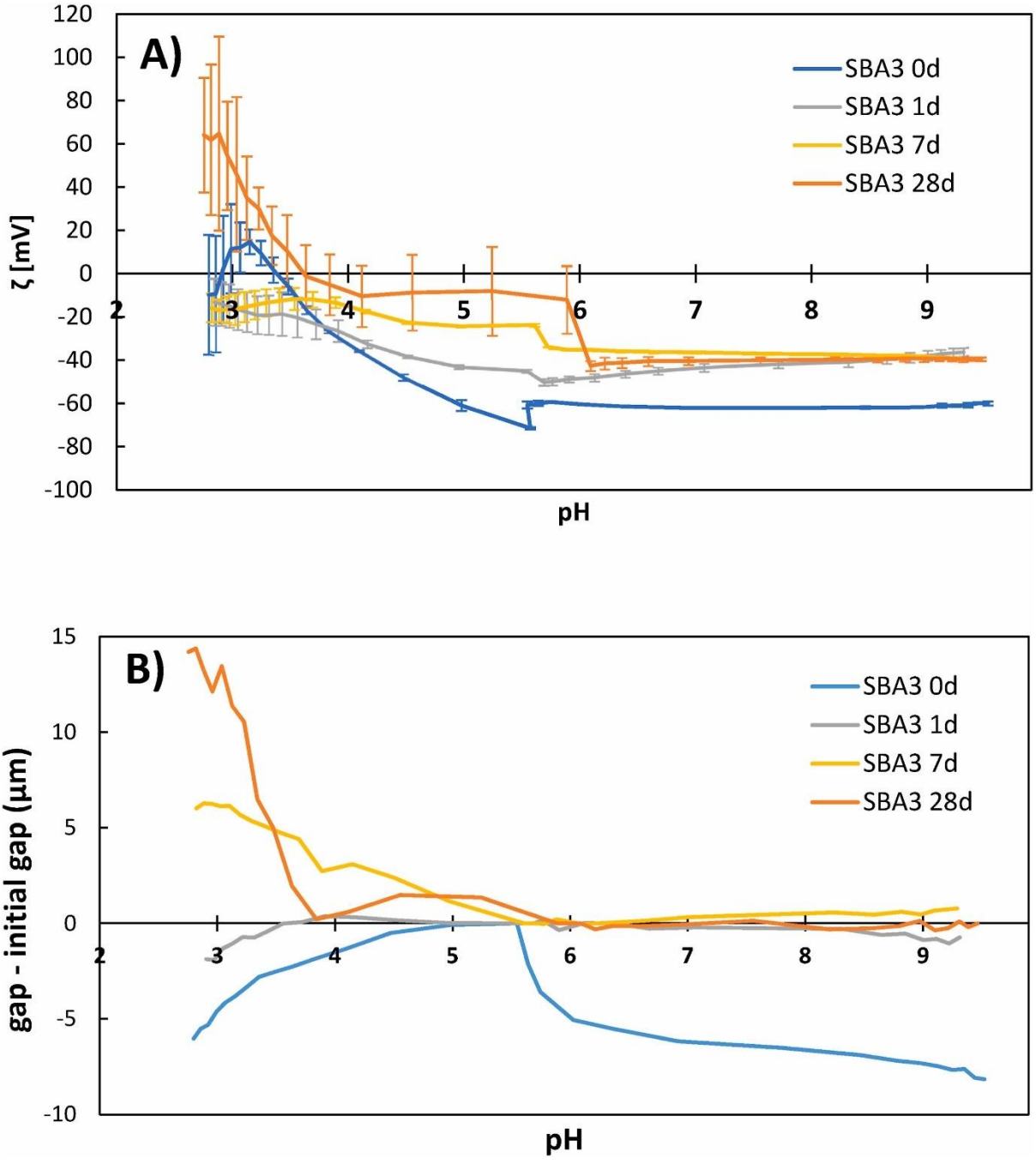

Figure 41: Zeta potential titration curves (A) and gap variation (B, measured gap – initial gap) of SBA3 before and after soaking in SBF.

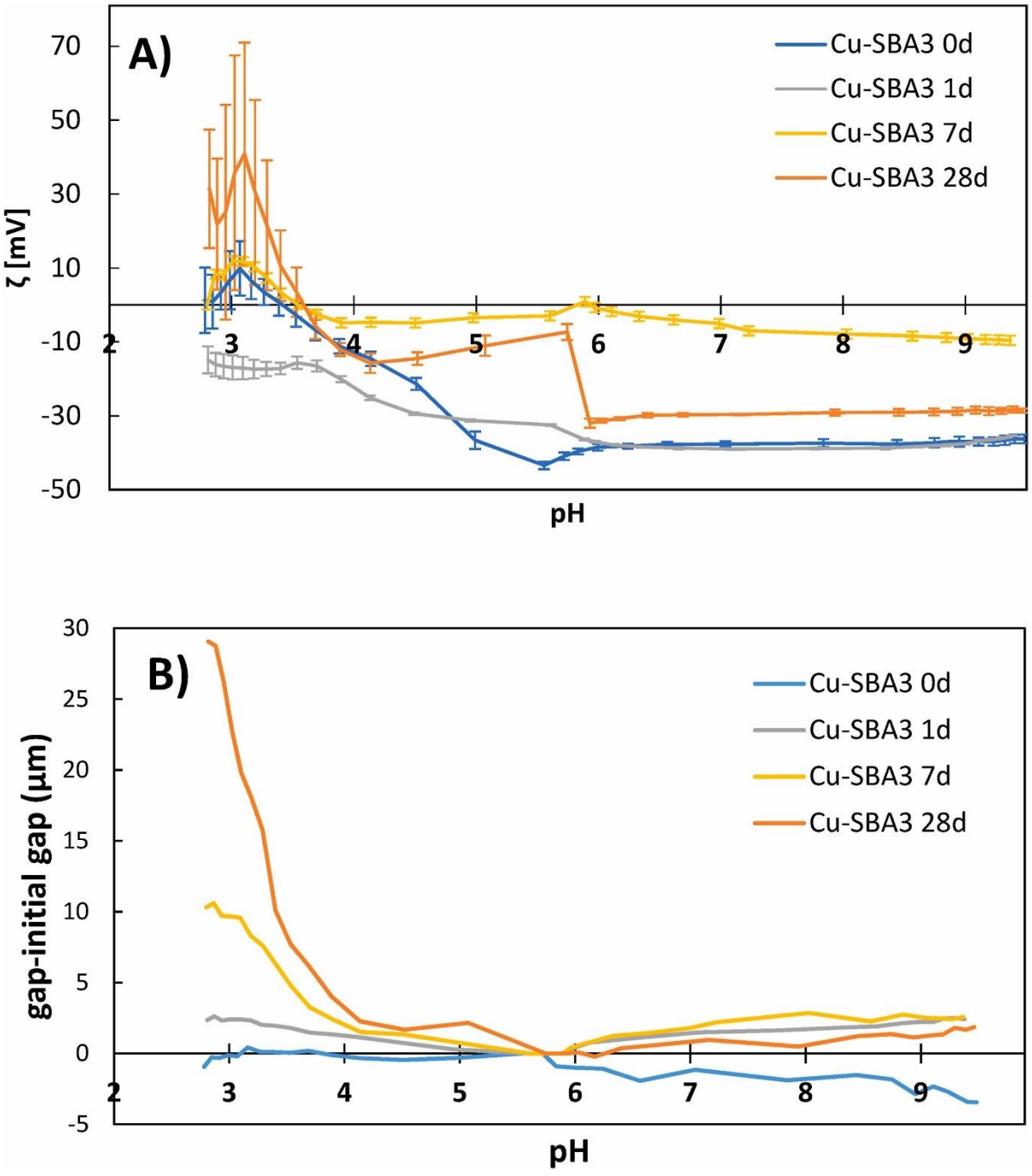

Figure 42: Zeta potential titration curves (A) and gap variation (B, measured gap – initial gap) of Cu-SBA3 0.001 M before and after soaking in SBF.

The isoelectric point (IEP) gives information on the balance between the charged surface functional groups with either acidic (deprotonation) or basic (protonation) behavior in contact with the solution (253). The IEP value of both unsoaked SBA3 (SBA3 0d) and ion-exchanged unsoaked Cu-SBA3 (Cu-SBA3 0d) is around 3.4, which indicates that both surfaces have a small prevalence of acidic functional groups (supposedly OH groups) since an IEP of 4 is expected for a surface without the prevalence of any charged functional groups (32). Both curves have a plateau starting from pH 5.5. This agrees with the presence of acidic functional groups and demonstrates they are completely deprotonated at any pH higher than 5.5 on both glasses (253). The ion-exchange process, at least in the tested concentration of 0.001 M, does not impact the surface zeta potential and acidic behavior of the hydroxyl groups.

A different slope of the curves is noticed on SBA3 and Cu-SBA3 at a pH lower than the plateau. The slope of the titration curve around the IEP, before reaching any eventual plateau, is related to surface hydrophilicity: if the material is hydrophobic, the water molecules are weakly adsorbed, and they are easily replaced by the hydroxyl (in the basic range) or hydronium ions (in the acidic range). The surface acquires a progressively higher absolute value of the zeta potential (high slope of the curve) by changing the pH. On the contrary, the absolute value of the zeta potential slowly changes with the pH of the solution if the surface is hydrophilic (slow slope of the curve). The observed slopes of the curves can be related to a larger hydrophilicity on Cu-SBA3. Hydrophilicity can be related to a larger amount of total hydroxyl groups on the surface.

The standard deviation of the zeta potential values refers to the chemical stability (reactivity) of the surface during the measurement. An evident increase in the standard deviation occurs around the IEP and below it evidencing a strong reactivity of both surfaces in a very acidic environment(254).

Looking at the gap variation during the pH titration, a reduction of the gap is observed on SBA3 both in the acidic and in the basic range attributable to the formation of a silica gel layer and a small expansion of the sample; this expansion is limited to few micrometers and slightly higher than the lowest significant variation of the gap that is about 5 micrometers. Almost no gap variation has been registered on Cu-SBA3 during the pH titrations evidencing a different type of silica gel layer with a reduced expansion.

Considering the SBF-soaked samples, the zeta potential titration measurements can give some information on the formed hydroxyapatite layer. As a reference, the IEP of synthetic hydroxyapatite has been reported to be around 5.5 and it has a zeta potential of about -30 mV at any pH higher than 6 (255). Dissolution of hydroxyapatite formed on bioactive materials is reported at a pH lower than 4, as it occurs in inflammatory conditions (254). None of the soaked samples has an IEP close to the value of synthetic hydroxyapatite. The measured IEPs are close to those of the glasses before soaking or not detectable (as in the case of SBA3 and Cu-SBA3 soaked for 1 day and SBA3 soaked for 7 days). The standard deviations of the curves of the soaked samples have an evident increase at a pH lower than 4. The deviation of the gap is negative, and it is evident below pH 4 on the samples soaked for 7-28 days. Considering the shapes of the titration curves, all of them have a plateau in the basic pH range with an onset around pH 6 and a value of about -30 mV.

All obtained data can be interpreted considering that the formed hydroxyapatite is dissolved and detached from the substrates when pH goes down below pH 4. The detachment leaves exposed the glass surface, and the IEP of hydroxyapatite is not measured. On the other side, hydroxyapatite is almost stable in the basic range (no gap variation detected, low standard deviation of zeta potential, and a plateau at a zeta potential value close to that of hydroxyapatite). The thickness of the detached surface layer is higher in the case of Cu-SBA3 (10

micrometers and 30 micrometers on the sample soaked for 7 and 28 days, respectively) than on SBA3 (5 micrometers and 15 micrometers on the sample soaked for 7 and 28 days, respectively). This result agrees with the larger amount of hydroxyapatite registered through XRD on Cu-SBA3 after soaking. The samples soaked for 1 day did not have a detectable detachment of hydroxyapatite because of its low thickness, in agreement with XRD, but their curves are clearly different from those of the as-prepared glasses according to their surface reaction in SBF.

These data can be compared with a similar work performed on SBA2, a composition that differs from SBA3 very slightly with its lower Na_2O amount (18 mol% vs. 26 mol%) (253,254). The behavior of the two glasses is similar, both as-prepared and after soaking, the main difference is that the as-prepared SBA2 is reactive in the basic range (pH>8) and not in the acidic range as SBA3 is. Cu-SBA3 soaked for 28 days shows a larger detachment and thicker layer of hydroxyapatite than both SBA2 and SBA3. The curve of SBA3 soaked for 7 days is a bit different from the others registered in this work, but it is similar to what was detected on SBA2 soaked for 7 days: it has a low zeta potential value along the whole titration curve. It can be explained by the evolution of hydroxyapatite during its maturation (254). The shape of the curve of SBA3 soaked for 7 days is not far from that of SBA3 soaked for 1 day, according to the lower bioactivity of this glass.

Due to the expected lower toxicity of copper ions compared to silver ions (221), the comparison between Ag-SBA2 and Cu-SBA3 cytocompatibility is of interest in the current study. In the present research the surface characterization was performed through wettability analysis by static contact angle measurement, followed by the EDS analysis of the glass surfaces before and after soaking in cell culture medium, and the quantification of released Ag/Cu-ions by ICP-OES to further understand the cytocompatibility results obtained in the same research.

The results from EDS, ICP-OES, and contact angle measurement are reported in Fig. 43, Fig. 44, Fig. 45.

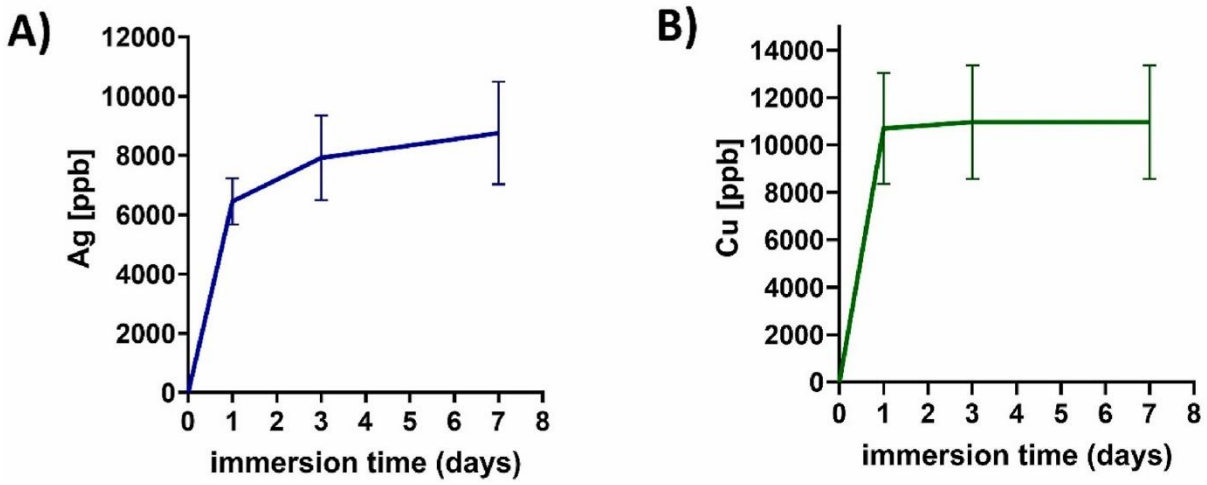

Figure 43: Release of ion-exchanged Ag-ions from Ag-SBA2 (A) and Cu-ions from Cu-SBA3 (B) up to 7 days in pure α-MEM culture medium analyzed by ICP-OES.

Soaking of doped glasses, Ag-SBA2 and Cu-SBA3, in pure α-MEM culture medium without added serum and antibiotics for up to 7 days was performed to evaluate the kinetics of silver and copper release in conditions close to cell culture. The concentrations of released Ag+ (A) and Cu2+ (B) in pure α-MEM are reported in Fig. 43.

According to Fig. 43A, both surface-doped glasses release most of the doped ionic Ag/Cu during the first day of soaking. In the case of Ag-SBA2, the release of Ag+ from the surface occurs in a slightly more controlled manner over multiple days, the maximum value being about 7400 µg/L after seven days of soaking. However, in terms of Cu-SBA3, the maximum value of released Cu2+ ions (about 10 000 µg/L) is reached already on the first day. For both glasses, the standard deviation for the ion release was found to be high, which raises questions about whether the amount of doped ions varies between ion-exchanged samples. In addition, some concerns about the accuracy of the measured amount of silver

release by the ICP-OES technique can be raised, since it could be affected by the high affinity of silver with proteins present in serum (256). In this measurement, the ion release was performed only in α-MEM without added serum, which minimizes the issue.

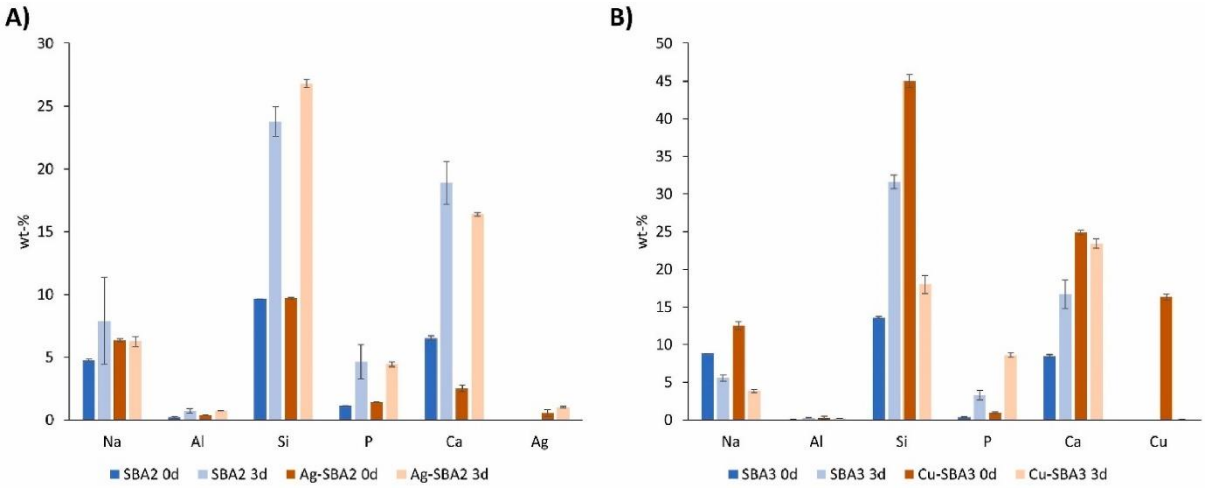

Figure 44: EDS results in weight percentages of the surfaces of A) SBA2 and Ag-SBA2 before (0d) and after [3d] soaking in α-MEM, and B) SBA3 and Cu-SBA3 before (0d) and after [3d] soaking in α-MEM.

EDS results (Fig. 44) were found to be well in agreement with the ICP-OES results. After three days of soaking in α-MEM, a very low amount (<1 wt-%) of Cu-ions seems to be present on the Cu-SBA3 sample surfaces, compared to the initial amount of around 16 wt-%. This suggests that the Cu-ion layer is completely released in only a couple of days of soaking. In the case of Ag-SBA2, it seems that after soaking for 3 days, there is still a remaining layer of silver ions on the samples, since the EDS results both before and 3 days after soaking show around 1 wt-% of silver. The remaining silver on the soaked discs can also be seen with naked eye as a brown color on the disc surface. This is also shown in the ICP-OES analysis with more controlled silver ion release over multiple days. However, it should be noted that the penetration depth of EDS analysis is known to be higher than one micron, which might undermine the usability of this method

for evaluating thin surface layers (257). The thickness of the Ag-ion layer of Ag-SBA2 has been previously estimated to be a few nanometers through transmission electron microscopy (TEM) by the authors (173), and therefore, other methods, such as X-ray photoelectron spectroscopy (XPS) or secondary ion mass spectroscopy (SIMS) with lower penetration depth could further clarify the chemical composition of the ion-exchanged surfaces (258). In the case of Ag-SBA2 the XPS results are already reported previously by the authors (173), even more confirming the presence of ionic silver as an outermost layer on the glass surface.

ICP-OES and EDS results show an initial burst release of the doped ions from the glass surface. This release could be detrimental to cell viability. To investigate that, the behavior of hASCs in presence of these glasses has been studied with different methods. Also, the ion release from these glasses during cell culture experiments has been investigated.

In addition, the effect of ion exchange to the surface wettability (hydrophobicity/hydrophilicity) of the glasses was investigated. In Fig. 45 the contact angles of the undoped and Ag/Cu-doped glasses are reported.

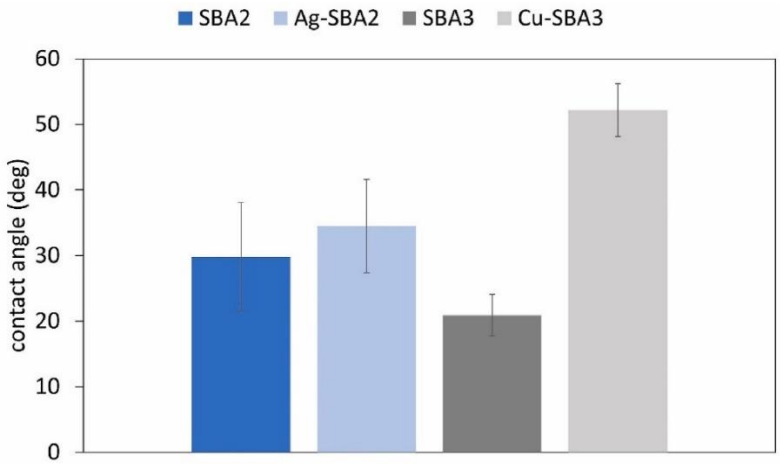

Figure 45: Wettability of the Ag-SBA2 and Cu-SBA3 compared to their undoped controls SBA2 and SBA3, respectively.

In general, both bioactive glass composition SBA2 and SBA3 are found to be hydrophilic with a contact angle around 20–30°. The ion-exchange process is seen to increase the contact angle in both cases of Ag- and Cu-doping. Especially the Cu-doping by ion exchange is seen to increase the contact angle up to 50°. According to the literature cells are known to better attach to hydrophilic surfaces (259). Ensuring the cell attachment is essential for the further cell spreading and proliferation, and therefore the survival of anchorage-dependent cells, such as mesenchymal stem cells also of interest of the present research.

4.5.2 Biological characterization

4.5.2.1 Cytocompatibility evaluation

First, to study the cytocompatibility of the different glasses doped with Ag- and Cu-ions (Ag-SBA2 0.03M, and Cu-SBA3 0.001M, respectively), the effect of the extracts coming from the glasses immersed in a culture medium was investigated by doing an indirect cytotoxicity test. Adherent cells were exposed to the extracts in the conditioned medium for up to 7 days. Fig. 46 shows the images of the cells cultured in the conditioned medium for 1 day, 3 days, and 7 days (on the left) and Ag- and Cu-ion concentrations in the conditioned medium used for the cell culture (on the right). For the dissolution products of both doped glasses, no inhibitory effect on hASCs spreading and growing was detected at any time point, when compared to the control images (cell grown on TCPS with normal medium without glass dissolution products). In addition, no changes in cell morphology were detected. These results show that the glass extracts containing the released ions are probably not toxic to the cells.

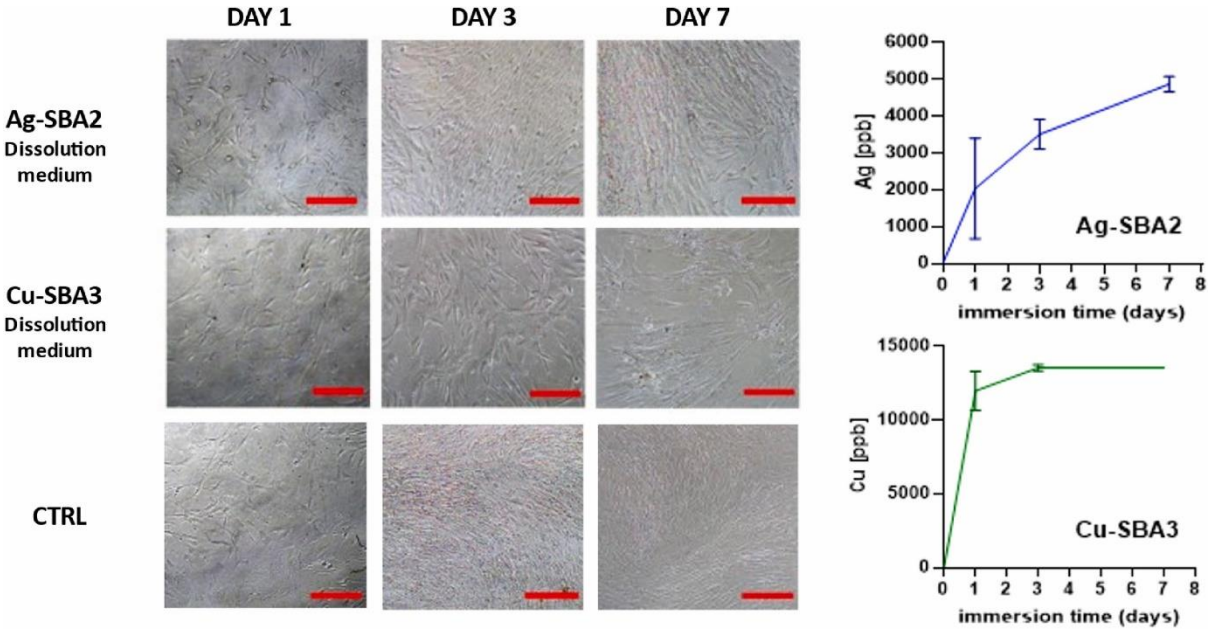

Figure 46: Light microscopy images of hASCs cultured with the glass dissolution products (left) and graphs showing the corresponding released concentration of doped ions (Ag or Cu) by ICP-OES analysis (right). Scale bars 200 µm.

The result for Ag-SBA2 is in line with previously published cytocompatibility analysis with human progenitor osteoblasts (hFOBs) (173), where Ag-SBA2 samples were found cytocompatible. In the case of Cu-SBA3, no previous cell studies have been published. In the literature, there are different concentrations of Cu-ions stated to be toxic for hASCs. For example, Thyparambil et al. found a decrease in hASCs viability with Cu-doped (0.4 wt-%) bioactive glass 13–93B (260), while Mishra et al. reported cytotoxicity of undiluted Cu-doped borophosphate glass extract, Cu ion concentration being around 2 ppm, towards hASCs (261). Dose-dependent toxicity of Cu has also been evidenced in mouse fibroblasts, where the median lethal dose of Cu-ions was found to be around 46 ppm (262). The values seem to vary depending on the sample, culturing conditions and used cell line, and therefore, it is challenging to compare with concentrations detected in this work. In our indirect culture experiment, the

concentration of Cu-ions in the medium does not appear to be cytotoxic to the cells.

After confirming the cytocompatibility of the glass extracts, hASCs viability was studied upon direct culture on glass discs by live/dead staining after 1, 3, and 7 days of culture.

As seen in Fig. 47, the undoped glasses (SBA2 and SBA3) supported the cell viability, similarly to the positive control, thus demonstrating that the glass composition is suitable for cell culture. Ag-SBA2 seems to inhibit cell viability after 1 day of culture, however, the cell number appears to increase slightly after 3 days. Therefore, one can hypothesize that the fast release of Ag-ions over the first day of culture is toxic to cells, but the toxicity decreases for a longer immersion time, with the changes of the medium, showing the cells trying to recover. In the case of the Cu-SBA3, it appears to be highly toxic in 1 day, killing all the cells. No living cells can be seen on day 1 and therefore they cannot recover later. This agrees with the high Cu-ion release occurring on day 1 evidenced by ICP-OES analysis (Fig. 3). However, as shown in the indirect cell culture (Fig. 46), the cytotoxicity of doped glasses does not seem to arise from the concentration of the released ions in the medium, but rather from the fast release and the direct contact of the hASCs to the sample surface. This type of contact-killing phenomenon could arise due to factors such as local burst release of ions, redox or catalytic activities of the ions, or the formation of reactive oxygen species (263,264).

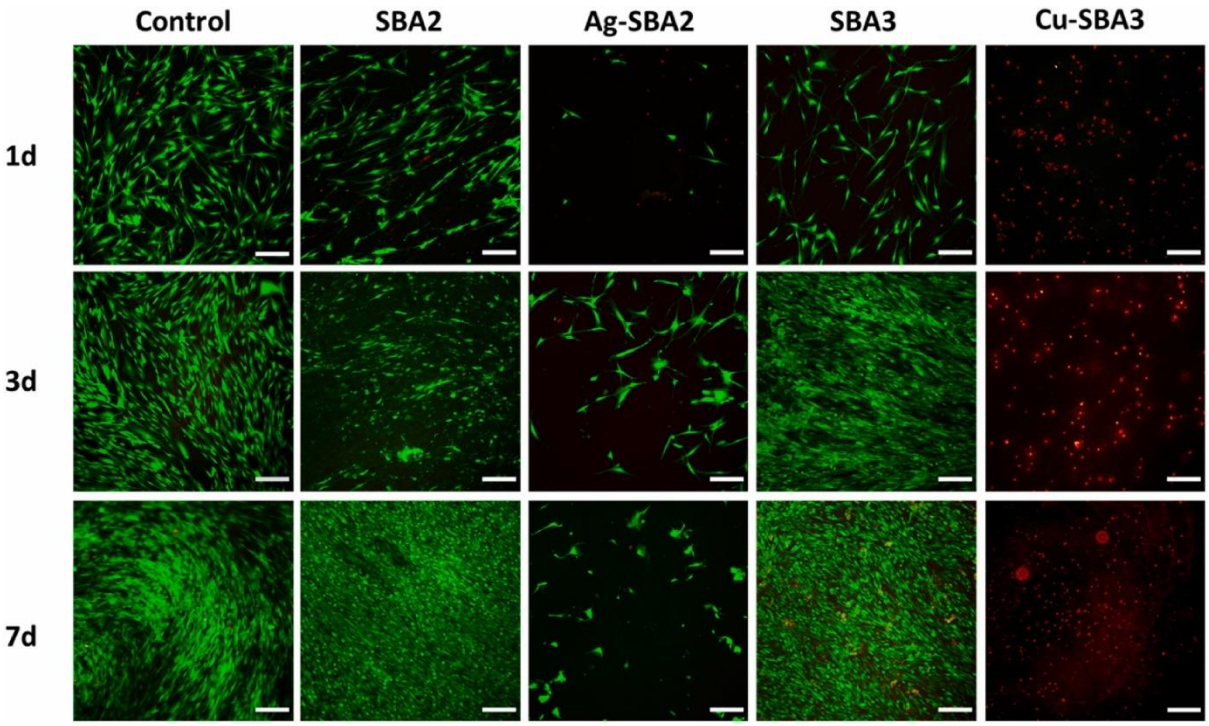

Figure 47: Cell viability on bioactive glass discs at 1, 3, and 7d. Viability was analyzed with Live/dead staining. Scale bars 200 µm.

To promote cell adhesion, viability, and proliferation (265), while maintaining the release of ions from the glasses, each material was coated with fibronectin, as shown in Fig. 48.

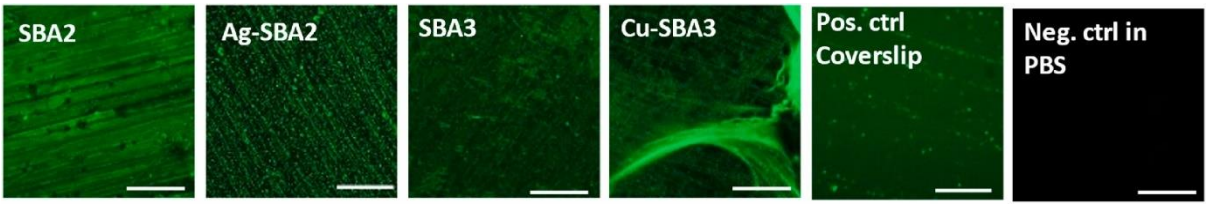

Figure 48: Confocal microscopy images of the glasses surface with adsorbed 488-Alexa labeled fluorescent fibronectin. Scale bars 30 µm.

Before cell culture, all samples were coated with fluorescently labeled fibronectin and imaged by confocal fluorescence microscopy to confirm protein

adsorption. The green fluorescence in the images can be assigned to the fluorescently labeled fibronectin because no autofluorescence was observed on any of the sample surfaces. As reported previously by Azizi et al. (266), adsorption of fibronectin on the silicate-based bioactive glass can promote cell adhesion and spreading. The confocal images (Fig. 48) confirm that the fibronectin was adsorbed and homogeneously covering the sample discs for each condition, which is expected to improve the cell adhesion.

After checking the uniform adsorption of fibronectin on the glass discs, cell culture was performed on the materials with the adsorbed fibronectin, and the live/dead images are presented in Fig. 49.

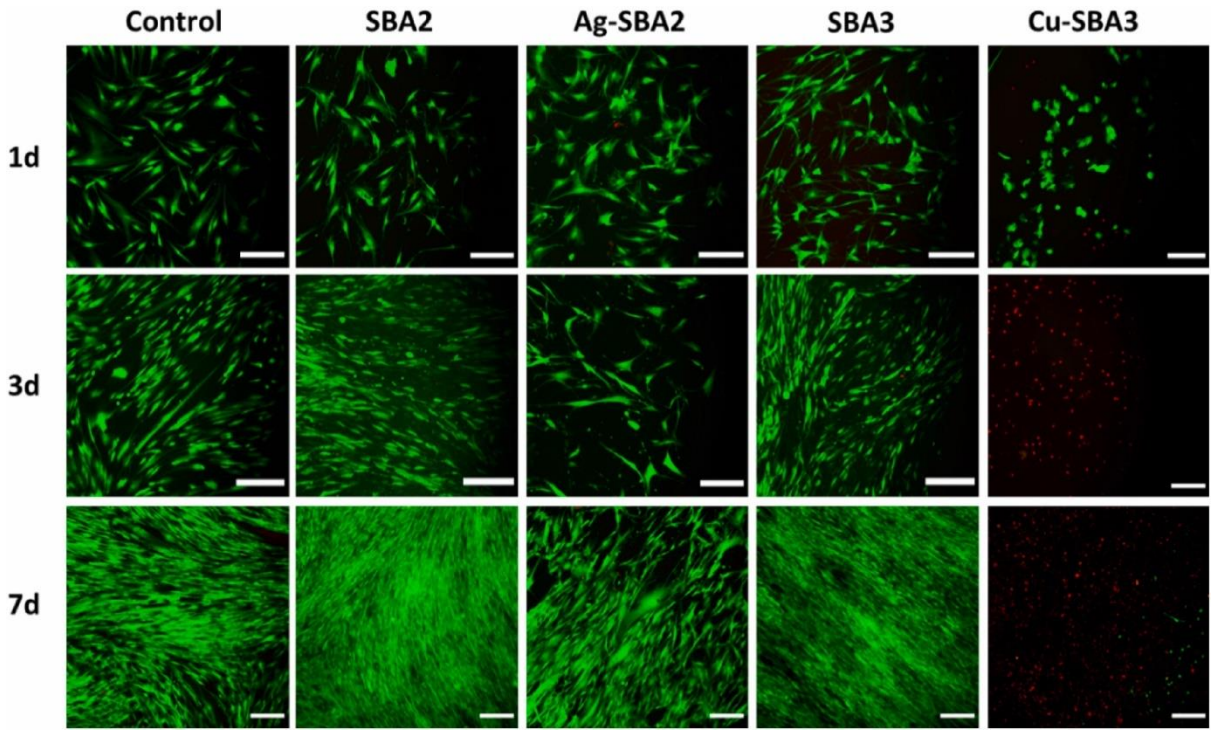

Figure 49: Cell viability on fibronectin-coated bioactive glass discs at 1, 3, and 7d. Viability was analyzed with Live/dead staining. Scale bars 200 µm.

The fibronectin-coating can be seen to enhance hASC viability and proliferation, especially in the case of Ag-SBA2. More viable cells are observed at all time points compared to Ag-SBA2 without added fibronectin (Fig. 49). In the case of Cu-SBA3, fibronectin adsorption does not seem to improve cell viability, as seen in Fig. 49 with red cells indicating cell death. However, the fibronectin may delay the release of Cu-ions, as some cells appear to be alive on day 1, but their death is evident only after 3 days of culture.

This observation is also supported by the quantitative CyQUANT cell proliferation assay (Fig. 50). Without fibronectin coating (Fig. 50A), the cell number of hASCs is significantly decreased with the doped Ag and Cu glasses compared to SBA2 and SBA3 respectively. Fig. 50B shows that even with the fibronectin coating, the same significant decrease is still observed. However, when the doped glasses are compared with and without fibronectin (Fig. 50C), it is observed that the fibronectin allows a significantly higher cell proliferation on day 1 for Cu-SBA3 glass and days 1 and 7 for Ag-SBA2. Differences in values between the different conditions on day 1 could be due to differences in viability, different attachment efficiencies as well as differences in proliferation rates. However, these results show that even if the fibronectin allows an improvement of cell proliferation on the doped glasses, it is still not enough to reach the ability to support the proliferation of the SBA2 and SBA3 glasses.

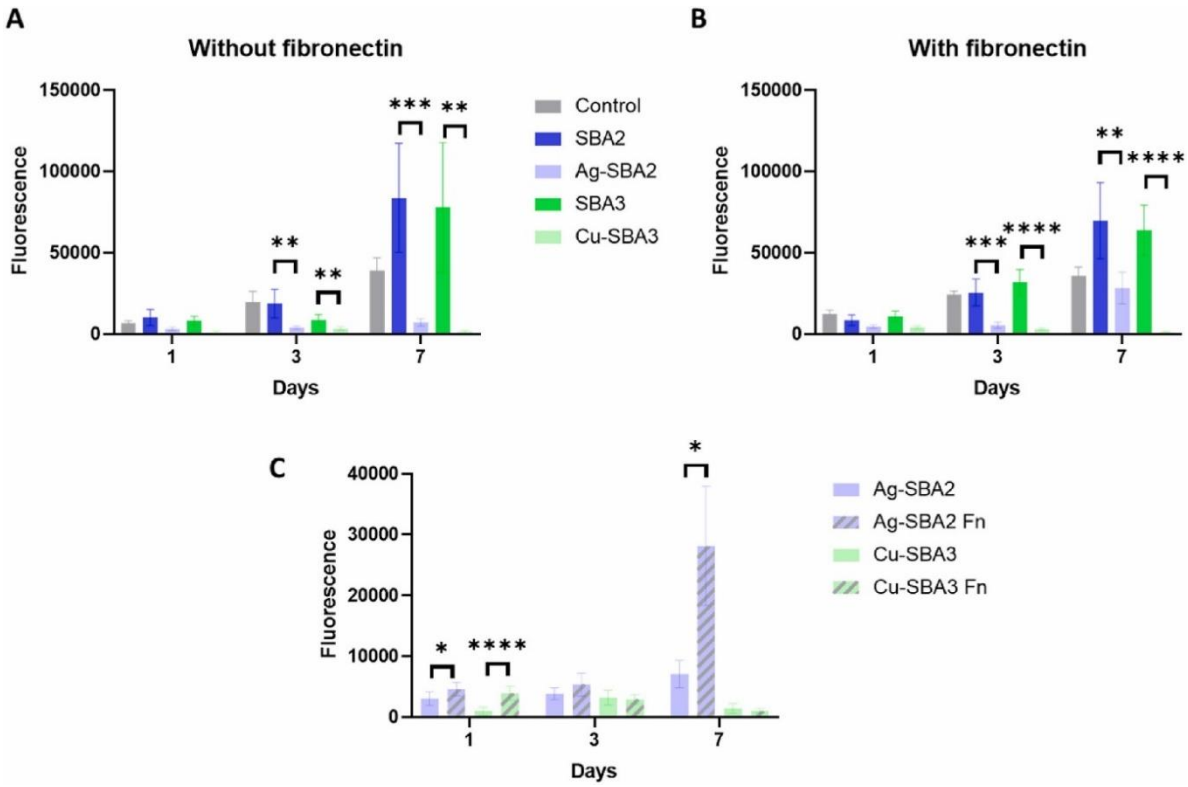

Figure 50: Proliferation of hASCs cultured on TCPS (control), SBA2, Ag-SBA2, SBA3, and Cu-SBA3 discs for 7 days, A) without, or B) with fibronectin (Fn) coating, analyzed by CyQUANT Cell Proliferation Assay kit. C) Comparison of Ag-SBA2 and Cu-SBA3 with and without fibronectin (Fn) (*p < 0.05, **p < 0.01, ***p < 0.001, ****p < 0.0001).

To verify that the coating of adsorbed fibronectin does not prevent the release of Ag/Cu-ions from the glass surfaces, ICP-OES analysis was performed for the cell culture medium from both the direct culture with and without fibronectin. The release kinetics of these ions in the cell cultures are displayed in Fig. 51.

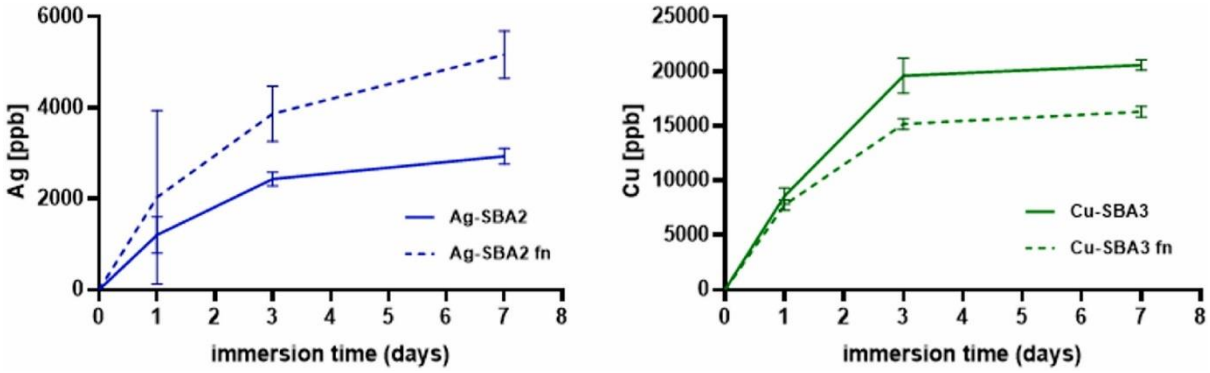

Figure 51: Release of Ag and Cu ions from uncoated Ag-SBA2 and Cu-SBA3, compared to fibronectin (fn) -coated samples (Ag-SBA2-fn and Cu-SBA3-fn) measured by ICP-OES.

When comparing the release kinetics of Ag- and Cu-ions of the cell culture experiments with and without fibronectin (Fig. 51), in both cases the doped ions are seen to be released. However, some differences between the bare samples and the ones with adsorbed fibronectin were detected. In general, release kinetics follow the same pattern in both cases, where the ion leaching is most evident in the beginning of soaking in cell culture. In the case of Ag-SBA2, the release of Ag-ions continues until 7 days of cell culture, especially with the added fibronectin, where measured maximum Ag-ion concentration is seen to be higher. With the high standard deviations especially in the case of the 1-day timepoint, these differences could be simply due to the differences in the ion-exchange process. Regarding Cu-SBA3, the concentration of released Cu-ions was slightly lower with the presence of adsorbed fibronectin, but in both cases the Cu-ion release continues only until 3 days of soaking in the cell culture.

In addition, when comparing the Ag- and Cu-release of Fig. 51 to the one displayed in Fig. 46 with similar cell culture conditions, the overall release kinetics are found to follow a similar pattern. For Ag-SBA2 the release is seen to continue for 7 days in all measured conditions, also when soaked in pure α-MEM culture medium without added serum or cells (Fig. 43). However, in the case of

Cu-SBA3, all the ICP measurements performed in cell culture conditions show Cu-ion release during 3 days of soaking (Fig. 43, Fig. 51), while the Cu-ion release without added serum or cells (Fig. 43) occurs only until 1 day of soaking. It seems that the presence of cells delays the release of ion-exchanged Cu-ions from the Cu-SBA3 surface. In general, some differences in the maximum released concentrations of both Ag- and Cu-ions are detected between the different measurements, possibly due to inconsistencies in the ion exchange process. Especially in the case of Cu-SBA3 the differences in maximum release are found to be more evident, suggesting that the ion-exchange process of Cu-ions may lead to less uniform ion coating compared to Ag-doped SBA2.

Another way to prevent the negative effect of the initial ion release burst on the cells, glass discs were pre-incubated in the basic α-MEM culturing medium before cell culture. Especially in the in vitro static cell cultures, pre-treatment of BAG samples is recommended due to their high initial reactivity (267). When BAGs get in contact with an aqueous environment, the fast ion-exchange phenomenon on their surface leads to a burst release of alkaline ions and their exchange with H_3O^+ ions from the solution, so the following local pH increase (267,268). The alkalinization of the surrounding medium to some extent is known to benefit alkaline phosphatase (ALP) activity and osteogenesis (269), but too high pH value, especially together with burst release of ions from the BAG can be detrimental to cell viability.

The assessment of cell viability, proliferation, and morphology was carried out after pre-incubating glass discs for 24 h in a basic α-MEM culture medium before cell seeding. As displayed in Fig. 52, in the case of all the tested glasses, hASCs stayed viable in direct contact with glass surfaces for up to 14 days. When comparing the undoped and Ag-/Cu -ion doped glasses, no difference in hASCs viability was detected. It seems that the 24 h pre-incubation is enough to limit the excessive surface reactivity of the studied BAGs.

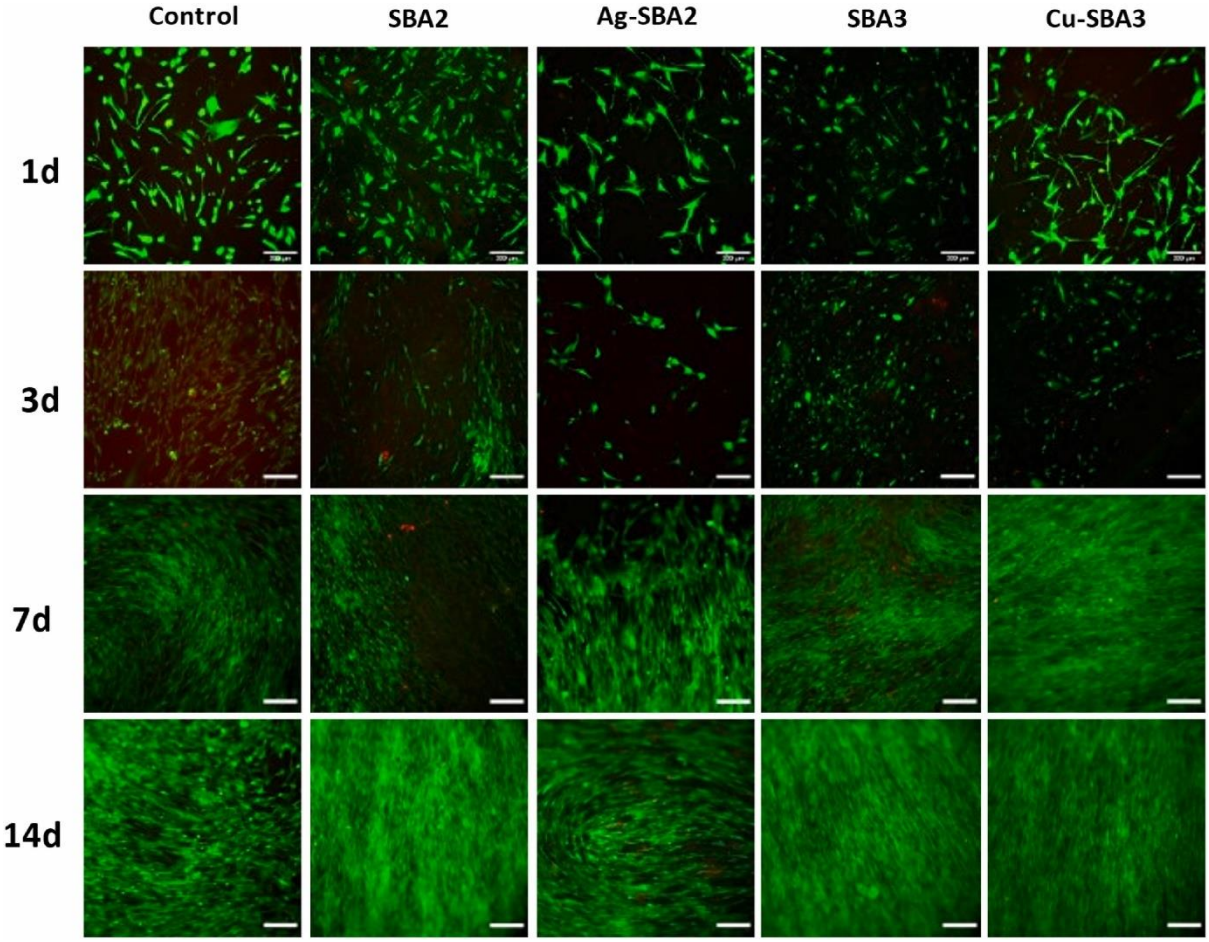

Figure 52: Cell viability on pre-incubated bioactive glass discs at 1, 3, 7, and 14 days. Viability was analyzed with Live/dead staining. Scale bars 200 µm.

In addition to the Live/Dead images, the cell proliferation during the 14 days of culture was assessed with CyQuant proliferation assay (Fig. 53). As demonstrated in Fig. 53, the cell proliferation followed a similar trend for all the compositions. Initially, during the first three days of culture, proliferation decreased for all compositions compared to the control, and the cell number is

significantly lower on the doped glasses compared to the undoped ones. But after 14 days, the cell amount was approximately similar for all glasses and the control.

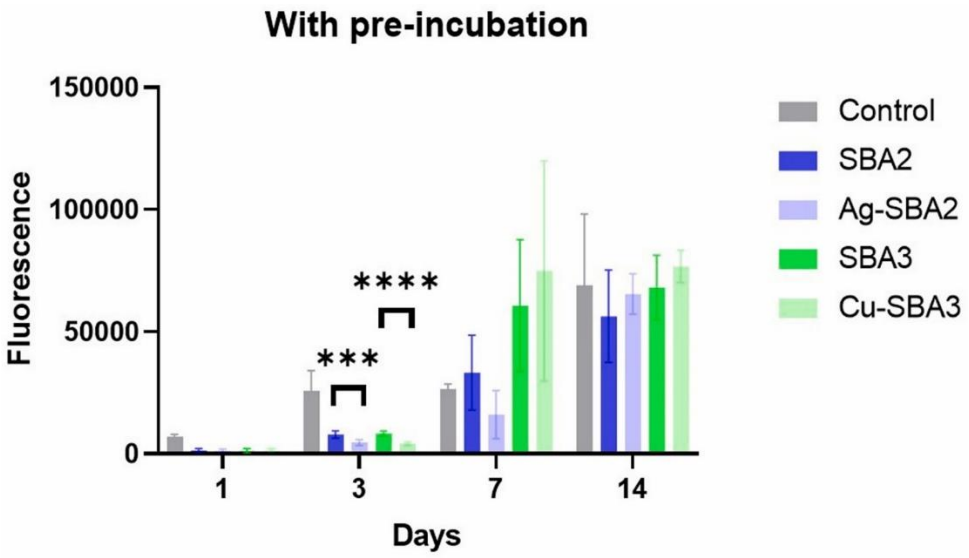

Figure 53: Proliferation of hASCs cultured on TCPS (control), and on pre-incubated SBA2, Ag-SBA2, SBA3, and Cu-SBA3 discs for 14 days, analyzed by CyQUANT Cell Proliferation Assay kit (*p < 0.001, ****p < 0.0001).**

The ability of the hASCs to spread on the 24-h pre-incubated BAG discs was evaluated by staining the actin cytoskeleton and the nuclei. As evidenced in 4, the cell spreading was not affected by the glasses. All the cells grew in tight contact with each other forming a confluent cell layer, except in the case of Ag-SBA2, where individual cells are more evident due to lower cell growth. However, when observing the cell shape, all cells appeared spindle-shaped, which is known to be typical for MSCs (270).

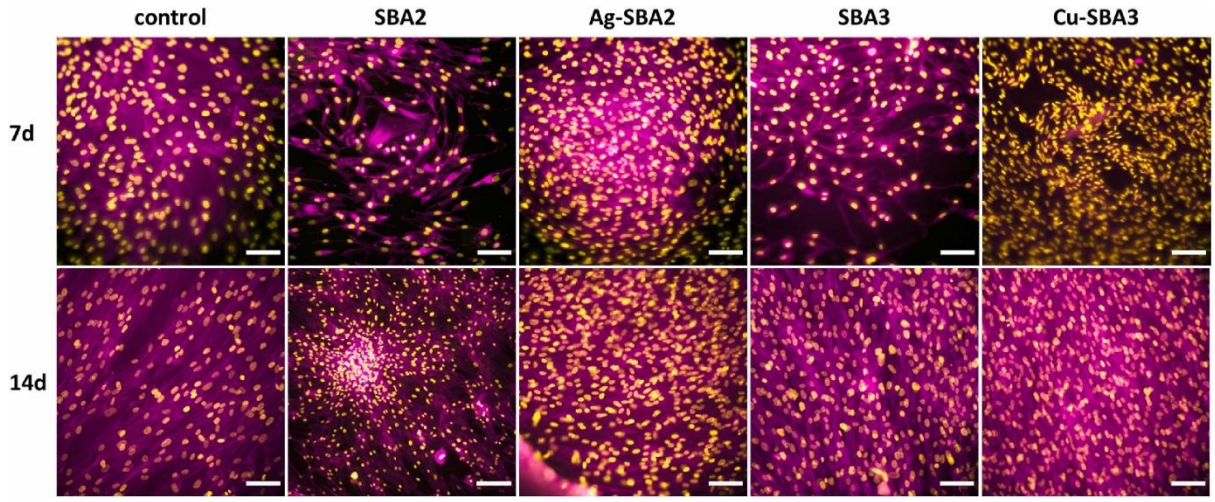

Figure 54: Morphology of hASCs on TCPS (control), SBA2, Ag-SBA2, SBA3, and Cu-SBA3 discs in α-MEM complete medium analyzed by Nuclei (DAPI - yellow) and Actin (Phalloidin - magenta) immunostaining after 7 days and 14 days of culture. Scale bar 50 µm.

In addition, the release of surface-doped ions is evaluated (Table 11) by ICP-OES analysis to assess whether using the standard pre-incubation time for bioactive glasses will eliminate the ion-exchanged layer of ions on the samples needed for the antibacterial effect (267).

Table 10: Ag- and Cu-ion release, from Ag-SBA2 and Cu-SBA3, during pre-incubation and in between cell culture time points (0-1d, 1d-3d, 3d-7d), measured by ICP-OES. *) UDL = under the detection limit of the instrument.

Immersion interval	**Ag-ion release [ppb] from Ag-SBA2**	**Cu-ion release [ppb] from Cu-SBA3**
Pre-incubation 24h	300.0 ± 141.4	21 433.3 ± 4921.7
In contact with hASCs 0-1d	5500 ± 707.1	150.0 ± 70.7

In contact with hASCs 1-3d	566.7 ± 152.8	UDL*
In contact with hASCs 3-7d	UDL*	UDL*

As displayed in Tables 11 and in the case of Ag-SBA2, Ag-ions are being released from the surface already during the pre-incubation, but only partially. The majority of Ag-ions are released after one day in cell culture, and as seen in Fig. 50, Fig. 51, Fig. 52, this concentration does not seem to compromise hASCs viability in direct cell culture. The antibacterial effect of Ag-SBA2 has been previously proved for samples without pre-incubation (173), and therefore, further antibacterial evaluations would be needed to confirm that the pre-incubation does not prevent this effect. In the case of Cu-SBA3, a great majority of surface-doped Cu ions are released during the 24-h pre-incubation. Therefore, in the following cell culture, Cu-SBA3 resembles more its reference glass SBA3 without the ion-exchanged layer of Cu ions. It is also probable that the possible antibacterial effect of Cu-SBA3 will be lost if pre-conditioning is used prior contact with the biological environment.

Balancing between the critical concentration for antibacterial performance and cytocompatibility is a challenge when optimizing multifunctional biomaterials for biomedical use. Above certain concentrations, both Ag^{+} and Cu^{2+} are known to be toxic to cells. However, it is difficult to state an exact toxic concentration due to the static in vitro culture conditions, where the lack of fluid flow and replenishment magnifies local concentrations and pH value changes. Therefore, instead of using preconditioning, which might compromise the release of antibacterial ions, the use of more dynamic culturing conditions could diminish

the problem and prevent steep local ion concentration gradients toxic to cells (271,272). It is also to be noted that rapid initial release of antibacterial ions, such silver or copper ions, could be necessary to treat early infection, even if it would also cause initial cell toxicity. In vivo conditions, new cells will be available, and once the first antimicrobial effect is implemented through burst release of antibacterial ions, the material surfaces are no longer found toxic and enable further cell adhesion and proliferation.

4.5.2.2 Antibacterial activity evaluation

In addition, both doped glasses have been shown to have antibacterial properties against *S. aureus*, as reported by the authors (173,234). However, the previous analysis of antibacterial activity was performed on Cu-SBA3 glass powder with different ion exchange conditions than the one optimized and described in this Thesis. Therefore, the antibacterial activity of 0.001 M Cu-SBA3 was here studied.

According to the results obtained from the morphological and glass surface phase analyses (detailed in previous sections) of Cu^{2+}-doped samples in ion-exchanged solution with different concentrations of Cu^{2+} (0.001, 0.01, and 0.05 M), SBA3 in the lowest concentration of the ion-exchanged solution (Cu-SBA3 0.001 M) was chosen for in vitro biological assessments. To differentiate between the antibacterial and antibiofilm properties of specimens towards *S. aureus* MDR, two different protocols were used: ISO 22196 standard protocol for antibacterial evaluation and UPO protocol for antiadhesive and antibiofilm evaluation (detailed in section 2.3.2) (173). Fig. 55 (A-C) shows the results of metabolic activity, bacterial colonies count (CFU), and SEM that were obtained from ISO22196 standard protocol. After 24 h of direct inoculation of *S. aureus* on the samples' surfaces, metabolic activity analysis of bacterial strains showed a statistically significant difference of ~52% between Cu doped SBA3 and undoped SBA3 (Fig. 55 A; $p < 0.01$ represented by **). Additionally, surface-adherent viable bacterial

colonies count (CFU) revealed that the number of bacterial cells attached to Cu-SBA3 surfaces was approximately 1 log less than the ones attached to the control samples (Fig. 55 B; $p < 0.01$ indicated by **). This difference in metabolic activity and the number of surface-attached bacterial cells between CU-SBA3 and undoped SBA3 was visually confirmed by means of SEM images that were taken in two different magnifications (1500X and 4000X, Fig. 55 C). As shown in the SEM image of undoped SBA3, most part of the control sample surfaces was covered by a layer of bacterial biofilm; while few aggregations of bacterial cells were observed on the surface of Cu-SBA3, in agreement with ~52% and ~1 log reduction of metabolic activity and viable bacterial colonies count, respectively.

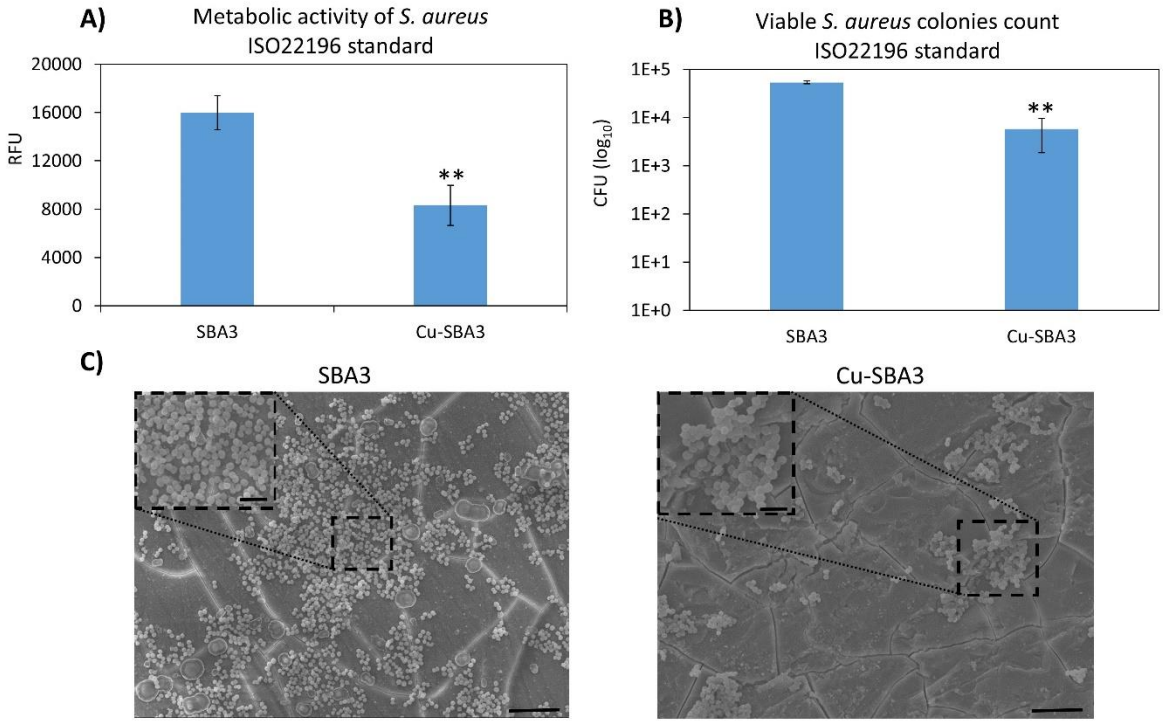

Figure 55: Antibacterial test according to ISO 22196 standard after 24 h incubation at 37 °C: A) Metabolic activity of *S. aureus* MDR on the specimens' surfaces; B) Viable surface-attached bacterial colonies count (CFU), C) SEM images taken in two different magnifications (1500X in the image and 4000X in the left corner inset with scale bars 10 and 5 µm respectively). ** indicates p value < 0.01 and bars represent standard deviations.

To evaluate the specific behavior of the doped samples (Cu-SBA3) concerning bacterial adhesion and biofilm formation, the UPO protocol was utilized. In this case, the sterile samples were fully submerged into 500 µL of *S. aureus* MDR suspension and the impact of Cu-SBA3 on bacterial attachment and biofilm formation was evaluated by measuring bacterial metabolic activity, surface-adherent CFU and SEM at two different time points: i) early time point (6 h) that it was selected based on the results obtained from ion release evaluation (Fig. 40); as shown in Fig. 40, Cu^{2+} released from the samples' surfaces during the first 3 days of soaking in the SBF and inflammatory solution (acetate buffer at pH 5). Therefore, 6 h was chosen to evaluate whether Cu-doped SBA3 was able to decline bacterial adhesion on the samples' surfaces or not; ii) late time point (24 h) to investigate the effect of Cu-SBA3 on bacterial biofilm formation onto the samples' surfaces. The results of bacterial metabolic activity, adherent viable colonies count, and SEM are presented in Fig. 56 A-C. According to the results of metabolic activity and CFU, after 6 h of bacterial inoculation onto the specimens' surfaces and incubation, no statistically significant difference in adherent bacteria was observed between Cu-SBA3 and undoped SBA3 (control sample) surfaces. However, after 24 h, the metabolic activity of *S. aureus* MDR showed a reduction of approximately 52% on the Cu-SBA3 surfaces in comparison to undoped SBA3 (p-value <0.01 indicated by **; Fig. 56 A); in addition, CFU count results demonstrated that adherent bacterial colonies onto the Cu doped samples' surfaces decreased about 0.6 log in comparison to attached colonies onto the control samples (p-value <0.05 indicated by *; Fig. 56 B). These results were in line with SEM images that were taken at two different magnifications (1500X and 4000X with scale bars 10 µm and 5 µm, respectively; Fig. 56 C). After 6 h, few bacterial colonies adhered to the samples' surfaces and no difference in colony number was observed between Cu-doped SBA3 and undoped SBA3 samples. After 24 h of inoculation and incubation, attached bacterial cells on the SBA3 samples' surfaces grew and bacterial microcolonies (biofilm) formed on the surfaces of control

samples. While some single colonies detected on Cu-SBA3 surfaces indicating that released Cu^{2+} ions from the doped samples during 24 h in contact with bacterial suspension showed antibiofilm properties (Fig. 56 C) as the same results that were obtained from ISO protocol.

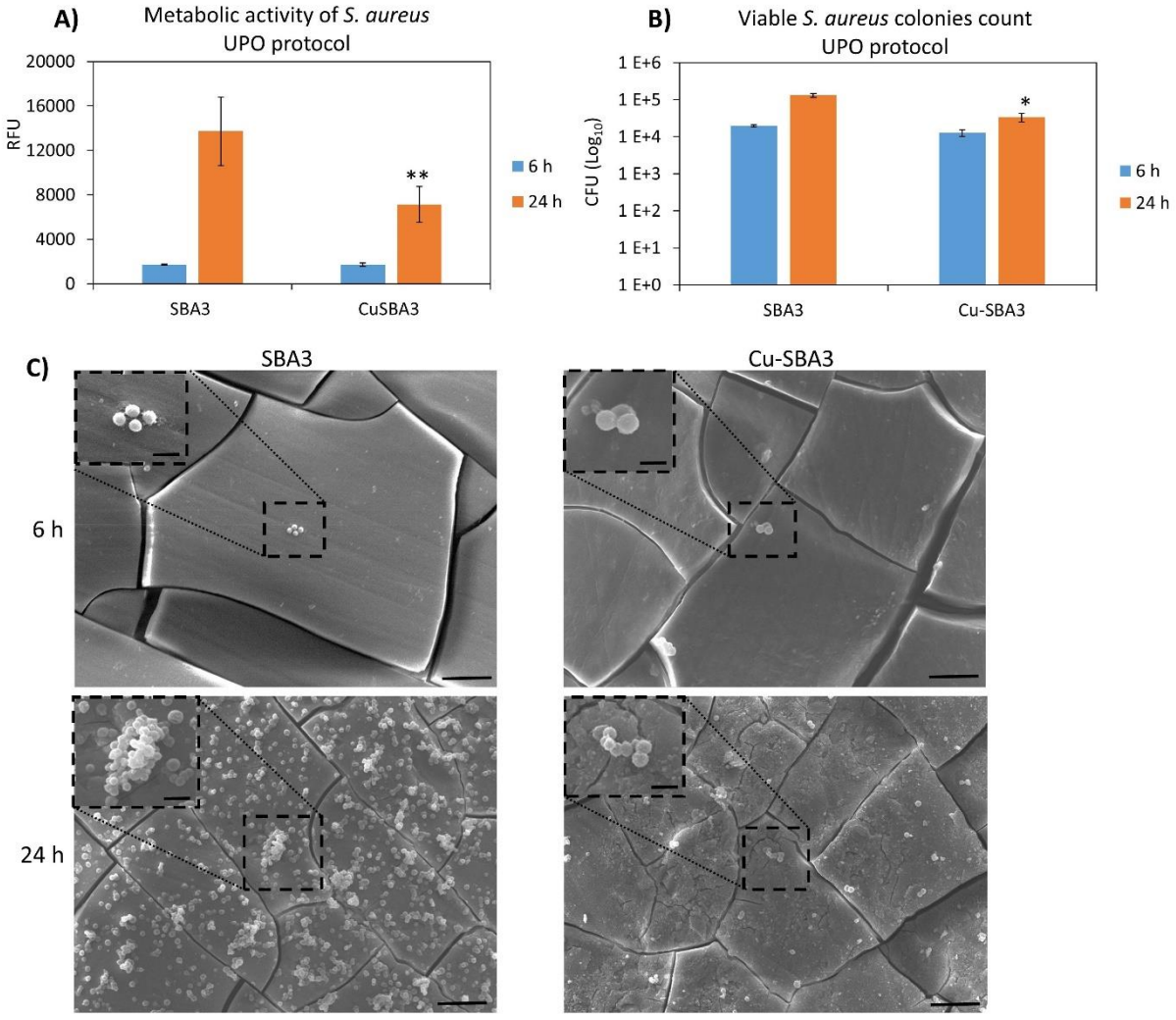

Figure 56: Antiadhesive and antibiofilm test according to the UPO protocol after 6 and 24 h incubation at 37 °C, respectively: A) Metabolic activity of *S. aureus* MDR on the specimens' surfaces; B) Viable surface-attached bacterial colonies count (CFU), C) SEM images taken in two different magnifications (1500X in the image and 4000X in the left corner inset with scale bars 10 and 5 µm respectively). * and indicate $p < 0.05$ and $p < 0.01$, respectively; bars represent standard deviations.**

For both protocols (ISO 22196 standard and UPO protocol), antibacterial activity (R score) was calculated by the difference between the average of the common logarithm of the number of viable bacteria recovered from the undoped control samples (U_t) and doped ones (A_t) after 24 h; indeed, R score reveals the effectiveness of an antibacterial agent (173,245). The results are presented in Table 12 as well as the count of the initial inoculum ($U_0 = 3.7$) that was confirmed in the magnitude of 5E3.

Table 11: R score values calculated by the colony-forming unit (CFU) count immediately after inoculation (U0) and after 24 h of culture in direct contact with the specimens' surface (Ut for untreated and At for treated samples).

Sample	Protocol	Log_{10} CFU Count (U_0)	Log_{10} CFU Count (U_t, A_t)	(R) score
SBA3	ISO 22196	3.7	4.7	Control sample
Cu-SBA3	ISO 22196	3.7	3.7	1
SBA3	UPO	3.7	5.1	Control sample
Cu-SBA3	UPO	3.7	4.5	0.6

The results obtained from in vitro evaluation of antibacterial and antibiofilm properties for Cu^{2+} doped SBA3 in comparison to undoped SBA3 revealed that doped specimens in lower ion-exchange solution (0.001 M) had no impact on the attachment of *S. aureus* MDR on to samples' surfaces (after 6 h); while during 24 h, antibacterial and antibiofilm properties of Cu-SBA3 has initiated due to release of Cu^{2+} ions into the LB broth and both used protocols (ISO 22196 standard and UPO protocol) showed more or less the same results, a 50% reduction for metabolic activity and between 0.6 and 1 log decrease for surface-adherent

bacterial colonies. Moreover, from the result of the R score obtained from two investigated protocols (0.6 and 1 for UPO and ISO 22196 protocols, respectively), it was concluded that the effectiveness of Cu-SBA3 samples by using these two protocols was more or less the same.

These results are in agreement with previous literature. Pierre et al. investigated the biological properties of homogeneous calcium phosphate coating on titanium dental implants that were doped with Cu exchange post-treatment at different concentrations (0.001, 0.05, and 0.01 M) towards Gram-positive and Gram-negative bacterial strains at two time points (4 and 24 h). They reported that after 4 h, there was a low reduction of adherent Gram-negative onto the samples doped with Cu in comparison to undoped specimens, while for Gram-positive bacterial strains, no noticeable difference was observed. However, after 24 h of inoculation, a significant reduction of CFU of about 2 log for both Gram-positive and Gram-negative bacterial strains was observed (273). Regarding Cu-doped bioactive glasses, Popescu et al. conducted a study on the antibacterial activity of Cu-containing bioactive glass-ceramics against *S. aureus*. They found that the glass with 0.5 mol% CuO exhibited the lowest minimum inhibitory concentration and bactericidal concentration against *S. aureus.* Additionally, they observed that the release of Cu^{2+} ions from this glass after 24-h soaking in deionized water was similar to the values measured in our study (Fig. 40C) (274). In another investigation, which examined the effect of Cu^{2+}-ion release from a calcium-phosphate glass with varying Cu content on *S. aureus,* a strong correlation was found between the concentration of released Cu^{2+} and the bactericidal properties (275). Nevertheless, while it is generally observed that higher copper content correlates with improved antibacterial performance, it is crucial to consider that elevated concentrations of copper can potentially generate an excessive quantity of free radicals, which may induce cytotoxicity (276). Therefore, it is crucial to carefully control the release kinetics of copper to ensure an optimal balance between antibacterial efficacy and potential cytotoxic effects.

Even though the here studied glass shows potential to be used as an antibacterial material it is pivotal to further assess its cytocompatibility and Cu^{2+} leaching in the used culturing conditions. Cu-SBA3 discs have been found to decrease human adipose stem cell viability in direct culture, possibly due to the rapid release of Cu^{2+} from glass surface in the cell culture (277). Instead, when employing an indirect culture the cells stayed viable with healthy morphology, suggesting only contact killing phenomenon. However, these preliminary tests made with one cell line were only a starting point for deeper understanding of the cytocompatibility and possible osteogenic potential or angiogenic properties of the Cu-SBA3 glass.

4.6 Conclusion

In this comprehensive study, bioactive glass surfaces, were successfully doped with either ionic Cu^{2+} or Ag^{+} through an ion exchange process in aqueous solution. The concentration of the Cu(II)acetate ion exchange solution was optimized, with 0.001 M being chosen for further analyses. The Cu-doping of SBA3 surfaces was found to maintain their amorphous nature and enhance bioactivity, evidenced by increased hydroxyapatite formation compared to undoped surfaces. It is worth noting that physicochemical characterization and antibacterial analyses for Ag-SBA2 have been previously studied and published by the authors and therefore not the focus in this chapter.

Moreover, the antibacterial properties of Cu-doped SBA3 against Gram-positive *Staphylococcus aureus* MDR were extensively evaluated, revealing a significant reduction in bacterial metabolic activity and surface-adherent bacterial cells count. SEM images confirmed the antibacterial efficacy with minimal viable colonies observed on Cu-SBA3 surfaces.

In evaluating the cytocompatibility of both Cu-SBA3 and Ag-SBA2 bioactive glasses towards hASCs, contrasting results were observed. Direct contact with Cu-SBA3 compromised hASCs viability, suggesting cytotoxicity. However, a significant improvement in cytocompatibility was noted after 24 hours of pre-incubation, or with using an indirect culture. Nonetheless, the abrupt release of Cu-ions within the initial 24 hours underscores the necessity for refining the ion-exchange process to maintain sustained antibacterial efficacy without compromising cell survival. Conversely, Ag-SBA2 exhibited a different cytocompatibility profile. Direct contact compromised hASCs viability, indicating cytotoxic effects. However, direct culture with fibronectin adsorption to the glass surfaces revealed enhanced cell attachment, viability, and proliferation. In addition, indirect culture with glass dissolution products didn’t negatively affect cell response. The rapid release of Ag-ions from Ag-SBA2 could provide early infection prevention benefits, while a more gradual release supports cytocompatibility. Nevertheless, further investigations are essential to assess long-term cytocompatibility and antibacterial performance, affirming Ag-SBA2's suitability for bone infection treatment.

Chapter 5: Bioactive glass-ceramic hierarchical 3D scaffolds for bone substitution

5.1 Introduction

Over the past couple of decades, tissue engineering has emerged as a promising avenue for restoring and regenerating tissues and organs affected by trauma, diseases, or aging (278). Various tissues have seen successful regeneration through these methods, offering a potential solution to the scarcity of transplantable tissues and organs. While autografts remain the gold standard for bone defect treatment, issues like limited supply and donor site complications present significant challenges (279). Alternatives like bone allografts, while available, come with their own set of drawbacks such as high cost and risks of disease transmission and immune rejection. Synthetic biomaterials have shown promise as bone substitutes, yet their clinical success still lags behind autologous bone procedures (280).

Given the limitations of current treatments and their impact on healthcare expenses, there's a growing interest in developing new bone substitutes. At the heart of bone tissue engineering lies the scaffold—a porous structure designed to facilitate new tissue formation by providing a matrix with interconnected porosity and tailored surface chemistry to support cell growth, nutrient exchange, and waste removal (281).

This chapter presents a literature review covering the essential properties and considerations of an ideal ceramic scaffold for bone regeneration applications, followed by an overview of different scaffold fabrication methods. Given the emphasis of this study on scaffolds realized via the foam replica method, particular attention is paid to the current state of the art in scaffold preparation using this method. Additionally, the potential for incorporating antimicrobial Ag-ions into the scaffold is discussed.

5.2 Key properties of a scaffold for bone regeneration

Designing a scaffold involves a balance, requiring interconnected pores for tissue ingrowth, nutrient transport, and angiogenesis, while also managing resorption rates and mechanical properties like stiffness, strength, and fracture resistance. These characteristics are often interdependent, making the design, characterization, and translation of synthetic implants into clinical applications quite challenging (282). Figure 57 provides a summary of the key properties essential for an ideal scaffold.

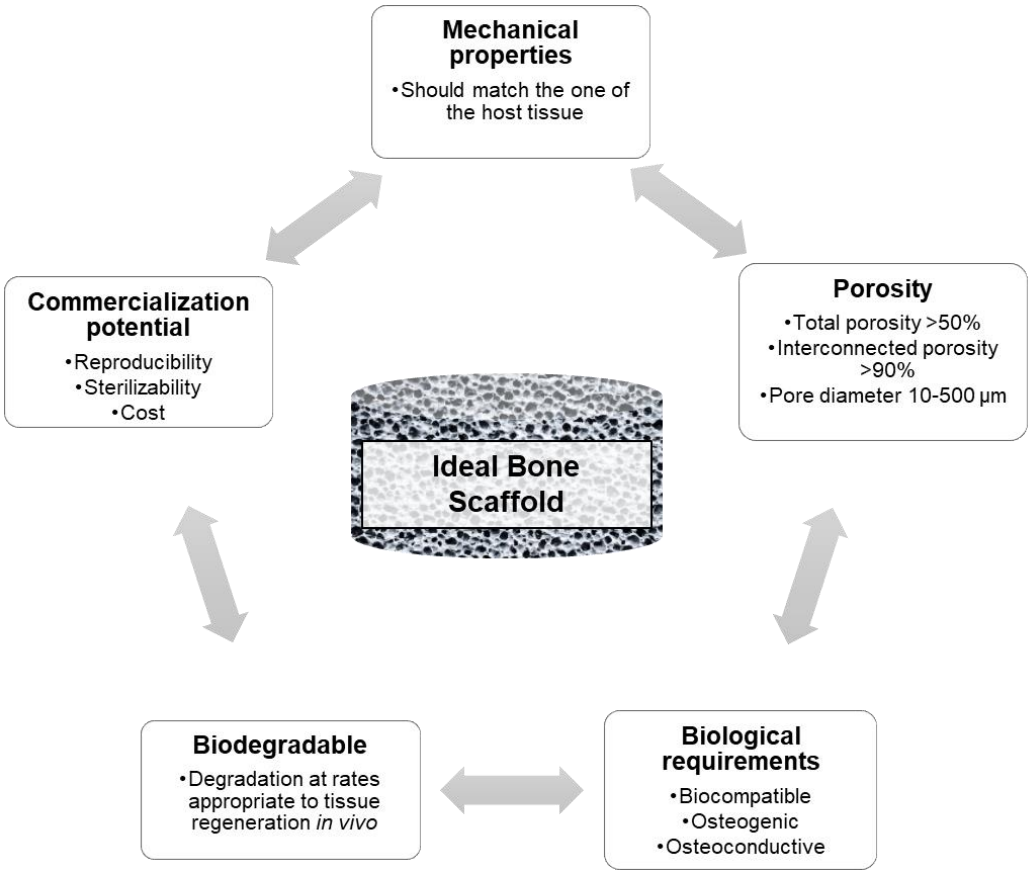

Figure 57: Summary of key properties for a scaffold for bone regeneration

A primary role of bone tissue engineering scaffolds lies in serving as a template for cells to adhere, proliferate, differentiate, and organize into healthy bone tissue as the scaffold gradually degrades (281). This function is closely associated with osteoconductivity, crucial not only for preventing the formation of fibrous encapsulation of the scaffold but also for fostering a strong bond between the scaffold and the host bone.

The *in vivo* biodegradation rate serves as another pivotal criterion for biomaterial selection in scaffold fabrication, tailored to align with the pace of tissue regeneration. When utilizing biodegradable materials, understanding the time-dependent variation in their mechanical properties and structural integrity is crucial, as scaffold strength must be adequate to provide mechanical stability during the period of new tissue formation in load-bearing sites. Additionally, disposal and removal of degradation by-products in biodegradable scaffolds necessitate careful consideration, as accumulation of ionic dissolution species could incite local inflammatory responses due to poor metabolic activity and vascularization in surrounding tissues, impeding by-product elimination (283,284).

Achieving a proper balance between scaffold strength and stiffness is essential to ensure mechanical integrity during physiological activities and appropriate load transfer to surrounding tissue while avoiding excessive resorption. Customization of scaffold mechanical properties is challenging due to the diverse stimuli encountered at different bone sites in the human body, necessitating adaptability based on specific applications, implantation sites, patient age, lifestyle, and health. Ceramics, despite their intrinsic fragility, are utilized in bone tissue engineering, with composite scaffolds combining bioceramics and biocompatible polymers to mitigate brittleness and enhance suitability for clinical applications (285).

One of the most essential requirements is the porosity of the scaffold. Human bone exhibits a hierarchical structure across various dimensional levels, ranging from the nanoscale to the macroscale (286). Mimicking this complexity, an ideal bone tissue scaffold should feature an interconnected porous structure with high permeability, characterized by open porosity exceeding 50% and pore diameters ranging from 10 to 500 μm to facilitate cell seeding, tissue ingrowth,

vascularization, nutrient delivery, and waste removal. Microporosity (approximately 2–10 μm) is vital for immediate protein and cell adhesion, migration, and osteointegration, while larger pore sizes (>300 μm) promote enhanced new bone formation, increased ingrowth, and capillary formation. However, excessively high scaffold porosity compromises mechanical properties, necessitating a balanced approach based on repair needs, remodeling rates, and scaffold degradation rates (281).

Moreover, scaffolds should be customizable to match specific defect morphologies in individual patients, allowing fabrication into complex or irregular shapes. Scaffold material synthesis and fabrication processes should also accommodate sterilization and commercialization requirements, ensuring scalability, cost-effectiveness, and preservation of original characteristics post-sterilization (287).

However, the criteria of surgeons and engineers may not always align perfectly. From an engineering perspective, an ideal scaffold is a tough bioactive material that could be made into an openly porous structure resembling cancellous bone. Surgeons typically prefer porous materials with mechanical properties akin to cortical bone, amenable to on-the-spot shaping in the operating theater, and capable of either expanding to fill bone defects or being injectable into them (129).

5.3 Overview of scaffold manufacturing methods

The first attempt to produce a bioactive glass-based scaffold dates back to 2002 when Sepulveda et al. pioneered this effort (288). They employed a sol-gel process combined with *in situ* foaming to achieve a macroporous structure. Since then, numerous research groups have aimed to identify the optimal manufacturing process for producing an "ideal" scaffold. This ideal process should yield scaffolds possessing bone-like mechanical properties, controlled porosity,

appropriate surface topography, and without any harmful substances such as solvents or additives required during production. Moreover, an ideal scaffold should be reproducible and consistent to enable mass production with uniform characteristics. Additionally, customization may offer significant value in meeting individual patient needs. Importantly, scaffold manufacturing should be economically viable, efficient, and safe for both workers and the environment. A summary of the most common manufacturing techniques to produce ceramic-based bone tissue engineering scaffolds is provided in Table 14.

Table 12: Summary of the most common ceramic-based scaffold manufacturing techniques in bone applications(283)

Major group	Technological class	Specific methods
Conventional (top-down approach)	Foaming technologies	Gel-casting foaming (289), sol-gel foaming (288,290), H_2O_2 foaming (291)
	Thermal consolidation of particles	Without use of porogens (292,293); Organic phase burning-out: polymeric porogens (294,295), starch consolidation (296), rice husk method (297,298)
	Porous polymer replication	Coating methods (299–301), foam replication (302,303)
	Freeze-drying	Freeze-casting of suspensions (304,305), ice-segregation-induced self-assembly combined with sol-gel (306)
	Thermally induced phase separation	(307)
	Solvent casting and particulate leaching	(308)

Additive manufacturing (bottom-up approach)	Selective laser sintering	(309)
	Stereolithography	(310)
	Direct ink writing	3D printing (311), ink-jet printing (312), robocasting (313,314)

The “conventional” technologies include the traditional top-down manufacturing methods, which entail removing specific sections from a bulk material to achieve the desired shape and porosity (283). Typically, all these methods enable the production of glass, glass-ceramic, and polymer/glass composite scaffolds.

Foaming technologies involve utilizing a foaming agent in conjunction with melt-derived or sol-gel bioactive glasses. Typically, a slurry or colloidal suspension (sol) is prepared, and the foaming agent is introduced to generate air bubbles, thus creating porosity within the material. Methods for pore formation in the scaffold include direct gas injection, vigorous agitation, gas generation via chemical reactions, or thermal decomposition of peroxides (315). However, common drawbacks of foaming techniques include the presence of closed pores, limited interconnectivity within the porous network, formation of a nonporous outer layer, and scaffolds with mechanical properties that are merely acceptable due to their high brittleness.

Thermal consolidation methods involve incorporating sacrificial particles or templates into the green body, which is then typically subjected to sintering. These pore-forming agents are commonly natural polymers (such as starch or rice husk) or synthetic polymers (like PE particles). These techniques offer relatively low costs and enable the production of bioceramic and glass products with complex shapes, facilitated by advanced forming technologies for the green

bodies. The degree of porosity can be adjusted by controlling the progression of densification, and structures with varying porosity gradients can be achieved by combining sacrificial templates/particles with different characteristics. However, achieving high levels of porosity (>70 vol.%) and optimal pore interconnectivity is often challenging (283).

To achieve a higher level of porosity and create a structure more alike to natural bone with interconnected macropores, researchers have turned to utilizing polymeric foams as templates for producing biomedical scaffolds. The capacity to fabricate polymeric foams with precise 3D pore/strut architectures has been well established, allowing for structures with fully open porosity and void volumes exceeding 90%. The fundamental approach involves replicating the foam's structure by coating the struts and walls with a glass (or ceramic) slurry, followed by consolidation. Depending on whether a burning-out treatment is conducted, composite, glass, and glass-ceramic scaffolds can be produced (316).

Freeze-drying offers an alternative approach to utilizing organic templates for porosity generation, leveraging the formation of ice crystals to create the scaffold's porous structure. Initially, a suspension containing ceramic (or glass) particles undergoes rapid and directional freezing, leading to the formation of elongated ice crystals from the solvent(s). Following solvent removal, scaffold consolidation takes place. This method's versatility is significant and highly attractive, allowing for the production of porous scaffolds using polymers, ceramics, and glasses, manufactured through both melting and sol-gel techniques.

Additionally, there are alternative methods such as thermally induced phase separation (TIPS) and solvent-casting and particulate leaching, primarily employed for producing polymeric scaffolds. However, these techniques can also yield resorbable polymer/glass porous composites (282).

Additive Manufacturing (AM) methods represent a bottom-up approach wherein the scaffold is constructed layer by layer, providing the capability to fabricate intricate shapes and details unattainable through conventional technologies. These methods typically involve the integration of sacrificial particles or templates into the green body, which is subsequently subjected to sintering. The process begins with a CAD model or even a computed tomography (CT) scan of the intended object. This model is then sliced into layers along one of its axes, and the AM constructs the object by sequentially adding each layer according to a layer-wise strategy. Ideally, AM methods can process a wide range of materials, including metals, polymers, ceramics, glasses, and even biological matter for biofabrication purposes (317).

AM technologies concerning ceramic materials can be categorized into two groups: direct and indirect fabrication techniques. With direct AM methods, it is possible to produce a finished artifact without requiring additional post-processing. In direct AM, ceramic particles are melted (on the surface) and consolidated during the object's formation, achieved either through a laser beam in selective laser sintering (SLS) or via electron beam melting. If post-treatments like de-binding and sintering are necessary, the AM technologies are considered indirect methods. Examples of indirect methods include extrusion-based techniques like robocasting, stereolithography-based methods, or the fusion of bed powders (3D printing) (283).

Although AM methods offer superior control over scaffold geometry and pore/strut characteristics, along with scalability to industrial levels, challenges persist in producing highly porous scaffolds with porosity exceeding 70 vol.%, particularly bone-like structures with thin struts ranging from a few micrometers to tens of micrometers (318). Despite advancements, AM methods still encounter limitations, often resulting in scaffolds comprising large rods or struts/walls with

sizes exceeding 40-50 µm due to inherent resolution constraints, even with state-of-the-art equipment (317).

5.3.1 State of the art of the foam replica method

The foam replica method refers to replicating the porous structure of a sacrificial template to obtain its replicas from ceramic or glass particles, which are then sintered around the organic sacrificial template that is simultaneously burnt-off (302). This method was first applied in 2006 by Chen et al. and Park et al. (303,319) in the field of bone tissue engineering with a slurry containing bioactive glass particles, but the process concept was developed as early as the 1960s for other industrial applications, e.g. making filtering products (320). Briefly, the method generally consists of the steps of template immersion in the glass (ceramic) particle-containing slurry, drying, burning out of the foam, and sintering of the material, which, like the choice of template, can be tuned to achieve the desired structural properties of the final product (Fig. 58) (302).

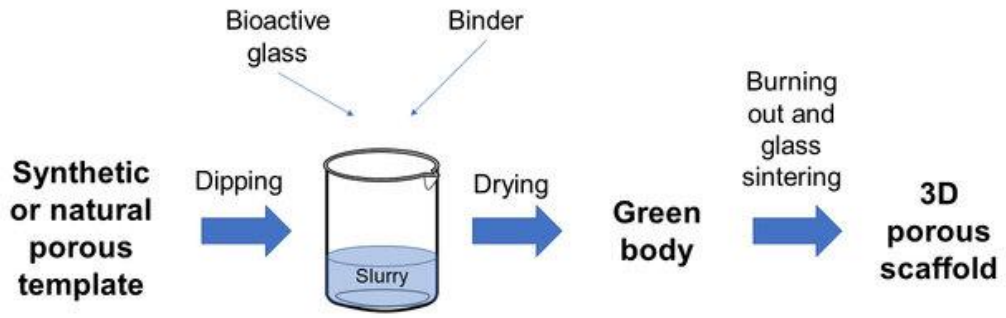

Figure 58: Schematic of the foam replica method (316)

The advantages of the foam replica method include its simplicity, affordability, and effectiveness in developing highly porous and interconnected three-dimensional scaffolds (302). For example, synthetic (e.g., polyurethane

(PU) sponge (303,319)) or natural templates (e.g., marine sponges (321), demineralized bone matrix (322)) with different pore sizes and distributions can be selected for the foam replica method, and there is also the possibility of using either melt-derived (303,319) or sol-gel glasses (323,324) as well as glass-ceramics (325,326) in the slurry, which also makes the method very versatile.

Silver (Ag) could be incorporated into bioceramic-based scaffolds to add antibacterial properties using various processes such as coating, doping, and mixing in different forms (327), for example, particles (328,329), and oxides (330–332). Silver was incorporated for the first time into a porous bioactive glass scaffold in 2006 by the sol-gel foaming method (333). Other examples of Ag-doped sol-gel glass-ceramic scaffolds by foam replica (PU sponge) are also reported in (332,334). However, the sol-gel foaming process is complex and time-consuming, and porous products obtained from it are typically weaker from a mechanical viewpoint. On the other hand, scaffolds prepared from melt-derived bioactive glass-ceramic powder have been Ag-doped by including AgNO3 in the slurry (335). Scaffolds prepared by the foam replica method can exhibit a multiscale porosity if they combine melt-derived and sol-gel mesoporous bioactive glasses (MBGs). For instance, Ag-doped MBG-coated 45S5 melt-derived scaffolds were fabricated by using a natural marine sponge as a template (336). Silver can also be added by a post-processing treatment: in this regard, 45S5 glass powder was used with PU foam to prepare scaffolds, which were then coated with Ag nanoparticles by immersing the scaffolds into the nanoparticle suspension (328).

To incorporate antibacterial silver only on the surface of the scaffold without affecting the material bulk properties, an ion exchange method has been implemented. In the process, the surface of the glass replaces its monovalent ions with the desired ions present in the ion exchange solution. For instance, the authors have prepared Ag-doping in an aqueous solution of AgNO3 for glass-

ceramic scaffolds based on different glass composition and ion-exchange process parameters (337) than the here-studied SBA2. In addition to using aqueous solution, Newby et al. have implemented a molten AgNO3 salt bath to coat 45S5 foam-replicated scaffold with Ag ions by ion exchange (338).

This work aimed to prepare 3D macroporous bioactive glass-ceramic foams, which were then characterized in terms of thermal, morphological, and mechanical properties. In addition, a possibility to dope the scaffold surface with antibacterial Ag ions via ion-exchange process in aqueous solution has been investigated. The effect of Ag-doping on the scaffold structure, composition and in vitro bioactivity has been assessed, followed by the analysis of Ag-leaching in Simulated Body Fluid (SBF). Finally, the antibacterial effect of Ag-doped scaffold was confirmed towards *Staphylococcus epidermidis*.

5.4 Materials and methods

5.4.1 Starting glass synthesis

A melt-derived silicate bioactive glass, referred to as SBA2 ($48SiO_2$-$18Na_2O$-$30CaO$-$3P_2O_5$-$0.43B_2O_3$-$0.57Al_2O_3$, in mol.%) was used as a starting material for scaffold fabrication. The SBA2 glass was synthesized by melting high-purity raw precursors (SiO_2, Na_2CO_3, $CaCO_3$, $Ca_3(PO_4)_2$, H_3BO_3, Al_2O_3, Sigma Aldrich) in a platinum crucible in the air at 1450 °C for one hour. The melt was then quenched into distilled water to obtain a frit, which was dried at room temperature and further ground by zirconia ball milling *(*Pulverisette 0, Fritsch, Germany). The obtained glass powder was sieved with a stainless-steel sieve (Giuliani Technologies Srl, Italy) to obtain particles with a grain size below 32 μm for scaffold fabrication.

5.4.2. Glass characterization by thermal analyses

The glass transition temperature (T_g) and the peak crystallization temperature (T_c) of the SBA2 glass were determined by differential thermal analysis (DTA; DTA404PC, Netzsch, Germany). The heating rate used was 5 C°/min. 50 mg of SBA2 powder was heated to 1300 °C in a platinum crucible using Al_2O_3 powder as a reference. T_g was determined at the inflection point of the DTA curve, as obtained from the first derivative of the thermal plot. T_c was determined at the maximum of the exothermic peak.

Hot stage microscopy (HSM; Hesse Instruments EM 301, Hesse Instruments, Germany) was performed to quantify the shrinkage due to sintering by measuring the variation of specimen size during a controlled heating process. HSM was performed in the air, and the heating rate used was 5 C°/min. The pellet of SBA2 was prepared by manually pressing SBA2 powder using a small cylindrical mold.

5.4.3 Scaffolds fabrication

The scaffolds were fabricated by following a modified version of the protocol described elsewhere (339). Shortly, a commercially available PU foam in the form of cubic blocks (10 x 10 x 10 mm^3) was used as the scaffold template. The cubes were immersed in a water-based slurry with a weight composition of 30% SBA2 glass, 64% distilled water, and 6% of poly(vinyl alcohol) (PVA) as a binder. Briefly, the PVA granules were dissolved in water under continuous stirring at 80 °C. The water evaporated during PVA dissolution was added back to the slurry to achieve the desired weight composition. Then the SBA2 powder was dispersed in the solution and stirred until a homogeneous mixture was obtained. The PU foam cubes were immersed into the slurry for 60 seconds, extracted, and compressed along the three spatial directions to 60% of thickness to uniformly remove the excess slurry. The impregnation/compression cycle was repeated three times, and finally, the fourth cycle was repeated without compression. The cubes were dried

at room temperature for 6 hours and thermally treated to remove the organic template and sinter the inorganic phase. The SBA2-derived scaffolds were sintered for 3 h at 620 °C to obtain an amorphous material (SBA-620), or at 850 °C for producing a glass-ceramic (SBA2-850).

5.4.4 Ion exchange

The Ag-doping by ion exchange was performed only for the scaffolds sintered at 850 °C (SBA2-850), being the most promising according to the results from mechanical tests. The ion exchange was performed by following the original protocol optimized for bulk glass discs (340). Briefly, the porous SBA-derived cubes were immersed in an aqueous solution of 0.03 M $AgNO_3$ (Sigma Aldrich) and soaked at 37 °C for 1 hour. Then, the cubes were rinsed with bi-distilled water and left to dry in ambient conditions. The Ag-doped glass-derived scaffolds will be referred to as Ag-SBA2 from now on.

5.4.5 Scaffold characterization

Scaffold morphology, porosity, and crystalline structure

The morphology and architecture of the scaffolds were studied using both Scanning Electron Microscopy, (SEM, JCM-6000Plus, JEOL) and Field Emission Scanning Electron Microscopy, (FESEM, Merlin electron microscope, ZEISS, Germany). A thin layer of platinum was used as a coating on scaffolds to make them conductive prior to the analysis. FESEM equipped with Energy-dispersive X-ray Spectroscopy Energy Dispersive X-ray spectrometry (EDS) was utilized for morphological and elemental analyses.

The total porosity of scaffold was estimated by density measurements. The density of the scaffolds was determined from the mass and volume of the sintered

cubes. Then, the volumetric porosity (vol.%) of the scaffolds was calculated by applying the following formula:

$$1 - \frac{\rho s}{\rho o}\, x\, 100\%$$

where ρs is the density of sintered scaffold, and ρo is the typical density of solid (non-porous) bioactive glass (2.7 g/cm^3) (341).

X-ray diffraction (XRD, Malvern PANalytical X'Pert PRO diffractometer), using the Bragg-Brentano camera geometry and the Cu Kα incident radiation, was performed on both types of scaffolds (SBA2-620 and SBA2-850) to study their crystalline structure and phase composition. The 2θ range used for sample measurements was from 10° to 70°. The data from the obtained spectra were further analyzed by using the X-Pert HighScore Software and PCPDF database.

Mechanical properties

To evaluate the mechanical strength of the scaffolds, a crushing test (MTS Criterion Model 43, cross-head speed = 0.5 mm/min) was performed to obtain the stress-strain curves and maximum compressive strength. Samples with parallel surfaces were used for the test. The compressive strength was calculated as the ratio between the maximal load registered during the test and the cross-sectional resistant area.

A mechanical crushing test was also performed for Ag-doped scaffolds to compare the mechanical properties of undoped and Ag-doped scaffolds.

In vitro bioactivity and ion leaching test

The *in vitro* bioactivity of scaffolds was evaluated by immersing the samples in Simulated Body Fluid (SBF) according to the protocol developed by Kokubo and Takadama (235). The mass-to-volume ratio between the scaffolds and SBF

was 1.5 mg/mL, according to the recommendation of the TC04 glass Committee (342). The SBF-immersed cubes were kept in an orbital shaker (37 °C, 120 RPM) for 1 day, 3 days, 7 days, 14 days, and 28 days. The pH of the solutions was monitored at every timepoint.

To characterize the bioactivity and following hydroxyapatite nucleation, the SBF-soaked cubes were then analyzed by FESEM-EDS. Prior to the FESEM-EDS analysis, the scaffolds were coated with a thin layer of chromium. In addition, Fourier-transform infrared spectroscopy with an attenuated total reflectance (ATR) equipment (FTIR-ATR, Nicolet, iS50 FTIR Spectrometers, Thermo Scientific), using software OMNIC, was utilized to identify the formation of reaction phases during the immersion of the scaffolds in SBF. The FTIR measurement was performed on the powder carefully removed from the surface of the SBF-immersed scaffolds in the frequency range of 400-4000 cm^{-1}, accumulating 16 scans with a resolution of 4 cm^{-1}.

In addition, Ag leaching was quantified from the SBF solution by Inductively coupled plasma mass spectrometry (ICP-MS; iCAP Q ICP-MS, Thermo Fischer Scientific).

Antibacterial properties

The antibacterial evaluation was performed by an inhibition halo test (Kirby-Bauer test) according to the NCCLS standard (343), using a standard strain of *Staphylococcus aureus* (ATCC 29213). The reason for choosing *S. aureus* is its common involvement in bone infections (344). Briefly, a 0.5 McFarland solution, which contains approximately 1 x 10^8 colony forming units (CFU)/ mL, was prepared by dissolving some *S. aureus* colonies, grown on a blood agar plate, in physiological solution; the turbidity of the solution was determined with an optical instrument—Phoenix Spec BD McFarland (Becton, Dickinson and

Company, Franklin Lakes, NJ, USA). This bacterial suspension was evenly distributed on a Mueller Hinton agar plate (Becton, Dickinson and Company, Franklin Lakes, NJ, USA), and the scaffolds were placed in contact with the agar and incubated overnight at 37 °C. At the end of incubation, the inhibition zone was observed and measured.

Statistical analysis

Results of porosity calculation, mechanical tests, antibacterial experiments were expressed as mean ± standard deviation. Statistical differences between the groups were analysed by Student's t-test ($p < 0.05$) and properly indicated, if relevant.

5.5 Results and discussion

In order to decide the sintering temperatures for scaffolds, DTA and HSM analyses were performed on the cylindrical pellets compacted from the SBA2 glass powder. Combined DTA and HSM graphs are shown in Figure 59.

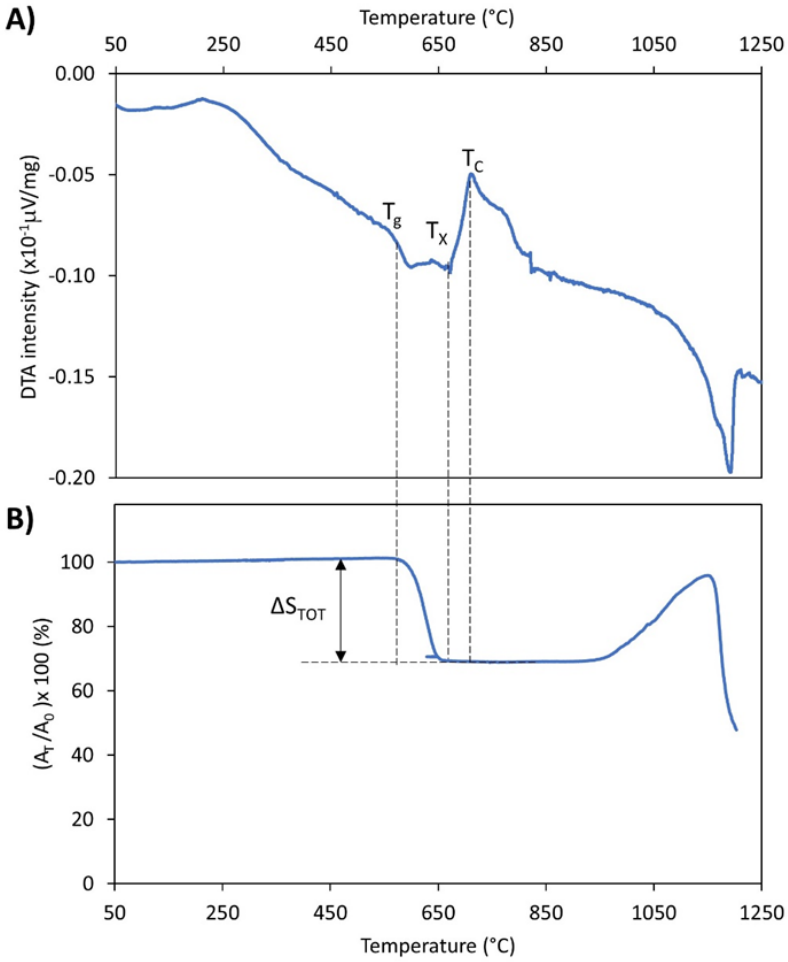

Figure 59: Thermal analyses on SBA2: A) DTA plot with Tg = glass transition temperature, Tx = onset crystallization temperature, and Tc = peak crystallization temperature; and B) HSM plot, shrinkage variation as a function of temperature, ΔS_{TOT}= maximum shrinkage

As shown in Figure 59, the glass transition temperature was detected around 570 °C.

The HSM curve (Figure 59) reveals that SBA2 exhibits a one-step densification behavior (ΔSTOT around 30%). The glass starts to shrink around the glass transition temperature detected by the DTA analysis. This is also the very beginning of viscous flow sintering. The pellet continues to shrink and reaches the

maximum shrinkage at Tx (around 670 °C). If the temperature keeps increasing, glass expansion is detected, which is seen as increasing AT /A0. Around the melting onset at 1150 °C the glass is seen shrinking rapidly again in the HSM curve. Similar expansion is seen in other papers dealing with bioactive glasses (345) or non-biomedical glass compositions (346).

From the viewpoint of glass stability against crystallization, the difference between Tx and Tg (TX –Tg = 670 – 570 = 100 °C) can be examined. In general, the greater this difference, the lower the tendency for the glass to crystallize upon heating.

Another way to assess the glass stability relies on assessing the Hruby parameter K_H (347):

$$K_H = \frac{T_X - T_g}{T_M - T_x}$$

As a rule of thumb, the greater the K_H, also the greater the glass stability against crystallization upon heating. In the case of SBA2 glass, we found K_H = 0.192, which is higher – for example – than the Hruby parameter assessed for 45S5 glass, in which sintering and crystallization are competing phenomena (345).

Sinterability can also be quantified by using the parameter $S_C = T_X - T_{MS}$, where T_{MS} is the temperature at maximum shrinkage detected by HSM measurement (346). In our case S_C = 670 – 650 = 20 °C > 0, which would suggest full sintering before crystallization (346); in other words, we could theoretically obtain a totally amorphous product after sintering. On the other hand, achieving adequate densification – and hence satisfactory mechanical properties – may require long time if sintering is performed below Tx.

Therefore, based on the thermal analyses, the glass SBA2 seems to exhibit a high sinterability and is suitable for being used for scaffold fabrication. However, because the DTA and HSM analyses were performed on the cylindrical pellets compacted from the glass powder instead of the scaffold cubes with polymeric PU foam inside, these results are only a starting point to find optimal sintering temperature.

Based on thermal analyses, two different sintering temperatures, T_{s1} and T_{s2}, were chosen for further characterization:

1) $T_{s1} = T_g + 50$ °C, to obtain an amorphous glass scaffold (sintering at 620 °C), and

2) T_{s2} well after the detected T_C peak, to obtain a glass-ceramic scaffold with full densification and expected higher mechanical strength (sintering at 850 °C).

Next, the morphology and architecture of sintered scaffolds were evaluated by SEM (Figure 60).

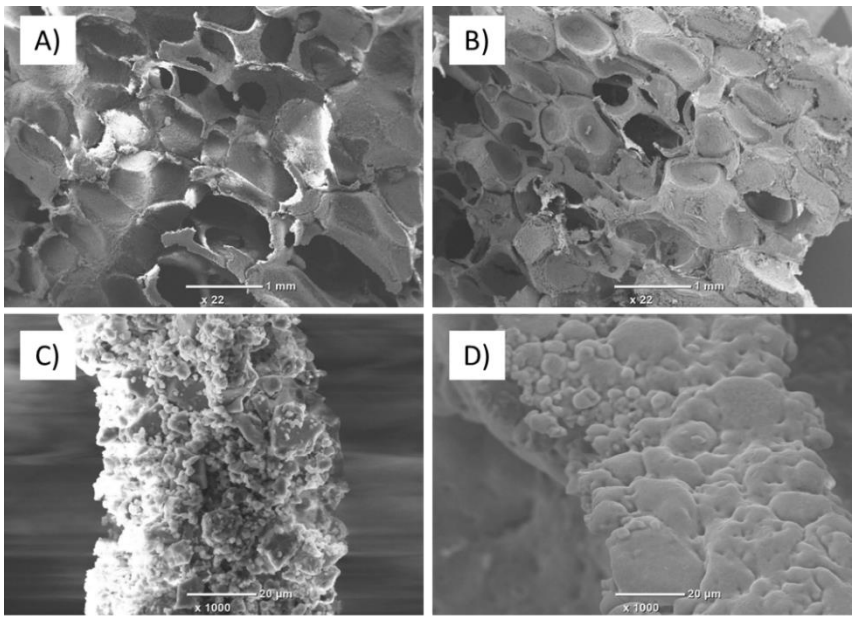

Figure 60: SBA2-derived scaffold architecture and morphology: A) SBA2-620 scaffold (magn. 22x); B) SBA2-850 scaffold (magn. X22); C) SBA2-620 scaffold (magn. X1000); D) SBA2-850 scaffold (magn. X1000).

As shown in Fig 60, for both scaffolds PU sponge architecture was faithfully replicated, successfully mimicking the structure of natural cancellous bone. Smoother and more densified struts as well as less distinguishable single glass particles were seen in the scaffold sintered at higher temperature (Fig. 63B and D, 850 °C).

Next, both scaffolds were characterized by XRD to evidence any formation of crystalline phases. (Figure 61)

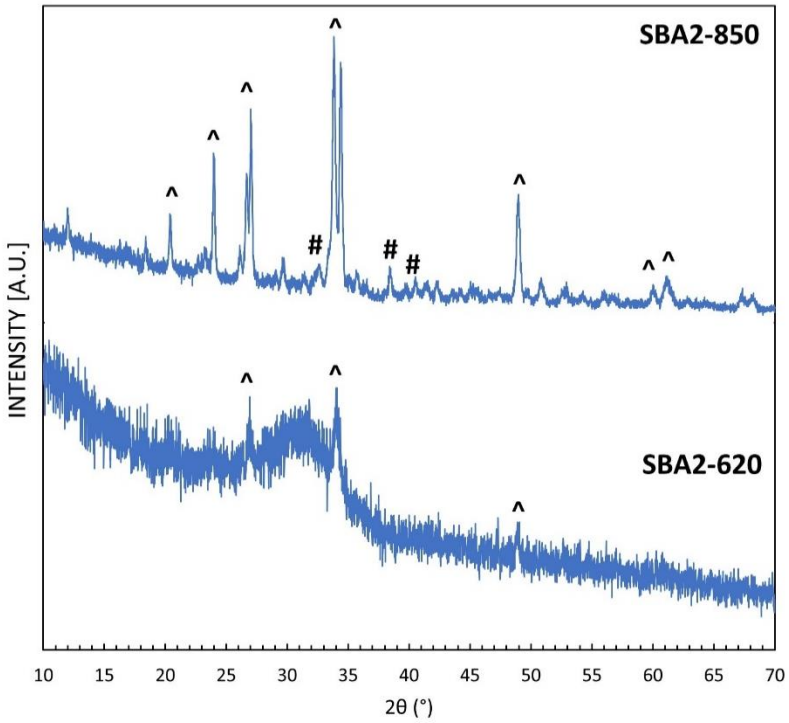

Figure 61: XRD patterns of SBA2 scaffolds sintered at 620 °C and 850 °C. ^ = combeite, # = silicorhenanite

The XRD pattern of SBA2 glass without any heat treatment is reported elsewhere (232). As regards SBA2-620 (Figure 61), a broad halo was detected along with some very minor diffraction peaks due to the initial nucleation of combeite ($Na_2Ca_2Si_3O_9$, ref 00-002-0961); however, the XRD pattern reveals a predominantly amorphous material.

The SBA2-850 scaffold was found glass-ceramic with many evident crystalline peaks. The two main phases identified were combeite ($Na_2Ca_2Si_3O_9$, ref 00-002-0961), and silicorhenanite ($Na_2Ca_4(PO_4)_2SiO_4$, ref 00-032-1053). Similar peaks have been reported by other authors regarding thermally treated

45S5 (319,348,349), thus suggesting the high bioactivity of SBA2-derived materials.

In general, the mechanical properties of a 3D scaffold can be determined by using stress-strain curves and the maximum compressive strength can be derived from these plots. Figure 62 displays some examples of the typical stress-strain curves of the scaffolds produced.

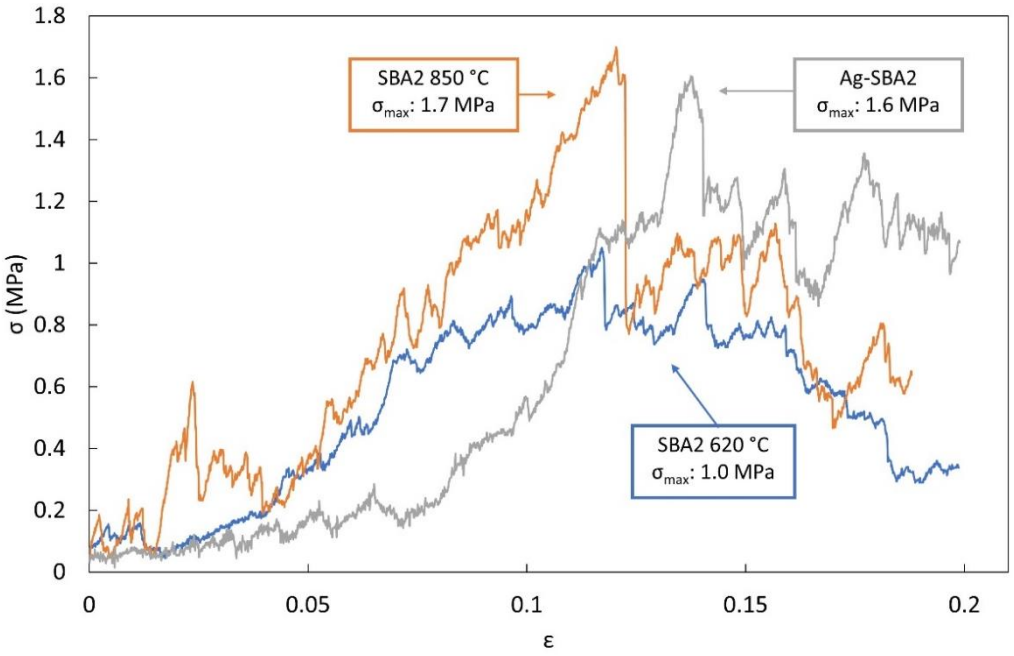

Figure 62: Examples of stress-strain curves of scaffolds sintered at 620 °C and 850 °C, and Ag-doped scaffold sintered at 850 °C.

For all scaffolds, multiple peaks ("jagging") are detected on the stress-strain curve. The reason for that is typical of brittle porous ceramics: when a load is applied to the scaffold, the thinnest struts crack at stress-concentrating sites which causes a temporary decline of the stress. On the other hand, the overall structure can still bear increasing loads, thus determining the new increase in stress values.

First, a positive slope is noted until the maximum temporary stress is reached. Then, thicker struts of the scaffold start to fracture, which leads to a negative slope. The repetition of this behaviour yields the irregular profile of the stress-strain curve.

Table 15 summarizes the porosity and compressive strength values of all scaffold types.

Table 13: Comparison of the scaffold features.

Scaffold	Total porosity (vol.%)	Peak stress (compressive strength) (MPa)
SBA2-620	74.6 ± 2.8	0.9 ± 0.2
SBA2-850	75.1 ± 1.4	1.5 ± 0.3
Ag-SBA2 (850 °C)	77.4 ± 4.9	1.4 ± 0.3

As reported in Table 15 and Figure 62, the glass-ceramic scaffold possesses superior compressive strength compared to the amorphous one. This phenomenon was expected as it is generally known that the crystalline phases embedded in the amorphous matrix can enhance the strength and fracture toughness of the glass (350). Indeed, also higher sintering temperature will lead to more densified and stronger struts of the scaffold, hence achieving greater compressive strength.

The compressive strength of glass-ceramic scaffold was found comparable to that of cancellous bone. The compressive strength of spongy bone (not the single strut) is around 0.2-4 MPa (319). Since the scaffolds are intended for use in contact with bone tissue, it is important to match the mechanical properties with the ones of hard tissue. A lower mechanical strength can lead to failure of the material and, on the other hand, a strength higher than that of the bone can lead to stress shielding phenomenon.

The compressive strength is directly related to the porosity level and the organization of the struts in the three-dimensional space. As seen in Table 1, SBA2-620 and SBA2-850 scaffolds have a high degree of porosity (~75 vol%) with no statistically significant difference. In general, highly interconnected porosity of a scaffold is essential to promote bone and vascular ingrowth (351). However, the strength and stiffness progressively decrease when the volume fraction of porosity increases and, therefore, it is important to balance porosity and mechanical integrity. Other factors affecting the mechanical properties include the composition of the initial glass and the slurry, and parameters of the foam replica method, such as the number of consecutive dipping cycles, and the duration of every single immersion. Indeed, also sintering temperature and the heating rate used play an important role in the process.

Due to the unsatisfactory mechanical properties of the amorphous scaffold, further experiments and characterization are performed only for the glass-ceramic scaffolds (i.e., SBA2-850). By using ion exchange in aqueous solution of silver nitrate the glass-ceramic scaffolds were doped with Ag-ions (Ag-SBA2) on their surface to add antibacterial properties.

The morphology and compositional analyses by EDS of Ag-doped scaffold are shown in Figure 63.

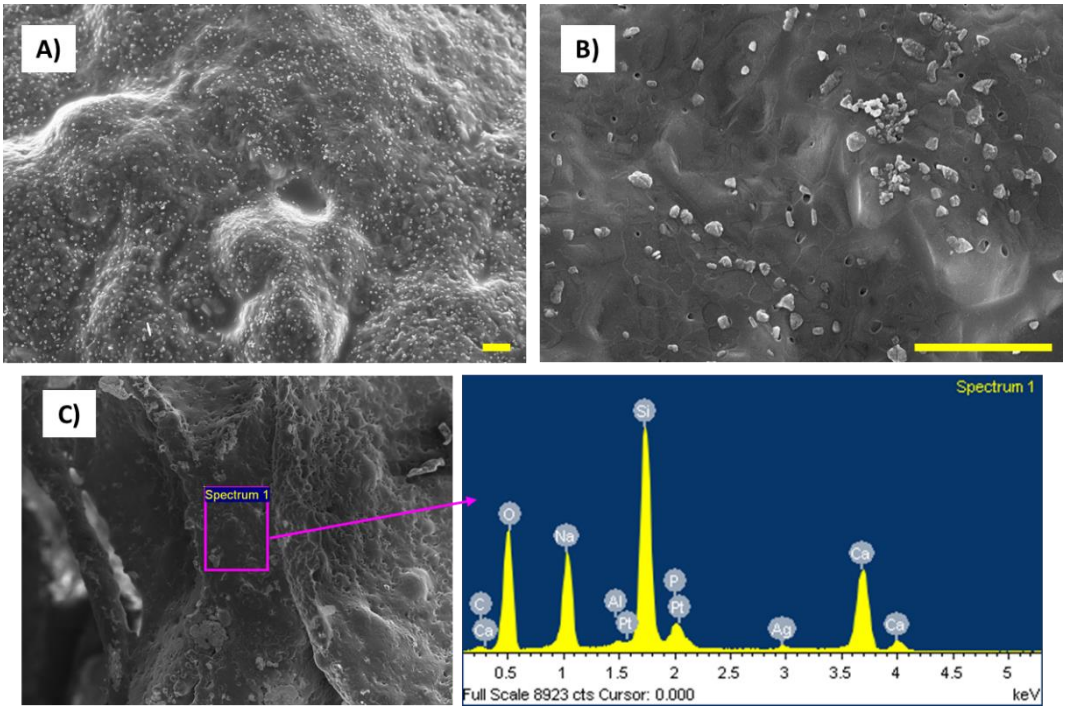

Figure 63: A) and B) FESEM of Ag-doped SBA2-850 scaffold, scale bars 1 µm. C) EDS analysis of the Ag-doped SBA2-850 scaffold surface.

Compositional analysis confirmed the presence of Ag on the scaffold surface, as revealed by EDS spectrum. Small particles with size around 100-200 nm – probably attributable to silver carbonate – were also observed on the walls of the struts by FESEM analysis. This finding is consistent with previous work with same glass after the ion-exchange process in silver nitrate (232). However, quantification is not possible due to the very small amount of silver (which is close to the detection limit for this technique) and the curvature of the surface analyzed.

Next, the mechanical crushing test was repeated for the Ag-doped SBA2-850 scaffolds to see whether the ion-doping on the scaffold surface affects its compressive strength (Figure 62). As displayed in Figure 62 and Table 15, no

statistically significant difference was found between undoped and Ag-doped scaffolds in terms of total porosity and maximum compressive strength. Therefore, the process of Ag-doping does not seem to affect the mechanical strength of the scaffolds.

The characterization of Ag-doped SBA2-850 scaffold was continued with analyzing its *in vitro* bioactivity by immersing the scaffold cubes in SBF up to 28 days. The results of the test (FESEM images, EDS analysis) are reported in Figure 64 and Table 16.

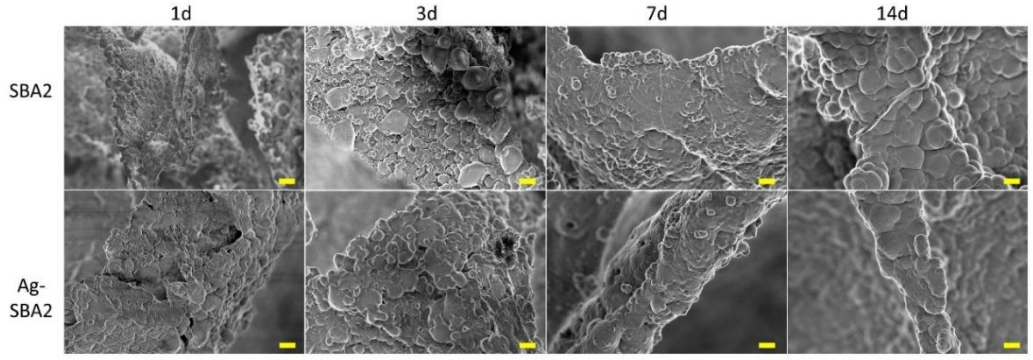

Figure 64: FESEM images of the morphology of SBF-soaked SBA2-850 scaffolds, undoped and doped with Ag, up to 14 days, scale bar 20 µm with 1000x magnification.

Table 14: Ca/P ratio of SBF-soaked SBA2-850 scaffolds derived from the EDS analysis.

	Time point (day)				
Ca/P ratio	*0d*	*1d*	*3d*	*7d*	*14d*
SBA2	5.68	1.89	1.89	2.32	1.58
Ag-SBA2	5.28	1.79	1.88	1.75	1.89

As shown in Figure 64, for both undoped and the Ag-doped SBA2-850 scaffold the typical globular "cauliflower" morphology of hydroxyapatite is visible already after 3 days of immersion in SBF. After 14 days, the struts of scaffolds are continuously coated by hydroxyapatite. The compositional analysis by EDS (Table 16) further confirms the fast bioactivity kinetics because the calculated Ca/P ratio suggests the surface to be coated with a hydroxyapatite-like layer. The Ca/P ratio of natural hydroxyapatite is known to be 1.67 (352), which is very close to the value registered here, already after one day of soaking in SBF.

In general, the glass-ceramic nature of the scaffold seems not to suppress the bioactivity mechanism. In previous works, amorphous SBA2 glass discs have been found to show some hydroxyapatite precipitation already after one day of soaking in SBF, and a clear layer of hydroxyapatite was observed after 3 days in SBF (353). In a porous scaffold, the reactive surface is larger as compared to bulk samples, which can indeed accelerate the bioactivity kinetics. This is seen also in our case with fast hydroxyapatite nucleation and a fast increase in the pH of the soaking solution during the immersion.

The bioactivity of the glass-ceramic scaffolds was further investigated by FTIR analysis. Figure 65 displays the FTIR-ATR spectra of both undoped and Ag-doped scaffolds prior (0d) and after (1-28d) SBF immersion.

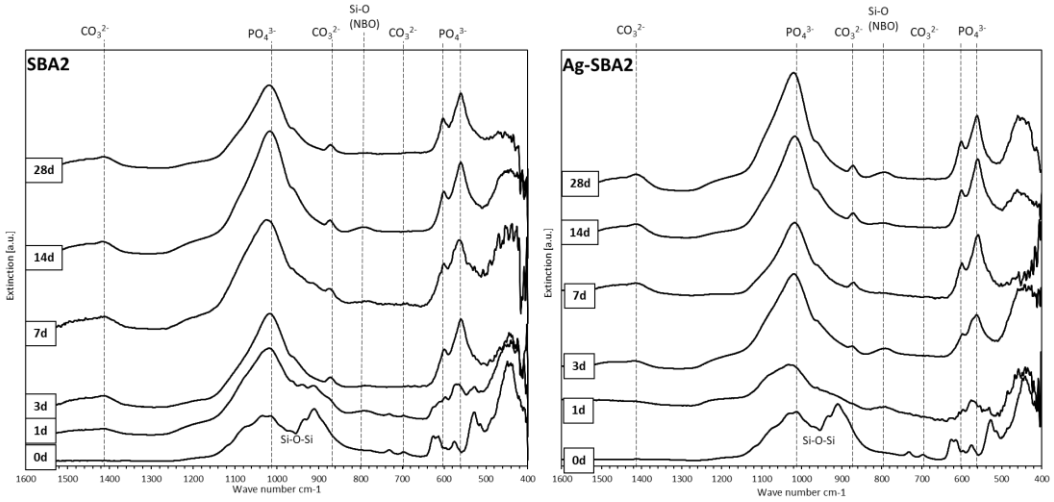

Figure 65: FTIR-ATR spectra of SBF-soaked SBA2-850 scaffolds up to 28 days. 0d is the control without SBF immersion. On the left: undoped SBA2-850, and on the right: Ag-doped SBA2-850 scaffold.

When comparing the FTIR spectra of 1-28d soaked scaffolds to the 0d unsoaked one, there are clear differences in terms of peak intensities. However, spectra of undoped and Ag-doped scaffolds exhibit similar characteristic bands without any significant differences regarding to their peak positions.

For the 0d control samples, the main band corresponds to the V_{asym} (Si-O-Si) intense broad band at 1020 cm^{-1}, with an overlapping to phosphate group as both PO and SiO groups absorb in this region.

For 1-day soaked scaffolds, a band around 560-610 cm^{-1} can be detected, which is characteristic for amorphous calcium phosphate formation (354,355). In addition, the presence of a broad band at ~1450 cm^{-1} corresponds to $\nu_3(CO_3^{2-})$ band of carbonates adsorbed on the surface (355,356), which suggests B-type substitution, e.g., a carbonate replacing a phosphate group (357). This peak also gets more evident after 3 days of soaking in SBF.

A sharpened phosphate band at ~1015 cm^{-1} (357) is already visible in scaffolds immersed for 1 day. The peak intensity increases, and the peak sharpens starting from 3 days of SBF immersion.

From 3 days of SBF soaking, at ~570 and ~600 cm^{-1} a sharp double band is detected. This indicates the presence of V_4(P-O-P), the bending mode of P-O-P bond in hydroxyapatite, or possibly other calcium orthophosphates, including octacalcium phosphate (355,357). This is in line with our observations from FESEM and EDS (Figure 7A and B), where hydroxyapatite can be detected after 3 days of immersion for both SBA2 and Ag-SBA2 scaffolds.

Another characteristic band seen after 3 days of soaking is $V_2(CO_3^2)$ sharp peak at ~871 cm^{-1}, for CO_3^{2-} group, which indicates carbonate substitution in the apatite, resulting in hydroxycarbonate apatite (357,358).

In addition to studying the bioactivity kinetics of the glass-ceramic scaffold, the leaching of Ag during SBF soaking was also evaluated with ICP-MS (Figure 66).

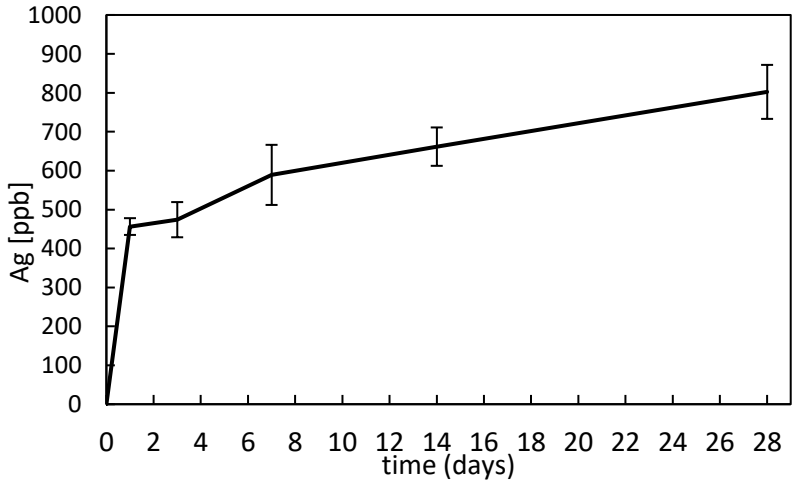

Figure 66: Ag leaching from Ag-doped SBA2-850 scaffolds soaked in SBF.

As it can be observed in Figure 66, more than half of the total of Ag , around 450 ppb, was released during the first 24 hours. Similar release profiles of rapid initial release of Ag-ions from bioactive glass scaffolds have also been observed in the literature (359). In general, this type of fast initial release of antibacterial agents is the most beneficial to prevent early infection after surgical treatment. However, Ag- release continues up to 28 days without any noticeable plateau suggesting that some amount of silver remains on the surface of the scaffold. Even though the first couple of days are the most critical for the development of post-surgical infections, it would also be useful to have prolonged release to maintain antibacterial effect in case of late infections (360).

Finally, an assessment of the antibacterial performance of the Ag-doped SBA2-850 scaffold was performed by zone of inhibition test.

Scaffold	Halo size
SBA2	0.0 ± 0.0 mm
Ag-SBA2	4.3 ± 0.4 mm

Figure 67: Antibacterial zone of inhibition against *S. epidermidis.*

As shown in Figure 67, the inhibition zone test towards *S. epidermidis* strain demonstrated the antibacterial effect of Ag-doped SBA2 scaffold. A clear

inhibition zone around Ag-SBA2, about 4-5 mm, is detected compared to the control undoped scaffold. Ag-SBA2 as bulk discs has been previously shown to be antibacterial reducing its surface colonization from drug-resistant strain of *Staphylococcus aureus* (173). In addition, the antibacterial Ag-SBA2 discs are cytocompatible with both bone progenitor cells (173), and human adipose stem cells (277). However, in order to verify and further characterize the antibacterial properties of porous 3D Ag-SBA2 instead of bulk discs, more antibacterial tests (bacteria proliferation metabolic assay, CFU count) are planned for the future. Also, it is critical to balance between antibacterial capability and biocompatibility and, therefore, also cytocompatibility tests are needed in the future.

5.6 Conclusions

In this work, a porous SBA2 bioactive glass-based scaffold using the foam replica method was successfully prepared and characterized. Two different sintering temperatures were compared: one resulting in an amorphous scaffold (620 °C), and another one yielding a glass-ceramic one (850 °C). Both scaffolds closely resembled the 3D architecture of natural trabecular bone and exhibited high porosity of approximately 75 vol.%. However, due to its superior mechanical properties, only the glass-ceramic scaffold was the focus of further analysis.

The selected glass-ceramic scaffold SBA2-850 was then subjected to silver doping via ion exchange in aqueous solution, which did not alter either the 3D architecture or the mechanical strength of the glass-ceramic sample. Silver was found to be successfully introduced, covering the scaffold surface. When comparing the *in vitro* bioactivity of both Ag-doped and undoped SBA2-850 scaffold, no significant difference was observed. Both scaffolds were highly bioactive, promoting the precipitation of hydroxyapatite after just three days of soaking in SBF, as confirmed by FESEM, EDS and FTIR analysis. Furthermore, the antibacterial performance of the Ag-SBA2 towards *S. epidermidis* was

successfully demonstrated, and the Ag leaching behavior in SBF was found to be optimal for preventing both early and late infections after surgery.

Although the compressive strength of the obtained scaffold (around 1.5 MPa) was satisfactory and comparable to that of natural bone, alternative fabrication techniques, such as additive manufacturing, may yield even stronger scaffolds with higher mechanical performance and reproducibility. The foam replication was adopted in this study to initially validate the feasibility of the here proposed concepts, i.e. the study of a bone-like, bioactive and antibacterial multifunctional scaffold. Looking at the future, the scaffold developed in this study could find a possible application as a bone substitution material with antibacterial properties without using traditional antibiotics. This would be a significant achievement considering the societal and medical challenges related to the abuse of antibiotics and bacterial resistance issues. However, further research deserves to be carried out to evaluate the biocompatibility of the scaffold for potential clinical applications.

Chapter 6: Conclusion and future perspectives

This thesis study explored the physicochemical surface characterization and optimization of PREMUROSA project reference materials with the general goal of crafting multifunctional materials capable of promoting both osseointegration and antibacterial activity for musculoskeletal regeneration. The materials under investigation included metallic and ceramic varieties, such as bioactive glasses and bioactive glass-ceramics deployed either in bulk form or as 3D scaffolds, along with titanium alloy discs subjected to polishing or chemical treatment. Following the physicochemical assessment, biological characterization was undertaken to determine the response of cells and bacteria to these developed materials.

The first part of the thesis work focused on surface functionalization utilizing the FDA-approved antimicrobial peptide, nisin, on Ti6Al4V-ELI titanium alloy discs, either polished or chemically treated. Nisin, renowned for its broad antibacterial spectrum, was physically adsorbed onto material surfaces and characterized via various analytical techniques. Notably, functionalization conducted at pH 6 demonstrated heightened efficacy, positioning nisin to expose its hydrophobic tail outward—an essential prerequisite for antimicrobial efficacy. Evaluation under physiological and inflammatory conditions unveiled gradual nisin release, underscoring its potential to prevent biofilm formation and combat *S.aureus* colonization. Of particular interest was the chemically treated nisin-functionalized titanium, which exhibited a synergistic blend of anti-microfouling properties

alongside antibacterial action, hinting at a promising avenue for developing implant surfaces resilient to bacterial colonization without resorting to antibiotics.

The second part of the thesis work focused to the surfaces of bioactive glasses doped with antibacterial metal ions, namely silver (Ag) or copper (Cu), via an ion-exchange process. This thesis work optimized the ion exchange process for Cu-doped glass and subjected it to comprehensive characterization encompassing morphology, composition, *in vitro* bioactivity, and ion leaching under physiological and inflammatory pH conditions. Cu-ion doping was found to increase *in vitro* bioactivity kinetics and subsequent hydroxyapatite precipitation, with zeta potential titration confirming the surface chemical stability of the glass across both pH ranges. Antibacterial assessments against *S.aureus* underscored significant reductions in metabolic activity and colony-forming units, underscoring the potential of Cu-doped glass as a bioactive and antibacterial surface for orthopedic applications.

While offering antimicrobial properties through ion-doping, the challenge lies in maintaining cytocompatibility. Evaluation of Ag-doped SBA2 and Cu-doped SBA3 discs on human adipose stem cells (hASCs) revealed initial cytotoxicity, reduced through pre-treatment of glass discs or exposure to dissolution byproducts. Fibronectin adsorption further improved the cytocompatibility of Ag-SBA2, whereas ongoing optimization is requisite for Cu-SBA3. This research underscores the potential of Ag-SBA2 in early infection treatment while ensuring long-term cytocompatibility and bioactivity. To harness Cu-SBA3 for biomedical applications, further optimization of the ion-exchange process is warranted to ensure sustained cell viability upon contact with the glass surface.

Lastly, the third thesis topic addresses the challenge of fabricating highly porous, mechanically robust, and antibacterial bioactive glass-ceramic scaffolds for bone

substitution. Utilizing the foam replica method, scaffolds with interconnected macropores were crafted and sintered at varying temperatures. Scaffolds sintered at higher temperatures exhibited notable porosity and mechanical strength, prompting hydroxyapatite formation post-soaking in simulated body fluid (SBF), thus affirming *in vitro* bioactivity. To confer antibacterial efficacy, silver (Ag) ions were introduced via ion exchange, with subsequent compositional analysis confirming successful doping and sustained silver release in SBF. Antibacterial activity against *S. epidermidis* was confirmed, signaling the potential of Ag-doped bioactive glass-ceramic scaffolds in antibacterial bone substitution applications.

Despite the diversity of materials studied, this thesis endeavors to provide insights into the biological responses they incite, as illustrated in Table 15 summarizing the biological outcomes of various multifunctional materials.

Table 15: Summary of biological performance of the studied materials of the thesis

	Cytocompatibility	**Antibacterial activity**	**Immune response**
Ag-SBA2	Bone progenitor cells: +++ hASCs: ++ PBMCs: -	Antibacterial effect (*S.aureus, S.epidermidis)*	Toxic effect towards PBMCs (Appendix A)
Cu-SBA3	hASCs: - PBMCs: +++	Antibacterial effect (*S.aureus)*	Early evidence on fibrotic tissue formation prevention (Appendix A)
Ti64-ELI-MP NISIN	Research ongoing	Anti-microfouling, effect on biofilm maturation (*S.aureus*)	Research ongoing
Ti64-ELI-CT NISIN	Research ongoing	Anti-microfouling, moderate antibacterial effect (*S.aureus*)	Research ongoing

In recent years, there has been a noticeable shift in clinical demand toward multifunctional surfaces capable of eliciting targeted responses from various cell types, including osteoblasts, fibroblasts, and macrophages, as well as combating infectious agents like bacteria and viruses. This intricate interplay between biological stimuli and surface responses has emerged as the central focus of contemporary biomaterial research. However, as depicted in Table 15, achieving a balance between antibacterial efficacy and cytocompatibility remains a considerable challenge. Furthermore, the complexity of biological systems is underscored by the varying responses exhibited by different cell lines in terms of cytocompatibility and immune modulation. Looking ahead, these materials may serve as integral components within antibacterial systems, either in conjunction with antibiotics or through the exploration of synergistic combinations of different antimicrobial agents.

However, the importance of the dose effect of antibacterial agents within the delicate balance of medical applications cannot be overstated. Achieving an optimal concentration of these agents is crucial for their efficacy while ensuring minimal adverse effects on the surrounding biological environment. One approach to enhance the effectiveness of antibacterial agents involves establishing a covalent link to the surface, thereby providing a long-lasting effect. However, this strategy may not be suitable in scenarios where a controlled release of the antibacterial agent is necessary to exert its biological action, as is often the case with many antibacterial agents. Moreover, even if a chemical link is established, there remains uncertainty regarding the durability of the grafted molecule's stability or its effectiveness in the desired configuration. In such instances, alternative mechanisms such as physisorption, chemisorption, or ion exchange can be employed to achieve temporary grafting. These mechanisms offer flexibility in controlling the release rate of the antibacterial agent, allowing for the attainment

of an effective antibacterial concentration while maintaining a delicate balance with biocompatibility requirements.

The biomaterials investigated herein demonstrate promising potential for applications in regenerative medicine, owing to their ability to simultaneously exhibit antibacterial, antibiofilm, and regenerative properties. Nevertheless, to ensure their safe and effective use, it is imperative to comprehensively explore and understand the interactions and reactions between diverse cell lines and biomaterials within the dynamic biological milieu of the body. Additionally, various types of implants, such as scaffolds, grafts, and coatings, require adaptation to distinct anatomical sites, each presenting unique environmental challenges.

Despite their multiple advantages, novel and modified biomaterials often face hurdles in transitioning to the market due to the lack of comprehensive clinical trials, data, and post-operative follow-ups. Overcoming these obstacles demands concerted efforts and administrative coordination. Conducting *in vivo* animal studies and refining *in vitro* and *in silico* models to more accurately replicate physiological conditions represent vital intermediate steps before progressing to human trials, furnishing more robust data for subsequent stages of development.

Another challenge not to be underestimated is the phenomenon of bacterial resistance to antibacterial agents, such as antibiotics, and more recently even certain metal ions. Overexposure and misuse of antibacterial agents have historically led to the emergence of resistant bacterial strains, jeopardizing the efficacy of these vital treatments. This underscores the urgent need for a continuous evolution in the development of antibacterial drugs and biomaterials. As bacteria adapt and develop resistance mechanisms, there arises a critical imperative to innovate and refine existing strategies to stay ahead of the evolving microbial threat. This necessitates a proactive approach in designing antibacterial

interventions that can effectively combat resistance while minimizing adverse effects on patients and the environment.

While numerous challenges remain to be addressed, the findings presented in this thesis offer valuable insights into the diverse biological responses elicited by different biomaterial surfaces. Moreover, they serve as a promising foundation for future research endeavors aimed at advancing the development of multifunctional biomaterial surfaces for musculoskeletal applications.

References

1. Hook AL, Alexander MR, Winkler DA. Chapter 8 - Materiomics: A Toolkit for Developing New Biomaterials. In: Blitterswijk CAV, De Boer J, editors. Tissue Engineering (Second Edition) [Internet]. Oxford: Academic Press; 2014 [cited 2024 Mar 12]. p. 253–81. Available from: https://www.sciencedirect.com/science/article/pii/B9780124201453000080

2. Ratner BD. Surface Properties and Surface Characterization of Biomaterials. 2013;34–55.

3. Capuani S, Malgir G, Chua CYX, Grattoni A. Advanced strategies to thwart foreign body response to implantable devices. Bioeng Transl Med. 2022;7(3):e10300.

4. Gadelmawla ES, Koura MM, Maksoud TMA, Elewa IM, Soliman HH. Roughness parameters. J Mater Process Technol. 2002 Apr 10;123(1):133–45.

5. International Organization for Standardization (ISO). ISO 25178-2:2021. Geometrical product specifications (GPS) Surface texture: Areal. Part 2: Terms, definitions and surface texture parameters. 2021.

6. Wang Z, Cui X, Ma H, Kang Y, Deng Z. Effect of Surface Roughness on Ultrasonic Testing of Back-Surface Micro-Cracks. Appl Sci. 2018 Aug;8(8):1233.

7. Warchomicka F. 12 - Surface topographies on the micro and nanoscale of metal alloys for tissue regeneration. In: Guarino V, Iafisco M, Spriano S, editors. Nanostructured Biomaterials for Regenerative Medicine [Internet]. Woodhead Publishing; 2020 [cited 2024 Feb 20]. p. 315–36. (Woodhead Publishing Series in Biomaterials). Available from: https://www.sciencedirect.com/science/article/pii/B9780081025949000127

8. Wang H, Chu PK. Chapter 4 - Surface Characterization of Biomaterials. In: Bandyopadhyay A, Bose S, editors. Characterization of Biomaterials [Internet]. Oxford: Academic Press; 2013 [cited 2024 Feb 16]. p. 105–74. Available from: https://www.sciencedirect.com/science/article/pii/B9780124158009000048

9. Gross L, Schuler B, Pavliček N, Fatayer S, Majzik Z, Moll N, et al. Atomic Force Microscopy for Molecular Structure Elucidation. Angew Chem Int Ed. 2018;57(15):3888–908.

10. Yuan X, Kang Y, Zuo J, Xie Y, Ma L, Ren X, et al. Micro/nano hierarchical structured titanium treated by NH4OH/H2O2 for enhancing cell response. PLOS ONE. 2018 Mar 5;13(5):e0196366.

11. Narayanan R, Seshadri SK, Kwon TY, Kim KH. Calcium phosphate-based coatings on titanium and its alloys. J Biomed Mater Res B Appl Biomater. 2008;85B(1):279–99.

12. Boyan BD, Hummert TW, Dean DD, Schwartz Z. Role of material surfaces in regulating bone and cartilage cell response. Biomaterials. 1996 Jan 1;17(2):137–46.

13. Dee KC, Puleo DA, Bizios R. An Introduction to Tissue-Biomaterial Interactions. John Wiley & Sons; 2003. 251 p.

14. Thasneem YM, Sharma CP. *In Vitro* Characterization of Cell–Biomaterials Interactions. In: Bandyopadhyay A, Bose S, editors. Characterization of Biomaterials [Internet]. Oxford: Academic Press; 2013 [cited 2024 Feb 16]. p. 175–205. Available from: https://www.sciencedirect.com/science/article/pii/B978012415800900005X

15. Mark Saltzman W, Kyriakides TR. Chapter Twenty - Cell Interactions with Polymers. In: Lanza R, Langer R, Vacanti J, editors. Principles of Tissue Engineering (Third Edition) [Internet]. Burlington: Academic Press; 2007 [cited 2024 Feb 16]. p. 279–96. Available from: https://www.sciencedirect.com/science/article/pii/B978012370615750024X

16. Loesberg WA, te Riet J, van Delft FCMJM, Schön P, Figdor CG, Speller S, et al. The threshold at which substrate nanogroove dimensions may influence fibroblast alignment and adhesion. Biomaterials. 2007 Sep;28(27):3944–51.

17. Dalby MJ, Gadegaard N, Wilkinson CDW. The response of fibroblasts to hexagonal nanotopography fabricated by electron beam lithography. J Biomed Mater Res A. 2008 Mar 15;84(4):973–9.

18. Bettinger CJ, Zhang Z, Gerecht S, Borenstein JT, Langer R. Enhancement of In Vitro Capillary Tube Formation by Substrate Nanotopography. Adv Mater Deerfield Beach Fla. 2008;20(1):99–103.

19. Bollenl CML, Lambrechts P, Quirynen M. Comparison of surface roughness of oral hard materials to the threshold surface roughness for bacterial plaque retention: A review of the literature. Dent Mater. 1997 Jul 1;13(4):258–69.

20. Srivastava S. Understanding Bacteria. Springer Science & Business Media; 2003. 496 p.

21. Wu Y, Zitelli JP, TenHuisen KS, Yu X, Libera MR. Differential response of Staphylococci and osteoblasts to varying titanium surface roughness. Biomaterials. 2011 Feb 1;32(4):951–60.

22. Kargozar S, Kermani F, Mollazadeh Beidokhti S, Hamzehlou S, Verné E, Ferraris S, et al. Functionalization and Surface Modifications of Bioactive Glasses (BGs): Tailoring of the Biological Response Working on the Outermost Surface Layer. Materials. 2019 Jan;12(22):3696.

23. Ratner BD. 1.2.2 - The Nature of Matter and Materials. In: Wagner WR, Sakiyama-Elbert SE, Zhang G, Yaszemski MJ, editors. Biomaterials Science (Fourth Edition) [Internet]. Academic Press; 2020 [cited 2024 Feb 23]. p. 37–40. Available from: https://www.sciencedirect.com/science/article/pii/B9780128161371000040

24. Davies MC, Lynn RAP. A review: Secondary ion mass spectrometry (SIMS of polymeric biomaterials. Clin Mater. 1990 Jan 1;5(2):97–114.

25. Dumas P, Weldon MK, Chabal YJ, Williams GP. Molecules at surfaces and interfaces studied using vibrational spectroscopies and related techniques. Surf Rev Lett. 1999 Apr;06(02):225–55.

26. Schmidt DR, Waldeck H, Kao WJ. Protein Adsorption to Biomaterials. In: Puleo DA, Bizios R, editors. Biological Interactions on Materials Surfaces: Understanding and Controlling Protein, Cell, and Tissue Responses [Internet]. New York, NY: Springer US; 2009 [cited 2023 Nov 22]. p. 1–18. Available from: https://doi.org/10.1007/978-0-387-98161-1_1

27. Cao B, Peng Y, Liu X, Ding J. Effects of Functional Groups of Materials on Nonspecific Adhesion and Chondrogenic Induction of Mesenchymal Stem Cells on Free and Micropatterned Surfaces. ACS Appl Mater Interfaces. 2017 Jul 19;9(28):23574–85.

28. Kanduč M, Schneck E, Netz RR. Understanding the “Berg limit”: the 65° contact angle as the universal adhesion threshold of biomatter. Phys Chem Chem Phys. 2024 Jan 3;26(2):713–23.

29. Wei J, Igarashi T, Okumori N, Igarashi T, Maetani T, Liu B, et al. Influence of surface wettability on competitive protein adsorption and initial attachment of osteoblasts. Biomed Mater Bristol Engl. 2009 Aug;4(4):045002.

30. Xu LC, Siedlecki CA. Effects of surface wettability and contact time on protein adhesion to biomaterial surfaces. Biomaterials. 2007 Aug;28(22):3273–83.

31. Morán G, Méallet-Renault R, Morán G, Méallet-Renault R. Superhydrophobic Surfaces Toward Prevention of Biofilm- Associated Infections. In: Bacterial Pathogenesis and Antibacterial Control [Internet]. IntechOpen; 2017 [cited 2024 Jan 23]. Available from: https://www.intechopen.com/chapters/58291

32. Luxbacher T. The ZETA guide: Principles of the streaming potential technique. Anton Paar GmbH Graz Austria [Internet]. 2014 [cited 2023 Oct 31]; Available from: https://scholar.google.com/scholar?cluster=6353645538050137310&hl=en&oi=scholarr

33. Brash JL, Horbett TA. Proteins at Interfaces. In: Proteins at Interfaces II [Internet]. American Chemical Society; 1995 [cited 2023 Dec 19]. p. 1–23. (ACS Symposium Series; vol. 602). Available from: https://doi.org/10.1021/bk-1995-0602.ch001

34. Bernhard C, Roeters SJ, Franz J, Weidner T, Bonn M, Gonella G. Repelling and ordering: the influence of poly(ethylene glycol) on protein adsorption. Phys Chem Chem Phys PCCP. 2017 Oct 25;19(41):28182–8.

35. Wei Q, Becherer T, Angioletti-Uberti S, Dzubiella J, Wischke C, Neffe AT, et al. Protein interactions with polymer coatings and biomaterials. Angew Chem Int Ed Engl. 2014 Jul 28;53(31):8004–31.

36. Chen S, Zheng J, Li L, Jiang S. Strong resistance of phosphorylcholine self-assembled monolayers to protein adsorption: insights into nonfouling properties of zwitterionic materials. J Am Chem Soc. 2005 Oct 19;127(41):14473–8.

37. Wang K, Zhou C, Hong Y, Zhang X. A review of protein adsorption on bioceramics. Interface Focus. 2012 Mar 22;2(3):259–77.

38. Peng ZG, Hidajat K, Uddin MS. Adsorption of bovine serum albumin on nanosized magnetic particles. J Colloid Interface Sci. 2004 Mar 15;271(2):277–83.

39. van der Veen M, Norde W, Stuart MC. Electrostatic interactions in protein adsorption probed by comparing lysozyme and succinylated lysozyme. Colloids Surf B Biointerfaces. 2004 May 1;35(1):33–40.

40. Garland A, Shen L, Zhu X. Mobile precursor mediated protein adsorption on solid surfaces. Prog Surf Sci. 2012 Jan 1;87(1):1–22.

41. Rabe M, Verdes D, Seeger S. Understanding protein adsorption phenomena at solid surfaces. Adv Colloid Interface Sci. 2011 Feb 17;162(1):87–106.

42. Habimana O, Semião AJC, Casey E. The role of cell-surface interactions in bacterial initial adhesion and consequent biofilm formation on nanofiltration/reverse osmosis membranes. J Membr Sci. 2014 Mar 15;454:82–96.

43. Anselme K, Davidson P, Popa AM, Giazzon M, Liley M, Ploux L. The interaction of cells and bacteria with surfaces structured at the nanometre scale. Acta Biomater. 2010 Oct 1;6(10):3824–46.

44. Anselme K. Osteoblast adhesion on biomaterials. Biomaterials. 2000 Apr 1;21(7):667–81.

45. Rana D, Ramasamy K, Leena M, Pasricha R, Manivasagam G, Ramalingam M. Surface Functionalization of Biomaterials. In: Biology and Engineering of Stem Cell Niches [Internet]. Elsevier Inc.; 2017 [cited 2023 Nov 22]. p. 331–43. Available from: http://www.scopus.com/inward/record.url?scp=85040579647&partnerID=8YFLogxK

46. Hasan J, Crawford RJ, Ivanova EP. Antibacterial surfaces: the quest for a new generation of biomaterials. Trends Biotechnol. 2013 May 1;31(5):295–304.

47. Yamaguchi S, Spriano S, Cazzola M. 13 - Fast and effective osseointegration of dental, spinal, and orthopedic implants through tailored chemistry of inorganic surfaces. In: Guarino V, Iafisco M, Spriano S, editors. Nanostructured Biomaterials for Regenerative Medicine [Internet]. Woodhead Publishing; 2020 [cited 2020 Sep 23]. p. 337–77. (Woodhead Publishing Series in Biomaterials). Available from: http://www.sciencedirect.com/science/article/pii/B9780081025949000139

48. Sadowska JM, Genoud KJ, Kelly DJ, O'Brien FJ. Bone biomaterials for overcoming antimicrobial resistance: Advances in non-antibiotic antimicrobial approaches for regeneration of infected osseous tissue. Mater Today. 2021 Jun 1;46:136–54.

49. Ferraris S, Vernè E. Chapter 9:Surface Functionalization of Bioactive Glasses: Reactive Groups, Biomolecules and Drugs on Bioactive Surfaces for

Smart and Functional Biomaterials. In: Bioactive Glasses [Internet]. 2016 [cited 2020 Sep 22]. p. 221–35. Available from: https://pubs.rsc.org/en/content/chapter/bk9781782629764-00221/978-1-78262-976-4

50. Taye MB, Ningsih HS, Shih SJ. Exploring the advancements in surface-modified bioactive glass: enhancing antibacterial activity, promoting angiogenesis, and modulating bioactivity. J Nanoparticle Res. 2024 Feb 3;26(2):28.

51. Verné E, Vitale-Brovarone C, Bui E, Bianchi CL, Boccaccini AR. Surface functionalization of bioactive glasses. J Biomed Mater Res A. 2009;90A(4):981–92.

52. Verné E, Ferraris S, Vitale-Brovarone C, Spriano S, Bianchi CL, Naldoni A, et al. Alkaline phosphatase grafting on bioactive glasses and glass ceramics. Acta Biomater. 2010 Jan 1;6(1):229–40.

53. Ferraris S, Vitale-Brovarone C, Bretcanu O, Cassinelli C, Vernè E. Surface functionalization of 3D glass–ceramic porous scaffolds for enhanced mineralization in vitro. Appl Surf Sci. 2013 Apr 15;271:412–20.

54. Chen QZ, Rezwan K, Françon V, Armitage D, Nazhat SN, Jones FH, et al. Surface functionalization of Bioglass®-derived porous scaffolds. Acta Biomater. 2007 Jul 1;3(4):551–62.

55. Gruian C, Vanea E, Simon S, Simon V. FTIR and XPS studies of protein adsorption onto functionalized bioactive glass. Biochim Biophys Acta. 2012 Jul;1824(7):873–81.

56. El-Fiqi A, Lee JH, Lee EJ, Kim HW. Collagen hydrogels incorporated with surface-aminated mesoporous nanobioactive glass: Improvement of physicochemical stability and mechanical properties is effective for hard tissue engineering. Acta Biomater. 2013 Dec 1;9(12):9508–21.

57. Hum J, Boccaccini AR. Collagen as Coating Material for 45S5 Bioactive Glass-Based Scaffolds for Bone Tissue Engineering. Int J Mol Sci. 2018 Jun;19(6):1807.

58. Lopes JH, Fonseca EMB, Mazali IO, Magalhães A, Landers R, Bertran CA. Facile and innovative method for bioglass surface modification: Optimization studies. Mater Sci Eng C. 2017 Mar 1;72:86–97.

59. Cazzola M, Vernè E, Cochis A, Sorrentino R, Azzimonti B, Prenesti E, et al. Bioactive glasses functionalized with polyphenols: in vitro interactions with

healthy and cancerous osteoblast cells. J Mater Sci. 2017 Aug 1;52(15):9211–23.

60. Schuhladen K, Roether JA, Boccaccini AR. Bioactive glasses meet phytotherapeutics: The potential of natural herbal medicines to extend the functionality of bioactive glasses. Biomaterials. 2019 Oct 1;217:119288.

61. Kaur M, Singh K. Review on titanium and titanium based alloys as biomaterials for orthopaedic applications. Mater Sci Eng C. 2019 Sep 1;102:844–62.

62. Rack HJ, Qazi JI. Titanium alloys for biomedical applications. Mater Sci Eng C. 2006 Sep 1;26(8):1269–77.

63. W. Nicholson J. Titanium Alloys for Dental Implants: A Review. Prosthesis. 2020 Jun;2(2):100–16.

64. Souza JCM, Sordi MB, Kanazawa M, Ravindran S, Henriques B, Silva FS, et al. Nano-scale modification of titanium implant surfaces to enhance osseointegration. Acta Biomater. 2019 Aug 1;94:112–31.

65. Zhu C, Lv Y, Qian C, Qian H, Jiao T, Wang L, et al. Proliferation and osteogenic differentiation of rat BMSCs on a novel Ti/SiC metal matrix nanocomposite modified by friction stir processing. Sci Rep. 2016 Dec 13;6(1):38875.

66. Akshaya S, Rowlo PK, Dukle A, Nathanael AJ. Antibacterial Coatings for Titanium Implants: Recent Trends and Future Perspectives. Antibiotics. 2022 Nov 29;11(12):1719.

67. Xue T, Attarilar S, Liu S, Liu J, Song X, Li L, et al. Surface Modification Techniques of Titanium and its Alloys to Functionally Optimize Their Biomedical Properties: Thematic Review. Front Bioeng Biotechnol [Internet]. 2020 [cited 2024 Feb 22];8. Available from: https://www.frontiersin.org/articles/10.3389/fbioe.2020.603072

68. Liu YC, Lin GS, Lee YT, Huang TC, Chang TW, Chen YW, et al. Microstructures and cell reaction of porous hydroxyapatite coatings on titanium discs using a novel vapour-induced pore-forming atmospheric plasma spraying. Surf Coat Technol. 2020 Jul 15;393:125837.

69. Zhang M, Pu X, Chen X, Yin G. In-vivo performance of plasma-sprayed CaO-MgO-SiO2-based bioactive glass-ceramic coating on Ti-6Al-4V alloy for bone regeneration. Heliyon. 2019 Nov;5(11):e02824.

70. Maleki-Ghaleh H, Hafezi M, Hadipour M, Nadernezhad A, Aghaie E, Behnamian Y, et al. Effect of Tricalcium Magnesium Silicate Coating on the Electrochemical and Biological Behavior of Ti-6Al-4V Alloys. PLOS ONE. 2015 Sep 18;10(9):e0138454.

71. Miola M, Ferraris S, Di Nunzio S, Robotti PF, Bianchi G, Fucale G, et al. Surface silver-doping of biocompatible glasses to induce antibacterial properties. Part II: plasma sprayed glass-coatings. J Mater Sci Mater Med. 2009 Mar 1;20(3):741–9.

72. Chen CS, Chang JH, Srimaneepong V, Wen JY, Tung OH, Yang CH, et al. Improving the *in vitro* cell differentiation and *in vivo* osseointegration of titanium dental implant through oxygen plasma immersion ion implantation treatment. Surf Coat Technol. 2020 Oct 15;399:126125.

73. Lin Z, Li SJ, Sun F, Ba DC, Li XC. Surface characteristics of a dental implant modified by low energy oxygen ion implantation. Surf Coat Technol. 2019 May 15;365:208–13.

74. Yang P, Huang N, Leng Y, Wan G, Zhao A, Chen J, et al. Functional inorganic films fabricated by PIII(-D) for surface modification of blood contacting biomaterials: Fabrication parameters, characteristics and antithrombotic properties. Surf Coat Technol. 2007 Apr 23;201(15):6828–32.

75. Cao H, Cui T, Jin G, Liu X. Cellular responses to titanium successively treated by magnesium and silver PIII&D. Surf Coat Technol. 2014 Oct 15;256:9–14.

76. Hempel F, Finke B, Zietz C, Bader R, Weltmann KD, Polak M. Antimicrobial surface modification of titanium substrates by means of plasma immersion ion implantation and deposition of copper. Surf Coat Technol. 2014 Oct 15;256:52–8.

77. Yu L, Jin G, Ouyang L, Wang D, Qiao Y, Liu X. Antibacterial activity, osteogenic and angiogenic behaviors of copper-bearing titanium synthesized by PIII&D. J Mater Chem B. 2016 Feb 21;4(7):1296–309.

78. Hauschild G, Hardes J, Gosheger G, Stoeppeler S, Ahrens H, Blaske F, et al. Evaluation of osseous integration of PVD-silver-coated hip prostheses in a canine model. BioMed Res Int. 2015;2015:292406.

79. Sarraf M, Razak BA, Nasiri-Tabrizi B, Dabbagh A, Kasim NHA, Basirun WJ, et al. Nanomechanical properties, wear resistance and *in-vitro* characterization of Ta2O5 nanotubes coating on biomedical grade Ti–6Al–4V. J Mech Behav Biomed Mater. 2017 Feb 1;66:159–71.

80. He Y, Zhang Y, Shen X, Tao B, Liu J, Yuan Z, et al. The fabrication and in vitro properties of antibacterial polydopamine-LL-37-POPC coatings on micro-arc oxidized titanium. Colloids Surf B Biointerfaces. 2018 Oct 1;170:54–63.

81. Spriano S, Yamaguchi S, Baino F, Ferraris S. A critical review of multifunctional titanium surfaces: New frontiers for improving osseointegration and host response, avoiding bacteria contamination. Acta Biomater. 2018 Oct 1;79:1–22.

82. Coelho PG, Granjeiro JM, Romanos GE, Suzuki M, Silva NRF, Cardaropoli G, et al. Basic research methods and current trends of dental implant surfaces. J Biomed Mater Res B Appl Biomater. 2009;88B(2):579–96.

83. Buser D, Broggini N, Wieland M, Schenk RK, Denzer AJ, Cochran DL, et al. Enhanced Bone Apposition to a Chemically Modified SLA Titanium Surface. J Dent Res. 2004 Jul 1;83(7):529–33.

84. Vlacic-Zischke J, Hamlet SM, Friis T, Tonetti MS, Ivanovski S. The influence of surface microroughness and hydrophilicity of titanium on the up-regulation of TGFβ/BMP signalling in osteoblasts. Biomaterials. 2011 Jan 1;32(3):665–71.

85. Ferraris S, Venturello A, Miola M, Cochis A, Rimondini L, Spriano S. Antibacterial and bioactive nanostructured titanium surfaces for bone integration. Appl Surf Sci. 2014 Aug 30;311:279–91.

86. Kim HM, Miyaji F, Kokubo T, Nakamura T. Apatite-Forming Ability of Alkali-Treated Ti Metal in Body Environment. J Ceram Soc Jpn. 1997;105(1218):111–6.

87. Ho WF, Lai CH, Hsu HC, Wu SC. Surface modification of a Ti–7.5Mo alloy using NaOH treatment and Bioglass® coating. J Mater Sci Mater Med. 2010 May 1;21(5):1479–88.

88. Flores CY, Diaz C, Rubert A, Benítez GA, Moreno MS, Fernández Lorenzo de Mele MA, et al. Spontaneous adsorption of silver nanoparticles on Ti/TiO2 surfaces. Antibacterial effect on *Pseudomonas aeruginosa*. J Colloid Interface Sci. 2010 Oct 15;350(2):402–8.

89. Govindharajulu JP, Chen X, Li Y, Rodriguez-Cabello JC, Battacharya M, Aparicio C. Chitosan-Recombinamer Layer-by-Layer Coatings for Multifunctional Implants. Int J Mol Sci. 2017 Feb;18(2):369.

90. Ferraris S, Spriano S. Antibacterial titanium surfaces for medical implants. Mater Sci Eng C. 2016 Apr 1;61:965–78.

91. Ghilini F, Rodríguez González MC, Miñán AG, Pissinis D, Creus AH, Salvarezza RC, et al. Highly Stabilized Nanoparticles on Poly-l-Lysine-Coated Oxidized Metals: A Versatile Platform with Enhanced Antimicrobial Activity. ACS Appl Mater Interfaces. 2018 Jul 18;10(28):23657–66.

92. Cazzola M, Barberi J, Ferraris S, Cochis A, Cempura G, Czyrska-Filemonowicz A, et al. Bioactive Titanium Surfaces Enriched with Silver Nanoparticles Through an In Situ Reduction: Looking for a Balance Between Cytocompatibility and Antibacterial Activity. Adv Eng Mater. 2023;25(2).

93. Ferraris S, Spriano S, Miola M, Bertone E, Allizond V, Cuffini AM, et al. Surface modification of titanium surfaces through a modified oxide layer and embedded silver nanoparticles: Effect of reducing/stabilizing agents on precipitation and properties of the nanoparticles. Surf Coat Technol. 2018;344:177–89.

94. Duewelhenke N, Krut O, Eysel P. Influence on Mitochondria and Cytotoxicity of Different Antibiotics Administered in High Concentrations on Primary Human Osteoblasts and Cell Lines. Antimicrob Agents Chemother. 2007 Jan;51(1):54–63.

95. Rams TE, Degener JE, van Winkelhoff AJ. Antibiotic resistance in human peri-implantitis microbiota. Clin Oral Implants Res. 2014;25(1):82–90.

96. Rahmati M, Silva EA, Reseland JE, Heyward CA, Haugen HJ. Biological responses to physicochemical properties of biomaterial surface. Chem Soc Rev. 2020 Aug 3;49(15):5178–224.

97. National Institute of Biomedical Imaging and Bioengineering. National Institute of Biomedical Imaging and Bioengineering. 2017 [cited 2023 Dec 18]. Biomaterials. Available from: https://www.nibib.nih.gov/science-education/science-topics/biomaterials

98. Rajesh P s. m., Verma S, Verma V. Host Response of Implanted Biomaterials. In: Biosurfaces [Internet]. John Wiley & Sons, Ltd; 2014 [cited 2024 Jan 23]. p. 106–25. Available from: https://onlinelibrary.wiley.com/doi/abs/10.1002/9781118950623.ch3

99. Chandorkar Y, K R, Basu B. The Foreign Body Response Demystified. ACS Biomater Sci Eng. 2019 Jan 14;5(1):19–44.

100. Felgueiras HP, Antunes JC, Martins MCL, Barbosa MA. 1 - Fundamentals of protein and cell interactions in biomaterials. In: Barbosa MA, Martins MCL, editors. Peptides and Proteins as Biomaterials for Tissue Regeneration and Repair [Internet]. Woodhead Publishing; 2018 [cited 2023 Dec 19]. p. 1–27. Available from: https://www.sciencedirect.com/science/article/pii/B9780081008034000012

101. Chen Y, Sun W, Tang H, Li Y, Li C, Wang L, et al. Interactions Between Immunomodulatory Biomaterials and Immune Microenvironment: Cues for Immunomodulation Strategies in Tissue Repair. Front Bioeng Biotechnol [Internet]. 2022 [cited 2024 Jan 16];10. Available from: https://www.frontiersin.org/articles/10.3389/fbioe.2022.820940

102. Golias C, Charalabopoulos A, Stagikas D, Charalabopoulos K, Batistatou A. The kinin system--bradykinin: biological effects and clinical implications. Multiple role of the kinin system--bradykinin. Hippokratia. 2007 Jul;11(3):124–8.

103. Babensee JE. 2.2.2 - Inflammation, Wound Healing, the Foreign-Body Response, and Alternative Tissue Responses. In: Wagner WR, Sakiyama-Elbert SE, Zhang G, Yaszemski MJ, editors. Biomaterials Science (Fourth Edition) [Internet]. Academic Press; 2020 [cited 2024 Jan 17]. p. 737–46. Available from: https://www.sciencedirect.com/science/article/pii/B9780128161371000489

104. Sridharan R, Cameron AR, Kelly DJ, Kearney CJ, O'Brien FJ. Biomaterial based modulation of macrophage polarization: a review and suggested design principles. Mater Today. 2015 Jul 1;18(6):313–25.

105. Kyriakides TR, Foster MJ, Keeney GE, Tsai A, Giachelli CM, Clark-Lewis I, et al. The CC chemokine ligand, CCL2/MCP1, participates in macrophage fusion and foreign body giant cell formation. Am J Pathol. 2004 Dec;165(6):2157–66.

106. Anderson J. Biological responses to materials. Annu Rev Mater Res. 2001 Jan 1;31:81–110.

107. Grainger DW. All charged up about implanted biomaterials. Nat Biotechnol. 2013 Jun;31(6):507–9.

108. Londono R, Badylak SF. Chapter 1 - Factors Which Affect the Host Response to Biomaterials. In: Badylak SF, editor. Host Response to Biomaterials [Internet]. Oxford: Academic Press; 2015 [cited 2024 Jan 24]. p. 1–12. Available from: https://www.sciencedirect.com/science/article/pii/B9780128001967000013

109. Morais JM, Papadimitrakopoulos F, Burgess DJ. Biomaterials/Tissue Interactions: Possible Solutions to Overcome Foreign Body Response. AAPS J. 2010 Jun 1;12(2):188–96.

110. He Y, Hower J, Chen S, Bernards MT, Chang Y, Jiang S. Molecular Simulation Studies of Protein Interactions with Zwitterionic Phosphorylcholine Self-Assembled Monolayers in the Presence of Water. Langmuir. 2008 Sep 16;24(18):10358–64.

111. Avula MN, Grainger DW. Addressing Medical Device Challenges with Drug–Device Combinations. In: Drug-Device Combinations For Chronic Diseases [Internet]. John Wiley & Sons, Ltd; 2015 [cited 2024 Jan 17]. p. 1–38. Available from: https://onlinelibrary.wiley.com/doi/abs/10.1002/9781119002956.ch01

112. Barchowsky A. 2.2.5 - Systemic and Immune Toxicity of Implanted Materials. In: Wagner WR, Sakiyama-Elbert SE, Zhang G, Yaszemski MJ, editors. Biomaterials Science (Fourth Edition) [Internet]. Academic Press; 2020 [cited 2024 Jan 17]. p. 791–9. Available from: https://www.sciencedirect.com/science/article/pii/B9780128161371000519

113. Helmus MN, Gibbons DF, Cebon D. Biocompatibility: meeting a key functional requirement of next-generation medical devices. Toxicol Pathol. 2008 Jan;36(1):70–80.

114. Chen Q, Thouas GA. Metallic implant biomaterials. Mater Sci Eng R Rep. 2015 Jan 1;87:1–57.

115. Drummond J, Tran P, Fary C. Metal-on-Metal Hip Arthroplasty: A Review of Adverse Reactions and Patient Management. J Funct Biomater. 2015 Jun 26;6(3):486–99.

116. FDA United States Food and Drug Administration: Center for Device and Radiological Health. Biological Responses to Metal Implants. 2019.

117. Pajarinen J, Jämsen E, Konttinen YT, Goodman SB. Innate Immune Reactions in Septic and Aseptic Osteolysis Around Hip Implants. J Long Term Eff Med Implants. 2014;24(4):283–96.

118. Terkawi MA, Matsumae G, Shimizu T, Takahashi D, Kadoya K, Iwasaki N. Interplay between Inflammation and Pathological Bone Resorption: Insights into Recent Mechanisms and Pathways in Related Diseases for Future Perspectives. Int J Mol Sci [Internet]. 2022 Feb [cited 2024 Jan 24];23(3). Available from: https://www.ncbi.nlm.nih.gov/pmc/articles/PMC8836472/

119. Francolini I, Hall-Stoodley L, Stoodley P. 2.2.8 - Biofilms, Biomaterials, and Device-Related Infections. In: Wagner WR, Sakiyama-Elbert SE, Zhang G, Yaszemski MJ, editors. Biomaterials Science (Fourth Edition) [Internet]. Academic Press; 2020 [cited 2024 Jan 17]. p. 823–40. Available from: https://www.sciencedirect.com/science/article/pii/B9780128161371000544

120. Hall-Stoodley L, Stoodley P. Evolving concepts in biofilm infections. Cell Microbiol. 2009;11(7):1034–43.

121. Flemming HC, Wingender J. The biofilm matrix. Nat Rev Microbiol. 2010 Sep;8(9):623–33.

122. Fux CA, Wilson S, Stoodley P. Detachment characteristics and oxacillin resistance of Staphyloccocus aureus biofilm emboli in an in vitro catheter infection model. J Bacteriol. 2004 Jul;186(14):4486–91.

123. Anderl JN, Franklin MJ, Stewart PS. Role of Antibiotic Penetration Limitation in Klebsiella pneumoniae Biofilm Resistance to Ampicillin and Ciprofloxacin. Antimicrob Agents Chemother. 2000 Jul;44(7):1818–24.

124. Lewis K. Persister cells and the riddle of biofilm survival. Biochem Biokhimiia. 2005 Feb;70(2):267–74.

125. Davis-Fields M, Bakhtiari LA, Lan Z, Kovach KN, Wang L, Cosgriff-Hernandez EM, et al. Assaying How Phagocytic Success Depends on the Elasticity of a Large Target Structure. Biophys J. 2019 Oct 15;117(8):1496–507.

126. Le KY, Park MD, Otto M. Immune Evasion Mechanisms of Staphylococcus epidermidis Biofilm Infection. Front Microbiol. 2018;9:359.

127. Hofstee MI, Muthukrishnan G, Atkins GJ, Riool M, Thompson K, Morgenstern M, et al. Current Concepts of Osteomyelitis: From Pathologic Mechanisms to Advanced Research Methods. Am J Pathol. 2020 Jun 1;190(6):1151–63.

128. Epstein G, Ferreira N. Dead space management strategies in the treatment of chronic osteomyelitis: a retrospective review. Eur J Orthop Surg Traumatol. 2022 Sep 16;33.

129. Jones JR. Review of bioactive glass: From Hench to hybrids. Acta Biomater. 2013 tammikuu;9(1):4457–86.

130. Hench LL, Paschall HA. Direct chemical bond of bioactive glass-ceramic materials to bone and muscle. J Biomed Mater Res. 1973;7(3):25–42.

131. Hench LL, Polak JM. Third-generation biomedical materials. Science. 2002;295(5557):1014+1016-1017.

132. Sanders DM, Hench LL. Mechanisms of Glass Corrosion. J Am Ceram Soc. 1973;56(7):373–7.

133. Stanić V. Variation in Properties of Bioactive Glasses After Surface Modification. In: Kaur G, editor. Clinical Applications of Biomaterials: State-of-the-Art Progress, Trends, and Novel Approaches [Internet]. Cham: Springer International Publishing; 2017 [cited 2024 Jan 22]. p. 35–63. Available from: https://doi.org/10.1007/978-3-319-56059-5_2

134. Lallukka M. Bioactive Glass/Gelatin Hybrid Biomaterials for Bone Tissue Engineering. 2020 [cited 2024 Jan 22]; Available from: https://trepo.tuni.fi/handle/10024/119719

135. Lee KJ, Goodman SB. Identification of periprosthetic joint infection after total hip arthroplasty. J Orthop Transl. 2015 Jan 1;3(1):21–5.

136. World Health Organization. Antimicrobial resistance: global report on surveillance [Internet]. World Health Organization; 2014 [cited 2022 Jan 23]. xxii, 232 p. Available from: https://apps.who.int/iris/handle/10665/112642

137. Moretta A, Scieuzo C, Petrone AM, Salvia R, Manniello MD, Franco A, et al. Antimicrobial Peptides: A New Hope in Biomedical and Pharmaceutical Fields. Front Cell Infect Microbiol [Internet]. 2021 [cited 2023 Nov 22];11. Available from: https://www.frontiersin.org/articles/10.3389/fcimb.2021.668632

138. Huan Y, Kong Q, Mou H, Yi H. Antimicrobial Peptides: Classification, Design, Application and Research Progress in Multiple Fields. Front Microbiol [Internet]. 2020 [cited 2023 Nov 22];11. Available from: https://www.frontiersin.org/articles/10.3389/fmicb.2020.582779

139. Dept of Pathology & Microbiology UNMC. APD3 Antimicrobial Peptide Database [Internet]. 2023. Available from: https://aps.unmc.edu/

140. Pasupuleti M, Schmidtchen A, Malmsten M. Antimicrobial peptides: key components of the innate immune system. Crit Rev Biotechnol. 2012 Jun 1;32(2):143–71.

141. Boparai JK, Sharma PK. Mini Review on Antimicrobial Peptides, Sources, Mechanism and Recent Applications. Protein Pept Lett. 2020 Dec;27(1):4–16.

142. Keymanesh K, Soltani S, Sardari S. Application of antimicrobial peptides in agriculture and food industry. World J Microbiol Biotechnol. 2009 Jun 1;25(6):933–44.

143. Hancock REW, Sahl HG. Antimicrobial and host-defense peptides as new anti-infective therapeutic strategies. Nat Biotechnol. 2006 Dec;24(12):1551–7.

144. Mazurkiewicz-Pisarek A, Baran J, Ciach T. Antimicrobial Peptides: Challenging Journey to the Pharmaceutical, Biomedical, and Cosmeceutical Use. Int J Mol Sci. 2023 Jan;24(10):9031.

145. Małaczewska J, Kaczorek-Łukowska E. Nisin-A lantibiotic with immunomodulatory properties: A review. Peptides. 2021 Mar;137:170479.

146. Sahl HG, Jack RW, Bierbaum G. Biosynthesis and Biological Activities of Lantibiotics with Unique Post-Translational Modifications. Eur J Biochem. 1995;230(3):827–53.

147. Khan A, Vu KD, Riedl B, Lacroix M. Optimization of the antimicrobial activity of nisin, Na-EDTA and pH against gram-negative and gram-positive bacteria. LWT - Food Sci Technol. 2015 Apr 1;61(1):124–9.

148. Breukink E, de Kruijff B. The lantibiotic nisin, a special case or not? Biochim Biophys Acta BBA - Biomembr. 1999 Dec 15;1462(1):223–34.

149. Zhou H, Fang J, Tian Y, Lu XY. Mechanisms of nisin resistance in Gram-positive bacteria. Ann Microbiol. 2014 Jun;64(2):413–20.

150. Lallukka M, Gamna F, Gobbo VA, Prato M, Najmi Z, Cochis A, et al. Surface Functionalization of Ti6Al4V-ELI Alloy with Antimicrobial Peptide Nisin. Nanomaterials. 2022 Jan;12(23):4332.

151. Fernández L, Delgado S, Herrero H, Maldonado A, Rodríguez JM. The bacteriocin nisin, an effective agent for the treatment of staphylococcal mastitis during lactation. J Hum Lact Off J Int Lact Consult Assoc. 2008 Aug;24(3):311–6.

152. De Kwaadsteniet M, Doeschate KT, Dicks LMT. Nisin F in the treatment of respiratory tract infections caused by Staphylococcus aureus. Lett Appl Microbiol. 2009 Jan;48(1):65–70.

153. Millette M, Cornut G, Dupont C, Shareck F, Archambault D, Lacroix M. Capacity of Human Nisin- and Pediocin-Producing Lactic Acid Bacteria To Reduce Intestinal Colonization by Vancomycin-Resistant Enterococci. Appl Environ Microbiol. 2008 Apr;74(7):1997–2003.

154. van Staden DA, Brand AM, Endo A, Dicks LMT. Nisin F, intraperitoneally injected, may have a stabilizing effect on the bacterial population in the gastro-intestinal tract, as determined in a preliminary study with mice as model. Lett Appl Microbiol. 2011 Aug;53(2):198–201.

155. Heunis TDJ, Smith C, Dicks LMT. Evaluation of a nisin-eluting nanofiber scaffold to treat Staphylococcus aureus-induced skin infections in mice. Antimicrob Agents Chemother. 2013 Aug;57(8):3928–35.

156. Joo NE, Ritchie K, Kamarajan P, Miao D, Kapila YL. Nisin, an apoptogenic bacteriocin and food preservative, attenuates HNSCC tumorigenesis via CHAC1. Cancer Med. 2012 Dec;1(3):295–305.

157. Kamarajan P, Hayami T, Matte B, Liu Y, Danciu T, Ramamoorthy A, et al. Nisin ZP, a Bacteriocin and Food Preservative, Inhibits Head and Neck Cancer Tumorigenesis and Prolongs Survival. PLOS ONE. 2015 Jan 7;10(7):e0131008.

158. Preet S, Bharati S, Panjeta A, Tewari R, Rishi P. Effect of nisin and doxorubicin on DMBA-induced skin carcinogenesis--a possible adjunct therapy. Tumour Biol J Int Soc Oncodevelopmental Biol Med. 2015 Nov;36(11):8301–8.

159. Jia Z, He M, Wang C, Chen A, Zhang X, Xu J, et al. Nisin reduces uterine inflammation in rats by modulating concentrations of pro- and anti-inflammatory cytokines. Am J Reprod Immunol N Y N 1989. 2019 May;81(5):e13096.

160. Kindrachuk J, Jenssen H, Elliott M, Nijnik A, Magrangeas-Janot L, Pasupuleti M, et al. Manipulation of innate immunity by a bacterial secreted peptide: lantibiotic nisin Z is selectively immunomodulatory. Innate Immun. 2013 Jun;19(3):315–27.

161. Bastarrachea LJ, Denis-Rohr A, Goddard JM. Antimicrobial Food Equipment Coatings: Applications and Challenges. Annu Rev Food Sci Technol. 2015;6(1):97–118.

162. Espejo HM, Bahr DF. Application of oxidized metallic surfaces as a medium to store biochemical agents with antimicrobial properties. Surf Coat Technol. 2019 Aug 25;372:312–8.

163. Espejo HM, Díaz-Amaya S, Stanciu LA, Bahr DF. Nisin infusion into surface cracks in oxide coatings to create an antibacterial metallic surface. Mater Sci Eng C. 2019 Dec 1;105:110034.

164. Hage M, Chihib NE, Abdallah M, Khelissa S, Crocco B, Akoum H, et al. Nisin-based coatings for the prevention of biofilm formation: Surface characterization and antimicrobial assessments. Surf Interfaces. 2021 Dec 1;27:101564.

165. Thébault P, Ammoun M, Boudjemaa R, Ouvrard A, Steenkeste K, Bourguignon B, et al. Surface functionalization strategy to enhance the antibacterial effect of nisin Z peptide. Surf Interfaces. 2022;30.

166. Lou T, Bai X, He X, Yuan C. Antifouling performance analysis of peptide-modified glass microstructural surfaces. Appl Surf Sci. 2021 Mar 1;541:148384.

167. Dart A, Sarviya N, Babaie A, Clare J, Bhave M, Sumer H, et al. Highly active nisin coated polycaprolactone electrospun fibers against both Staphylococcus aureus and Pseudomonas aeruginosa. Biomater Adv. 2023 Nov 1;154:213641.

168. Chanachai S, Chaichana W, Insee K, Benjakul S, Aupaphong V, Panpisut P. Physical/Mechanical and Antibacterial Properties of Orthodontic Adhesives Containing Calcium Phosphate and Nisin. J Funct Biomater. 2021 Dec;12(4):73.

169. Spriano S, Verne' E, Ferraris S. Multifunctional titanium surfaces for bone integration. EP2214732, 2009.

170. Riccucci G, Ferraris S, Reggio C, Bosso A, Örlygsson G, Ng CH, et al. Polyphenols from Grape Pomace: Functionalization of Chitosan-Coated Hydroxyapatite for Modulated Swelling and Release of Polyphenols. Langmuir. 2021 Dec 28;37(51):14793–804.

171. Wu, Souheng. Polymer Interface and Adhesion. 1st ed. New York, NY: Routledge; 1982.

172. Rivera LR, Cochis A, Biser S, Canciani E, Ferraris S, Rimondini L, et al. Antibacterial, pro-angiogenic and pro-osteointegrative zein-bioactive glass/copper based coatings for implantable stainless steel aimed at bone healing. Bioact Mater. 2021;6(5):1479–90.

173. Cochis A, Barberi J, Ferraris S, Miola M, Rimondini L, Vernè E, et al. Competitive Surface Colonization of Antibacterial and Bioactive Materials Doped with Strontium and/or Silver Ions. Nanomaterials. 2020 Jan;10(1):120.

174. Harrison JJ, Stremick CA, Turner RJ, Allan ND, Olson ME, Ceri H. Microtiter susceptibility testing of microbes growing on peg lids: a

miniaturized biofilm model for high-throughput screening. Nat Protoc. 2010 Jul;5(7):1236–54.

175. Qian J, Chen Y, Wang Q, Zhao X, Yang H, Gong F, et al. Preparation and antimicrobial activity of pectin-chitosan embedding nisin microcapsules. Eur Polym J. 2021 Aug 15;157:110676.

176. Fael H, Demirel AL. Nisin/polyanion layer-by-layer films exhibiting different mechanisms in antimicrobial efficacy. RSC Adv. 2020;10(17):10329–37.

177. Rollema HS, Kuipers OP, Both P, de Vos WM, Siezen RJ. Improvement of solubility and stability of the antimicrobial peptide nisin by protein engineering. Appl Environ Microbiol. 1995 Aug;61(8):2873–8.

178. Kulkarni M, Patil-Sen Y, Junkar I, Kulkarni CV, Lorenzetti M, Iglič A. Wettability studies of topologically distinct titanium surfaces. Colloids Surf B Biointerfaces. 2015;129:47–53.

179. Yu Z, Ma L, Ye S, Li G, Zhang M. Construction of an environmentally friendly octenylsuccinic anhydride modified pH-sensitive chitosan nanoparticle drug delivery system to alleviate inflammation and oxidative stress. Carbohydr Polym. 2020;236.

180. Ferraris S, Prato M, Vineis C, Varesano A, Gautier di Confiengo G, Spriano S. Coupling of keratin with titanium: A physico-chemical characterization of functionalized or coated surfaces. Surf Coat Technol. 2020 Sep 15;397:126057.

181. Héquet A, Humblot V, Berjeaud JM, Pradier CM. Optimized grafting of antimicrobial peptides on stainless steel surface and biofilm resistance tests. Colloids Surf B Biointerfaces. 2011 Jun 1;84(2):301–9.

182. Kuwano K, Tanaka N, Shimizu T, Nagatoshi K, Nou S, Sonomoto K. Dual antibacterial mechanisms of nisin Z against Gram-positive and Gram-negative bacteria. Int J Antimicrob Agents. 2005;26(5):396–402.

183. Powell C. X-ray Photoelectron Spectroscopy Database XPS,Version 4.1, NIST Standard Reference Database 20 [Internet]. 1989 [cited 2022 Sep 15]. Available from: http://srdata.nist.gov/xps/

184. Shin JM, Gwak JW, Kamarajan P, Fenno JC, Rickard AH, Kapila YL. Biomedical applications of nisin. J Appl Microbiol. 2016;120(6):1449–65.

185. Rahnamaeian M. Antimicrobial peptides: Modes of mechanism, modulation of defense responses. Plant Signal Behav. 2011;6(9):1325–32.

186. Najmi Z, Kumar A, Scalia AC, Cochis A, Obradovic B, Grassi FA, et al. Evaluation of Nisin and LL-37 Antimicrobial Peptides as Tool to Preserve Articular Cartilage Healing in a Septic Environment. Front Bioeng Biotechnol [Internet]. 2020 [cited 2020 Sep 24];8. Available from: https://www.frontiersin.org/articles/10.3389/fbioe.2020.00561/full

187. Shivaee A, Rajabi S, Farahani HE, Imani Fooladi AA. Effect of sub-lethal doses of nisin on Staphylococcus aureus toxin production and biofilm formation. Toxicon. 2021;197:1–5.

188. Sorrentino R, Cochis A, Azzimonti B, Caravaca C, Chevalier J, Kuntz M, et al. Reduced bacterial adhesion on ceramics used for arthroplasty applications. J Eur Ceram Soc. 2018 Mar 1;38(3):963–70.

189. Ferraris S, Warchomicka F, Barberi J, Cochis A, Scalia AC, Spriano S. Contact Guidance Effect and Prevention of Microfouling on a Beta Titanium Alloy Surface Structured by Electron-Beam Technology. Nanomaterials. 2021 Jun;11(6):1474.

190. Blackman LD, Fros MK, Welch NG, Gengenbach TR, Qu Y, Pasic P, et al. Dual Action Antimicrobial Surfaces: Alternating Photopatterns Maintain Contact-Killing Properties with Reduced Biofilm Formation. Macromol Mater Eng. 2020;305(10):2000371.

191. Kim J joo, Kim K, Choi YS, Kang H, Kim DM, Lee JC. Polysulfone based ultrafiltration membranes with dopamine and nisin moieties showing antifouling and antimicrobial properties. Sep Purif Technol. 2018 Aug 31;202:9–20.

192. Li W, Thian ES, Wang M, Wang Z, Ren L. Surface Design for Antibacterial Materials: From Fundamentals to Advanced Strategies. Adv Sci. 2021;8(19):2100368.

193. Andre C, de Jesus Pimentel-Filho N, de Almeida Costa PM, Vanetti MCD. Changes in the composition and architecture of staphylococcal biofilm by nisin. Braz J Microbiol. 2019 Oct 1;50(4):1083–90.

194. Black CRM, Goriainov V, Gibbs D, Kanczler J, Tare RS, Oreffo ROC. Bone Tissue Engineering. Curr Mol Biol Rep. 2015 Sep 1;1(3):132–40.

195. Schatkoski VM, Larissa do Amaral Montanheiro T, Canuto de Menezes BR, Pereira RM, Rodrigues KF, Ribas RG, et al. Current advances concerning

the most cited metal ions doped bioceramics and silicate-based bioactive glasses for bone tissue engineering. Ceram Int. 2021 helmikuu;47(3):2999–3012.

196. Li B, Webster TJ. Bacteria antibiotic resistance: New challenges and opportunities for implant-associated orthopedic infections. J Orthop Res. 2018;36(1):22–32.

197. Maffulli N, Papalia R, Zampogna B, Torre G, Albo E, Denaro V. The management of osteomyelitis in the adult. The Surgeon. 2016 joulukuu;14(6):345–60.

198. Wright JA, Nair SP. Interaction of staphylococci with bone. Int J Med Microbiol IJMM. 2010 Feb;300(2–3):193–204.

199. Frei A, Verderosa AD, Elliott AG, Zuegg J, Blaskovich MAT. Metals to combat antimicrobial resistance. Nat Rev Chem. 2023 Mar;7(3):202–24.

200. Fromm KM. Give silver a shine. Nat Chem. 2011 Feb;3(2):178–178.

201. Vishwanath N, Whitaker C, Allu S, Clippert D, Jouffroy E, Hong J, et al. Silver as an Antibiotic-Independent Antimicrobial: Review of Current Formulations and Clinical Relevance. Surg Infect. 2022 Nov;23(9):769–80.

202. Eckhardt S, Brunetto PS, Gagnon J, Priebe M, Giese B, Fromm KM. Nanobio Silver: Its Interactions with Peptides and Bacteria, and Its Uses in Medicine. Chem Rev. 2013 Jul 10;113(7):4708–54.

203. Li R, Jia Z, Trush MA. Defining ROS in Biology and Medicine. React Oxyg Species Apex NC. 2016;1(1):9–21.

204. Vincent M, Duval RE, Hartemann P, Engels-Deutsch M. Contact killing and antimicrobial properties of copper. J Appl Microbiol. 2018;124(5):1032–46.

205. Santo CE, Quaranta D, Grass G. Antimicrobial metallic copper surfaces kill Staphylococcus haemolyticus via membrane damage. MicrobiologyOpen. 2012;1(1):46–52.

206. Dalecki AG, Crawford CL, Wolschendorf F. Chapter Six - Copper and Antibiotics: Discovery, Modes of Action, and Opportunities for Medicinal Applications. In: Poole RK, editor. Advances in Microbial Physiology [Internet]. Academic Press; 2017 [cited 2022 Sep 19]. p. 193–260. (Microbiology of Metal Ions; vol. 70). Available from: https://www.sciencedirect.com/science/article/pii/S0065291117300073

207. Khodashenas B. The Influential Factors on Antibacterial Behaviour of Copper and Silver Nanoparticles. Indian Chem Eng. 2016 Jul 2;58(3):224–39.

208. Kaya S, Cresswell M, Boccaccini AR. Mesoporous silica-based bioactive glasses for antibiotic-free antibacterial applications. Mater Sci Eng C. 2018 Feb 1;83:99–107.

209. Fong L, Tan K, Tran C, Cool J, Scherer MA, Elovaris R, et al. Interaction of dietary zinc and intracellular binding protein metallothionein in postnatal bone growth. Bone. 2009 Jun 1;44(6):1151–62.

210. Balasubramanian P, Strobel LA, Kneser U, Boccaccini AR. Zinc-containing bioactive glasses for bone regeneration, dental and orthopedic applications. Biomed Glas [Internet]. 2015 Jul 29 [cited 2024 Feb 23];1(1). Available from: https://www.degruyter.com/document/doi/10.1515/bglass-2015-0006/html

211. Phan TN, Buckner T, Sheng J, Baldeck JD, Marquis RE. Physiologic actions of zinc related to inhibition of acid and alkali production by oral streptococci in suspensions and biofilms. Oral Microbiol Immunol. 2004;19(1):31–8.

212. Lansdown ABG, Mirastschijski U, Stubbs N, Scanlon E, Ågren MS. Zinc in wound healing: Theoretical, experimental, and clinical aspects. Wound Repair Regen. 2007;15(1):2–16.

213. Pasqualini R, Barbas CF, Arap W. Vessel maneuvers: Zinc fingers promote angiogenesis. Nat Med. 2002 Dec;8(12):1353–4.

214. Chen A, Shi Q, Feng J, Ouyang Y, Chen Y, Tan S. Dissociation of outer membrane for *Escherichia coli* cell caused by cerium nitrate. J Rare Earths. 2010 Apr 1;28(2):312–5.

215. Goh YF, Alshemary AZ, Akram M, Abdul Kadir MR, Hussain R. *In-vitro* characterization of antibacterial bioactive glass containing ceria. Ceram Int. 2014 Jan 1;40(1, Part A):729–37.

216. Bernstein LR. Mechanisms of Therapeutic Activity for Gallium. Pharmacol Rev. 1998 Dec 1;50(4):665–82.

217. Collery P, Keppler B, Madoulet C, Desoize B. Gallium in cancer treatment. Crit Rev Oncol Hematol. 2002 Jun 1;42(3):283–96.

218. Pourshahrestani S, Zeimaran E, Kadri NA, Gargiulo N, Samuel S, Vasudevaraj Naveen S, et al. Gallium-containing mesoporous bioactive glass

with potent hemostatic activity and antibacterial efficacy. J Mater Chem B. 2016;4(1):71–86.

219. Miola M, Massera J, Cochis A, Kumar A, Rimondini L, Vernè E. Tellurium: A new active element for innovative multifunctional bioactive glasses. Mater Sci Eng C. 2021 Apr 1;123:111957.

220. Diba M, Boccaccini AR. 9 - Silver-containing bioactive glasses for tissue engineering applications. In: Baltzer N, Copponnex T, editors. Precious Metals for Biomedical Applications [Internet]. Woodhead Publishing; 2014 [cited 2022 Jan 21]. p. 177–211. Available from: https://www.sciencedirect.com/science/article/pii/B9780857094346500093

221. Kargozar S, Mozafari M, Ghodrat S, Fiume E, Baino F. Copper-containing bioactive glasses and glass-ceramics: From tissue regeneration to cancer therapeutic strategies. Mater Sci Eng C. 2021 Feb 1;121:111741.

222. Palza H, Escobar B, Bejarano J, Bravo D, Diaz-Dosque M, Perez J. Designing antimicrobial bioactive glass materials with embedded metal ions synthesized by the sol–gel method. Mater Sci Eng C. 2013 lokakuu;33(7):3795–801.

223. Goh YF, Alshemary AZ, Akram M, Abdul Kadir MR, Hussain R. Bioactive Glass: An In-Vitro Comparative Study of Doping with Nanoscale Copper and Silver Particles. Int J Appl Glass Sci. 2014;5(3):255–66.

224. Schuhladen K, Wang X, Hupa L, Boccaccini AR. Dissolution of borate and borosilicate bioactive glasses and the influence of ion (Zn, Cu) doping in different solutions. J Non-Cryst Solids. 2018 Dec 15;502:22–34.

225. Ahmed AA, Ali AA, Mahmoud DAR, El-Fiqi AM. Study on the preparation and properties of silver-doped phosphate antibacterial glasses (Part I). Solid State Sci. 2011 May 1;13(5):981–92.

226. Bari A, Bloise N, Fiorilli S, Novajra G, Vallet-Regí M, Bruni G, et al. Copper-containing mesoporous bioactive glass nanoparticles as multifunctional agent for bone regeneration. Acta Biomater. 2017 Jun 1;55:493–504.

227. Akhtach S, Tabia Z, Bricha M, El Mabrouk K. Structural characterization, *in vitro* bioactivity, and antibacterial evaluation of low silver-doped bioactive glasses. Ceram Int. 2021 Oct 15;47(20):29036–46.

228. Phetnin R, Rattanachan ST. Preparation and antibacterial property on silver incorporated mesoporous bioactive glass microspheres. J Sol-Gel Sci Technol. 2015 Aug 1;75(2):279–90.

229. Xie H, Wang P, Wu J. Effect of exposure of osteoblast-like cells to low-dose silver nanoparticles: uptake, retention and osteogenic activity. Artif Cells Nanomedicine Biotechnol. 2019 joulukuu;47(1):260–7.

230. Rivadeneira J, Gorustovich A. Bioactive glasses as delivery systems for antimicrobial agents. J Appl Microbiol. 2017;122(6):1424–37.

231. Vernè E, Nunzio SD, Bosetti M, Appendino P, Vitale Brovarone C, Maina G, et al. Surface characterization of silver-doped bioactive glass. Biomaterials. 2005 Sep 1;26(25):5111–9.

232. Miola M, Fucale G, Maina G, Verné E. Antibacterial and bioactive composite bone cements containing surface silver-doped glass particles. Biomed Mater. 2015 Oct;10(5):055014.

233. Miola M, Cochis A, Kumar A, Arciola CR, Rimondini L, Verné E. Copper-Doped Bioactive Glass as Filler for PMMA-Based Bone Cements: Morphological, Mechanical, Reactivity, and Preliminary Antibacterial Characterization. Materials. 2018 Jun;11(6):961.

234. Miola M, Verné E. Bioactive and Antibacterial Glass Powders Doped with Copper by Ion-Exchange in Aqueous Solutions. Materials [Internet]. 2016 May 24 [cited 2020 Sep 15];9(6). Available from: https://www.ncbi.nlm.nih.gov/pmc/articles/PMC5456756/

235. Kokubo T, Takadama H. How useful is SBF in predicting in vivo bone bioactivity? Biomaterials. 2006 May 1;27(15):2907–15.

236. Bingel L, Groh D, Karpukhina N, Brauer DS. Influence of dissolution medium pH on ion release and apatite formation of Bioglass® 45S5. Mater Lett. 2015 Mar 15;143:279–82.

237. Rajamäki K, Nordström T, Nurmi K, Åkerman KEO, Kovanen PT, Öörni K, et al. Extracellular Acidosis Is a Novel Danger Signal Alerting Innate Immunity via the NLRP3 Inflammasome. J Biol Chem. 2013 May 10;288(19):13410–9.

238. Kyllönen L, Haimi S, Mannerström B, Huhtala H, Rajala KM, Skottman H, et al. Effects of different serum conditions on osteogenic differentiation of human adipose stem cells in vitro. Stem Cell Res Ther. 2013 Feb 15;4(1):17.

239. Patrikoski M, Juntunen M, Boucher S, Campbell A, Vemuri MC, Mannerström B, et al. Development of fully defined xeno-free culture system for the preparation and propagation of cell therapy-compliant human adipose stem cells. Stem Cell Res Ther. 2013 Mar 7;4(2):27.

240. Hyväri L, Ojansivu M, Juntunen M, Kartasalo K, Miettinen S, Vanhatupa S. Focal Adhesion Kinase and ROCK Signaling Are Switch-Like Regulators of Human Adipose Stem Cell Differentiation towards Osteogenic and Adipogenic Lineages. Stem Cells Int. 2018 Sep 12;2018:2190657.

241. Bourin P, Bunnell BA, Casteilla L, Dominici M, Katz AJ, March KL, et al. Stromal cells from the adipose tissue-derived stromal vascular fraction and culture expanded adipose tissue-derived stromal/stem cells: a joint statement of the International Federation for Adipose Therapeutics and Science (IFATS) and the International Society for Cellular Therapy (ISCT). Cytotherapy. 2013 Jun;15(6):641–8.

242. Dominici M, Le Blanc K, Mueller I, Slaper-Cortenbach I, Marini F, Krause D, et al. Minimal criteria for defining multipotent mesenchymal stromal cells. The International Society for Cellular Therapy position statement. Cytotherapy. 2006;8(4):315–7.

243. Cochis A, Azzimonti B, Della Valle C, De Giglio E, Bloise N, Visai L, et al. The effect of silver or gallium doped titanium against the multidrug resistant Acinetobacter baumannii. Biomaterials. 2016 Feb 1;80:80–95.

244. Ferraris S, Cochis A, Cazzola M, Tortello M, Scalia A, Spriano S, et al. Cytocompatible and Anti-bacterial Adhesion Nanotextured Titanium Oxide Layer on Titanium Surfaces for Dental and Orthopedic Implants. Front Bioeng Biotechnol [Internet]. 2019 [cited 2020 Sep 24];7. Available from: https://www.frontiersin.org/articles/10.3389/fbioe.2019.00103/full

245. International Standard Organisation (ISO). ISO 22196:2011 Measurement of antibacterial activity on plastics and other non-porous surfaces. 2011.

246. Vourlias G. Application of X-rays Diffraction for Identifying Thin Oxide Surface Layers on Zinc Coatings. Coatings. 2020 Oct;10(10):1005.

247. Zheng K, Dai X, Lu M, Hüser N, Taccardi N, Boccaccini AldoR. Synthesis of copper-containing bioactive glass nanoparticles using a modified Stöber method for biomedical applications. Colloids Surf B Biointerfaces. 2017 Feb 1;150:159–67.

248. Wang H, Zhao S, Xiao W, Xue J, Shen Y, Zhou J, et al. Influence of Cu doping in borosilicate bioactive glass and the properties of its derived scaffolds. Mater Sci Eng C. 2016 Jan 1;58:194–203.

249. Stoll VS, Blanchard JS. [4] Buffers: Principles and practice. In: Deutscher MP, editor. Methods in Enzymology [Internet]. Academic Press; 1990 [cited

2023 Oct 20]. p. 24–38. (Guide to Protein Purification; vol. 182). Available from: https://www.sciencedirect.com/science/article/pii/007668799082006N

250. Bulina NV, Eremina NV, Vinokurova OB, Ishchenko AV, Chaikina MV. Diffusion of Copper Ions in the Lattice of Substituted Hydroxyapatite during Heat Treatment. Materials. 2022 Jan;15(16):5759.

251. Ressler A, Žužić A, Ivanišević I, Kamboj N, Ivanković H. Ionic substituted hydroxyapatite for bone regeneration applications: A review. Open Ceram. 2021 Jun 1;6:100122.

252. Blochberger M, Hupa L, Brauer DS. Influence of zinc and magnesium substitution on ion release from Bioglass 45S5 at physiological and acidic pH. Biomed Glas [Internet]. 2015 Sep 14 [cited 2023 Mar 20];1(1). Available from: https://www.degruyter.com/document/doi/10.1515/bglass-2015-0009/html

253. Ferraris S, Yamaguchi S, Barbani N, Cazzola M, Cristallini C, Miola M, et al. Bioactive materials: In vitro investigation of different mechanisms of hydroxyapatite precipitation. Acta Biomater. 2020 Jan 15;102:468–80.

254. Ferraris S, Yamaguchi S, Barbani N, Cristallini C, Gautier di Confiengo G, Barberi J, et al. The mechanical and chemical stability of the interfaces in bioactive materials: The substrate-bioactive surface layer and hydroxyapatite-bioactive surface layer interfaces. Mater Sci Eng C. 2020 Mar 1;116:111238.

255. Botelho CM, Lopes MA, Gibson IR, Best SM, Santos JD. Structural analysis of Si-substituted hydroxyapatite: zeta potential and X-ray photoelectron spectroscopy. J Mater Sci Mater Med. 2002 Dec 1;13(12):1123–7.

256. Li H, Michael Siu KW, Guevremont R, Yves Le Blanc JC. Complexes of silver(I) with peptides and proteins as produced in electrospray mass spectrometry. J Am Soc Mass Spectrom. 1997 Aug 1;8(8):781–92.

257. Titus D, James Jebaseelan Samuel E, Roopan SM. Chapter 12 - Nanoparticle characterization techniques. In: Shukla AK, Iravani S, editors. Green Synthesis, Characterization and Applications of Nanoparticles [Internet]. Elsevier; 2019 [cited 2022 Jul 19]. p. 303–19. (Micro and Nano Technologies). Available from: https://www.sciencedirect.com/science/article/pii/B9780081025796000125

258. Markoulidis F. A Review on Surface Analysis Techniques. 2009.

259. Cai S, Wu C, Yang W, Liang W, Yu H, Liu L. Recent advance in surface modification for regulating cell adhesion and behaviors. Nanotechnol Rev. 2020 Jan 1;9(1):971–89.

260. Thyparambil NJ, Gutgesell LC, Hurley CC, Flowers LE, Day DE, Semon JA. Adult stem cell response to doped bioactive borate glass. J Mater Sci Mater Med. 2020 Jan 21;31(2):13.

261. Mishra A, Ojansivu M, Autio R, Vanhatupa S, Miettinen S, Massera J. In-vitro dissolution characteristics and human adipose stem cell response to novel borophosphate glasses. J Biomed Mater Res A. 2019;107(9):2099–114.

262. Cao B, Zheng Y, Xi T, Zhang C, Song W, Burugapalli K, et al. Concentration-dependent cytotoxicity of copper ions on mouse fibroblasts in vitro: effects of copper ion release from TCu380A vs TCu220C intra-uterine devices. Biomed Microdevices. 2012 Aug 1;14(4):709–20.

263. Cervantes-Cervantes MP, Calderón-Salinas JV, Albores A, Muñoz-Sánchez JL. Copper increases the damage to DNA and proteins caused by reactive oxygen species. Biol Trace Elem Res. 2005 Mar 1;103(3):229–48.

264. Miola M, Bertone E, Vernè E. In situ chemical and physical reduction of copper on bioactive glass surface. Appl Surf Sci. 2019 Mar 30;495:143559.

265. Parisi L, Toffoli A, Ghezzi B, Mozzoni B, Lumetti S, Macaluso GM. A glance on the role of fibronectin in controlling cell response at biomaterial interface. Jpn Dent Sci Rev. 2020 Mar 1;56(1):50–5.

266. Azizi L, Turkki P, Huynh N, Massera JM, Hytönen VP. Surface Modification of Bioactive Glass Promotes Cell Attachment and Spreading. ACS Omega. 2021 Sep 7;6(35):22635–42.

267. Ciraldo FE, Boccardi E, Melli V, Westhauser F, Boccaccini AR. Tackling bioactive glass excessive in vitro bioreactivity: Preconditioning approaches for cell culture tests. Acta Biomater. 2018 heinäkuu;75:3–10.

268. Li A, Lv Y, Ren H, Cui Y, Wang C, Martin RA, et al. In vitro evaluation of a novel pH neutral calcium phosphosilicate bioactive glass that does not require preconditioning prior to use. Int J Appl Glass Sci. 2017;8(4):403–11.

269. Tan J, Wang D, Cao H, Qiao Y, Zhu H, Liu X. Effect of Local Alkaline Microenvironment on the Behaviors of Bacteria and Osteogenic Cells. ACS Appl Mater Interfaces. 2018 Dec 12;10(49):42018–29.

270. Debnath T, Chelluri LK. Standardization and quality assessment for clinical grade mesenchymal stem cells from human adipose tissue. Hematol Transfus Cell Ther. 2019;41(1):7–16.

271. Hupa L, Fagerlund S, Massera J, Björkvik L. Dissolution behavior of the bioactive glass S53P4 when sodium is replaced by potassium, and calcium with magnesium or strontium. J Non-Cryst Solids. 2016 Jan 15;432:41–6.

272. Taipale S, Ek P, Hupa M, Hupa L. Continuous measurement of the dissolution rate of ions from glasses. Adv Mater Res. 2008;39–40:341–6.

273. Pierre C, Bertrand G, Pavy I, Benhamou O, Rey C, Roques C, et al. Antibacterial Electrodeposited Copper-Doped Calcium Phosphate Coatings for Dental Implants. J Funct Biomater. 2023 Jan;14(1):20.

274. Popescu RA, Magyari K, Vulpoi A, Trandafir DL, Licarete E, Todea M, et al. Bioactive and biocompatible copper containing glass-ceramics with remarkable antibacterial properties and high cell viability designed for future in vivo trials. Biomater Sci. 2016 Jul 19;4(8):1252–65.

275. Foroutan F, McGuire J, Gupta P, Nikolaou A, Kyffin BA, Kelly NL, et al. Antibacterial Copper-Doped Calcium Phosphate Glasses for Bone Tissue Regeneration. ACS Biomater Sci Eng. 2019 Nov 11;5(11):6054–62.

276. Koohkan R, Hooshmand T, Tahriri M, Mohebbi-Kalhori D. Synthesis, characterization and in vitro bioactivity of mesoporous copper silicate bioactive glasses. Ceram Int. 2018 Feb 1;44(2):2390–9.

277. Lallukka M, Houaoui A, Miola M, Miettinen S, Massera J, Verné E. In vitro cytocompatibility of antibacterial silver and copper-doped bioactive glasses. Ceram Int [Internet]. 2023 Aug 31 [cited 2023 Sep 13]; Available from: https://www.sciencedirect.com/science/article/pii/S0272884223025518

278. Esdaille CJ, Washington KS, Laurencin CT. Regenerative engineering: a review of recent advances and future directions. Regen Med. 2021 May;16(5):495–512.

279. Schmidt AH. Autologous bone graft: Is it still the gold standard? Injury. 2021 Jun 1;52:S18–22.

280. Steijvers E, Ghei A, Xia Z. Manufacturing artificial bone allografts: a perspective. Biomater Transl. 2022 Mar 28;3(1):65–80.

281. Gerhardt LC, Boccaccini AR. Bioactive Glass and Glass-Ceramic Scaffolds for Bone Tissue Engineering. Materials. 2010 Jul;3(7):3867–910.

282. Roseti L, Parisi V, Petretta M, Cavallo C, Desando G, Bartolotti I, et al. Scaffolds for Bone Tissue Engineering: State of the art and new perspectives. Mater Sci Eng C. 2017 Sep 1;78:1246–62.

283. Baino F, Fiume E, Barberi J, Kargozar S, Marchi J, Massera J, et al. Processing methods for making porous bioactive glass-based scaffolds—A state-of-the-art review. Int J Appl Ceram Technol. 2019;16(5):1762–96.

284. Henkel J, Woodruff MA, Epari DR, Steck R, Glatt V, Dickinson IC, et al. Bone Regeneration Based on Tissue Engineering Conceptions — A 21st Century Perspective. Bone Res. 2013 Dec;1(1):216–48.

285. Fu Q, Saiz E, Rahaman MN, Tomsia AP. Bioactive glass scaffolds for bone tissue engineering: state of the art and future perspectives. Mater Sci Eng C. 2011 Oct 10;31(7):1245–56.

286. Reznikov N, Shahar R, Weiner S. Bone hierarchical structure in three dimensions. Acta Biomater. 2014 Sep 1;10(9):3815–26.

287. Baino F, Vitale-Brovarone C. Three-dimensional glass-derived scaffolds for bone tissue engineering: Current trends and forecasts for the future. J Biomed Mater Res A. 2011;97A(4):514–35.

288. Sepulveda P, Jones JR, Hench LL. Bioactive sol-gel foams for tissue repair. J Biomed Mater Res. 2002;59(2):340–8.

289. Wu ZY, Hill RG, Yue S, Nightingale D, Lee PD, Jones JR. Melt-derived bioactive glass scaffolds produced by a gel-cast foaming technique. Acta Biomater. 2011 Apr 1;7(4):1807–16.

290. Baino F, Fiume E, Miola M, Leone F, Onida B, Verné E. Fe-doped bioactive glass-derived scaffolds produced by sol-gel foaming. Mater Lett. 2019 Jan 15;235:207–11.

291. Huan Z, Chang J, Zhou J. Low-temperature fabrication of macroporous scaffolds through foaming and hydration of tricalcium silicate paste and their bioactivity. J Mater Sci. 2010 Feb 1;45(4):961–8.

292. Fu Q, Rahaman MN, Bal BS, Huang W, Day DE. Preparation and bioactive characteristics of a porous 13–93 glass, and fabrication into the articulating surface of a proximal tibia. J Biomed Mater Res A. 2007;82A(1):222–9.

293. Liang W, Rahaman MN, Day DE, Marion NW, Riley GC, Mao JJ. Bioactive borate glass scaffold for bone tissue engineering. J Non-Cryst Solids. 2008 Mar 15;354(15):1690–6.

294. Brovarone CV, Verné E, Appendino P. Macroporous bioactive glass-ceramic scaffolds for tissue engineering. J Mater Sci Mater Med. 2006 Nov;17(11):1069–78.

295. Zhang H, Ye XJ, Li JS. Preparation and biocompatibility evaluation of apatite/wollastonite-derived porous bioactive glass ceramic scaffolds. Biomed Mater. 2009 Jul;4(4):045007.

296. Vitale-Brovarone C, Vernè E, Bosetti M, Appendino P, Cannas M. Microstructural and in vitro characterization of SiO2-Na2O-CaO-MgO glass-ceramic bioactive scaffolds for bone substitutes. J Mater Sci Mater Med. 2005 Oct 1;16(10):909–17.

297. Matsuoka C, Teranishi T, Hayashi H, Kishimoto A. Utilizing Rice Husk for Ceramic and Glass Foams as Matrix and Foaming Agent. J Jpn Soc Powder Powder Metall. 2018;65(8):475–80.

298. Wu SC, Hsu HC, Hsiao SH, Ho WF. Preparation of porous 45S5 Bioglass®-derived glass–ceramic scaffolds by using rice husk as a porogen additive. J Mater Sci Mater Med. 2009 Jun 1;20(6):1229–36.

299. Fiorilli S, Baino F, Cauda V, Crepaldi M, Vitale-Brovarone C, Demarchi D, et al. Electrophoretic deposition of mesoporous bioactive glass on glass–ceramic foam scaffolds for bone tissue engineering. J Mater Sci Mater Med. 2015 Jan 13;26(1):21.

300. Lao J, Dieudonné X, Benbakkar M, Jallot É. Bioactive glass coating on gelatin scaffolds at ambient temperature: easy route to make polymer scaffolds become bioactive. J Mater Sci. 2017 Aug 1;52(15):9129–39.

301. Roether JA, Boccaccini AR, Hench LL, Maquet V, Gautier S, Jérôme R. Development and in vitro characterisation of novel bioresorbable and bioactive composite materials based on polylactide foams and Bioglass® for tissue engineering applications. Biomaterials. 2002 Sep 1;23(18):3871–8.

302. Chen J, Roether A, Boccaccini A. Tissue engineering scaffolds from bioactive glass and composite materials. Top Tissue Eng. 2008 Jan 1;4.

303. Park YS, Kim KN, Kim KM, Choi SH, Kim CK, Legeros RZ, et al. Feasibility of three-dimensional macroporous scaffold using calcium phosphate glass and polyurethane sponge. J Mater Sci. 2006 Jul 1;41(13):4357–64.

304. Fu Q, Rahaman MN, Bal BS, Brown RF. Preparation and in vitro evaluation of bioactive glass (13–93) scaffolds with oriented microstructures for repair and regeneration of load-bearing bones. J Biomed Mater Res A. 2010;93A(4):1380–90.

305. Liu X, Rahaman MN, Fu Q, Tomsia AP. Porous and strong bioactive glass (13-93) scaffolds prepared by unidirectional freezing of camphene-based suspensions. Acta Biomater. 2012 Jan 1;8(1):415–23.

306. Minaberry Y, Jobbágy M. Macroporous Bioglass Scaffolds Prepared by Coupling Sol–Gel with Freeze Drying. Chem Mater. 2011 May 10;23(9):2327–32.

307. Maquet V, Boccaccini AR, Pravata L, Notingher I, Jérôme R. Porous poly(*α*-hydroxyacid)/Bioglass® composite scaffolds for bone tissue engineering. I: preparation and in vitro characterisation. Biomaterials. 2004 Aug 1;25(18):4185–94.

308. Niu Y, Guo L, Liu J, Shen H, Su J, An X, et al. Bioactive and degradable scaffolds of the mesoporous bioglass and poly(l -lactide) composite for bone tissue regeneration. J Mater Chem B. 2015;3(15):2962–70.

309. Liu J, Hu H, Li P, Shuai C, Peng S. Fabrication and Characterization of Porous 45S5 Glass Scaffolds via Direct Selective Laser Sintering. Mater Manuf Process. 2013 Jun 1;28(6):610–5.

310. Tesavibul P, Felzmann R, Gruber S, Liska R, Thompson I, Boccaccini AR, et al. Processing of 45S5 Bioglass® by lithography-based additive manufacturing. Mater Lett. 2012 May 1;74:81–4.

311. Mancuso E, Alharbi N, Bretcanu OA, Marshall M, Birch MA, McCaskie AW, et al. Three-dimensional printing of porous load-bearing bioceramic scaffolds. Proc Inst Mech Eng [H]. 2017 Jun 1;231(6):575–85.

312. Preethi Soundarya S, Haritha Menon A, Viji Chandran S, Selvamurugan N. Bone tissue engineering: Scaffold preparation using chitosan and other biomaterials with different design and fabrication techniques. Int J Biol Macromol. 2018 Nov 1;119:1228–39.

313. Baino F, Barberi J, Fiume E, Orlygsson G, Massera J, Verné E. Robocasting of Bioactive SiO_2-P_2O_5-CaO-MgO-Na_2O-K_2O Glass Scaffolds. J Healthc Eng. 2019 Apr 11;2019:e5153136.

314. Franco J, Hunger P, Launey ME, Tomsia AP, Saiz E. Direct write assembly of calcium phosphate scaffolds using a water-based hydrogel. Acta Biomater. 2010 Jan 1;6(1):218–28.

315. Baino F, Novajra G, Vitale-Brovarone C. Bioceramics and Scaffolds: A Winning Combination for Tissue Engineering. Front Bioeng Biotechnol [Internet]. 2015 [cited 2020 Sep 23];3. Available from: https://www.frontiersin.org/articles/10.3389/fbioe.2015.00202/full

316. Fiume E, Ciavattini S, Verné E, Baino F. Foam Replica Method in the Manufacturing of Bioactive Glass Scaffolds: Out-of-Date Technology or Still Underexploited Potential? Materials. 2021 Jan;14(11):2795.

317. Wu Y, Lu Y, Zhao M, Bosiakov S, Li L. A Critical Review of Additive Manufacturing Techniques and Associated Biomaterials Used in Bone Tissue Engineering. Polymers. 2022 Jan;14(10):2117.

318. Chen TH, Ghayor C, Siegenthaler B, Schuler F, Rüegg J, De Wild M, et al. Lattice Microarchitecture for Bone Tissue Engineering from Calcium Phosphate Compared to Titanium. Tissue Eng Part A. 2018 Oct;24(19–20):1554–61.

319. Chen QZ, Thompson ID, Boccaccini AR. 45S5 Bioglass®-derived glass–ceramic scaffolds for bone tissue engineering. Biomaterials. 2006 Apr 1;27(11):2414–25.

320. Karl S, Somers AV. Method of making porous ceramic articles [Internet]. US3090094A, 1963 [cited 2023 Feb 3]. Available from: https://patents.google.com/patent/US3090094A/en

321. Cunningham E, Dunne N. Comparative Characterisation of 3-D Hydroxyapatite Scaffolds Developed Via Replication of Synthetic Polymer Foams and Natural Marine Sponges. J Tissue Sci Eng [Internet]. 2011 [cited 2023 Feb 3];s1. Available from: https://www.omicsonline.org/comparative-characterisation-of-3-d-hydroxyapatite-scaffolds-developed-via-replication-of-synthetic-polymer-foams-and-natural-marine-sponges-2157-7552.S1-001.php?aid=2213

322. Xia W, Chang J. Bioactive glass scaffold with similar structure and mechanical properties of cancellous bone. J Biomed Mater Res B Appl Biomater. 2010;95B(2):449–55.

323. Cabanas-Polo S, Philippart A, Boccardi E, Hazur J, Boccaccini AR. Facile production of porous bioactive glass scaffolds by the foam replica technique

combined with sol–gel/electrophoretic deposition. Ceram Int. 2016 Apr 1;42(5):5772–7.

324. Navalón C, Ros-Tárraga P, Murciano A, Velasquez P, Mazón P, De Aza PN. Easy manufacturing of 3D ceramic scaffolds by the foam replica technique combined with sol-gel or ceramic slurry. Ceram Int. 2019 Oct 15;45(15):18338–46.

325. Aguilar-Reyes EA, León-Patiño CA, Villicaña-Molina E, Macías-Andrés VI, Lefebvre LP. Processing and in vitro bioactivity of high-strength 45S5 glass-ceramic scaffolds for bone regeneration. Ceram Int. 2017 Jun 15;43(9):6868–75.

326. Possolli NM, Raupp-Pereira F, Klegues Montedo OR, Arcaro S. LZS bioactive glass-ceramic scaffolds: Colloidal processing, foam replication technique and mechanical properties to bone tissue engineering. Open Ceram. 2022 Mar 1;9:100219.

327. Zhao C, Liu W, Zhu M, Wu C, Zhu Y. Bioceramic-based scaffolds with antibacterial function for bone tissue engineering: A review. Bioact Mater. 2022 Dec 1;18:383–98.

328. Oliveira RLMS, Barbosa L, Hurtado CR, Ramos L de P, Montanheiro TLA, Oliveira LD, et al. Bioglass-based scaffolds coated with silver nanoparticles: Synthesis, processing and antimicrobial activity. J Biomed Mater Res A. 2020;108(12):2447–59.

329. Shuai C, Xu Y, Feng P, Wang G, Xiong S, Peng S. Antibacterial polymer scaffold based on mesoporous bioactive glass loaded with in situ grown silver. Chem Eng J. 2019 Oct 15;374:304–15.

330. Bellantone M, Williams HD, Hench LL. Broad-Spectrum Bactericidal Activity of Ag2O-Doped Bioactive Glass. Antimicrob Agents Chemother. 2002 Jun;46(6):1940–5.

331. Chatzistavrou X, Fenno JC, Faulk D, Badylak S, Kasuga T, Boccaccini AR, et al. Fabrication and characterization of bioactive and antibacterial composites for dental applications. Acta Biomater. 2014 Aug 1;10(8):3723–32.

332. Marsh AC, Mellott NP, Crimp M, Wren A, Hammer N, Chatzistavrou X. Ag-doped Bioactive Glass-Ceramic 3D Scaffolds: Microstructural, Antibacterial, and Biological Properties. J Eur Ceram Soc. 2021 Jun 1;41(6):3717–30.

333. Jones JR, Ehrenfried LM, Saravanapavan P, Hench LL. Controlling ion release from bioactive glass foam scaffolds with antibacterial properties. J Mater Sci Mater Med. 2006 Nov 1;17(11):989–96.

334. Marsh AC, Mellott NP, Pajares-Chamorro N, Crimp M, Wren A, Hammer ND, et al. Fabrication and multiscale characterization of 3D silver containing bioactive glass-ceramic scaffolds. Bioact Mater. 2019 Dec 1;4:215–23.

335. Miola M, Verné E, Vitale-Brovarone C, Baino F. Antibacterial Bioglass-Derived Scaffolds: Innovative Synthesis Approach and Characterization. Int J Appl Glass Sci. 2016;7(2):238–47.

336. Ciraldo FE, Arango-Ospina M, Goldmann WH, Beltrán AM, Detsch R, Gruenewald A, et al. Fabrication and characterization of Ag- and Ga-doped mesoporous glass-coated scaffolds based on natural marine sponges with improved mechanical properties. J Biomed Mater Res A. 2021;109(8):1309–27.

337. Balagna C, Vitale-Brovarone C, Miola M, Verné E, Canuto RA, Saracino S, et al. Biocompatibility and Antibacterial Effect of Silver Doped 3D-Glass-Ceramic Scaffolds for Bone Grafting , Biocompatibility and Antibacterial Effect of Silver Doped 3D-Glass-Ceramic Scaffolds for Bone Grafting. J Biomater Appl. 2011 Feb 1;25(6):595–617.

338. Newby PJ, El-Gendy R, Kirkham J, Yang XB, Thompson ID, Boccaccini AR. Ag-doped 45S5 Bioglass®-based bone scaffolds by molten salt ion exchange: processing and characterisation. J Mater Sci Mater Med. 2011 Mar 1;22(3):557–69.

339. Vitale-Brovarone C, Baino F, Verné E. High strength bioactive glass-ceramic scaffolds for bone regeneration. J Mater Sci Mater Med. 2009 Feb 1;20(2):643–53.

340. Di Nunzio S, Vernè E. PROCESS FOR THE PRODUCTION OF SILVER-CONTAINING PROSTHETIC DEVICES [Internet]. Turin; EP 1 819 372 B1, 2005 [cited 2022 Jan 21]. Available from: https://data.epo.org/publication-server/document?iDocId=3551608&iFormat=0

341. Hench LL, Wilson J. Surface-active biomaterials. Science. 1984 Nov 9;226(4675):630–6.

342. Maçon ALB, Kim TB, Valliant EM, Goetschius K, Brow RK, Day DE, et al. A unified in vitro evaluation for apatite-forming ability of bioactive glasses and their variants. J Mater Sci Mater Med. 2015 Feb;26(2):115.

343. National Committee for Clinical Laboratory Standards. Performance Standards for Antimicrobial Disk Susceptibility Tests; Approved Standard: M2-A7 9th edition. NCCLS, Villanova, PA, USA; 2003.

344. García Del Pozo E, Collazos J, Cartón JA, Camporro D, Asensi V. Bacterial osteomyelitis: microbiological, clinical, therapeutic, and evolutive characteristics of 344 episodes. Rev Espanola Quimioter Publicacion Of Soc Espanola Quimioter. 2018 Jun;31(3):217–25.

345. Baino F, Ferraris M, Bretcanu O, Verné E, Vitale-Brovarone C. Optimization of composition, structure and mechanical strength of bioactive 3-D glass-ceramic scaffolds for bone substitution: J Biomater Appl [Internet]. 2011 Dec 29 [cited 2020 Nov 30]; Available from: https://journals.sagepub.com/doi/10.1177/0885328211429193

346. Lara C, Pascual MJ, Durán A. Glass-forming ability, sinterability and thermal properties in the systems RO–BaO–SiO2 (R=Mg, Zn). J Non-Cryst Solids. 2004 Nov 15;348:149–55.

347. Hrubý A. Evaluation of glass-forming tendency by means of DTA. Czechoslov J Phys B. 1972 Nov 1;22(11):1187–93.

348. Bernache-assollant D. Govin: Structural transformations of bioactive glass 45S5 with thermal treatments, Acta Materialia 56. 2007 Jan 1 [cited 2023 May 29]; Available from: https://www.academia.edu/79060368/Govin_Structural_transformations_of_bioactive_glass_45S5_with_thermal_treatments_Acta_Materialia_56

349. Bretcanu O, Chatzistavrou X, Paraskevopoulos K, Conradt R, Thompson I, Boccaccini AR. Sintering and crystallisation of 45S5 Bioglass® powder. J Eur Ceram Soc. 2009;29(16):3299.

350. Kaur G, Kumar V, Baino F, Mauro JC, Pickrell G, Evans I, et al. Mechanical properties of bioactive glasses, ceramics, glass-ceramics and composites: State-of-the-art review and future challenges. Mater Sci Eng C. 2019 Nov 1;104:109895.

351. Hing KA. Bioceramic Bone Graft Substitutes: Influence of Porosity and Chemistry. Int J Appl Ceram Technol. 2005;2(3):184–99.

352. Dorozhkin SV, Epple M. Biological and Medical Significance of Calcium Phosphates. Angew Chem Int Ed. 2002;41(17):3130–46.

353. Ferraris S, Yamaguchi S, Barbani N, Cristallini C, Gautier di Confiengo G, Barberi J, et al. The mechanical and chemical stability of the interfaces in

bioactive materials: The substrate-bioactive surface layer and hydroxyapatite-bioactive surface layer interfaces. Mater Sci Eng C. 2020 Nov 1;116:111238.

354. Cerruti M, Greenspan D, Powers K. Effect of pH and ionic strength on the reactivity of Bioglass® 45S5. Biomaterials. 2005 May 1;26(14):1665–74.

355. Mačković M, Hoppe A, Detsch R, Mohn D, Stark WJ, Spiecker E, et al. Bioactive glass (type 45S5) nanoparticles: in vitro reactivity on nanoscale and biocompatibility. J Nanoparticle Res. 2012 Jun 22;14(7):966.

356. Du H, Williams CT, Ebner AD, Ritter JA. In Situ FTIR Spectroscopic Analysis of Carbonate Transformations during Adsorption and Desorption of CO2 in K-Promoted HTlc. Chem Mater. 2010 Jun 8;22(11):3519–26.

357. Groh D, Döhler F, Brauer DS. Bioactive glasses with improved processing. Part 1. Thermal properties, ion release and apatite formation. Acta Biomater. 2014 Oct;10(10):4465–73.

358. Lu X, Leng Y. Theoretical analysis of calcium phosphate precipitation in simulated body fluid. Biomaterials. 2005 Apr 1;26(10):1097–108.

359. Wang H, Zhao S, Cui X, Pan Y, Huang W, Ye S, et al. Evaluation of three-dimensional silver-doped borate bioactive glass scaffolds for bone repair: Biodegradability, biocompatibility, and antibacterial activity. J Mater Res. 2015 Sep 1;30(18):2722–35.

360. Chen X, Zhou J, Qian Y, Zhao L. Antibacterial coatings on orthopedic implants. Mater Today Bio. 2023 Apr 1;19:100586.

APPENDIX A: Characterization of nanotextured titanium alloy lattice structure surfaces for bone integration

Introduction

The rising interest in Additive Manufacturing (AM) of titanium alloys for biomedical purposes stems from its capacity to craft tailored implants in terms of shape, size, porosity, and even material composition and mechanical traits, especially beneficial for bone substitution (1). These characteristics render it an attractive technology for medical applications, evolving towards highly individualized solutions. Moreover, AM techniques offer rapid, scalable production with minimal post-processing, resulting in material and cost efficiencies.

The most common additive manufacturing methods for fabricating titanium scaffolds include powder bed fusion techniques such as Selective Laser Melting (SLM) and Electron Beam Melting (EBM). These methods facilitate the creation of intricate three-dimensional porous titanium structures with interconnected pores, adjustable pore sizes, and suitable mechanical properties (2). Despite their advantages, challenges persist, including porosity regulation, surface roughness, and residual stresses that can compromise mechanical properties (3). Additionally, a significant challenge lies in removing unmelted particles from lattice structures. In the context of biomedical applications, and especially in orthopedic implants where the secure bone attachment is essential, these particles within lattice

structures can jeopardize structural integrity, biocompatibility, and mechanical strength if not effectively eliminated (4). Moreover, the knowledge about surface treatments for fast and stable osseointegration must be revised and applied to 3D lattice structures obtained through AM.

This study aimed to apply a patented thermochemical treatment (Spriano et al., EP2214732) to titanium alloy lattice structures fabricated via the SLM technique and investigate its influence on sample morphology, 3D lattice structure, unmelted particles, and surface micro and nano-roughness. Prior research has shown that this surface treatment enhances *in vitro* bioactivity, wettability, osseointegration and osteoblast differentiation, and prevents bacterial adhesion (5,6). Furthermore, the viability of implementing this surface treatment on practical biomedical devices, such as 3D acetabular cups or dental screws, has been demonstrated (5). These initial assessments of both untreated and treated sample surfaces are anticipated to provide insights into the effects of the treatment on sample surface and structure, facilitating future biological assays in more intricate and realistic settings.

Materials and Methods

Sample preparation

The 3D lattice samples, provided by PREMUROSA project partner BTech Innovation, were 8 mm x 8 mm squares with approximately 2mm thickness, manufactured by a powder bed fusion technique selective laser melting (SLM). Before the chemical treatment, samples underwent a cleaning process: they were sonicated in acetone for 5 minutes followed by two rounds of sonication in ultra-pure water for 10 minutes each and dried under a laminar hood. The chemical treatment was then applied according to a patented protocol previously described

(85,366). This procedure involves an acid etching step utilizing hydrofluoric acid (HF) to eliminate the native oxide layer, succeeded by a controlled oxidation stage employing hydrogen peroxide (H_2O_2). The objective of this treatment is to generate a micro- and nanotextured titanium oxide layer rich in –OH groups. The resultant samples are denoted as Chemically Treated (CT), while untreated washed samples are labeled as control (CTRL).

Sample characterization

Field emission scanning electron microscopy (FESEM, SupraTM 40, Zeiss) was conducted on both CTRL and CT samples to evaluate their morphology. Furthermore, the samples underwent characterization via micro-CT scan (Fraunhofer IKTS). VGSTUDIO 3.5 MAX software used to analyze the images, while ImageJ software was employed to determine the total porosity and average pore size. This involved utilizing the maximum Feret diameter, representing the longest distance between any two points along the boundary of an object perpendicular to a specified direction, as well as the minimum Feret diameter, indicating the smallest distance between two tangents on opposite sides of a particle or object (8).

Results and discussion

Both the CTRL and CT samples underwent characterization via FESEM to analyze the impact of the chemical treatment on the lattice surface (Fig. A1). Furthermore, the examination aimed to assess the macrostructure's integrity post-treatment and the presence of unmelted particles.

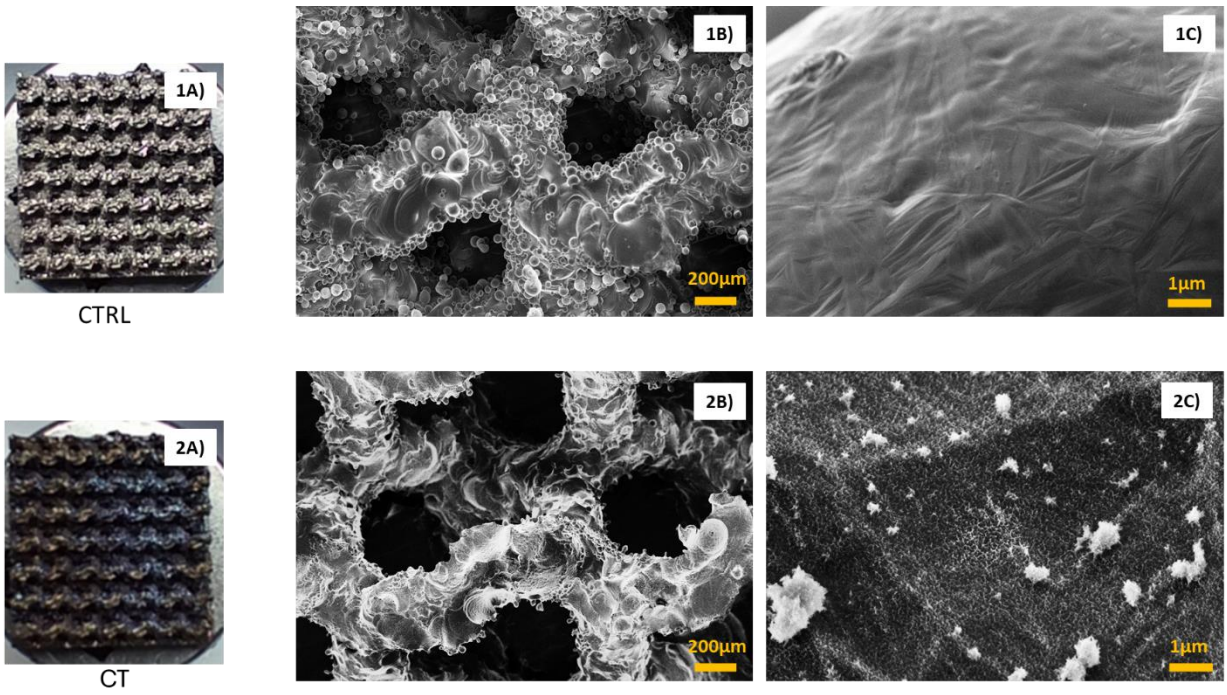

Figure A1. *FESEM images of the surface of CTRL (top row, 1A-C) and CT (bottom row, 2A-C).*

As illustrated in Fig. A1, a noticeable distinction between the CTRL and CT samples was evident to the naked eye, with a discernible color change observed on the surface (Fig. A1A, A2A). Upon closer examination of the lattice macrostructure (Fig. A1B, A2B), fewer unmelted particles were apparent on the surface of the CT-treated lattice, while the integrity of the struts and overall 3D structure remained unaffected. At higher magnification, the characteristic sponge-like nanotexture of the CT-treated sample was clearly visible, dispersed across the surface (Fig. A2C). Moreover, the presence of titanium oxide deposits (depicted as white clusters) was also observed on the CT sample.

To ensure that the CT nanotexture adequately covered the lattice structure throughout its entirety, FESEM images were captured from various regions of a cross-section of the sample (Fig. A2).

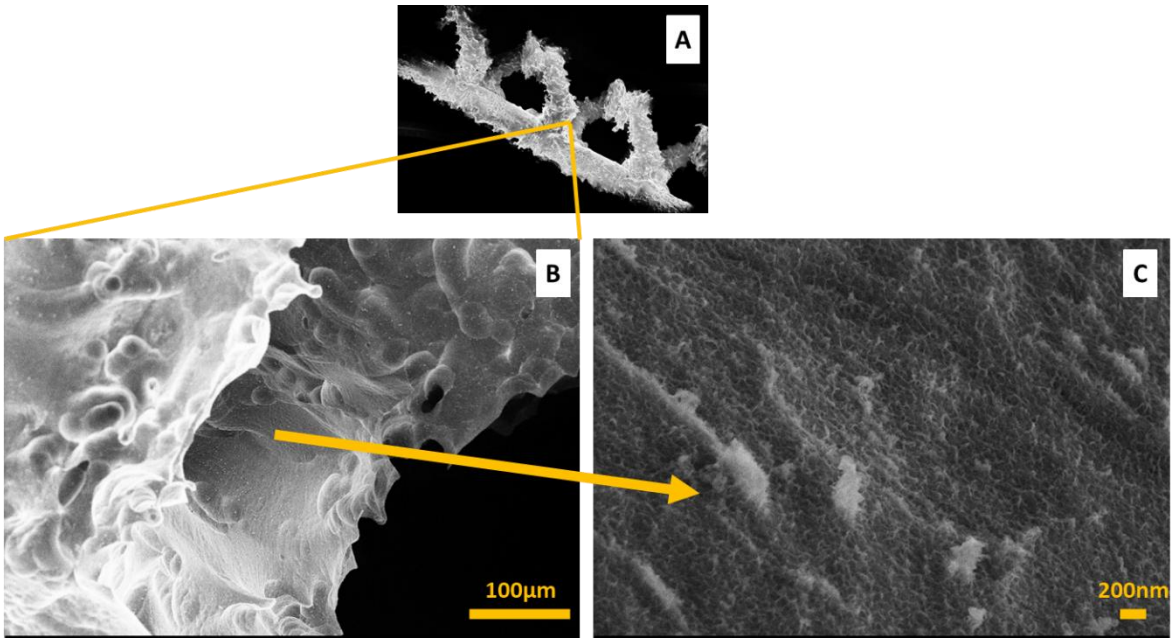

Figure A2. *FESEM images from the cross-section of the CT sample.*

Upon examination of the cross-sectional area of the CT sample, it was observed that the CT nanotexture uniformly covered the entire surface, including within the lattice structure. This observation was validated through images captured from multiple regions, one example of which is depicted in Figure A2.

To further elucidate the impact of the CT etching treatment on lattice structure and morphology, a micro-CT scan was conducted (Fig A3-4, Table A1). Notably, micro-CT scanning can be utilized to evaluate pore structure and size within scaffolds, offering non-destructive visualization and measurement of pore interconnectivity (9).

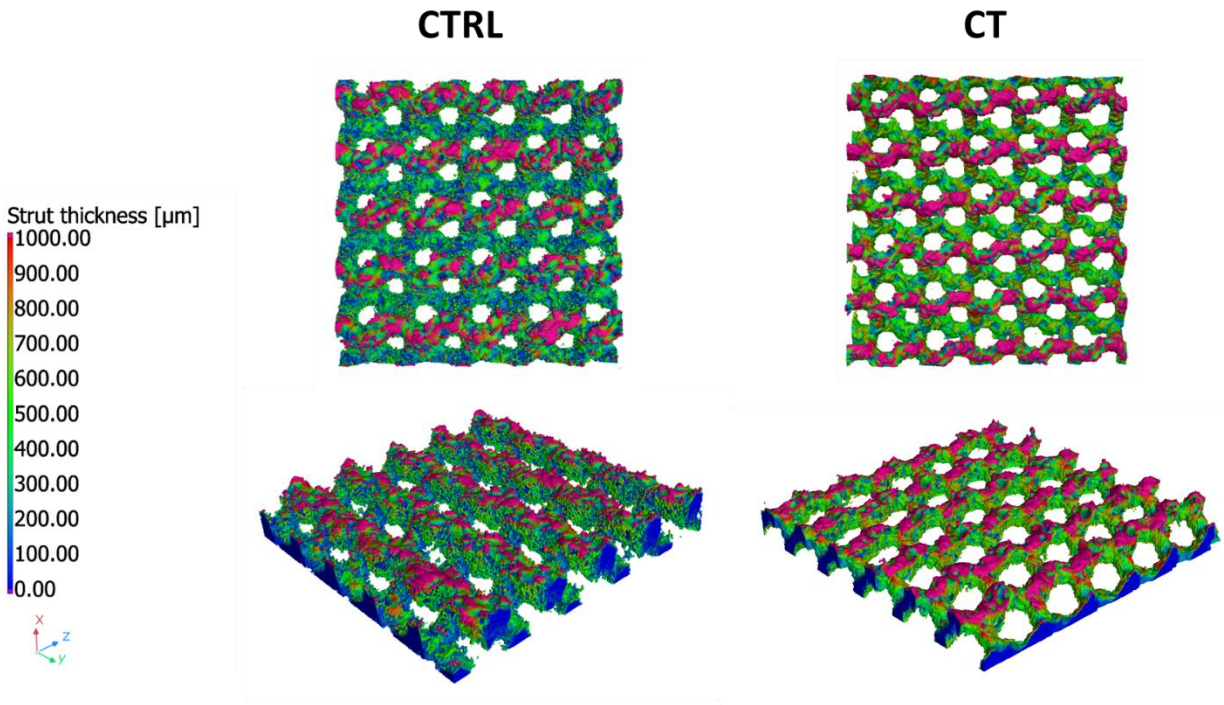

Figure A3. *The strut thickness (µm) of both CTRL and CT samples obtained from micro-CT scan.*

Once more, the elimination of unmelted particles is prominently evident in the micro-CT images. Concurrently, there was an observable increase in pore size, likely attributed in part to this particle removal. Notably, there appeared to be minimal difference in strut size before and after CT etching treatment. Previous studies have underscored the significance of post-processing methods, such as chemical or electrochemical techniques, in eliminating unmelted particles from the internal structure of titanium scaffolds fabricated via SLM (4). Additionally, the size of pores within the lattice structure can impact the ease of unmelted particle removal, with larger pore sizes facilitating this process (10).

Evaluation of pore size and total porosity was conducted from the top view of the CT images, with the results, along with strut thickness measurements, compiled in Table A1.

Table A1. *The strut thickness, total porosity and average pore size of CTRL and CT samples calculated by using the Feret diameter.*

	Strut thickness (mean ± stdev.)	**Pore size**		**Total porosity (%Area)**
CTRL	284 ± 100.30 µm	**MaxFeret** 579.14 µm	**MinFeret** 429.74 µm	13.78 %
CT	267 ± 74.47 µm	**MaxFeret** 990.90 µm	**MinFeret** 687.79 µm	23.78 %

The calculated values for strut thickness exhibit minimal variance between each other. In addition to the impact of acid etching, the observed variability in strut diameters within lattice structures may stem from partially entrained particles embedded in the struts at the interface between melted and unmelted powder (11). Conversely, as evidenced by the micro-CT images and summarized in Table A1, the CT sample demonstrated larger pore sizes ranging from 690-990 µm compared to the CTRL sample's range of 430-580 µm. Additionally, the total porosity increased from approximately 14% to nearly 24% with the CT sample.

Pore size plays a crucial role in determining mechanical properties and biocompatibility. Literature presents differing viewpoints on the optimal pore size for bone scaffolds. Some studies suggest that pore sizes between 200 and 600 µm are generally suitable for tissue-engineered scaffolds, allowing ample space for osteoblasts and vascular tissue ingrowth (12). Conversely, others advocate for a broader range of mean pore sizes from 200 to 1,600 µm with porosity reaching nearly 60% for bone tissue engineering scaffolds (13). Consequently, it will be imperative to assess in future investigations whether the CT sample exhibits lower mechanical strength compared to the CTRL sample due to the increased pore size

and total porosity. A specific design of the 3D structure, including the pore size, can be developed taking into account the modification induce by the etching step to get the target lattice at the end of the overall manufacturing process.

Conclusion

In this investigation, Ti6Al4V alloy samples featuring a 3D lattice structure, produced via SLM, underwent a chemical treatment aimed at establishing a nanotextured titanium oxide layer on the surface, characterized by multiscale topography. Through analyses employing FESEM and micro-CT, it was observed that the lattice structure of the CT sample was effectively covered with a uniform nanotexture, preserving the integrity of the macrostructure. Furthermore, the CT-treated sample surface exhibited minimal presence of unmelted particles within the lattice. Interestingly, pore size enlargement was noted on CT samples, while strut thickness remained comparable to untreated CTRL samples. Overall, these findings represent a promising foundation for subsequent biological investigations and a possible realization of multifunctional surfaces with added active antibacterial agents on the surface by surface functionalization techniques.

References

1. Ferraris S, Spriano S. Porous Titanium by Additive Manufacturing: A Focus on Surfaces for Bone Integration. Metals. 2021 Sep;11(9):1343.

2. Distefano F, Pasta S, Epasto G. Titanium Lattice Structures Produced via Additive Manufacturing for a Bone Scaffold: A Review. J Funct Biomater. 2023 Mar;14(3):125.

3. Sing SL, An J, Yeong WY, Wiria FE. Laser and electron-beam powder-bed additive manufacturing of metallic implants: A review on processes, materials and designs. J Orthop Res. 2016;34(3):369–85.

4. Wysocki B, Idaszek J, Szlązak K, Strzelczyk K, Brynk T, Kurzydłowski KJ, et al. Post Processing and Biological Evaluation of the Titanium Scaffolds for Bone Tissue Engineering. Materials. 2016 Mar;9(3):197.

5. Ferraris S, Cochis A, Cazzola M, Tortello M, Scalia A, Spriano S, et al. Cytocompatible and Anti-bacterial Adhesion Nanotextured Titanium Oxide Layer on Titanium Surfaces for Dental and Orthopedic Implants. Front Bioeng Biotechnol [Internet]. 2019 May 9 [cited 2024 Apr 17];7. Available from: https://www.frontiersin.org/articles/10.3389/fbioe.2019.00103

6. Ferraris S, Venturello A, Miola M, Cochis A, Rimondini L, Spriano S. Antibacterial and bioactive nanostructured titanium surfaces for bone integration. Appl Surf Sci. 2014 Aug 30;311:279–91.

7. Ferraris S, Spriano S, Pan G, Venturello A, Bianchi CL, Chiesa R, et al. Surface modification of Ti–6Al–4V alloy for biomineralization and specific biological response: Part I, inorganic modification. J Mater Sci Mater Med. 2011 Mar 1;22(3):533–45.

8. Merkus HG. Particle Size, Size Distributions and Shape. In: Merkus HG, editor. Particle Size Measurements: Fundamentals, Practice, Quality [Internet]. Dordrecht: Springer Netherlands; 2009 [cited 2024 Apr 17]. p. 13–42. Available from: https://doi.org/10.1007/978-1-4020-9016-5_2

9. Bartos M. MICRO-CT IN TISSUE ENGINEERING SCAFFOLDS DESIGNED FOR BONE REGENERATION: PRINCIPLES AND APPLICATION. Ceram - Silik. 2018 Mar 5;194–9.

10. Pawlak A, Szymczyk P, Ziolkowski G, Chlebus E, Dybala B. Fabrication of microscaffolds from Ti-6Al-7Nb alloy by SLM. Rapid Prototyp J. 2015 Jan 1;21(4):393–401.

11. Xiao L, Song W, Wang C, Liu H, Tang H, Wang J. Mechanical behavior of open-cell rhombic dodecahedron Ti–6Al–4V lattice structure. Mater Sci Eng A. 2015 Jul 29;640:375–84.

12. Yu H, Matthew HW, Wooley PH, Yang SY. Effect of porosity and pore size on microstructures and mechanical properties of poly-ε-caprolactone-hydroxyapatite composites. J Biomed Mater Res B Appl Biomater. 2008;86B(2):541–7.

13. Choudhary N, Ghosh C, Sharma V, Roy P, Kumar P. Investigations on effect of pore architectures of additively manufactured novel hydroxyapatite coated PLA/Al2O3 composite scaffold for bone tissue engineering. Rapid Prototyp J. 2023 Jan 1;29(5):1061–79.

APPENDIX B: Human T-Cell Responses to Metallic Ion-Doped Bioactive Glasses

Hugo Abreu [1,2] , Mari Lallukka [3] , Marta Miola [3] , Silvia Spriano [3] , Enrica Vernè [3] , Davide Raineri [1,2] , Massimiliano Leigheb [1,4], Mario Ronga [1,4] , Giuseppe Cappellano [1,2,*,†] and Annalisa Chiocchetti [1,2,†]

[1] Department of Health Sciences, Interdisciplinary Research Center of Autoimmune Diseases-IRCAD, Università del Piemonte Orientale, 28100 Novara, Italy; hugo.abreu@uniupo.it (H.A.); davide.raineri@med.uniupo.it (D.R.); massimiliano.leigheb@gmail.com (M.L.); mario.ronga@med.uniupo.it (M.R.); annalisa.chiocchetti@med.uniupo.it (A.C.)

[2] Center for Translational Research on Autoimmune and Allergic Diseases-CAAD, Università del Piemonte Orientale, 28100 Novara, Italy

[3] Applied Science and Technology Department, Politecnico di Torino, 10129 Torino, Italy; mari.lallukka@polito.it (M.L.); marta.miola@polito.it (M.M.); silvia.spriano@polito.it (S.S.); enrica.verne@polito.it (E.V.)

[4] Orthopaedics and Traumatology Unit, “Maggiore della Carità” Hospital, 28100 Novara, Italy

[*] Correspondence: giuseppe.cappellano@med.uniupo.it

[†] These authors contributed equally to this work.

Abstract: Biomaterials are extensively used as replacements for damaged tissue with bioactive glasses standing out as bone substitutes for their intrinsic osteogenic properties. However, biomaterial implantation has the following risks: the development of implant-associated infections and adverse immune responses. Thus, incorporating metallic ions with known antimicrobial properties can prevent

infection, but should also modulate the immune response. Therefore, we selected silver, copper and tellurium as doping for bioactive glasses and evaluated the immunophenotype and cytokine profile of human T-cells cultured on top of these discs. Results showed that silver significantly decreased cell viability, copper increased the T helper (Th)-1 cell percentage while decreasing that of Th17, while tellurium did not affect either cell viability or immune response, as evaluated via multiparametric flow cytometry. Multiplex cytokines assay showed that IL-5 levels were decreased in the copper-doped discs, compared with its undoped control, while IL-10 tended to be lower in the doped glass, compared with the control (plastic) while undoped condition showed lower expression of IL-13 and increased MCP-1 and MIP-1β secretion. Overall, we hypothesized that the Th1/Th17 shift, and specific cytokine expression indicated that T-cells might cross-activate other cell types, potentially macrophages and eosinophils, in response to the scaffolds. Keywords: bioactive glasses; multiparametric flow cytometry; immunobiocompatibility; metallic ion doping; tissue regeneration; inflammation

1 Introduction

Musculoskeletal disorders (MSDs) are conditions that restrict movement of the body, causing injury and pain in tissues belonging to the musculoskeletal system, including muscles, bones and joints [1,2]. Among the most prevalent MSDs are osteoarthritis, rheumatoid arthritis, low back pain and bone fractures, generally associated with osteoporosis in the elderly population [1,3]. In fact, with the increase in the average life expectancy observed in the last century, there has been a steady rise in the incidence of MSDs [2]. Individuals affected by MSDs experience a spectrum of pain and discomfort, which depending on the severity of the symptoms, can range from a slight interference with the daily activities to complete movement impairment. Therefore, there is a pressing need for novel

therapies that can alleviate symptoms and improve the quality of life of MSD patients [1]. Biomaterials are designed and engineered to interact with biological systems for medical purposes. These materials play a crucial role in various fields, such as medicine, biotechnology and tissue engineering, where they can be used to replace or enhance natural biological structures or support specific functions within the body [4]. Biomaterials should be immunobiocompatible, meaning that they do not elicit a significant immune response or cytotoxicity when interacting with an organism, but also functional, whether they are functioning as a structural support, as promotors of tissue regeneration or vehicles for drug delivery. Among the different types of biomaterials on the orthopedic field, the most commonly used include the following: metals, more specifically titanium and stainless steel; polymers, either synthetic like polyethylene and polyurethane or natural such as collagen and hyaluronic acid; ceramics, for example, hydroxyapatite; bioactive glasses; and composites, which are the result of the combination of at least two different materials. Depending on their properties, these biomaterials can be used as implants, drug carriers for controlled delivery, artificial tissues/organs or diagnostic devices [5]. Damaged or diseased parts of the musculoskeletal system as well as dental abnormalities can be replaced by bioceramics since they have been modified for load-bearing purposes like bone grafts and cement, hip acetabular cups and dental implants [6,7]. Bioceramics and bioactive glasses have exceptional biocompatibility, corrosion resistance, a hard, crisp surface and osteoconductivity, i.e., the ability of bone-forming cells in the grafting area to migrate across a scaffold and gradually replace it with new bone tissue over time. Furthermore, they can directly interact with the living surrounding tissue and show convincing effects on wound healing after implantation, as in the cases of bioactive glasses and hydroxyapatite (HA). Due to their low friability, they are usually used in dental abnormalities and small bone fillings [7]. Among the described materials, bioactive glasses represent an interesting option due to their excellent biocompatibility and bioactivity. They are able to form a bond with

mineralized bone tissue in the physiological body environment by creating a calcium phosphate layer on their surface [8]. Over fifty years ago, Larry Hench introduced bioactive glasses, more specifically Bioglass® 45S5, the first commercially available glass for medical use [9,10]. The composition of most bioactive glasses is based on silica, sodium oxide, calcium oxide and phosphorous pentoxide. This composition allows for the alteration or combination of these basic elements, enabling the creation of different types of bioactive glasses with specific properties such as bone forming efficiency, degradability, antibacterial properties and even soft tissue regeneration and wound healing [11–13]. When the bioactive glass is implanted, it releases its main ions (calcium, sodium, phosphate and silica) to form carbonated hydroxyapatite (HCA), a bone-like mineral coating, through an ion exchange reaction between the glass surface and the surrounding tissue and fluids [13]. This apatite layer improves cellular adhesion and proliferation of osteogenic cells and it is gradually replaced by bone over time [14,15]. Conversely, excessive ion release may lead to undesired toxicity, therefore affecting cell viability and metabolic activity, which in turn can impair the tissue healing process. To counteract this effect, pre-treating the bioactive glasses prior to entering into contact with cells by incubating the material in cell culture medium or buffer can be a successful strategy [16]. In summary, advancements in biomaterials science have led to the development of increasingly sophisticated materials with tailored properties, enabling innovative solutions in healthcare and biotechnology. Researchers continually explore new biomaterials and their applications to improve patient outcomes and quality of life. However, in a living tissue, when a material is implanted, there will always be a physiologic immune response which represents the first step of tissue repair. Nowadays, biomaterials are being designed considering this immune response and modulating it for improving implant integration, avoiding the chronic inflammatory and foreign body reactions that may lead to the loss of function [17,18]. Fibroblasts and macrophages have been traditionally used for evaluating

biomaterial compatibility, such as in the case of silicone breast implants [19]. In the specific case of musculoskeletal regeneration, cytotoxicity is commonly evaluated on mesenchymal stem/stromal cells (MSCs) and osteoblasts [20], while the role of T-cells in tissue regeneration has only recently been explored; as of today, the reliable data on the role of T-cells are scarce [19,21]. The activation of the immune response requires three signals. Signal 1 is mediated by the binding of the T-cell receptor (TCR) to major histocompatibility complex (MHC) class molecules on antigen-presenting cells (APC); signal 2 is mediated by the engagement of co-stimulatory molecules such as B7.1 (CD80) and B7.2 (CD86) and lastly, cytokines drive the polarization of differentiated T helper (Th) cells towards several subsets, such as T helper (Th)-1, Th2, and to a lesser extent Th17 (signal 3) [22]. T-cells represent up to 70% of peripheral blood mononuclear cells (PBMCs) [23] and are able to modulate bone healing and osteogenesis through cytokine and growth factors secretion [21]. In fact, in vivo experiments showed that T-cell depletion directly impairs the osteoinduction process [24], particularly affecting the deposition of collagen and osteoblast organization [25]. In vitro, conditioned media of CD4+ Th lymphocytes can promote mesenchymal stem/stromal cell (MSC) mineralization [26]. Overall, the aim of this work was to elucidate how the interaction of T-cells with several metal-doped silica-based bioactive glasses, more specifically silver, copper and tellurium, could affect cell viability, T-cell immunophenotype and cytokine secretion. Silver and copper were introduced in the bioactive composition using the ion-exchange process, while tellurium was inserted together with the starting reactants during the glass synthesis via the melt and quenching process. These elements were selected since they have a therapeutic effect; Ag, Cu and Te possess antibacterial properties [27–29], Ag and Cu also have a pro-angiogenic effect [30,31] and Te possesses antioxidant properties [32]. However, the amount must be carefully tailored to avoid cytotoxic effects.

2 Results

Extensive physicochemical surface characterization of the doped glasses were previously reported by the authors [27,32–35]. Table 1 compares the most relevant properties of the glasses, regarding the content of the doped metal obtained via energy-dispersive X-ray spectroscopy (EDS) analysis, and the amount of doped metal ion leaching both in simulated body fluid (SBF) and in a cell medium obtained via inductively coupled plasma (ICP) spectroscopy, either combined via optical emission spectroscopy (OES) or mass spectrometry (MS).

Table 1. Summary of the properties of the doped glasses [33,35]; * α-MEM without added serum, 5% antibiotics, ** DMEM High Glucose, 1% L-Glutamine, 1% antibiotics. None of the used media contained any cells.

	AgSBA2	**CuSBA3**	**STe5**
Doping method	The surface of the glass (Ion exchange in aqueous solution of $AgNO_3$)	The surface of the glass (Ion exchange in aqueous solution of Cu $(CO_2CH_3)_2$)	The bulk of the glass (TeO_2 in the glass network as an oxide
Doped element content at-% (EDS)	0.7 ± 0.36	8.4 ± 0.18	3.4 ± 0.08
Doped ion leaching after 3 days in cell medium	7.9 ± 1.4 ppm * (ICP-OES)	11.0 ± 2.4 ppm * (ICP-OES)	5.6 ± 0.3 ppm ** (ICP-OES)
Doped ion leaching after 3 days in Simulated Body Fluid (SBF)	0.37 ± 0.13 ppm (ICP-MS)	0.14 ± 0.04 ppm (ICP-MS)	0.21 ± 0.07 ppm (ICP-MS)

2.1 Silver, but Not Copper or Tellurium Ion Doping Induces Apoptosis of PBMCs

Ions released from biomaterials upon contact with cell culture media may exert a toxic effect on immune cells. We evaluated the viability of PBMCs via flow cytometry after 48 h of culture, as seen in Figure 1a, using a fixable dye that can only be internalized by cells with permeable membranes, indicative of dead cells. In fact, we observed a of approximately 50%, on average, of PBMC viability when in contact with the silver-doped bioactive glass (Figure 1b),

therefore, this formulation was excluded from the further analysis. No significant differences were observed between the formulations containing copper and tellurium, along with their corresponding controls, when compared to the basal condition lacking any bioactive glass disc.

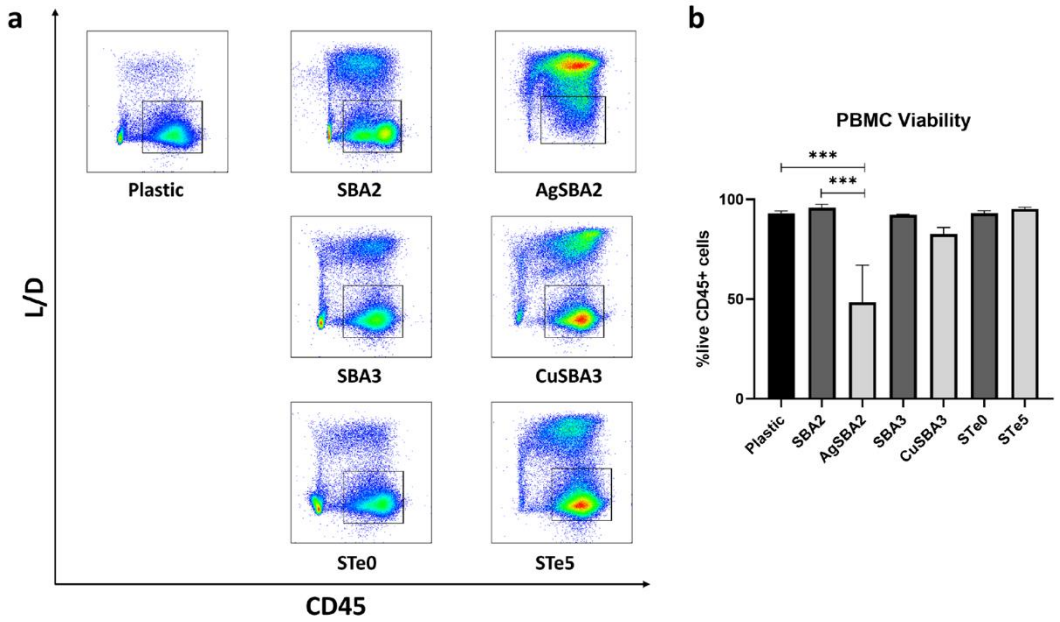

Figure 1. PBMC viability assay via flow cytometry. (a) Gating strategy: Viable lymphocytes were gated as negative for BD Horizon™ Fixable Viability Stain 780 (L/D^-) and $CD45^+$. (b) Bar graph representation of flow cytometry results are shown as average ± SEM. (n = 4). Ordinary one-way ANOVA with Tukey's post-hoc correction test was used. *** $p < 0.001$.

2.2. Immunophenotyping Reveals Th1/Th17 Shift Linked with Copper but Not Tellurium-Doping

To assess the immune response to the metal ion doping, PBMCs were cultured on top of bioactive glasses. In particular, the immunophenotype of T lymphocytes was evaluated via multiparametric flow cytometry, as depicted in Figure 2. The employed gating strategy (Supplementary Figure S1) allowed for the detection of several subsets of T lymphocytes, namely CD4+ T helper (Th) and CD8+ cytotoxic T-cells, further specified as naïve, effector, effector memory (EM) or terminally differentiated EM (TEMRA), based on the expression of CD45RA and CD197, regulatory T-cells (Tregs), CD25+CD127−, as well as Th1, Th2 and Th17, identified by their differential expression of CD183, CD194 and CD196 markers.

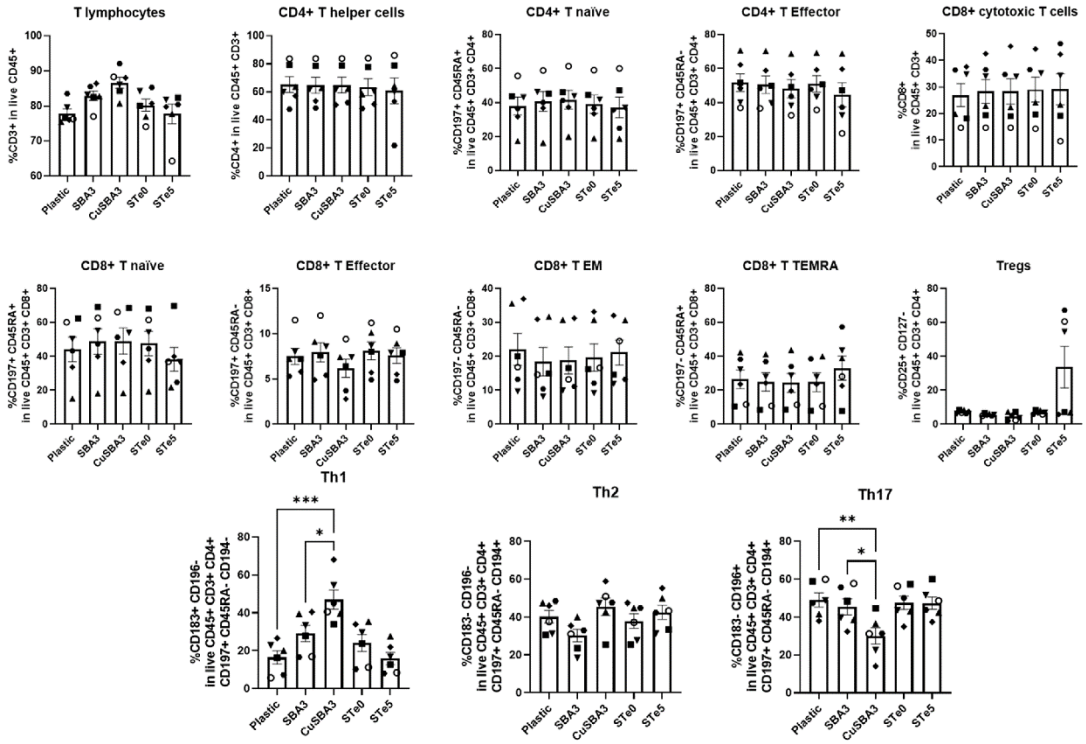

Figure 2. Immunophenotype of T-cells cultured in contact with bioactive glass discs assessed via multiparametric flow cytometry. Graphs represent the percentages of immune cells after 48 h culture without biomaterial (cell culture plate plastic—control), in contact with copper-

doped (CuSBA3) and tellurium-enriched discs (STe5) and their respective undoped controls (SBA3 and STe0, respectively). Data are shown as average ± SEM, (n = 6). Each symbol represents a different donor. According to the data normality (Shapiro–Wilk test), ordinary one-way ANOVA (with Tukey's post-hoc correction) or Kruskal–Wallis test (with Dunn's post-hoc correction) were used. * $p < 0.05$, ** $p < 0.01$, *** $p < 0.001$.

Results showed that T-cells cultured in contact with copper-doped bioactive glass discs exhibited an increased frequency of Th1 population, paralleled by a decrease in Th17 cells, compared with the negative control and to a lesser extent with its undoped counterpart. On the other hand, the tellurium-doped glass did not exhibit any statistically significant differences, although large standard deviations were verified in several subsets, more noticeably in the Treg population.

2.3. Cytokine Profile Response to Ion-Doped Bioactive Glasses

Considering the phenotypical variances observed during PBMC culture related exclusively to the copper-doped glass, in order to verify if the Th1/Th17 shift was paralleled by differential cytokine secretion, a further cytokine quantification ELISA was performed using a commercial multiplex kit. This comprised seventeen cytokines released from macrophage or T-cells exclusively, or by both cell populations (Figure 3). Among these, levels of GM-CSF and IL-4 were close to, or below the lower limit of quantification and thus, were not suitable for statistical comparison.

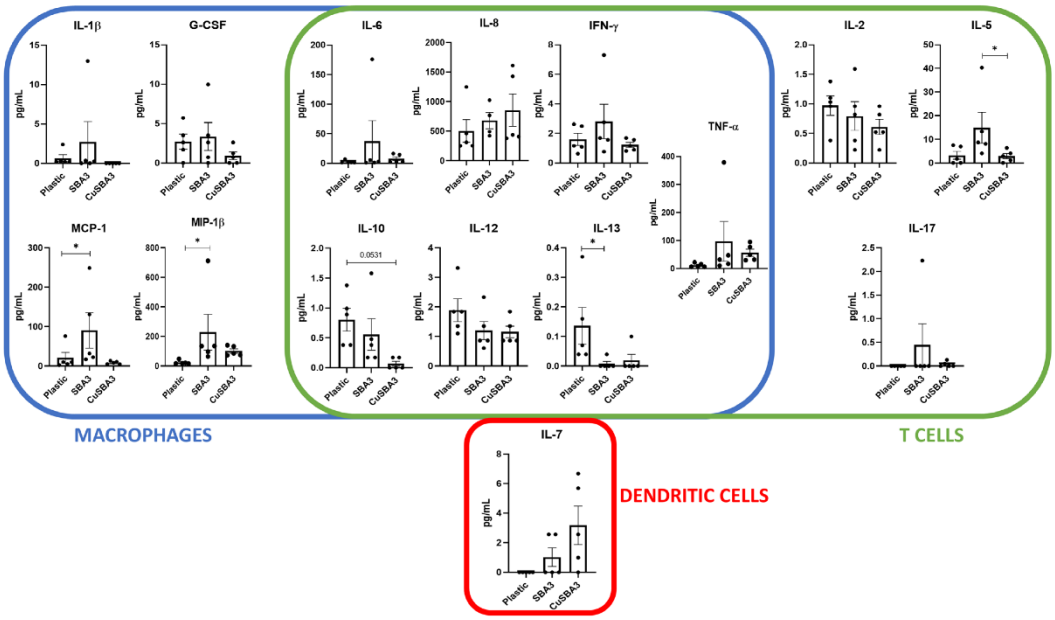

Figure 3. Cytokine expression levels of supernatants of PBMC culture in contact with copper-doped bioactive glass discs (CuSBA3) and its respective control (SBA3). Data are shown as average ± SEM, (n = 5). According to the data normality (Shapiro–Wilk test), RM one-way ANOVA (with Bonferroni post-hoc correction) or the Friedman test (with Dunn's post-hoc correction) were used. * $p < 0.05$.

We found a significantly reduced concentration of IL-5 in the supernatant of PBMCs cultured in contact with the copper-doped glasses condition, compared with its undoped counterpart. Copper-doped glasses also showed a trend in the decrease in IL-10 cytokine secretion in comparison with the control (plastic). Furthermore, IL-13 levels were significantly decreased in the undoped condition in comparison with plastic, while MCP-1 and MIP-1β cytokines were significantly increased. These findings indicated that the copper-doped bioactive glass exhibited a more similar cytokine profile to the plastic rather than to its respective undoped bioactive glass discs.

3 Discussion

Bioactive glasses commonly release their ions to the surrounding microenvironment. This opens the possibility of incorporating biologically active ions into their composition or onto their surface, which upon release, may promote specific biological functions such as cell proliferation or angiogenesis, or confer novel properties to the bioactive glass, for example an antimicrobial effect [36]. Thus, silver, copper and tellurium have been used as doping ions on the surface of bioactive glass discs. For Ag- and Cu-doped glass, the ion doping was performed via ion exchange which introduced the ions only on to the glass surface, while in the case of STe5, tellurium was part of the bulk glass network. These ions have already been studied in the context of their antimicrobial [27,28,29] and pro-angiogenic effects [30,31], as well as in bone tissue regeneration and cancer [37,38,39]. Nevertheless, the data regarding the impact of these formulations on T-cells are scarce. Considering this, and to extend the knowledge provided by previous studies on biofilm formation [27,28,32], we evaluated any effects on viability, T-cell immunophenotype and cytokine release of PBMCs cultured in contact with ion-doped bioactive glasses.

The ionic release test was performed using inductively coupled plasma-optical emission spectrometry (ICP-OES) and data on doped ion-leaching in both cell culture medium and simulated body fluid was added to Table 1. Regarding the doping ions' bio-assimilation, it was reported that blood cells like erythrocytes and macrophages are capable of assimilating Cu2+ through copper transporter 1 (CTR1) [40]. Also, silver ions (Ag+) seem to be captured by immune cells, such as neutrophils and macrophages, and exert similar effects as silver nanoparticles, specifically in the formation of neutrophils extracellular traps (NETs) and intracellular reactive oxygen species (ROS) [41]. Lastly, tellurite (TeO_3^{2-}) which releases Te4+ and represents the most abundant form of tellurium in nature, has

been shown not only to bind hemoglobin in erythrocytes but also to react with glutathione and to lead to ROS formation in leukocytes [42]. The cytotoxicity of the released ions (Ag+, Cu2+, Te4+) on different cell lines was investigated in previous reports [27,28,29,30,31], showing a different behavior based on the used method (indirect or direct). Any observed cytotoxic effects, in particular for copper, do not seem to arise from the dissolution products or specific ion concentrations in the medium, but rather from a burst release and contact toxicity with the doped glass surfaces. A recent publication by some of the coauthors used copper-doped bioactive glasses manufactured with the same methodology and evaluated its cytotoxicity using human adipose tissue-derived stem cells (hASCs) [33]. Indirect culture of hASCs with the conditioned media of CuSBA3 discs, soaked for 24 h in α-MEM supplemented with 5% human serum and 1% antibiotics (100 U/mL penicillin and 0.1 mg/mL streptomycin), did not affect cell viability, while direct contact with CuSBA3 led to extreme cytotoxicity. In accordance, when fibronectin was incorporated onto the surface of CuSBA3, ASCs cytocompatibility remained low, since the coating provided support for cell attachment but it did not prevent the direct contact between cells and bioactive glass disc. On the other hand, allowing the excessive burst ion release prior to the cell seeding through a 24 h pre-incubation in α-MEM rendered CuSBA3 cytocompatible [33]. In our study, we tested PBMCs directly cultured on the top of bioactive glasses. These cells mostly comprised non-adherent cells, therefore they tended not to be in direct contact with the bioactive glass discs. Given that, our data on PBMC viability are in line with the prior report regarding the indirect assays performed with adherent hASCs [33], in which the concentration of ions in the solution, about 10,000 μg/L, did not significantly impact cell viability. Overall, the reported cytotoxicity of copper-doped bioactive glasses was likely due to the contact but not necessarily to the concentration in solution.

In our study, we report the highly toxic effect of silver on PBMCs, as demonstrated by significantly reduced viability of PBMCs. Previous studies

showed that the elementary silver in the solution, not doped in any biomaterial, exhibits cytotoxicity in a dose-dependent manner [43]. While generally considered an element with low toxicity [44], there are some clinical data indicating that the exposure to silver may represent the primary cause responsible for damage in cornea, liver, kidney and neurological tissues [45], as well as causing leukopenia [46] and chronic heart inflammation [47]. Moreover, in vitro studies presented some drawbacks of its use, due to a notable impairment of fibroblast [48] and keratinocyte growth [49]. For the above reasons, we opted to focus our attention on the copper- and tellurium-doped formulations for further analyses.

Delving into the T-cell ion-induced phenotype, the main focus of our study, we found that both the tellurium-doped bioactive glass and its undoped control exhibited no discernible impact on the immunophenotype of T-cells. However, we did observe interindividual variability, commonly present when using primary cells, particularly evident in certain subsets, as shown by the high standard deviations detected. In this case, PBMC culture in contact with the tellurium-doped bioactive glass revealed that three out of six donors had a high frequency of Tregs (54.5–67.1%) while the other three donors exhibited a much lower frequency (5.8–7.1%). Also in other subsets, such as CD4+ T helper and CD8+ T TEMRA, albeit less noticeable, we still verified that the culture with the tellurium-doped bioactive glass caused a more variable effect on PBMC phenotype than the other conditions, which might indicate that the response to this element was highly subject-dependent. Although material implantation generally elicits a response by the host, recent biomaterial engineering approaches search to not only modulate it in order to minimize side effects, such as chronic inflammation and foreign body reaction, but also to attempt to improve desirable biological processes, for instance osteointegration [18,50]. Previous reports evidencing the protective effect of the tellurium doping against oxidative stress

coupled with our findings reporting no significant alterations in T-cell phenotype, can indicate that the tellurium-doped bioactive glass can be an interesting alternative to the currently used biomaterials for implantation [32].

On the other hand, culturing PBMCs in contact with the copper-doped bioactive glass led to a significant increase in Th1 cells, accompanied by a decrease in Th17 cells, compared with both its undoped counterpart (ordinary one-way ANOVA with Tukey's post-hoc correction; Th1: SBA3 vs. CuSBA3, p-value = 0.0332; Th17: SBA3 vs. CuSBA3, p-value = 0.0498) and plastic (ordinary one-way ANOVA with Tukey's post-hoc correction; Th1: CuSBA3 vs. Plastic, p-value = 0.0001; Th17: CuSBA3 vs. Plastic, p-value = 0.0097). Both cell subsets were derived from the polarization of naïve T-cells, typically exacerbated upon viral and bacterial infections, inducing cell-mediated immunity, mainly by stimulating antibody secretion from B-cells. In addition, both Th1 and Th17 cells are known for their pro-inflammatory phenotype due to their effector cytokine releases. However, their biogenesis and role in the immune system are different. While Th1 cells are generated in the presence of IL-12, IL-18 and IFN-γ cytokines, Th17 requires IL-6, IL-23 and TGF-β for its polarization. Furthermore, Th1 mainly produce IFN-γ and TNF-α, while Th17 cells generally release IL-17A, IL-17F and IL-22. Consequently, their functions are also distinguishable. Th1 are able to enhance APC activity and CD8+ T-cells/macrophage activation, protect against intracellular pathogens and participate in delayed type hypersensitivity, while Th17 acts on fungal and extracellular bacterial infections. Interestingly, Th subsets can cross-regulate each other, meaning that the secreted products of one cell type can stimulate the polarization of CD4+ naïve cells into another specific subset. Finally, Th cells are known to be highly plastic; Th17 cells are considered less stable and can for example differentiate into Th1 cells given the appropriate environmental setup [22]. As reviewed by Adusei et al., Th subsets are capable of modulating the processes of fibrosis and tissue regeneration through differential cytokine secretion [51]. T-cells were studied on fibrotic tissue

developed upon silicone implantation where an increase in CD4+ T-cells was detected in the capsular tissue, more notably, Tregs. Moreover, Tregs were more prominent in patients with milder symptoms compared to more severe cases, showing also a more suppressive effect in vitro. Additionally, the authors showed an increase secretion of IL-6, IL-8, IL-17, IFN-γ and TGF-β1 by immune cells present in the capsular tissue, indicative of a pro-inflammatory environment sustained by Th1 and Th17 cells [52].

The direct correlation between copper-doping in bioactive glasses and Th subsets is still ill-defined. However, understanding the complex interactions between the different constituents of the immune system can help elucidating this question. Professional APCs, such as dendritic cells (DCs) and macrophages, are responsible for T-cell activation, therefore any modulatory effect on these players can influence the state of Th cells [22]. Dey et al. reported that the addition of copper oxide nanoparticles to lymphocytes or macrophages in vitro leads to an increase in TNF-α, IFN-γ and IL-12 production; the latter two directly promote the polarization of CD4+ T-cells towards the Th1 phenotype [53]. Although we have not detected any significant changes regarding the aforementioned cytokines, it should be noted that we have evaluated the cytokine levels at 48 h instead of the 24 h used by the authors. Additionally, the physicochemical properties of nanoparticles also differ from the bulk materials, which may lead to slightly diverse biological reactions [54]. Nevertheless, the increase in the percentage of Th1 cells upon culture in contact with the copper-doped bioactive glass in our setting might indicate a similar pro-inflammatory effect of the copper doping.

Schuhladen et al. have evaluated the effect of increasing concentrations of copper-doped bioactive glass nanoparticles (Cu-BG-NPs) on murine DCs' phenotype and function. The authors found that the conditioned media containing the ionic dissolution products of Cu-BG-NPs significantly reduced the expression

of CD80 and CD86, the two ligands of CD28, which are essential for T-cell activation. Coupling the phenotype results with the cytokine expression evaluation, the authors concluded that higher concentrations of copper led to a decrease in the secretion of various cytokines such as IL-6 [55]. As previously mentioned, IL-6 is one key factor for the polarization of Th17 cells, therefore its copper-induced reduction might lead to a lower frequency of Th17 cells, which is in line with our results.

Interestingly, the cytokine evaluation of supernatants from PBMC culture with the copper-doped bioactive glass revealed a distinct pattern, different to what had been previously described. IL-5 was revealed as the only cytokine being significantly modulated between the copper-doped and its undoped control. Within the immune system, IL-5 is commonly produced by Th2, innate lymphoid cells type 2 (ILC2), mast cells, natural killer cells and eosinophils, acting particularly on eosinophil and B-cell growth [56,57]. In our setting, this cytokine appeared to be downmodulated in the copper-doped bioactive glass, achieving values similar to the negative control. Strikingly, another member of its family typically associated with Th2 response [58], namely IL-13, showed an inverse pattern, being under expressed in the undoped control in comparison with both other conditions. Notably, the proportion of Th2 cells did not change according to our immunophenotype results, even though their biological processes could be differentially modulated, therefore resulting in diverse secreted products.

Although often associated, even potentially acting upon some of the same molecules such as the signal transducer and activator of transcription 6 (STAT6), IL-5 and IL-13 are markedly different. As reviewed by Wu et al., IL-5 is mostly responsible for eosinophils' biological processes and survival, while IL-13 impacts more directly the B-cells and the Th2 subset [59]. Comparing with our results, the overexpression of IL-5 accompanied by a downregulation of IL-13 might lead to IL-5-mediated eosinophil activation, produced by Th2 cells.

Therefore, it would be relevant to clarify through in vivo testing the role of eosinophils in this context, considering that the tested PBMC fraction should contain only a residual percentage of these cells. In fact, the formation of eosinophilic clusters had been reported in mice after six weeks of bioactive glass implantation, which the authors considered a sign of a possible allergic reaction [60]. Overall, we consider that in the SBA3 condition, the IL-5 likely produced by Th2 cells will or could favor eosinophil activation instead of B-cells, due to the lack of IL-13.

Conversely, two chemokines were upregulated in the undoped bioactive glass, more specifically MCP-1/CCL2 and MIP-1β/CCL4, which are responsible for immune cell recruitment. Both are mostly produced by cells from the myeloid lineage, i.e., monocytes, macrophages and dendritic cells, although they can also be released by T-cells [61,62]. These cytokines have been already linked with the immune response to biomaterials, being secreted by neutrophils [63], macrophages [64] and T-cells [65] (reviewed in [18]). The fact that these pro-inflammatory chemoattractant molecules were significantly more present in the undoped condition might favor macrophage polarization into M1 phenotype, which can be responsible for balancing the inflammatory microenvironment [66], acting as a counterpart of the activated eosinophils.

Of note, no significant differences were found at the cytokine level between the copper-doped condition and the basal condition, without any bioactive glass, although in the case of IL-10, a trend of reduced production upon PBMC culture with the copper-doped discs was observed. The impact of this cytokine in fibrosis seems a paradox. While it is commonly linked to a type 2 response [66], it may also play a role in preventing or reducing the effects of fibrosis [67], therefore further research on this topic is needed (reviewed in [68]).

Our study presents some limitations. Macrophages are among the first cell types to interact with implants, therefore being the main focus of numerous studies that explore the impact of implants in the immune system. The multiplex ELISA panel used in this study allowed for an overview of the cytokines released by PBMCs due to the contact with the bioactive glasses, it did not permit the direct association of the cytokine profile with a specific subset, such as macrophages. Nevertheless, among the cytokines evaluated in PBMC cultures, two were mainly ascribed to macrophages, such as MCP-1 and MIP-1β. Even though the literature already describes the modulation of cytokine release in macrophages by metal ion-doped bioactive glasses, including copper [69,70,71,72,73], it would be of interest to complete the analysis of T-cell immunophenotyping with their interaction with macrophages by polarizing them in vitro. Second, we had to take into account our sample size and the observed variability of donors in their response to the different biomaterial. This variability reflected the diverse genetic backgrounds, immune statuses, and physiological conditions of individual donors that may affect the response. Third, our experimental design investigated the effects of each biomaterial in a static way, though in vivo, these biomaterials are aimed at repairing and reconstructing the defective bone which is a dynamic tissue and subjected to mechanical stress. Lastly, the tissue microenvironment could also induce the release of ions from each biomaterial by affecting the T-cell/macrophages interaction, even by modulating macrophage polarization, shifting them towards an anti-inflammatory profile [74].

Overall, the fact that the cytokine profile of the copper-doped bioactive glass was similar to the plastic control, together with the favoring of the Th1 response according to the immunophenotyping assay, indicates that copper-doping might be a valid strategy to prevent fibrotic tissue formation.ay, indicates that copper-doping might be a valid strategy to prevent fibrotic tissue formation.

4. Materials and Methods

4.1. Bioactive Glasses Preparation

In the present study, silica-based bioactive glasses were used as bulk discs. These materials were prepared and characterized as previously reported [27,32,33,34,35]. Briefly, the composition of SBA2 and SBA3 (undoped controls) are shown in Table 2.

Table 2. Composition of SBA2 and SBA3 control bioactive glasses.

Components	SBA2 (% mol)	SBA3 (% mol)
SiO_2	48	48
Na_2O	18	26
CaO	30	22
P_2O_5	3	3
B_2O_3	0.43	0.43
Al_2O_3	0.57	0.57

SBA2 and SBA3 were prepared via the melt and quenching process. The reactants were melted in a platinum crucible at 1450 °C for 1 h Subsequently, the melt was cooled in a brass mold to obtain glass bars, which were then annealed at 500 °C for 13 h and cut into slices of 2 mm thickness and about 1 cm in diameter. Then, the slices were polished with SiC abrasive papers up to 1200 grit to level the surfaces. Lastly, the introduction of silver (Ag^+) and copper (Cu^{2+}) ions onto

the surface of SBA2 and SBA3, respectively, was achieved through the ion-exchange process. The discs were submerged in an aqueous solution of either $AgNO^3$ (30 mM) or $Cu(CH^3COO)^2$ (1 mM) for 1 h, at 37 °C.

In the case of Te-doped glass (STe5), tellurium was directly introduced into the composition of the bioactive glass (named STe0) as a substitute for silica, as reported in Table 3.

Table 3. Composition of the STe0 control bioactive glass and STe5-doped bioactive glass.

Components	STe0 (% mol)	Ste5 (% mol)
SiO_2	48.6	43.6
Na_2O	16.7	16.7
CaO	34.2	34.2
P_2O_5	0.5	0.5
TeO_2	0.0	5.0

STe0 and STe5 were also prepared via the melt and quenching process. In this case, the reactants were melted in a platinum crucible at 1500 °C for 1 h, and then cooled in a brass mold to obtain glass bars, that were annealed at 550 °C for 13 h. These bars were cut into slices of similar dimensions as the previous discs and polished as before. All the aforementioned samples were sterilized by heating to 100 °C for 3 h.

4.2. Ion Release in Simulated Body Fluid (SBF) and Cell Medium

The ICP analyses summarized in Table 1, except for STe5, were previously published and reported [33,35]. The glass samples of STe5 were subjected to in vitro bioactivity tests by soaking them in simulated body fluid (SBF). The SBF was prepared using the protocol developed by Kokubo et al. [75]. Polished glass discs were immersed in 50 mL of SBF for fixed periods (1, 3, 7, 14, 28 days, here reported only 3-day timepoint) with five replicate samples of each glass per time point. Samples were maintained at 37 °C in an incubating shaker with an orbital speed of 120 rpm to simulate the physiological fluid flow. Solution at each time point was collected and the cumulative ion release for each sample was calculated by adding the ion release value at the selected time point to the previous ones. In the case of Te-ion release in cell medium (DMEM high glucose medium (Euroclone, Pero, Italy), supplemented additionally by penicillin/streptomycin and L-Glutamine (1% of both), STe5 specimens were soaked in the medium without FBS, 1.5 mL per disk in triplicates. Samples were maintained in the solution for 3 days, at 37 °C, 5% CO2 incubation. From both SBF and cell medium collected samples, the Te-ion release was determined via an inductively coupled plasma mass spectrometer (ICP-MS, iCAPTM Q, Thermo Fisher Scientific, Waltham, MA, USA).

4.3. Blood Specimen Collection

Peripheral blood was obtained from six healthy adult donors (25–45 years old) in cooperation with the Hospital Maggiore della Carità, Novara, Italy. From each donor, 10 mL of peripheral blood was withdrawn into lithium heparin collection tubes and immediately processed. The study was approved by the local ethics committee (prot. n. 675/CE).

4.4. Peripheral Blood Mononuclear Cells (PBMCs) Isolation

PBMCs were isolated from heparinized blood samples collected from healthy donors. The blood samples were mixed with equal amounts of phosphate buffer saline (PBS 1×) and were carefully overlaid on top of a density gradient isolation solution, Lympholyte-H (Cedarlane®, Burlington, ON, Canada). After centrifugation, the cell ring at the interface was collected, washed with PBS 1X, and cells were counted.

4.5. Assessment of Cell Viability via Flow Cytometry

PBMCs from four healthy adult donors were cultured in RPMI 1640, supplemented with 10% (v/v) heat-inactivated FBS, 100 U/mL penicillin/streptomycin, and 100 µg/mL gentamicin (Life technologies, Carlsbad, CA, USA), at 37 °C and 5% CO2. A total of 1 × 106 fresh cells/mL were seeded onto sterile discs of bioactive glasses (or in wells without bioactive glasses—negative control) for 48 h, keeping the polished side upwards. Afterwards, the media was removed, and cells were collected and washed with PBS-EDTA 2 mM. The cells were stained with a viability dye (BD Horizon™ Fixable Viability Stain 780 (Becton and Dickinson, Franklin Lakes, NJ, USA)) for 15 min, at 4 °C, to distinguish live and dead cells. After washing with PBS-EDTA, Human BD™ Fc block solution was added to block the non-specific binding of immunoglobulin to Fc receptors. Subsequently, cells were incubated with antiCD45 BUV395 mAb (clone: HI30), a pan-marker for all leukocytes. Lastly, the cells were washed and resuspended in PBS-EDTA for acquisition using a BD FACSymphony™ A5 flow cytometer (BD Biosciences, Franklin Lakes, NJ, USA). The samples were then analyzed using the BD FACSDIVA™ software version 9.0.

4.6. Immunobiocompatibility Assay

PBMCs from six healthy adult donors were cultured as previously described. After media removal, cells were washed with PBS-EDTA 2 mM and stained with a viability dye (BD Horizon™ Fixable Viability Stain 780) for 15 min, at 4 °C. Cells were then washed with PBS-EDTA and Human BD™ Fc block solution was added. Antigen surface staining was performed by adding an antibody mix containing mouse antiCD3 BUV496 monoclonal antibody (mAb) (clone: UCHT1), antiCD4 BUV737 mAb (clone: SK3), antiCD8 BUV805 mAb (clone: SK1), antiCD25 APC-R700 mAb (clone: 2A3), antiCD45 BUV395 mAb (clone: HI30), antiCD127 BV786 mAb (clone: HIL-7R-M21), antiCD45RA BUV563 mAb (clone: HI100), antiCD183 APC mAb (clone: IC6), antiCD194 PE-CF594 mAb (clone: 1G1), antiCD196 BV480 mAb (clone: 11A9) and antiCD197 BV711 mAb (clone: 150503) in BD Horizon™ Brilliant Stain Buffer for 20 min, at 4 °C. Lastly, the cells were washed and resuspended in PBS-EDTA for acquisition using a BD FACSymphony™ A5 flow cytometer. Data were then analyzed using the BD FACSDIVA™ software version 9.0. All reagents were purchased from Becton and Dickinson (Franklin Lakes, NJ, USA).

4.7. Enzyme-Linked Immunosorbent Assay (ELISA)

PBMCs from five healthy adult donors were cultured as previously described. Cell culture supernatants were collected after 48 h and cytokine levels were quantified using the Bio-Plex Pro Human Cytokine 17-plex Assay according to manufacturer's instructions (Bio-Rad, Hercules, CA, USA). This assay allows for the detection of a wide array of cytokines, specifically: G-CSF, GM-CSF, IFN-γ, IL-1β, IL-2, IL-4, IL-5, IL-6, IL-7, IL-8, IL-10, IL-12, IL-13, IL-17A, MCP-1, MIP-1β and TNF-α. The plate was run on a Bio-Plex 200 instrument (Bio-Rad, Hercules, CA, USA). The reported concentrations and detection limits were obtained through the standard curves generated by the kit's standards, using the

weighted 5PL curve fitting procedure in Bio-Plex Software Manager ™ version 6.2. Values under the lower limit of quantification (LLOQ) were extrapolated based on the 5PL logistic curve, as previously reported [76].

4.8. Statistical Analysis

Data were analyzed using one-way ANOVA, Friedman or Kruskal–Wallis test with post-hoc correction, according to the sample's normality, calculated using the D'Agostino–Pearson test. p-value below 0.05 was considered statistically significant. Statistical analyses were performed with GraphPad Instat software (Prism 8 version 8.4.3) (GraphPad Software, San Diego, CA, USA).

5 Conclusions

Although bioactive glasses have been used especially for hard tissue regeneration during the last decades, the complete evaluation of immune reaction towards these biomaterials is often lacking. Our approach targeted T-cells that can be responsible for many regulatory functions in the organism including inflammation, which is essential for tissue regeneration. Our findings showed not only that metal ion doping can cause the apoptosis of immune cells and modulate the expression of certain subsets of T-cells in vitro, but it can also impact the cytokine release. Our study reported the highly toxic effect of silver-doping on PBMCs, comparable to the known dose-dependent cytotoxicity of this element in solution, indicating that this formulation required further optimization before being used in in vivo studies. Even though tellurium-enriched bioactive glass did not notably affect PBMC viability, the presence of tellurium elicited a highly variable T-cell response among individuals, most notably within the Treg subset. Additional research is necessary to investigate the distinct immune responses of each individual to the presence of this ion. In regards to the copper-doping, we postulated that the Th17 to Th1 switch, together with the alteration in cytokines such as IL-5 and IL-13 and the chemokines MCP-1/CCL2 and MIP-1β/CCL4, can

modulate the immune response to bioactive glass implantation through cross-activation of cell types other than T lymphocytes, such as macrophages and possibly eosinophils. More importantly, the incorporation of copper on the surface of the bioactive glass greatly brought back the cytokine expression to the basal condition without biomaterial by improving its immunobiocompatibility.

Further studies are also needed to evaluate the effect of copper-doped bioactive glass in in vivo settings, where all the relevant players in the inflammatory response associated with tissue regeneration are present.

Supplementary Materials

The following supporting information can be downloaded at: https://www.mdpi.com/article/10.3390/ijms25084501/s1.

Author Contributions

Conceptualization S.S., E.V. and A.C.; methodology H.A. and M.L. (Mari Lallukka); software, D.R.; validation, D.R.; formal analysis, H.A. and G.C.; investigation, H.A. and G.C.; resources, A.C.; data curation, H.A.; writing—original draft preparation, H.A.; writing—review and editing, H.A., G.C. and A.C.; visualization, H.A.; supervision, M.M., M.L. (Massimiliamo Leigheb), M.R., S.S., E.V., G.C. and A.C.; project administration, A.C.; funding acquisition, A.C. All authors have read and agreed to the published version of the manuscript.

Funding

This research was funded by the European Union's Horizon 2020 Research and Innovation Program under the Marie Skłodowska-Curie grant agreement No. 860462-Project PREMUROSA to H.A., M.L. and A.C. This publication is part of

the project NODES, which has received funding from MUR—M4C2 1.5 of the PNRR with grant agreement No. ECS00000036 to G.C. and the European Union's Horizon 2020 Research and Innovation Program under Grant Agreement No. 953121, project FLAMIN-GO to A.C.

Institutional Review Board Statement

The study was conducted in accordance with the Declaration of Helsinki and approved by the Ethics Committee of the University of Eastern Piedmont (protocol OCEANIA 9/21).

Informed Consent Statement

Informed consent was obtained from all subjects involved in the study.

Data Availability Statement

The authors declare that the data supporting the findings of this study are included within the article or Supplementary Materials and are available from the corresponding author upon reasonable request.

Acknowledgments

We would like to thank the Next-Gen Flow Cytometry & Sorting Facility and the Protein Technologies Unit at the Center for Translational Research on Autoimmune and Allergic Diseases-CAAD, University of Eastern Piedmont, Novara, for their technical support. We would also like to thank Elżbieta Pańczyszyn for her assistance and Nataša Kustrimovic for language editing.

Conflicts of Interest

The authors declare no conflicts of interest.

References

1. Abreu, H.; Canciani, E.; Raineri, D.; Cappellano, G.; Rimondini, L.; Chiocchetti, A. Extracellular Vesicles in Musculoskeletal Regeneration: Modulating the Therapy of the Future. Cells 2022, 11, 43.

2. Cieza, A.; Causey, K.; Kamenov, K.; Hanson, S.W.; Chatterji, S.; Vos, T. Global Estimates of the Need for Rehabilitation Based on the Global Burden of Disease Study 2019: A Systematic Analysis for the Global Burden of Disease Study 2019. Lancet 2020, 396, 2006–2017.

3. Shen, Y.; Huang, X.; Wu, J.; Lin, X.; Zhou, X.; Zhu, Z.; Pan, X.; Xu, J.; Qiao, J.; Zhang, T.; et al. The Global Burden of Osteoporosis, Low Bone Mass, and Its Related Fracture in 204 Countries and Territories, 1990–2019. Front. Endocrinol. 2022, 13, 882241.

4. Agrawal, R.; Kumar, A.; Mohammed, M.K.A.; Singh, S. Biomaterial Types, Properties, Medical Applications, and Other Factors: A Recent Review. J. Zhejiang Univ. Sci. A 2023, 24, 1027–1042.

5. Freitas, J.; Santos, S.G.; Gonçalves, R.M.; Teixeira, J.H.; Barbosa, M.A.; Almeida, M.I. Genetically Engineered-MSC Therapies for Non-Unions, Delayed Unions and Critical-Size Bone Defects. Int. J. Mol. Sci. 2019, 20, 3430.

6. Salinas, A.J.; Vallet-Regí, M. Bioactive Ceramics: From Bone Grafts to Tissue Engineering. RSC Adv. 2013, 3, 11116–11131.

7. Pina, S.; Reis, R.L.; Oliveira, J.M. Ceramic biomaterials for tissue engineering. In Fundamental Biomaterials: Ceramics; Chapter 4; Elsevier: Maryland Heights, MO, USA, 2018.

8. Negut, I.; Ristoscu, C. Bioactive Glasses for Soft and Hard Tissue Healing Applications—A Short Review. Appl. Sci. 2023, 13, 6151.

9. Hench, L.L.; Splinter, R.J.; Allen, W.C.; Greenlee, T.K. Bonding Mechanisms at the Interface of Ceramic Prosthetic Materials. J. Biomed. Mater. Res. 1971, 5, 117–141.

10. Hench, L.L. The Story of Bioglass®. J. Mater. Sci. Mater. Med. 2006, 17, 967–980.

11. Ali, S.; Farooq, I.; Iqbal, K. A Review of the Effect of Various Ions on the Properties and the Clinical Applications of Novel Bioactive Glasses in Medicine and Dentistry. Saudi Dent. J. 2014, 26, 1–5.

12. Miguez-Pacheco, V.; Hench, L.L.; Boccaccini, A.R. Bioactive Glasses beyond Bone and Teeth: Emerging Applications in Contact with Soft Tissues. Acta Biomater. 2015, 13, 1–15.

13. Cannio, M.; Bellucci, D.; Roether, J.A.; Boccaccini, D.N.; Cannillo, V. Bioactive Glass Applications: A Literature Review of Human Clinical Trials. Materials 2021, 14, 5440.

14. Kaur, G.; Kumar, V.; Baino, F.; Mauro, J.C.; Pickrell, G.; Evans, I.; Bretcanu, O. Mechanical Properties of Bioactive Glasses, Ceramics, Glass-Ceramics and Composites: State-of-the-Art Review and Future Challenges. Mater. Sci. Eng. C 2019, 104, 109895.

15. Kaur, G.; Pickrell, G.; Sriranganathan, N.; Kumar, V.; Homa, D. Review and the State of the Art: Sol–Gel and Melt Quenched Bioactive Glasses for Tissue Engineering. J. Biomed. Mater. Res.—Part B Appl. Biomater. 2016, 104, 1248–1275.

16. Ciraldo, F.E.; Boccardi, E.; Melli, V.; Westhauser, F.; Boccaccini, A.R. Tackling Bioactive Glass Excessive in Vitro Bioreactivity: Preconditioning Approaches for Cell Culture Tests. Acta Biomater. 2018, 75, 3–10.

17. Williams, D.F. On the Mechanisms of Biocompatibility. Biomaterials 2008, 29, 2941–2953.

18. Franz, S.; Rammelt, S.; Scharnweber, D.; Simon, J.C. Immune Responses to Implants—A Review of the Implications for the Design of Immunomodulatory Biomaterials. Biomaterials 2011, 32, 6692–6709.

19. Cappellano, G.; Ploner, C.; Lobenwein, S.; Sopper, S.; Hoertnagl, P.; Mayerl, C.; Wick, N.; Pierer, G.; Wick, G.; Wolfram, D. Immunophenotypic Characterization of Human T Cells after in Vitro Exposure to Different Silicone Breast Implant Surfaces. PLoS ONE 2018, 13, e0192108.

20. Chraniuk, M.; Panasiuk, M.; Hovhannisyan, L.; Zoł˛edowska, S.; Nidzworski, D.; Ciołek, L.; Wo´zniak, A.; Jaegermann, Z.; Biernat, M.; Gromadzka, B. The Preliminary Assessment of New Biomaterials Necessitates a Comparison of Direct and Indirect Cytotoxicity Methodological Approaches. Polymers 2022, 14, 4522.

21. Zheng, K.; Niu, W.; Lei, B.; Boccaccini, A.R. Immunomodulatory Bioactive Glasses for Tissue Regeneration. Acta Biomater. 2021, 133, 168–186.

22. Owen, J.A.; Punt, J.; Stranford, S.A.; Jones, P.P.; Kuby, J. Kuby Immunology, 8th ed.; W.H. Freeman: New York, NY, USA, 2019.

23. Lozano-Ojalvo, D.; López-Fandiño, R.; López-Expósito, I. PBMC-derived T cells. In The Impact of Food Bioactives on Health: In Vitro and Ex Vivo Models; Chapter 16; Springer: Cham, Switzerland, 2015.

24. Zhao, Z.; Zhao, Q.; Gu, B.; Yin, C.; Shen, K.; Tang, H.; Xia, H.; Zhang, X.; Zhao, Y.; Yang, X.; et al. Minimally Invasive Implantation and Decreased Inflammation Reduce Osteoinduction of Biomaterial. Theranostics 2020, 10, 3533.

25. Khassawna, T.E.; Serra, A.; Bucher, C.H.; Petersen, A.; Schlundt, C.; Könnecke, I.; Malhan, D.; Wendler, S.; Schell, H.; Volk, H.D.; et al. T Lymphocytes Influence the Mineralization Process of Bone. Front. Immunol. 2017, 8, 562.

26. Grassi, F.; Cattini, L.; Gambari, L.; Manferdini, C.; Piacentini, A.; Gabusi, E.; Facchini, A.; Lisignoli, G. T Cell Subsets Differently Regulate Osteogenic Differentiation of Human Mesenchymal Stromal Cells in Vitro. J. Tissue Eng. Regen. Med. 2016, 10, 305–314.

27. Cochis, A.; Barberi, J.; Ferraris, S.; Miola, M.; Rimondini, L.; Vernè, E.; Yamaguchi, S.; Spriano, S. Competitive Surface Colonization of Antibacterial and Bioactive Materials Doped with Strontium and/or Silver Ions. Nanomaterials 2020, 10, 120.

28. Miola, M.; Verné, E. Bioactive and Antibacterial Glass Powders Doped with Copper by Ion-Exchange in Aqueous Solutions. Materials 2016, 9, 405.

29. Tang, A.; Ren, Q.; Wu, Y.; Wu, C.; Cheng, Y. Investigation into the Antibacterial Mechanism of Biogenic Tellurium Nanoparticles and Precursor Tellurite. Int. J. Mol. Sci. 2022, 23, 11697.

30. Kang, K.; Lim, D.H.; Choi, I.H.; Kang, T.; Lee, K.; Moon, E.Y.; Yang, Y.; Lee, M.S.; Lim, J.S. Vascular Tube Formation and Angiogenesis Induced by Polyvinylpyrrolidone-Coated Silver Nanoparticles. Toxicol. Lett. 2011, 205, 227–234.

31. Xie, H.; Kang, Y. Role of Copper in Angiogenesis and Its Medicinal Implications. Curr. Med. Chem. 2009, 16, 1304–1314.

32. Miola, M.; Massera, J.; Cochis, A.; Kumar, A.; Rimondini, L.; Vernè, E. Tellurium: A New Active Element for Innovative Multifunctional Bioactive Glasses. Mater. Sci. Eng. C 2021, 123, 111957.

33. Lallukka, M.; Houaoui, A.; Miola, M.; Miettinen, S.; Massera, J.; Verné, E. In Vitro Cytocompatibility of Antibacterial Silver and Copper-Doped Bioactive Glasses. Ceram. Int. 2023, 49, 36044–36055.

34. Ferraris, S.; Yamaguchi, S.; Barbani, N.; Cazzola, M.; Cristallini, C.; Miola, M.; Vernè, E.; Spriano, S. Bioactive Materials: In Vitro Investigation of Different Mechanisms of Hydroxyapatite Precipitation. Acta Biomater. 2020, 102, 468–480.

35. Lallukka, M.; Miola, M.; Najmi, Z.; Cochis, A.; Spriano, S.; Rimondini, L.; Verné, E. Cu-Doped Bioactive Glass with Enhanced in Vitro Bioactivity and Antibacterial Properties. Ceram. Int. 2024, 50, 5091–5103.

36. Mehrabi, T.; Mesgar, A.S.; Mohammadi, Z. Bioactive Glasses: A Promising Therapeutic Ion Release Strategy for Enhancing Wound Healing. ACS Biomater. Sci. Eng. 2020, 6, 5399–5430.

37. Pajares-Chamorro, N.; Wagley, Y.; Maduka, C.V.; Youngstrom, D.W.; Yeger, A.; Badylak, S.F.; Hammer, N.D.; Hankenson, K.; Chatzistavrou, X. Silver-Doped Bioactive Glass Particles for in Vivo Bone Tissue Regeneration and Enhanced Methicillin-Resistant Staphylococcus Aureus (MRSA) Inhibition. Mater. Sci. Eng. C 2021, 120, 111693.

38. Bari, A.; Bloise, N.; Fiorilli, S.; Novajra, G.; Vallet-Regí, M.; Bruni, G.; Torres-Pardo, A.; González-Calbet, J.M.; Visai, L.; Vitale-Brovarone, C. Copper-

Containing Mesoporous Bioactive Glass Nanoparticles as Multifunctional Agent for Bone Regeneration. Acta Biomater. 2017, 55, 493–504.

39. Zhang, Y.; Hu, M.; Zhang, W.; Zhang, X. Construction of Tellurium-Doped Mesoporous Bioactive Glass Nanoparticles for Bone Cancer Therapy by Promoting ROS-Mediated Apoptosis and Antibacterial Activity. J. Colloid Interface Sci. 2022, 610, 719–730.

40. Collins, J.F.; Prohaska, J.R.; Knutson, M.D. Metabolic Crossroads of Iron and Copper. Nutr. Rev. 2010, 68, 133–147.

41. Haase, H.; Fahmi, A.; Mahltig, B. Impact of Silver Nanoparticles and Silver Ions on Innate Immune Cells. J. Biomed. Nanotechnol. 2014, 10, 1146–1156.

42. Sandoval, J.M.; Verrax, J.; Vásquez, C.C.; Calderon, P.B. A Comparative Study of Tellurite Toxicity in Normal and Cancer Cells. Mol. Cell. Toxicol. 2012, 8, 327–334.

43. Hardes, J.; Streitburger, A.; Ahrens, H.; Nusselt, T.; Gebert, C.; Winkelmann, W.; Battmann, A.; Gosheger, G. The Influence of Elementary Silver versus Titanium on Osteoblasts Behaviour in Vitro Using Human Osteosarcoma Cell Lines. Sarcoma 2007, 2007, 026539.

44. Gosheger, G.; Hardes, J.; Ahrens, H.; Streitburger, A.; Buerger, H.; Erren, M.; Gunsel, A.; Kemper, F.H.; Winkelmann, W.; Von Eiff, C. Silver-Coated Megaendoprostheses in a Rabbit Model—An Analysis of the Infection Rate and Toxicological Side Effects. Biomaterials 2004, 25, 5547–5556.

45. Wan, A.T.; Conyers, R.A.J.; Coombs, C.J.; Masterton, J.P. Determination of Silver in Blood, Urine, and Tissues of Volunteers and Burn Patients. Clin. Chem. 1991, 37, 1683–1687.

46. Choban, P.S.; Marshall, W.J. Leukopenia Secondary to Silver Sulfadiazine: Frequency, Characteristics and Clinical Consequences. Am. Surg. 1987, 53, 515–517.

47. Tozzi, P.; Al-Darweesh, A.; Vogt, P.; Stumpe, F. Silver-Coated Prosthetic Heart Valve: A Double-Bladed Weapon. Eur. J. Cardio-Thoracic Surg. 2001, 19, 729–731.

48. McCauley, R.L.; Linares, H.A.; Pelligrini, V.; Herndon, D.N.; Robson, M.C.; Heggers, J.P. In Vitro Toxicity of Topical Antimicrobial Agents to Human Fibroblasts. J. Surg. Res. 1989, 46, 267–274.

49. Kuroyanagi, Y.; Kim, E.; Shioya, N. Evaluation of a Synthetic Wound Dressing Capable of Releasing Silver Sulfadiazine. J. Burn Care Rehabil. 1991, 12, 106–115.

50. Dhinasekaran, D.; Kumar, A. Fabrication of bioactive structures from sol-gel derived bioactive glass. In Bioactive Glasses and Glass-Ceramics: Fundamentals and Applications; Chapter 6; Wiley: Hoboken, NJ, USA, 2022.

51. Adusei, K.M.; Ngo, T.B.; Sadtler, K. T Lymphocytes as Critical Mediators in Tissue Regeneration, Fibrosis, and the Foreign Body Response. Acta Biomater. 2021, 133, 17–33.

52. Wolfram, D.; Rabensteiner, E.; Grundtman, C.; Böck, G.; Mayerl, C.; Parson, W.; Almanzar, G.; Hasenöhrl, C.; Piza-Katzer, H.;Wick, G. T Regulatory Cells and TH17 Cells in Peri-Silicone Implant Capsular Fibrosis. Plast. Reconstr. Surg. 2012, 129, 327e–337e.

53. Dey, A.; Manna, S.; Kumar, S.; Chattopadhyay, S.; Saha, B.; Roy, S. Immunostimulatory Effect of Chitosan Conjugated Green Copper Oxide Nanoparticles in Tumor Immunotherapy. Cytokine 2020, 127, 154958.

54. Huang, C.; Chen, X.; Xue, Z.; Wang, T. Effect of Structure: A New Insight into Nanoparticle Assemblies from Inanimate to Animate. Sci. Adv. 2020, 6, eaba1321.

55. Schuhladen, K.; Stich, L.; Schmidt, J.; Steinkasserer, A.; Boccaccini, A.R.; Zinser, E. Cu, Zn Doped Borate Bioactive Glasses: Antibacterial Efficacy and Dose-Dependent: In Vitro Modulation of Murine Dendritic Cells. Biomater. Sci. 2020, 8, 2143–2155.

56. Takatsu, K. Interleukin-5 and IL-5 Receptor in Health and Diseases. Proc. Japan Acad. Ser. B Phys. Biol. Sci. 2011, 87, 463–485.

57. Pelaia, C.; Paoletti, G.; Puggioni, F.; Racca, F.; Pelaia, G.; Canonica, G.W.; Heffler, E. Interleukin-5 in the Pathophysiology of Severe Asthma. Front. Physiol. 2019, 10, 1514.

58. Marone, G.; Granata, F.; Pucino, V.; Pecoraro, A.; Heffler, E.; Loffredo, S.; Scadding, G.W.; Varricchi, G. The Intriguing Role of Interleukin 13 in the Pathophysiology of Asthma. Front. Pharmacol. 2019, 10, 01387.

59. Wu, A.Y.; Sur, S.; Grant, J.A.; Tripple, J.W. Interleukin-4/Interleukin-13 versus Interleukin-5: A Comparison of Molecular Targets in Biologic Therapy for the Treatment of Severe Asthma. Curr. Opin. Allergy Clin. Immunol. 2019, 19, 30–37.

60. Asikainen, A.J.; Hagström, J.; Sorsa, T.; Noponen, J.; Kellomäki, M.; Juuti, H.; Lindqvist, C.; Hietanen, J.; Suuronen, R. Soft Tissue Reactions to Bioactive Glass 13-93 Combined with Chitosan. J. Biomed. Mater. Res.—Part A 2007, 83, 530–537.

61. Gschwandtner, M.; Derler, R.; Midwood, K.S. More Than Just Attractive: How CCL2 Influences Myeloid Cell Behavior Beyond Chemotaxis. Front. Immunol. 2019, 10, 491100.

62. Chen, R.; Ma, L.; Jiang, C.; Zhang, S. Expression and Potential Role of CCL4 in CD8+T Cells in NSCLC. Clin. Transl. Oncol. 2022, 24, 2420–2431.

63. Kobayashi, S.D.; Voyich, J.M.; Burlak, C.; DeLeo, F.R. Neutrophils in the Innate Immune Response. Arch. Immunol. Ther. Exp. 2005, 53, 505.

64. Jones, J.A.; Chang, D.T.; Meyerson, H.; Colton, E.; Il, K.K.; Matsuda, T.; Anderson, J.M. Proteomic Analysis and Quantification of Cytokines and Chemokines from Biomaterial Surface-Adherent Macrophages and Foreign Body Giant Cells. J. Biomed. Mater. Res.—Part A 2007, 83, 585–596.

65. Chang, D.T.; Jones, J.A.; Meyerson, H.; Colton, E.; Il, K.K.; Matsuda, T.; Anderson, J.M. Lymphocyte/Macrophage Interactions: Biomaterial Surface-Dependent Cytokine, Chemokine, and Matrix Protein Production. J. Biomed. Mater. Res.—Part A 2008, 87, 676–687.

66. Wick, G.; Grundtman, C.; Mayerl, C.; Wimpissinger, T.F.; Feichtinger, J.; Zelger, B.; Sgonc, R.; Wolfram, D. The Immunology of Fibrosis. Annu. Rev. Immunol. 2013, 31, 107–135.

67. Love, R.J.; Jones, K.S. Biomaterials, Fibrosis, and the Use of Drug Delivery Systems in Future Antifibrotic Strategies. Crit. Rev. Biomed. Eng. 2009, 37, 259–281.

68. Steen, E.H.; Wang, X.; Balaji, S.; Butte, M.J.; Bollyky, P.L.; Keswani, S.G. The Role of the Anti-Inflammatory Cytokine Interleukin-10 in Tissue Fibrosis. Adv. Wound Care 2020, 9, 184–198.

69. Varmette, E.A.; Nowalk, J.R.; Flick, L.M.; Hall, M.M. Abrogation of the Inflammatory Response in LPS-Stimulated RAW 264.7 Murine Macrophages by Zn- and Cu-Doped Bioactive Sol-Gel Glasses. J. Biomed. Mater. Res.—Part A 2009, 90, 317–325.

70. Barbeck, M.; Alkildani, S.; Mandlule, A.; Radenkovi´c, M.; Najman, S.; Stojanovi´c, S.; Jung, O.; Ren, Y.; Cai, B.; Görke, O.; et al. In Vivo Analysis of the Immune Response to Strontium- and Copper-Doped Bioglass. In Vivo 2022, 36, 2149–2165.

71. Weng, L.; Boda, S.K.; Teusink, M.J.; Shuler, F.D.; Li, X.; Xie, J. Binary Doping of Strontium and Copper Enhancing Osteogenesis and Angiogenesis of Bioactive Glass Nanofibers While Suppressing Osteoclast Activity. ACS Appl. Mater. Interfaces 2017, 9, 24484–24496.

72. Lin, R.; Deng, C.; Li, X.; Liu, Y.; Zhang, M.; Qin, C.; Yao, Q.; Wang, L.; Wu, C. Copper-Incorporated Bioactive Glass-Ceramics Inducing Anti-Inflammatory Phenotype and Regeneration of Cartilage/Bone Interface. Theranostics 2019, 9, 6300.

73. Rau, J.V.; Curcio, M.; Raucci, M.G.; Barbaro, K.; Fasolino, I.; Teghil, R.; Ambrosio, L.; De Bonis, A.; Boccaccini, A.R. Cu-Releasing Bioactive Glass Coatings and Their in Vitro Properties. ACS Appl. Mater. Interfaces 2019, 11, 5812–5820.

74. Chen, Y.; Guan, M.; Ren, R.; Gao, C.; Cheng, H.; Li, Y.; Gao, B.; Wei, Y.; Fu, J.; Sun, J.; et al. Improved Immunoregulation of Ultra-Low-Dose Silver Nanoparticle-Loaded TiO2 Nanotubes via M2 Macrophage Polarization by Regulating GLUT1 and Autophagy. Int. J. Nanomedicine 2020, 15, 2011–2026.

75. Kokubo, T.; Takadama, H. How Useful Is SBF in Predicting in Vivo Bone Bioactivity? Biomaterials 2006, 27, 2907–2915.

76. Breen, E.J.; Tan, W.; Khan, A. The Statistical Value of Raw Fluorescence Signal in Luminex XMAP Based Multiplex Immunoassays. Sci. Rep. 2016, 6, 26996.